UNIVERSITY OF SOUTHAMPTON

FACULTY OF ENGINEERING AND THE ENVIRONMENT

Aeronautics, Astronautics and Computational Engineering

Modelling and Design of Inductively Coupled Radio Frequency Gridded Ion Thrusters with an Application to Ion Beam Shepherd Type Space Missions

by

Mantas Dobkevicius

Thesis for the degree of Doctor of Philosophy

June 2017

UNIVERSITY OF SOUTHAMPTON

ABSTRACT

FACULTY OF ENGINEERING AND THE ENVIRONMENT
Aeronautics, Astronautics and Computational Engineering

Doctor of Philosophy

MODELLING AND DESIGN OF INDUCTIVELY COUPLED RADIO FREQUENCY
GRIDDED ION THRUSTERS WITH AN APPLICATION TO ION BEAM
SHEPHERD TYPE SPACE MISSIONS

by Mantas Dobkevicius

Recently proposed space missions such as Darwin, LISA and NGGM have encouraged the development of electric propulsion thrusters capable of operating in the micro-Newton (μN) thrust range. To meet these requirements, radio frequency (RF) gridded ion thrusters need to be scaled down to a few centimetres in size. Due to the small size of these thrusters, it is important to accurately determine the thermal and performance parameters. To achieve this, an RF ion thruster model has been developed, composed of plasma discharge, 2D axisymmetric ion extraction, 3D electromagnetic, 3D thermal and RF circuit models. The plasma discharge model itself is represented using 0D global, 2D axisymmetric and 3D molecular neutral gas, and Boltzmann electron transport sub-models. This is the first time such a holistic/comprehensive model has been created. The model was successfully validated against experimental data from the RIT 3.5 thruster, developed for the NGGM mission. Afterwards, the computational model was used to design an RF gridded ion thruster for an Ion Beam Shepherd (IBS) type space debris removal mission. Normally, the IBS method requires two thrusters: one for impulse transfer (IT) and one for impulse compensation (IC). This thesis proposes a novel thruster concept for the IBS type missions where a single Double-Sided Thruster (DST) simultaneously producing ion beams for the IT and IC purposes is used. The advantage of DST design is that it requires approximately half the RF power compared with two single-ended thrusters and it has a much simpler sub-system architecture, lower cost, and lower total mass. Such a DST thruster was designed, built and tested, with the requirements and constraints taken from the LEOSWEEP space debris removal mission. During the experimental campaign, a successful extraction of two ion beams was achieved. The thesis has shown that it is possible to control the thrust magnitudes from the IT and IC sides by varying the number of apertures in each ion optics system, proving that the DST concept is a viable alternative for the LOESWEEP mission.

Contents

List of Figures

List of Tables

Nomenclature

Greek symbols

α	Reaction rate [1/m^{3}s]
β	Ionisation fraction [1]
Γ	Reflection coefficient [1]; Particle flux [1/m^{2}s]
Γ_b	Beam flatness [1]
δ	Skin depth [m]
δ_B	Ion confinement factor [1]
ϵ	Energy [J]; Emissivity [1]
ϵ_p	Plasma permittivity [F/m]
η	Efficiency [1] or [%]
η_c	Clausing factor [1]
θ	Angle [°]
θ_d	Beam divergence half-angle [°]
κ	Thermal conductivity [W/mK]
λ	Wavelength [m]; Mean free path [m]
μ	Electron mobility [m^2/Vs]
ν	Collision frequency [Hz]; Poisson's ratio [1]
ρ	Charge density [C/m^3]
σ	Electrical conductivity [S/m]; Cross-section [m^2]
σ_{asp}	RMS contact surface asperities' height [m]
σ_k	Collision cross section for species k [m^2]
σ_m	Total scattering collision cross section [m^2]
σ_p	Plasma electrical conductivity [S/m]
σ_s	Total ion scattering cross section [m^2]
ϕ	Floating potential [V]
ϕ_p	Plasma floating potential [V]
ϕ_s	Plasma sheath potential [V]
Ψ	Stochastic heating parameter [1]
ω	Radial frequency [Hz]

Roman symbols

A	Area [m^2]
B	Magnetic field [T]; Susceptance [S]
C	Capacitance [F]
D	Electric displacement field [C/m^2]
D_a	Ion diffusion coefficient [m^2/s]
d	Distance [m]
E	Electric field [V/m]; Elastic modulus [Pa]
f	Oscillation frequency [Hz]; Fraction [1]
f_{os}	Screen grid open area fraction [1]
f_{oa}	Accel grid open area fraction [1]
G	Conductance [S]; Incident molecular flux [1/m^{2}s]
h	Ion density ratio [1]
I	Current [A]
I_{sp}	Specific impulse [s]
J	Current density [A/m^2]; Emitted molecular flux [1/m^{2}s]
K	Rate coefficient [m^3/s]; Reflected molecular flux [1/m^{2}s]
k_f	Field coupling coefficient [1]
L	Inductance [H]
L_{thr}	Thruster inductance [H]
M	Mass [kg]
$\tilde{M}$	Complex mutual inductance [H]
M_i	Ion mass [kg]
m_{asp}	RMS contact surface asperities' slope [rad]
m_e	Electron mass [kg]
$\dot{m}$	Propellant mass flow rate [kg/s] or [sccm]
n	Density [1/m^3]
P	Power [W]
p	Pressure [Pa] or [mTorr]
Q	Heat source [W]
R	Resistance [Ω]
R_c	Coil resistance [Ω]
R_p	Plasma resistance [Ω]
R'_{thr}	Total thruster resistance with plasma [Ω]
R'_p	Induced plasma resistance [Ω]
R'_0	Thruster resistance without plasma [Ω]
R^2	Coefficient of determination [1]
r	Radius [m]
S	Heat flux [W/m^2]
s	Sheath thickness [m]

T	Thrust [N]; Temperature [K] or [°C]
T_e	Electron temperature [K] or [eV]
T_{eff}	Effective ion optics transparency [1]
U	Potential [V]
U_c	Thermal contact conductance [W/m^{2}K]
u_B	Bohm velocity [m/s]
V	Voltage [V]
V_d	Discharge chamber volume [m^3]
v	Velocity [m/s]
W	Absorbed/lost power [W]
w	Material's work function [eV]
Z	Complex impedance [Ω]
Y	Complex admittance [S]
X	Reactance [S]
Q	Q-factor [1]; Heat source [W]

Constants

c	Speed of light in vacuum [299792458 m/s]
e	Elementary charge [1.619×10^{-19} C]
g	Earth's gravitational constant [9.807 m/s^2]
g_0	Amperes to sccm [13.938 sccm/A]
k_B	Boltzmann constant [$1.38064852 \times 10^{-23}$ J/K]
m_e	Electron mass [$9.10938291 \times 10^{-31}$ kg]
ϵ_0	Permittivity of free space [$8.85418782 \times 10^{-12}$ F/m]
μ_0	Permeability of free space [$1.25663706 \times 10^{-6}$ N/A^2]
σ	Stefan-Boltzmann constant [5.670367×10^{-8} W/m^{2}K^4]

Acronyms

AC	Alternating Current
Artemis	Advanced Relay and TEchnology MISsion
AUX	Auxiliary
C-C	Carbon-Carbon
CEX	Charge Exchange
CP	Cryopanel
DC	Direct Current
DQ	Data Acquisition
DST	Double-Sided Thruster
EEDF	Electron Energy Distribution Function
EM	Electromagnetic
EMF	Electromotive Force
EP	Electric Propulsion
EPS	Electric Propulsion Subsystem
EURECA	European Retrievable Carrier
GEO	Geostationary Equatorial Orbit
GIT	Gridded Ion Thruster
GNSS	Global Navigation Satellite System
GOCE	Gravity field and steady-state Ocean Circulation Explorer
GRACE	Gravity Recovery And Climate Experiment
HF	High Frequency
IBS	Ion Beam Shepherd
IC	Impulse Compensation
ICT	Impulse Compensation Thruster
IT	Impulse Transfer
ITT	Impulse Transfer Thruster
LEO	Low Earth Orbit
LEOSWEEP	Improving Low Earth Orbit Security with Enhanced EP
LISA	Laser Interferometer Space Antenna
MFC	Mass Flow Controller
NGGM	Next-Generation Gravity Mission
NSTAR	NASA Solar EP Technology Application Readiness

NTR	Neutraliser
PLL	Phase-Locked Loop
PPU	Power Processing Unit
PS	Power Supply
PSU	Power Supply Unit
RF	Radio Frequency
RFG	Radio Frequency Generator
RIT	Radio Frequency Ion Thruster
RTG	Radioisotope Thermoelectric Generator
RMS	Root Mean Square
SCCM	Standard Cubic Centimetres per Minute
SHV	Safe High Voltage
SMART	Small Missions for Advanced Research in Technology-1
SSG	Secondary Star Ground
SST	Satellite-to-Satellite Tracking
TS	Temperature Sensor

Declaration of Authorship

I, Mantas Dobkevicius, declare that the thesis entitled *Modelling and Design of Inductively Coupled Radio Frequency Gridded Ion Thrusters with an Application to Ion Beam Shepherd Type Space Missions* and the work presented in the thesis are both my own, and have been generated by me as the result of my own original research. I confirm that:

- this work was done wholly or mainly while in candidature for a research degree at this University;

- where any part of this thesis has previously been submitted for a degree or any other qualification at this University or any other institution, this has been clearly stated;

- where I have consulted the published work of others, this is always clearly attributed;

- where I have quoted from the work of others, the source is always given. With the exception of such quotations, this thesis is entirely my own work;

- I have acknowledged all main sources of help;

- where the thesis is based on work done by myself jointly with others, I have made clear exactly what was done by others and what I have contributed myself;

- parts of this work have been published as:

  ◇ **Journal papers**

    – Dobkevicius, M. and Feili, D. (2016). A coupled performance and thermal model for radio frequency gridded ion thrusters. *Eur. Phys. J. D*, 70 (11):227;
    – Dobkevicius, M. and Feili, D. (2017). Multi-physics model for radio frequency gridded ion thruster performance. *Journal of Propulsion and Power*, 0 (0):0;
    – Dobkevicius, M. and Feili, D. Double-sided ion thruster for contactless space debris removal: design and experimental results. *Journal of Propulsion and Power*, (in preparation);
    – Dobkevicius, M., Lotz, B., and Feili, D. Computational and experimental analysis of radio-frequency gridded ion thrusters with atmospheric gases as a propellant. *Journal of Propulsion and Power*, (in preparation).

◇ **Conference proceedings**

– Dobkevicius, M., Feili, D., and Müller, J. (2005). Comprehensive radio frequency ion thruster electromagnetic and thermal modelling. In *30th ISTS, 34th IEPC, 6th NSAT Joint Conference*, 04-10 July, Kobe, Japan;

– Dobkevicius, M., Feili, D., Smirnova, M., and Mingo, A. (2016). Double-sided ion thruster for contactless space debris removal. In *Space Propulsion 2016 Conference*, 02-06 May, Rome, Italy.

Signed:..

Date:..

Acknowledgements

I would like to start by thanking Dr Davar Feili for initiating the project, and for obtaining funding and equipment when needed. Then, I would like to thank Professor Neil D Sandham for allocating funding to manufacture the titanium ion optics system, for proofreading my work and for guiding me towards the finish of the PhD. Furthermore, I would like to thank and acknowledge Dr Benjamin Lotz from Cutting Edge Coatings (CEC) for preparing the RIT 3.5 test set-up in Giessen, Germany. I would also like to thank Benjamin for hospitality and for helping me when issues arose with the experimental set-up. My sincere thanks goes to Ms Maria Smirnova from TransMIT for helping me design the DST and, especially, for applying the aluminium tape on the SILUX screen grid. I would also like to thank Maria for giving me suggestions about the DST experimental campaign.

Also, I would like to thank Ms Aloha Mingo from TransMIT for dealing with suppliers and manufacturers when ordering DST parts. A big thanks goes to Mr Thomas Nimmerfroh for manufacturing the RF coil and the electrodes. Finally, I would like to thank TransMIT for providing funding to build the DST and for lending a majority of the experimental equipment needed to perform the DST experimental campaign at the University of Southampton. I also wish to thank Mr Johann Müller for spending his time teaching me the key points of RF thruster operation. His help was especially useful while I was trying to understand how the radio frequency generators work.

On a personal note, I would like to thank my family for supporting me morally and financially over all these years I have been a student. Especially, I would like to thank my mum who always believed in me and did everything she could to help me succeed. Last but not least, I would like to thank my wonderfull girlfriend Kristina for sticking with me through ups and downs I experienced while writing this thesis. Your love was one of the reasons I kept pushing myself and never stopped going forward. I would also like to thank all my friends who were with me either in the U.K. or in Lithuania. Finally, I would like to acknowledge that the research presented in this PhD was supported by the Engineering and Physical Sciences Research Council (EPSRC): funding reference - 1362213.

1

Introduction

In 1907 Goddard (1907) was first to mention a possibility of using electricity to produce thrust (Choueiri, 2004). He argued that the produced thrust would be sufficient to accelerate a spacecraft to very high velocities. Later, similar thoughts were put forward by Tsiolkovsky as well (Choueiri, 2004). However, only in 1968, a comprehensive description of the physics involved in electric propulsion (EP) was given by Jahn (1968). Such an interest in electric propulsion was spawned by the dreams of interplanetary travel. Scientists realised that using electricity it was possible to achieve very high exhaust velocities of the working gas, which meant a highly efficient propellant utilisation. Therefore, less propellant was needed compared to, for example, chemical propulsion, and the saved mass could be replaced with a useful payload. The first demonstration of EP in space occurred in 1964 when a pair of gridded ion engines using caesium and mercury were launched on the NASA's SERT 1 spacecraft (Kim et al., 2001). In 1971, for the first time, the USSR flew a pair of SPT-60 Hall thrusters for station keeping of the Meteor satellite (Bober et al., 1991). Since then, Russia has operated hundreds of Halls thrusters and is planning to extensively use Hall thrusters on future satellites.

In 1997, the U.S. began the commercial use EP with the launch of a Hughes XIPS gridded ion thruster using xenon. A major cornerstone in the application of EP for deep space missions was NASA's NSTAR ion thruster launched on board the Deep Space 1 spacecraft in 1998 (Brophy, 2002). More recent applications of EP include the JAXA's Hayabusa asteroid sample return mission using microwave ion thrusters

(Kuninaka, 2005) and ESA's SMART-1 (Koppel and Estublier, 2005) mission to the moon using Hall thrusters. Additionally, radio frequency (RF) gridded ion thrusters were used on board the Artemis (Killinger et al., 2007) spacecraft. Dawn (Garner et al., 2013) and BepiColombo (Snyder et al., 2012) are the two latest missions that have used EP for space exploration. The future of electric propulsion looks promising, with plans to employ it for missions aimed at asteroid mining (Brophy and Muirhead, 2013) and Mars sample return (Williams and Carroll, 2000).

Different electric propulsion systems exist depending on the way the exhaust gas is accelerated. The main three propulsion systems as defined by Jahn (1968) are:

- *electrothermal* - the propellant is heated electrically and accelerated through a specially designed nozzle;

- *electrostatic* - the propellant particles are first ionised and then accelerated using electric fields;

- *electromagnetic* - the ionised propellant particles are accelerated by interactions of external and internal magnetic fields with electric currents resulting from the ionised particle streams.

In this thesis, only the electrostatic method will be investigated. In particular, the analysis will be aimed at electrostatic thrusters that focus and accelerate ions using perforated grids biased at high potential. Such engines are commonly referred to as gridded ion thrusters (GIT). GIT are further sub-divided based on the way they produce plasma. The main ones in the direct current (DC) class are the ring-cusp (Wirz and Goebel, 2008) and Kaufman (Monterde et al., 1997) type gridded ion thrusters. They both use hollow cathodes to produce primary electrons inside the discharge chamber for gas ionisation. However, they differ in the way the magnetic fields are utilised to achieve plasma confinement. The alternating current (AC) class is comprised of RF (Groh and Loebt, 1991) and microwave frequency (Takao et al., 2014) gridded ion thrusters. They use oscillating magnetic fields to both ionise and confine the plasma; the difference is mainly in the operational frequency. In the early sixties, Professor Horst Loeb at the 1st Physical Institute of Justus-Liebig-University Giessen was one of the first to successfully utilise radio frequency waves to generate plasma for EP (Meusemann and Winter, 2005). Since then, a whole family of RF ion thrusters (RIT) with ioniser diameters ranging in size from 2.5 to 35 cm has been developed by Airbus, and some of the thrusters have been employed for space missions (Groh and Loebt, 1991).

One of the main thrusters from the RIT family is called the RIT 10. It was successfully used for ARTEMIS and EURECA missions (Leiter et al., 2001). The RIT 10 exhibits a nominal thrust of 15 mN and a specific impulse of 3,300 s (Leiter et al., 2001). The RIT 22, RIT XT and RIT EVO are more advanced thrusters designed and built on the RIT 10

heritage (Bassner et al., 2001). For instance, the RIT XT is a high-performance advanced thruster developed to act as a primary propulsion unit for interplanetary missions and house-keeping of heavy satellites in the geosynchronous equatorial orbit (GEO) (Leiter et al., 2009). It is able to produce thrust in the range of 50 to 150 mN and has a specific impulse of 4,200 - 4,500 s. Recently, there has been a sustained interest in scaling down the RIT family engines to micro-Newton (μN) thrust levels. This was done to meet the requirements of such future missions as LISA (Leiter et al., 2011) and Darwin (Kilter and Karlsson, 2004), where high precision thrust control is needed for formation flying or attitude control. The recently launched GOCE (Wallace et al., 2011) mission, for instance, required a precise thrust control to compensate for the atmospheric drag and to keep the spacecraft in the prescribed orbit.

1.1 Miniature ion thrusters

In this section, the Next-Generation Gravity Mission (NGGM) will be used as an example mission of where scaled-down thrusters are needed to accomplish the mission requirements (Smirnova et al., 2016a). The NGGM is a conceptual mission currently being studied by the European Space Agency (ESA). The NGGM mission plans to use a low-low satellite-to-satellite tracking (SST) technique to monitor the temporal variations of the Earth's gravity field over a long time span. Figure 1.1 indicates the main principles behind the NGGM mission (NG2 team, 2011).
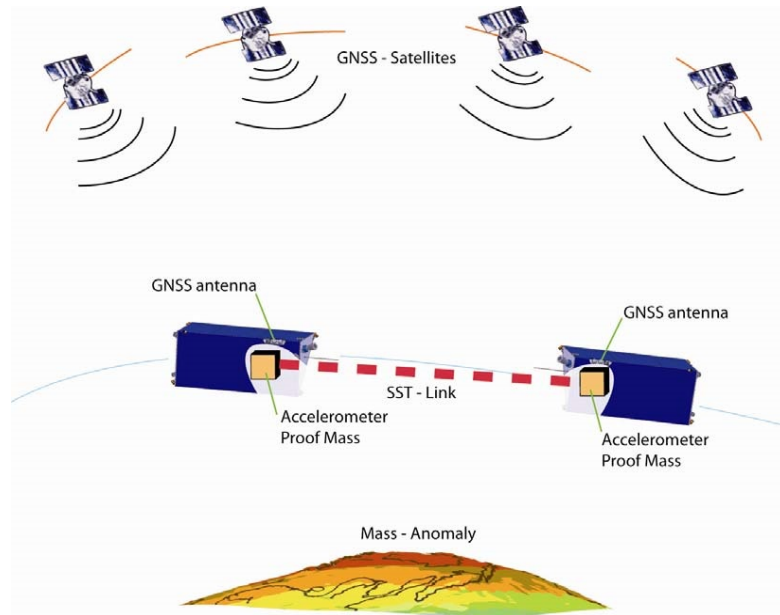
Figure 1.1: Principles behind the NGGM mission concept with representations of the satellite-to-satellite tracking (SST) and the global navigation satellite system (GNSS) (NG2 team, 2011).

The main scientific parameters of the NGGM are similar to those of the Gravity Recovery And Climate Experiment (GRACE) mission (Tapley et al., 2004), but with a much higher spatial resolution of around 100 km, which is comparable to that of the GOCE mission. Additionally, the NGGM is expected to provide higher temporal resolution compared to that of the GRACE mission which is limited to approximately one-month intervals between successive gravity field maps. The main objectives of the mission are to significantly improve the understanding of the mass change of ice sheets and glaciers, continental water cycles, ocean masses dynamics, solid-earth deformations and other geophysical phenomena. The NGGM mission plans to achieve these objectives through observations of the mass transportation within the Earth's system as derived from the consequent temporal variations of the gravity field (NG2 team, 2011; Tapley et al., 2004).

One of the key technologies needed to enable the NGGM mission is a micro-propulsion thruster system. The requirements imposed to such a propulsion system are summarised in the list below (Smirnova et al., 2016a):

- satellite orbit maintenance at its operational altitude;

- satellite loose formation control;

- implementation of the drag-free control at the level of each satellite;

- attitude control of each satellite;

- maintenance of the inter-satellite laser link.

The latest results from the NGGM preparatory studies have identified the preliminary requirements for the propulsion system. First, in order to cope with the large drag force and solar intensity variations encountered in such a long duration mission, a thrust dynamic range of over 40 is needed. Additionally, the thruster is required to have a low specific power for minimising the solar panel surface area and a high specific impulse for reducing propellant consumption. For instance, currently, around 50 kg of propellant mass is allocated for the mission lasting about 10 years. These and other requirements imposed on the micro-propulsion system by the NGMM mission are summarised in Table 1.1 (Feili et al., 2015a).

Electric propulsion was selected by the project team as the only type of propulsion system that could satisfy all the mission requirements as indicated in Table 1.1. In the end, the project team chose Dr Davar Feili to design an RF ion thruster for the mission. This was mainly because RF thrusters exhibit the required thrust dynamic range, have quick rise/fall times and a low specific power. Feili and his team developed a RIT 3.5 thruster that has a 3.5 cm diameter discharge chamber. The RIT 3.5 exhibits a thrust in the range between 50 μN and nearly 3 mN, a specific power of around 30 W/mN, and a specific impulse of up to 4,000 s (Feili et al., 2015a). However, due to the stringent

power, lifetime and thermal requirements, various modelling tools are still needed to optimise the thruster for the NGGM mission. Therefore, one of the goals of this thesis is to develop such modelling tools that could later be used to improve the RIT 3.5 thruster itself and to help design RF thrusters for other future space missions.

Parameter	Unit	Requirement
Minimum thrust	mN	0.05
Maximum thrust	mN	< 3
Thrust resolution	μN	0.5
Thrust noise		$< 1\mu\text{N}/\sqrt{\text{Hz}}$
Rise/fall time	ms	< 50
Slew rate	mN/s	> 0.5
Update command rate	Hz	10
Thrust non linearity		$< 2\%$
Lifetime	yr	> 10
Specific power	W/mN	< 40

Table 1.1: Requirements imposed by the NGGM mission on the micro-propulsion thruster.

1.2 Ion Beam Shepherd

Currently, there has been a lot of effort put into solving the space debris problem. It is estimated that there are around 6,000 tonnes and 15,000 trackable debris objects in the orbit (Bombardelli and Pelaez, 2011b). Bombardelli and Pelaez (2011b) have proposed an Ion Beam Shepherd (IBS) concept aimed at tackling the space debris problem. As Figure 1.2 illustrates, the IBS concept uses a highly collimated, neutralised ion beam produced by the primary propulsion system to generate a drag force on a debris object causing it to de-orbit (Bombardelli et al., 2011). The idea is to manoeuvre the debris object into a decay orbit. Once the debris is in the decay orbit, the atmospheric drag would cause the debris to come down. The issue with such an approach is to predict within a set certainty where the debris is going to come down, that is, to perform a controlled re-entry. To avoid casualties and destruction of property, the best place for debris to re-enter is over the South Pacific Ocean Unpopulated Area (SPOUA) (Kasai et al., 2015). Another option is raising the debris orbit to a disposal or a graveyard orbit. This option is especially relevant for debris objects in the GEO orbit.

A secondary propulsion system is also required to compensate for the thrust produced by the primary propulsion system and to match the satellite and debris orbits. The European Commission has financed a project called LEOSWEEP ("Improving Low Earth Orbit Security with Enhanced Electric Propulsion") that aims to demonstrate the first active space debris removal mission (Ruiz et al., 2014). The goal of the mission is to

de-orbit, using a controlled re-entry, a 1.5-ton Ukrainian rocket launcher upper-stage from a nearly polar low Earth orbit (LEO) in 170 days using the IBS method. Even though the initial IBS concept was aimed at targeting LEO objects, there are proposals to use the concept for GEO satellite de-orbiting and even asteroid deflection (Kitamura et al., 2011; Bombardelli and Pelaez, 2011a).
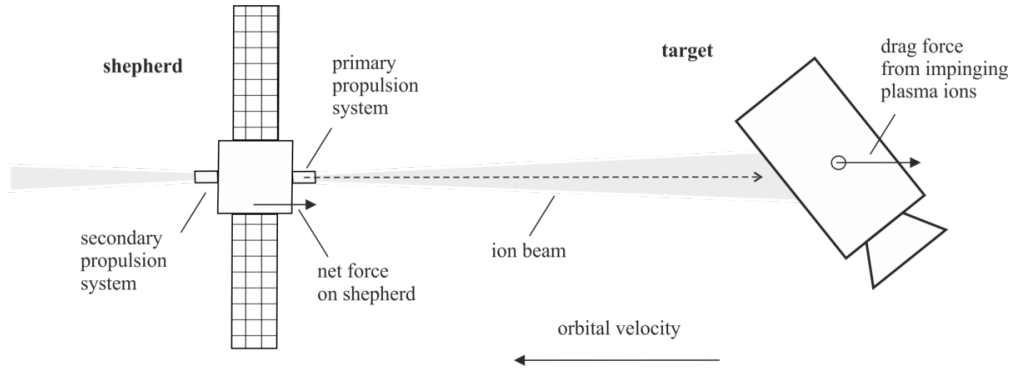
Figure 1.2: Principles behind the Ion Beam Shepherd space debris removal mission concept with indications of the shepherd satellite, the target debris, and the primary and secondary propulsion systems (Bombardelli and Pelaez, 2011b).

The LEOSWEEP project team has decided to use an RF gridded ion thruster designed by Feili et al. (2015b) for the primary propulsion system. An RF gridded thruster was chosen because it is capable of producing a beam with a divergence angle below 10°, which was necessary to have a high beam momentum transfer efficiency (Merino et al., 2011). Also, gridded ion thrusters have a high specific impulse ($\sim$ 3,000 s), which was needed to reduce the LEOSWEEP mission's total mass (Merino et al., 2011). The designed RF gridded ion thruster is expected to have a specific impulse of 5,261 s, a thrust of 31 mN and a divergence of 5 - 7° (Feili et al., 2015b). However, the team is yet to choose the secondary propulsion system needed to compensate for the 31 mN of thrust. Currently, a Hall thruster is thought to be the best candidate for this purpose. However, having two thrusters greatly complicates the design and increases costs. This thesis presents a novel thruster concept for the LEOSWEEP type missions where, instead of the proposed two-thruster design, a single Double-Sided Thruster (DST) simultaneously producing two ion beams is used. The beam from one side of the thruster is used for the impulse transfer, while the beam from another side is employed for the impulse compensation. Therefore, a single propulsion system is sufficient. The main advantage of such a design is a simpler sub-system architecture which results in a significantly reduced cost, weight, and complexity of the satellite.

1.3   Motivation for research and objectives

As already shown, electric propulsion thrusters have a variety of applications for space missions. Nevertheless, this thesis will focus only on the RF class thrusters. In particular, the RIT 3.5 thruster will be modelled and analysed. The main advantage of RF thrusters is their sub-system simplicity compared, for example, to ring-cusp thrusters. This is because RF thrusters do not require hollow cathodes for ionisation (Goebel and Katz, 2008) and have fewer power supplies. However, more information is needed regarding the power delivery to the plasma, thermal management and coil matching (Feili et al., 2009; Gartner et al., 2013). Furthermore, the current RIT thruster analysis tools use in-house software that is not available to everyone (Turkoz and Celik, 2014; Bauder et al., 2013; Takao et al., 2011). As a result, it is challenging to use such software because the user is not familiar with its inner workings. Therefore, one of the main aims of this thesis is to provide easily accessible and interpretable modelling tools for analysing RF thrusters.

The presence of accurate, comprehensive and easily interpretable models is especially important for scaled-down thrusters due to difficulty in measuring plasma parameters such as temperature, density and potential. For instance, since the RIT 3.5 discharge chamber is only a few centimetres in diameter, it precludes engineers from using usually applied interferometric measurements and probes to determine plasma properties (Winter et al., 2007). As a result, plasma properties have to be simulated based on the thruster's parameters that can be measured such as the screen grid current and input power. One could use in-depth plasma simulation tools, but these involve complicated codes that use fluid or kinetic equations to describe the behaviour of the plasma, take hours to solve and their accuracy is limited to the assumptions made in the model (Froese, 2007; Turkoz and Celik, 2014).

Furthermore, the Ion Beam Shepherd type missions require two propulsion systems to be installed on the shepherd satellite: one for the impulse transfer and one for the impulse compensation. This adds complexity and cost associated with the power processing unit (PPU) and the propellant supply system. One of the aims of this thesis is to develop a double-sided thruster concept that could be used as a substitute for the two-thruster design while having similar or better power and propellant requirements. In order to prove the concept, the thruster is to be designed, built and tested.

The following list summarises the main objectives of the thesis:

- develop an engineering RF gridded ion thruster performance model;

- develop a thermal RF gridded ion thruster model;

- combine the performance and thermal models to create a holistic RF gridded ion thruster model;

- use the holistic RF gridded ion thruster model to predict the RIT 3.5 thruster behaviour;

- conduct the RIT 3.5 thruster experimental campaign to determine performance parameters and temperature distributions for the model validation;

- design a proof-of-concept double-sided ion thruster for IBS type missions with the LEOSWEEP mission requirements set as constraints;

- build the double-sided ion thruster;

- perform an extensive experimental campaign to test the double-sided ion thruster in order to prove the concept.

1.4   Overview of the thesis

The layout of the thesis is structured in such a way as to make it easy for the reader to understand the material being analysed. In order to do so, the essential equations and background are given before a particular topic is described. Chapter 2 outlines the key principles and provides equations encompassing the main physics of electric propulsion, plasma, electromagnetic fields and RF gridded ion thruster operation. Additionally, Chapter 2 provides a comprehensive literature review regarding previous research efforts in modelling RF gridded ion thrusters. Chapter 3 explains the modelling approach behind the RF gridded ion thruster performance and thermal models. This is achieved by presenting the geometry of the problem, boundary conditions, mesh, main assumptions and equations. In Chapter 4, the RF thruster model validation against an analytical model and the experimental RIT 3.5 thruster data is performed and the results are discussed. Chapter 4 also provides the performance and thermal results obtained while simulating the RIT 3.5 thruster. Chapter 5 describes the IBS mission, and discusses the double-sided ion thruster concept requirements, design and construction. Chapter 6 outlines the DST and RIT 3.5 thrusters' experimental test campaigns. The results from the DST thruster experimental test campaign and a discussion regarding the thruster's performance are presented in Chapter 7. Finally, in Chapter 8, the main results obtained in this thesis are summarised and conclusions are drawn.

2

Background

This chapter provides background material on electric propulsion fundamentals as well as on RF and plasma physics phenomena. The focus is placed on concepts that will be used in developing the RF ion thruster model and in analysing the DST and RIT 3.5 thrusters' performances. Additionally, this chapter discusses principles behind the RF gridded ion thruster operation. What is more, main components of RF gridded ion thrusters are identified and their purpose explained. Finally, a comprehensive literature review regarding previous research efforts in inductive RF discharges, global models and RF ion thrusters is presented at the end of the chapter.

2.1 Electric propulsion fundamentals

2.1.1 The rocket equation

Electric rocket engines work on the same principles as chemical engines: they eject the propellant at very high velocities. The change in the propellant's velocity causes a change in the momentum. Based on the laws of conservation of momentum, this change in the momentum translates into a force acting on a rocket. This force is called the thrust T and it propels the rocket with the velocity v. One way to express the thrust is

(Fortescue et al., 2011)

$$T = M\frac{\mathrm{d}v}{\mathrm{d}t}, \tag{2.1}$$

where M is the mass of a rocket. However, according to Newton's third law, the thrust on a rocket is also equal to the rate of change of momentum of the propellant that is being expelled (Fortescue et al., 2011)

$$T = -\frac{\mathrm{d}}{\mathrm{d}t}(m_p v_{ex}) = -\dot{m}_p v_{ex}, \tag{2.2}$$

where v_{ex} and m_p are the exhaust velocity and mass of the propellant, respectively.

After using the above results and doing some manipulations, the Tsiolkovsky's rocket equation can be derived to find the change in the rocket's velocity ΔV as

$$\Delta V = v_{ex}\ln\frac{m_d + m_p}{m_d} = I_{sp}g\ln\frac{m_d + m_p}{m_d}, \tag{2.3}$$

where I_{sp} is the specific impulse as will be defined shortly, m_d is the total delivered mass and g is the Earth's gravitational constant. A full derivation of the Tsiolkovsky's equation can be found in the work by Fortescue et al. (2011). Equation 2.3 states that in order to exert a substantial change to the rocket's velocity, a high exhaust velocity v_{ex} and a lot of propellant mass m_p are needed. That is to say, if a large ΔV is required, only a propulsion system with a high v_{ex}, or I_{sp}, would be able to accomplish the mission. Otherwise, an impractically large rocket with enormous propellant tanks would be required.

Equation 2.3 can also be expressed in terms of the propellant mass m_p to highlight the importance of the exhaust velocity v_{ex} on the total delivered mass to a destination orbit/object m_d

$$m_p = m_d(e^{\Delta V/v_{ex}} - 1) = m_d(e^{\Delta V/(I_{sp}g)} - 1). \tag{2.4}$$

Equation 2.4 shows that the propellant mass increases exponentially with ΔV. To reduce the propellant requirements, the propellant exhaust velocity v_{ex} must be comparable or, preferably, much larger than the ΔV requirement. For instance, a return mission to Mars requires a ΔV of around 11 km/s (Brophy and Rodgers, 2000), which means that the exhaust velocity v_{ex} must be around 11 km/s as well or higher. Otherwise, the delivered payload mass m_d will be very small or a huge rocket will be required.

Therefore, for high ΔV and m_d missions it is preferable to use electric propulsion engines due to their capacity to achieve very high exhaust velocities. This can be proven by investigating, for example, the Dawn mission to the main belt asteroids Vesta and Ceres (Rayman et al., 2006). The mission requires delivering of a 790 kg satellite to Ceres while also visiting Vesta on the way. The total ΔV required to reach Ceres is around 12 km/s. In the first case, the Raptor chemical propulsion engine that is being developed by SpaceX to bring humans to Mars will be chosen as the main means of propulsion.

The Raptor engine has an I_{sp} of 382 s in a vacuum (Musk, 2016). Therefore, it can be calculated that to successfully achieve the Dawn mission goals using the Raptor engine, a total of about 2,000 kg of propellant would be required. If, however, an ion thruster that has an I_{sp} of 3,000 s (Marcucci and Polk, 2000) is chosen, only about 400 kg of propellant is needed for the mission. As a result, using electric propulsion, vast savings in mass and thus cost of a rocket can be achieved, enabling such high ΔV missions. Therefore, the Dawn mission did indeed use the electric propulsion instead of the chemical propulsion method. However, it is important to note that missions employing electric propulsion suffer from a transfer time penalty due to a low-thrust trajectory, as will be discussed in the following section.

2.1.2 Performance of electric thrusters

Electric thrusters are often characterised by a value of the specific impulse I_{sp} (Goebel and Katz, 2008)

$$I_{sp} = \frac{T}{\dot{m}_p g}. \tag{2.5}$$

By substituting Equation 2.2 into Equation 2.5, the specific impulse can also be expressed as

$$I_{sp} = \frac{v_{ex}}{g}. \tag{2.6}$$

The specific impulse is a measure of how efficiently an engine converts propellant into a useful thrust. The advantages of a high specific impulse magnitude regarding the amount of propellant required for a mission and a delivered payload mass were discussed in the previous section. However, thrusters that have a high specific impulse come at a cost. This can be understood by analysing the following equation (Sutton and Biblarz, 2010)

$$T = \frac{P_t 2\eta_t}{g I_{sp}}, \tag{2.7}$$

where P_t is the total power supplied to a propulsion system and η_t is the total efficiency of this system.

By looking at Equation 2.7, it can be seen that an increase in I_{sp}, with the total efficiency η_t and delivered power P_t being constant, decreases the produced thrust T. Therefore, electric rocket engines are generally low thrust, meaning that the impulse transfer time is long. The only way to increase the thrust without increasing the power is to improve the total efficiency η_t. Additionally, as was discussed by Jahn (1968), it is also important to notice that the power supply mass is almost linearly proportional to the specific impulse. Therefore, a high specific impulse also incurs a substantial power supply mass penalty. Eventually, there will come a point when the power supply mass outweighs the specific impulse benefit. As a result, a careful system optimisation is necessary.

In addition to the specific impulse, the propellant mass utilisation efficiency η_m is also introduced to account for ionised vs unionised propellant. For singly charged ions, the propellant mass utilisation efficiency is (Goebel and Katz, 2008)

$$\eta_m = \frac{I_b M_i}{e \dot{m}_p}, \tag{2.8}$$

where I_b is the extracted ion current, M_i is the ion mass and e is the electron charge. Furthermore, it can be shown that in the context of gridded ion engines

$$\eta_m \propto I_{sp}. \tag{2.9}$$

Therefore, a high mass utilisation efficiency leads to a high specific impulse and vice versa. Another commonly used parameter in defining an ion thruster's efficiency is the ion production efficiency (or the discharge loss) η_d given, for RF gridded ion thrusters, as (Goebel and Katz, 2008)

$$\eta_d = \frac{P_{in}}{I_b}, \tag{2.10}$$

where P_{in} is the RFG power that needs to be delivered to the plasma in order to produce the ion current I_b. Therefore, the discharge loss shows how much power (in watts) is needed to produce an ampere of current, giving it the units of W/A (or eV/ion). The lower the discharge loss, the more efficient the RFG power conversion to the ion current is. The propellant mass utilisation efficiency and the discharge loss are usually combined to produce an ion thruster performance curve, as shown in Figure 2.1.
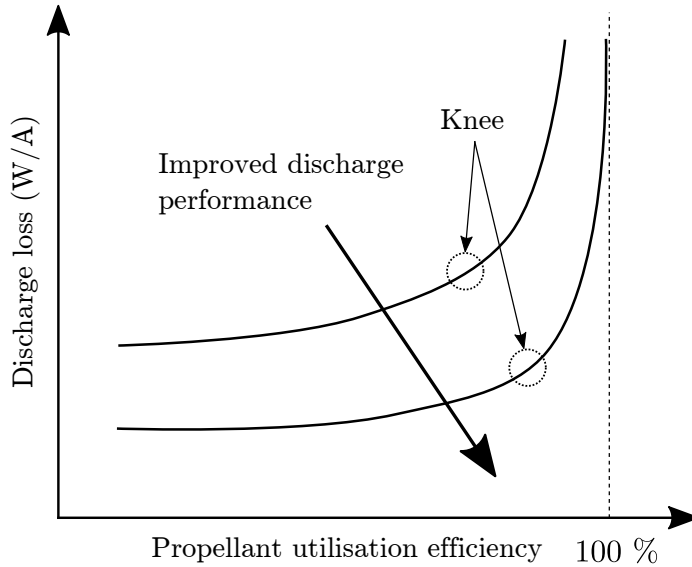
Figure 2.1: Common ion thruster performance curve depicting the discharge loss as a function of the mass utilisation efficiency.

As can be seen from Figure 2.1, as the propellant utilisation rises, the discharge loss increases as well. At low propellant utilisation efficiency values, the increase is nearly negligible, which is indicated by a flat trend. However, as the propellant utilisation efficiency

reaches a certain value (the knee), the discharge loss starts to increase exponentially. It is beneficial to operate a thruster at the highest possible mass utilisation efficiency, but, at the same time, at low discharge loss values as well. As a result, thrusters are often operated at the so-called knee of the curve, as indicated in Figure 2.1. The higher the propellant mass utilisation efficiency at which the knee occurs, the more efficient and optimised a thruster is. Furthermore, the lower the curve is on the discharge loss scale, the more efficient a thruster is. The reasons behind such a shape of the performance curve will be discussed in Chapter 4.

When analysing ion thrusters, it is important to define the thrust. Assuming a negligible fraction of doubly charged ions, for RF gridded ion engines, the thrust can be calculated as (Goebel and Katz, 2008)

$$T = \cos\theta_d \sqrt{\frac{2M_i}{e}} I_b \sqrt{V_b}, \tag{2.11}$$

where θ_d is the average half-angle divergence of the beam and V_b is the acceleration potential of the ions. The definition of V_b will be discussed in Chapter 3. Another parameter used to gauge the performance of an RF ion thruster is the electrical efficiency (Goebel and Katz, 2008)

$$\eta_e = \frac{I_b V_b}{I_b V_b + P_{in}}, \tag{2.12}$$

where the numerator represents the beam power $P_b = I_b V_b$ needed to accelerate the ions. Whereas, the denominator represents a sum of the beam power P_b and the RFG power P_{in} required to produce the ion current I_b. Finally, by combining all the aforementioned efficiency parameters, the total efficiency can be defined as (Goebel and Katz, 2008)

$$\eta_t = \cos\theta_d{}^2 \eta_e \eta_m. \tag{2.13}$$

In Chapter 4 and Chapter 7 all these parameters will be used to determine and analyse performance of the RIT 3.5 and DST ion thrusters, respectively.

2.2   RF physics

2.2.1   Electromagnetic fields

The whole of electrodynamics stands on the four Maxwell's laws

$$\nabla \cdot \boldsymbol{E} = \frac{1}{\epsilon_0}\rho, \tag{2.14}$$

$$\nabla \cdot \boldsymbol{B} = 0, \tag{2.15}$$

$$\nabla \times \boldsymbol{E} = -\frac{\partial \boldsymbol{B}}{\partial t}, \tag{2.16}$$

$$\nabla \times \boldsymbol{B} = \mu_0 \boldsymbol{J} + \mu_0 \epsilon_0 \frac{\partial \boldsymbol{E}}{\partial t}, \tag{2.17}$$

where the following list of variables has been used in the equations: E - electric field, ρ - charge density, ϵ_0 - permittivity of free space, B - magnetic field, μ_0 - permeability of free space and J - current density. Only the equations themselves are shown, derivations and an in-depth analysis are provided in the work by Griffiths (1999).

The first law given by Equation 2.14 is commonly referred to as Gauss's law, and it defines an electric field E generated by a collection of charges. The second law given by Equation 2.15 states that magnetic monopoles do not exist. That is, all magnets have the South and North poles. The third law given by Equation 2.16 is known as Faraday's law, and it provides the basis for understanding the electromagnetic induction. Faraday's law tells that a changing magnetic field B induces an electric field E, or generates an electromotive force (EMF). It does not matter as to how the change in the magnetic field is obtained. In the case of RF ion thrusters, the changing magnetic field is generated by an AC current flowing in the coil. Additionally, the minus sign in Equation 2.16 comes from Lenz's law. The minus sign indicates that an induced electric field will generate its own magnetic field that opposes the magnetic field that caused it. Finally, the fourth law given by Equation 2.17 is called the modified Ampere-Maxwell's law. It defines the concept of displacement currents. Ampere-Maxwell's law says that electric currents and changing electric fields produce magnetic fields. The fourth law is essential to the explanation of electromagnetic wave propagation in space.

The skin depth phenomenon is another important concept to analyse when discussing electromagnetic fields. The physics of the skin depth can be explained by considering Equation 2.16 and Equation 2.17. First, as depicted in Figure 2.2, an AC current I flowing through a conductor, according to Ampere-Maxwell's law, produces a changing magnetic field B. Due to Faraday's law, this B field induces the current, called an eddy current, I_w that opposes the actual current flow in the centre of the conductor and reinforces it at the edges, as seen from Figure 2.2. As a result, the inner part of the conductor is almost curentless. A majority of the current flows through a skin layer δ

near the outer boundaries of the conductor. In essence, the wire shown in Figure 2.2 could be made hollow since the inner part carries no current.
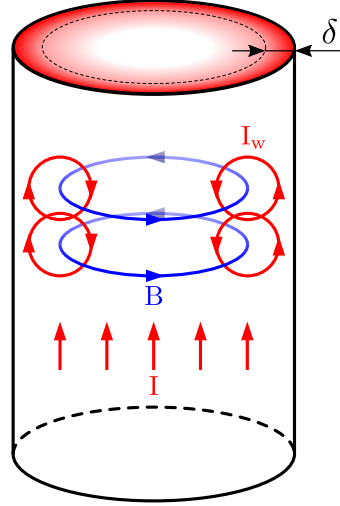
Figure 2.2: Representation of the skin effect phenomenon inside a conductor.

Mathematically, the skin depth δ is defined as the distance d from the surface of a conductor at which the current density J has fallen $1/e$ of the surface value J_s. The relationship can be expressed by the following equation

$$J = J_s e^{-d/\delta}. \tag{2.18}$$

Using the electrical conductivity of a conductor σ and the frequency of the field oscillations f, the skin depth can be calculated as (Chabert and Braithwaite, 2011)

$$\delta = \sqrt{\frac{2}{\omega \mu_0 \sigma}}, \tag{2.19}$$

where $\omega = 2\pi f$.

As can be seen from Equation 2.19, an increase in the frequency causes a decrease in the skin depth. Therefore, at high frequencies, due to a thin skin depth, the current flows only at the very edge of a conductor. This fact will be used in developing the electromagnetic model, as will be shown in Chapter 3. Finally, Equation 2.19 shows that as the electrical conductivity increases, the skin depth decreases.

2.2.2 Impedance and admittance

When analysing AC circuits, it is important to understand the concepts of impedance and admittance. For a thorough treatment of this topic, the reader should look into the work of William (2001). In this chapter, only main equations will be given and explained. The discussion is started by defining the impedance Z which is generally

expressed as a complex quantity with both real and imaginary parts

$$Z = R + jX, \tag{2.20}$$

the real part is called the resistance R, whereas the imaginary part is called the reactance X. For an inductor, the reactive component X_l is frequency dependent and can be calculated as $X_l = \omega L$. Therefore, for a lossless inductor for which $R = 0$, the inductive impedance Z_{ind} is

$$Z_{ind} = j\omega L, \tag{2.21}$$

where L is the inductance. It can be observed that as the frequency increases, the impedance of an inductor Z_{ind} increases as well. Furthermore, the voltage across an inductor $V(t)$ leads the current $I(t)$ by 90°, or j in the complex plane. This can be seen from Ohm's law as $V(t) = Z(\omega)I(t)$.

A capacitor exhibits a similar behaviour to that of an inductor. However, the capacitor's reactance is $X_c = 1/\omega C$. Therefore, for a lossless capacitor for which $R = 0$, the capacitive impedance Z_{cap} is

$$Z_{cap} = -j/\omega C. \tag{2.22}$$

However, contrary to the inductive impedance Z_{ind}, the capacitive impedance Z_{cap} decreases with frequency. Additionally, the current $I(t)$ across a capacitor leads the voltage $V(t)$ by 90°, or $-j$ in the complex plane. Note that since the resistive component R was set to zero, both the lossless inductor and capacitor do not dissipate any energy. In addition, the admittance Y is defined as a reciprocal of the impedance Z

$$Y = 1/Z = G + jB, \tag{2.23}$$

where G is called the conductance and B is referred to as the susceptance. For a purely resistive circuit, the former is defined as $1/R$, while for a purely inductive circuit, the latter is defined as $1/X$.

The impedance is a useful parameter when circuit's elements are connected in series since in such a case the element impedances add up. The admittance, on the other hand, is useful when elements are distributed in parallel since the corresponding admittances add up as well. As touched before, lossless inductors and capacitors do not dissipate any energy. This comes from the maximum power theorem which states that the average dissipated power P depends on the phase difference between the voltage and current $(\theta_v - \theta_i)$

$$P = \frac{V_m I_m}{2} \cos(\theta_v - \theta_i), \tag{2.24}$$

where V_m and I_m are the maximum (or peak) voltage and current values, respectively. For inductors and capacitors, the phase differences are equal to 90 and –90°, respectively. Therefore, $\cos(90°) = 0$ for both cases and thus $P = 0$ W. As a result, to transfer the maximum amount of power to a load, the phase difference between current and voltage

must be zero because $\cos(0°) = 1$. When $(\theta_v - \theta_i) = 0°$, it is said that the voltage and current are in phase, and such a circuit is called purely resistive.

2.2.3 Resonance

The resonance phenomenon is crucial to consider when a circuit's response to a particular frequency or a set of frequencies is important. To achieve resonance, a circuit must be composed, in some configuration, of resistors, inductors and capacitors. Two resonance cases: one for the series circuit and the other one for the parallel circuit, are shown in Figure 2.3(a) and Figure 2.3(b), respectively (Boylestad, 1997). As can be seen, at the resonant frequency f_r the circuit's response increases dramatically and reaches a peak. For the series circuit, the current reaches a maximum value at resonance, while for the parallel circuit the voltage reaches a maximum value. However, in both cases, the resonance is achieved when the circuit behaves resistively. That is, when the voltage and current are in phase. Remember that, as mentioned in Section 2.2.2, the same conditions also cause the maximum amount of power to be transferred to a load.

(a) Series circuit. (b) Parallel circuit.
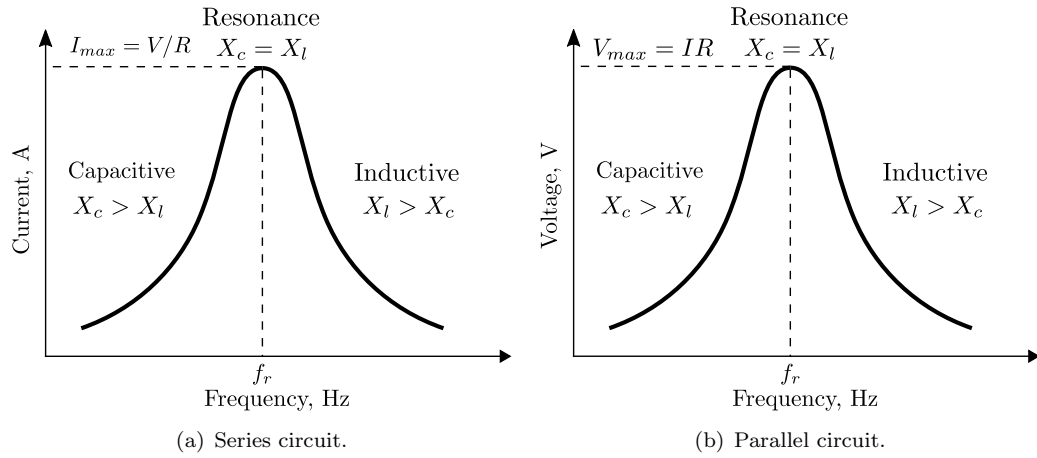
Figure 2.3: Illustration of the resonance phenomenon for the series and parallel circuits.

The efficiency of an inductor is often defined using a so-called Q-factor. The Q-factor is vital in determining the response of a resonant circuit and can be expressed as

$$Q = \frac{\omega L}{R}. \tag{2.25}$$

Note that Q is expressed as a ratio of the reactive power to the resistive power. Therefore, the larger the Q-factor, the more efficient a circuit is. This is because the resistive component R is smaller than the reactive component ωL. Since only the resistive component dissipates energy, it is beneficial to keep it to a minimum if power losses are to be minimised. Additionally, as can be seen from Equation 2.25, Q increases linearly with

the frequency. However, remember that as the frequency increases, the skin depth decreases. This causes a decrease in the area through which the current can flow, which in turn causes the resistance to rise. Therefore, Q peaks at some frequency and then starts to go down. As Figure 2.3 depicts, the inductive (X_l) and capacitive (X_c) reactances are equal at resonance. Therefore, if Q is sufficiently high, the resonance frequency f_r can be obtained by

$$f_r = \frac{1}{2\pi\sqrt{LC}}. \tag{2.26}$$

2.2.4 Transmission lines

The wavelength λ of a radio frequency wave can be defined as $\lambda = v/f$, where v is the phase speed. In a vacuum, v is equal to the speed of light c. Therefore, as the frequency f increases, the wavelength decreases. It is said that the cable connecting circuit's elements is "electrically large" if its length is larger than one-tenth of a wavelength. In such a case, waves travelling through the cable can be reflected back when they encounter a load. Otherwise, the cable is referred to as being "electrically short" and no special treatment is needed (William, 2001). Often, to transmit high-frequency waves, special cables called "coaxial cables" are used. As shown in Figure 2.4, a coaxial cable consists of a centre core conductor surrounded by an insulating dielectric, which is again surrounded by a metallic shield. In such a configuration, the electromagnetic waves are confined within the dielectric insulator and thus are less prone to losses and disturbances. The insulating material is commonly made out of Teflon.
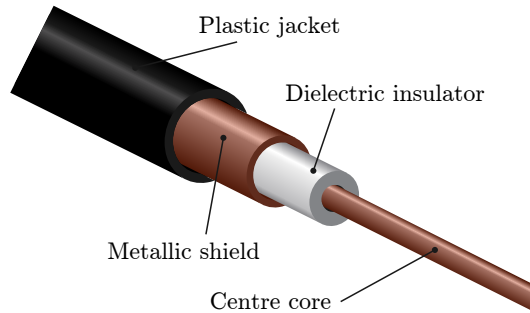
Figure 2.4: Schematic of a typical coaxial cable with all the main components.

Coaxial cables are a specific type of the transmission line used to transmit high-frequency signals through long distances. The transmission line is usually represented using a lumped element model shown in Figure 2.5. The lumped element model is made of the resistor R and the inductor L connected in series, the shunt resistor representing the dielectric strength G, and the capacitor C in parallel. Usually, these parameters are defined per unit length of the cable Δx. Therefore, the whole transmission line is then made up of many lumped elements added together with lengths Δx totalling an actual length l of the line (William, 2001).
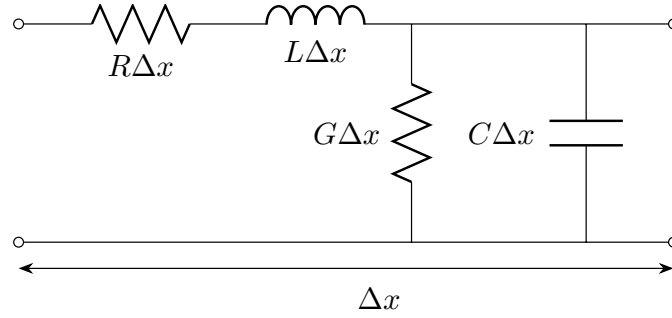
Figure 2.5: Representation of a transmission line using a lumped element model.

By using the Telegraph's equations, the characteristic impedance of a transmission line (or a coaxial cable) Z_0 can be calculated by using its electrical properties (William, 2001)

$$Z_0 = \sqrt{\frac{R + j\omega L}{G + j\omega C}}. \tag{2.27}$$

These electrical properties depend on the geometry of the cable and on the material properties of both the dielectric and conductor. Often, transmission lines are designed to have the impedance Z_0 equal to 50 Ω. Such a convention makes it easier to design power supplies, RF generators and other electronic equipment. This is because the impedance value to which they have to be matched is already known. The reason for this will be explained in the following section.

2.2.5   Matching

In real world conditions, transmission lines are connected at both ends either to a power supply or a load, as shown in Figure 2.6. As mentioned already, to avoid the power reflection, power supplies are designed to have the characteristic impedance Z_s equal to the coaxial cable's impedance Z_0. Nevertheless, the load impedance Z_l can vary greatly. This is especially true for RF thrusters since the plasma impedance depends on ion density, electron temperature and so on. These parameters fluctuate widely during the thruster's operation as the mass flow rate or input power is changed. If the load impedance is not equal to the characteristic cable impedance, power reflection will occur in terms of the reflected current I_r and voltage V_r. The reflected power makes the system less efficient because the power sent by the supply cannot be delivered to the load. A part of the reflected power is dissipated in the cable itself, while the other part goes to the power supply. As a result, the power supply can be overloaded and damaged. Furthermore, the electric insulation in the coaxial cable might break.
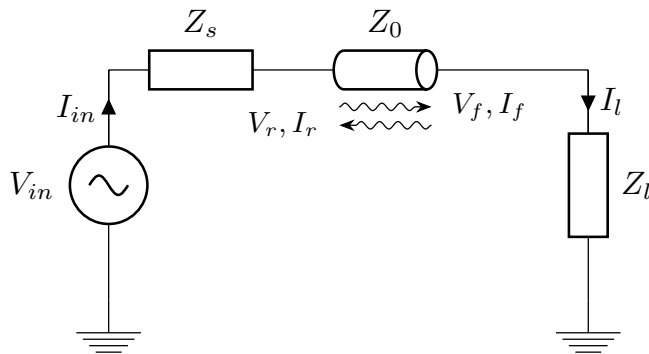
Figure 2.6: Principles of power reflection for an RF circuit composed of a power supply, coaxial cable and load.

The amount of reflected power is estimated using the reflection coefficient Γ. The reflection coefficient is defined as a ratio of the reflected voltage amplitude V_r to the forward voltage amplitude V_f. It is also related to the difference in the characteristic impedances between the cable and load (William, 2001)

$$\Gamma = \frac{V_r}{V_f} = \frac{Z_l - Z_0}{Z_l + Z_0}. \tag{2.28}$$

It is not possible to have the load impedance always to match the cable impedance. Therefore, to avoid the above-mentioned problems, a matching network is added between a coaxial cable and a load. The matching network transforms the load impedance as seen from the coaxial cable's terminals in such a way that it becomes equal to the cable's impedance. The process is usually called matching.

(a) L-type matching network.

(b) T-type matching network.

(c) Π-type matching network.
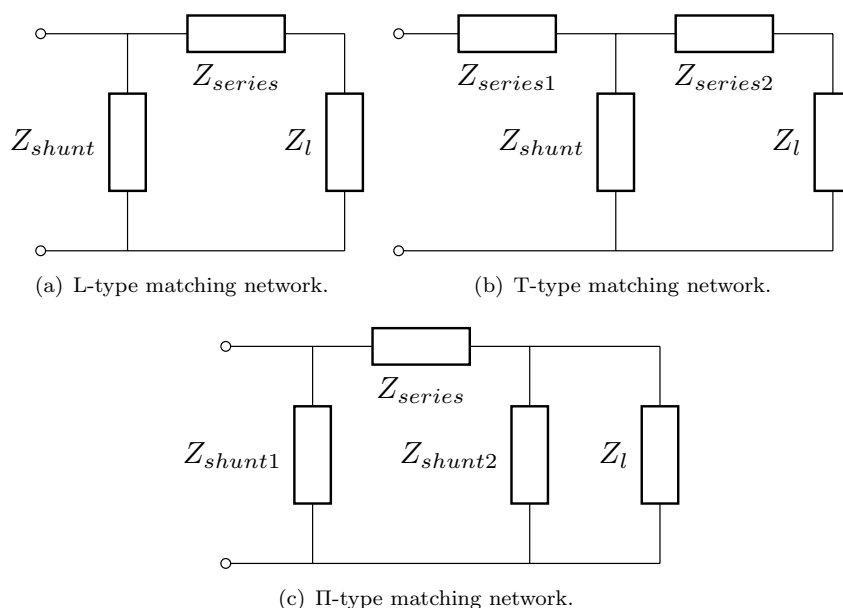
Figure 2.7: Schematic illustration of various types of matching networks based on the way the electrical components are arranged.

A properly designed matching network will transform the load impedance so that the reflection coefficient Γ is negligible, meaning all forward power goes to the load. Note that matching networks use only high Q reactive components to minimise the power loss. A list of typical matching networks is shown in Figure 2.7 (William, 2001). The optimum matching network configuration depends on whether the impedance has to be transformed to a lower or higher value, and a type of the load/RF generator. Impedance values of the matching network components are determined using either analytical equations or the Smith chart, as depicted in Figure 2.8. There are a few rules to remember when performing matching using the Smith chart. First, a capacitive reactance and an inductive reactance cancel if connected in series. Second, a susceptance can be cancelled by adding a capacitor or an inductor in parallel (William, 2001).
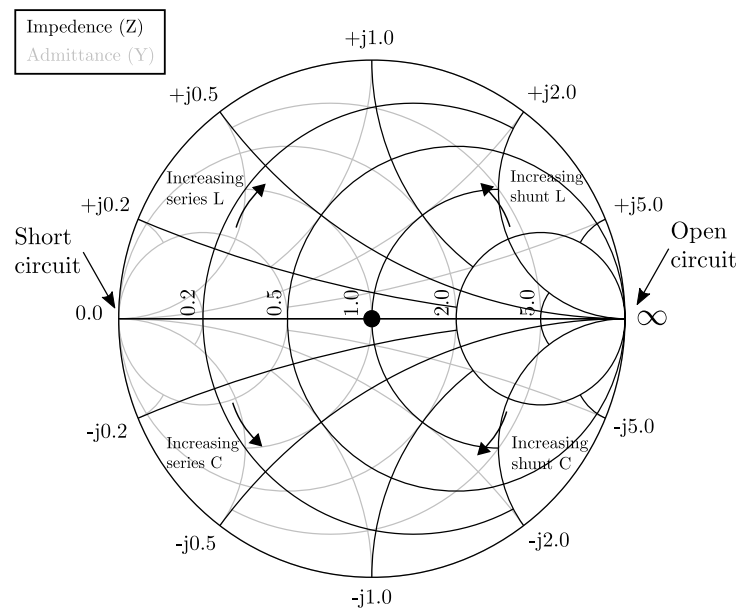
Figure 2.8: Principles behind the Smith chart that shows the equivalent circuit's impedance and admittance.

2.3   Plasma physics

2.3.1   Bulk plasma properties

This section discusses the main aspects of plasma physics that are relevant to the development of the RF ion thruster model. Only main equations and concepts will be explained with regards to plasma physics. For a detailed analysis of this topic, the reader should look at the works by Chen (2006) and Goldston and Rutherford (1995).
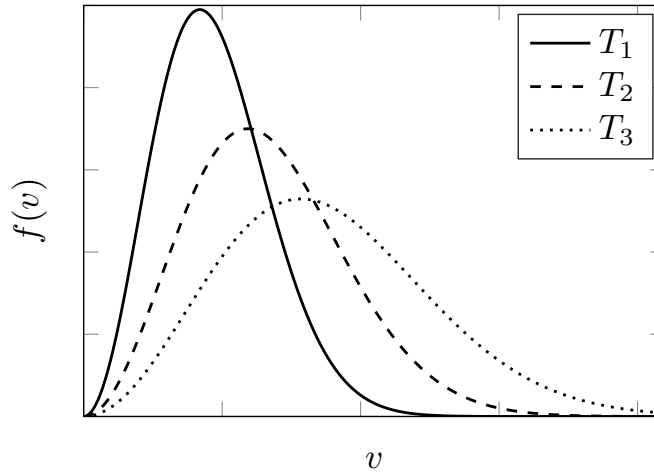
Figure 2.9: Maxwellian velocity distribution function for three different particle temperature values: $T_1 < T_2 < T_3$.

The plasma is defined as a collection of charged particles that respond to applied magnetic and electric fields. It is electrically quasi-neutral, meaning there are almost equal numbers of electrons and positive ions. This condition is broken only at the boundaries which are referred to as sheaths. The plasma is analysed by assuming that it can be described by average quantities such as temperature, density and potential. Often, plasma electrons follow what is called a Maxwellian distribution. The Maxwellian velocity distribution $f(v)$ relates the temperature T and the speed of particles v. Figure 2.9 depicts that as the temperature increases, the peak magnitude of the $f(v)$ curve decreases, but the tail of the curve shifts to higher v values.

Mathematically, the speed distribution $f(v)$ gives the proportion of particles with speeds between v and $v + \mathrm{d}v$ (Chabert and Braithwaite, 2011)

$$f(v) = n \left(\frac{m}{2\pi k_B T} \right)^{3/2} 4\pi v^2 \exp\left(\frac{-mv^2}{2k_B T} \right), \tag{2.29}$$

where n is the particle density, m is the particle mass and k_B is the Boltzmann constant. The particle density n can then be obtained by integrating $f(v)$ over all possible speeds

$$n = \int_0^\infty f(v)\mathrm{d}v. \tag{2.30}$$

Finally, the average (or mean) speed $\bar{v}$ of particles can be defined as

$$\bar{v} = \sqrt{\frac{8k_BT}{\pi m}}. \tag{2.31}$$

Using a similar approach, the average particle energy $\bar{\epsilon}$ can be determined assuming that $f(\epsilon)\mathrm{d}\epsilon$ represents a number of particles with kinetic energies between ϵ and $\epsilon + \mathrm{d}\epsilon$

$$\bar{\epsilon} = \frac{3}{2}k_BT. \tag{2.32}$$

It can be observed from Equation 2.32, that the average particle energy depends solely on the temperature T. In plasmas, the electron temperature is tens of thousands of Kelvin. However, ions have temperatures of only a few hundred Kelvin since they are much heavier than electrons. Due to a direct relationship between the plasma temperature and energy, temperature is often measured in eV. Note that 1eV is defined as

$$k_BT = 1eV = 1.602 \times 10^{-19} \text{ Joules.} \tag{2.33}$$

2.3.2 Collisions

Collisions between particles are characterised using a parameter known as the cross-section $\sigma(T)$. The value of a cross-section is proportional to the probability of a collision. The size of a cross-section depends on the relative velocities of the particles involved in the collision. However, as was shown in Equation 2.31 and Equation 2.32, the average particle velocity and energy can be solely determined by the temperature T. To better understand the concept of a cross-section, imagine a flux of particles having the mass m, density n, and fixed velocity v incident onto a collection of infinitely massive (stationary) target particles having the density n_g (Lieberman and Lichtenberg, 2005). This situation is illustrated in Figure 2.10. The number of incident particles per unit volume that undergo an interaction with the target particles within the differential distance $\mathrm{d}x$ can be expressed as (Chabert and Braithwaite, 2011)

$$\mathrm{d}n = -\sigma n n_g \mathrm{d}x. \tag{2.34}$$

Equation 2.34 shows that the constant of proportionally σ has units of area and thus is called the cross-section. The cross-section value for a particular interaction depends on the plasma temperature and the type of gas. Therefore, the values of cross-sections are provided in various tables and graphs as functions of the plasma temperature and gas type. In addition, the value of a cross-section depends on the interaction type. For instance, these are some of the different interactions that can occur: ionisation of a target particle, excitation of an incident particle and scattering of an incident particle (Lieberman and Lichtenberg, 2005).
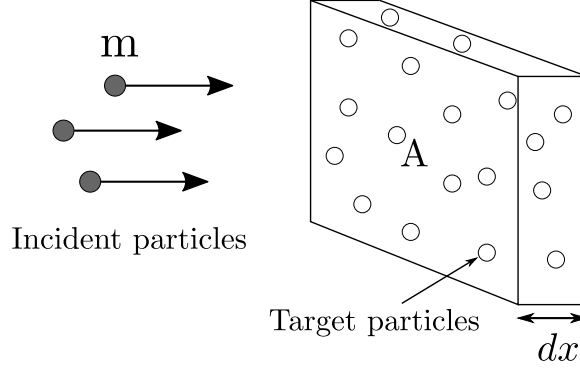
Figure 2.10: Collisions between incident particles with a collection of stationary target particles.

Another important parameter used to quantify the collision phenomena between the particles is called the mean free path λ. The mean free path is defined as the average distance travelled by a particle before making a collision

$$\lambda = \frac{1}{n_g \sigma}. \tag{2.35}$$

If, on the other hand, the target particles are not stationary but move with a Maxwellian velocity distribution, the mean free path λ, calculated from Equation 2.35, has to be multiplied by $1/\sqrt{2}$ to account for the average particle velocity. However, in this thesis, the multiplying factor will be omitted since in RF ion thrusters the electron temperature is much larger than the neutral gas temperature. Therefore, electrons see the neutral gas atoms as stationary. Furthermore, the collision frequency ν is defined as an inverse of the time between successive collisions. Using the parameters derived above, the collision frequency can be described as

$$\nu = (\lambda/v)^{-1} = n_g \sigma v. \tag{2.36}$$

Finally, the collision frequency per unit density is defined as

$$K = \sigma v, \tag{2.37}$$

where K is known as the rate coefficient (or constant). An advantage of using the rate constant is that it is independent of the particle density n_g. For plasmas, the rate constant depends only on the gas type and plasma temperature. Therefore, values for the rate constants as a function of the plasma temperature can be compiled in graphs and tables for various gases. Once the rate constant and the gas density n_g are known, the collision frequency can be calculated using Equation 2.36.

2.3.3 Sheaths

When dealing with plasma physics it is critical to understand the concept of sheaths, as shown in Figure 2.11 (Lieberman and Lichtenberg, 2005). Using Equation 2.31, the electron flux Γ_e to the ion flux Γ_i ratio can be approximated as (Goebel and Katz, 2008):

$$\frac{\Gamma_e}{\Gamma_i} = \sqrt{\frac{M_i T_e}{m_e T_i}}. \tag{2.38}$$

First, note that the ion mass M_i is thousands of times larger than the electron mass m_e. Furthermore, the electron temperature T_e is usually much higher than the ion temperature T_i. Therefore, the electron flux to the wall is much larger than the ion flux. This means that electrons are leaving plasma at a much faster rate. However, it was mentioned that plasma is quasi-neutral, meaning that equal numbers of positive and negative charges are contained in the volume. To satisfy this relationship, a positive potential with respect to the walls develops in a very thin layer at the wall called the sheath.
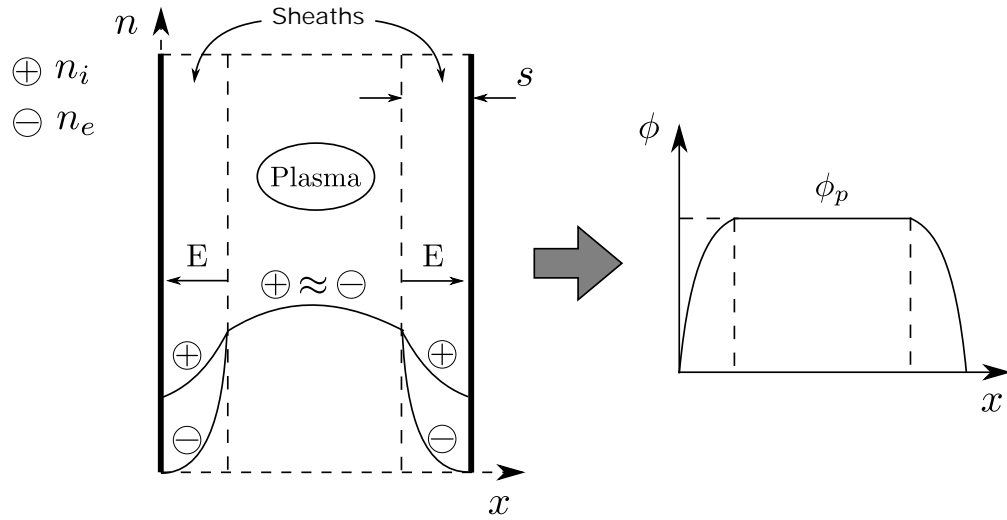
Figure 2.11: Explanation of the sheath phenomenon with an indication of ion and electron density distributions, a qualitative definition of the sheath thickness s, and a description of the plasma potential distribution.

As can be seen from Figure 2.11, the electric field E within the sheath is directed into the wall, which implies that ions are accelerated and electrons are decelerated in this region. This also impacts the density distribution in the plasma. Due to a strong electric field E in the sheath, the electron density n_e is significantly smaller in the sheath than in the plasma. The ion density n_i, however, is also lower in the sheath than in the plasma, but it is still much higher than the electron density. This results in the plasma potential ϕ_p being positive with respect to the walls.

Another property of the plasma is to screen electric charges. For instance, if a positive ion is placed inside the plasma it will start attracting electrons. However, the electrons

produce an electric field themselves that repels other electrons that would otherwise wish to come towards the ion. Therefore, the positive potential produced by the ion quickly diminishes. The distance through which the potential decreases by $1/e$ away from the test charge is called the Debye length λ_D. As a result, sheaths in plasma are only a few Debye lengths in distance. The Debye length does not depend directly on the dimensions or the size of the discharge. It depends solely on the plasma parameters, as can be seen in the following equation (Goebel and Katz, 2008)

$$\lambda_D = \sqrt{\frac{\epsilon_0 k_B T_e}{n_i e^2}}. \tag{2.39}$$

Imagine a sphere of charges with the radius r around a test charge. The way the potential ϕ falls off is then (Goebel and Katz, 2008)

$$\phi = \frac{e}{4\pi\epsilon_0 r} e^{-r/\lambda_D}. \tag{2.40}$$

Equation 2.40 shows that the potential decreases exponentially with the distance r. Therefore, due to the screening effect, at the distance r equal to just a few Debye lengths, the potential will be nearly zero. That is, the presence of the charge will not be felt further than this distance. Usually, the Debye length is equal to only tens of microns.

In practice, however, the sheath behaviour is more complicated. It can be shown that in order to have a stable sheath for ions to fall through, first, a pre-sheath must exist. The pre-sheath is mainly there to accelerate ions up to a certain velocity, called the Bohm velocity u_B, prior to entering the sheath itself (Lieberman and Lichtenberg, 2005)

$$u_B = \sqrt{\frac{k_B T_e}{M_i}}, \tag{2.41}$$

where M_i stands for the ion mass of a particular gas species.

A plot illustrating the pre-sheath is shown in Figure 2.12. First, notice that the plasma density at the edge of the sheath n_s is no longer equal to the bulk plasma density n_b. Rather, the plasma density at the sheath edge is around 40% lower than the plasma density at the centre

$$n_s \approx 0.6 n_b. \tag{2.42}$$

Furthermore, ions that arrive at the sheath edge fall through the potential ϕ_s. There are a few different types of sheaths that can occur in the plasma. These depend on the potential difference between the plasma and the wall (or the electrode) compared to the electron temperature (Goebel and Katz, 2008). If the potential difference is small compared to the electron temperature, the Debye sheath occurs. If, on the other hand, the potential difference is on the order of the electron temperature, the sheath with a pre-sheath occurs, as shown in Figure 2.12. However, if the potential difference is much

larger than the electron temperature, the Child-Langmuir sheath will be produced. In such a case, the electrons are repelled over a majority of the sheath thickness and the electron density goes almost to zero relatively close to the sheath edge to sustain the quasi-neutrality condition (Goebel and Katz, 2008).
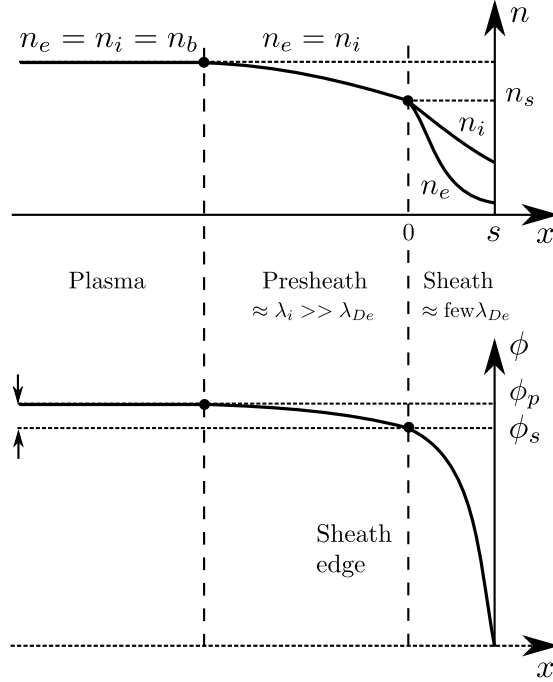
Figure 2.12: Description of the density and potential variations within the plasma and the pre-sheath in contact with a wall.

In a typical plasma, the Child-Langmuir sheaths can be on the order of 100 Debye lengths in size. When the Child-Langmuir sheath forms, the ion current density J_i that can pass through a planar sheath becomes space-charge limited. That is, the ion current cannot go above a certain value which depends on the voltage of the electrode U and the sheath thickness d (Goebel and Katz, 2008)

$$J_i = \frac{4\epsilon_0}{9} \sqrt{\frac{2e}{M_i}} \frac{U^{3/2}}{d^2}. \tag{2.43}$$

This observation will be employed a lot when talking about gridded ion thrusters due to a high potential applied to the ion optics system used to extract ions from the plasma. In an ion thruster, the sheath thickness is approximately equal to the distance between the screen and accel electrodes, as will be discussed in the following section.

2.4   RF thrusters

2.4.1   Geometry and working principles

Figure 2.13 depicts a common configuration RF gridded ion thruster. It consists of an insulating discharge chamber attached at one end to a set of perforated grids for ion extraction. The following definitions are used throughout the thesis when talking about a particular grid: "+" - screen grid, "−" - accel grid and "0" - decel grid. The discharge chamber has an opening that is connected to a gas inlet supplying the propellant. There is also a coil wrapped around the outer surface of the discharge chamber. The chamber is usually made out of an insulating material such as ceramics or glass, whereas the coil is made out of copper or silver in order to reduce Ohmic losses.
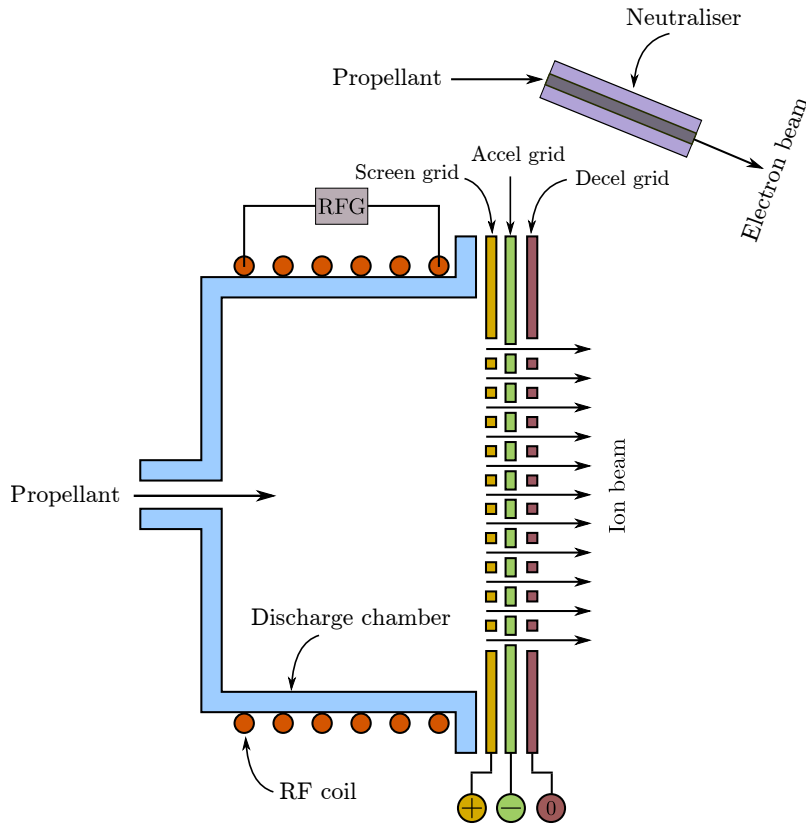
Figure 2.13: Schematic showing main RF gridded ion thruster components, including a neutraliser, as well as the key operational aspects.

The coil is connected to an RF generator (RFG) that powers it. Usually, there is a matching network installed between the RFG and the coil for impedance matching. The plasma generated in the discharge chamber floats with respect to the walls. Once a high voltage is applied to the extraction grids, ions are accelerated out of the discharge chamber to form an ion beam. There is also a neutraliser installed to neutralise the ion beam and prevent the thruster from reaching a high positive potential. Figure 2.14 shows an actual cutaway view of the RIT 10 thruster (Airbus, 2003). As can be seen,

the RIT 10 has all the main components as was discussed previously and depicted in Figure 2.13.
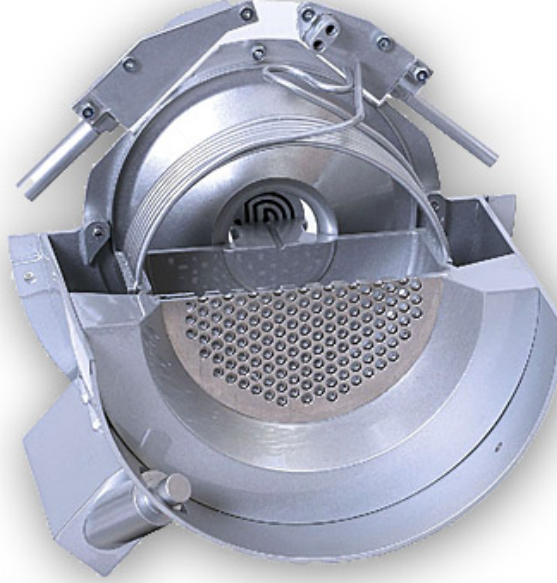
Figure 2.14: RIT 10 thruster having a discharge chamber that is 10 cm in diameter (Airbus, 2003).

2.4.2 Plasma generation

This sections discussed the plasma generation process inside the discharge chamber in more detail. Figure 2.15 shows main physical processes occurring inside an RF gridded ion thruster (Lotz, 2013). The figure also illustrates the charged particle distributions and the electric field E_{grid} generated by the ion optics system. Since the high frequency current I_c flows in the coil, according to Ampere's law, the axial time-varying magnetic field B_{alt} is induced in the plasma which, for a cylindrical geometry, can be expressed as

$$B_z = \frac{\mu_0 N I_c}{l} e^{i\omega t},$$ (2.44)

where N is the number of coil turns and l is the axial length of the coil. Furthermore, according to Faraday's law, the time varying magnetic field B_z induces the azimuthal electric field E_θ inside the plasma and all other conductors that surround the coil

$$E_\theta = \frac{-i\omega r}{2} B_z e^{i\omega t}.$$ (2.45)

However, in the plasma, electrons move much faster than the frequency of the electric field and thus see only a DC electric field component (Chabert and Braithwaite, 2011). Electrons are accelerated by this field before they make a collision with the neutral

atoms, thus ionising them. Therefore, there is the induced electron current I_p (or I_{ind}) flowing in the plasma. Such an ionisation process is called the collisional or Ohmic heating.
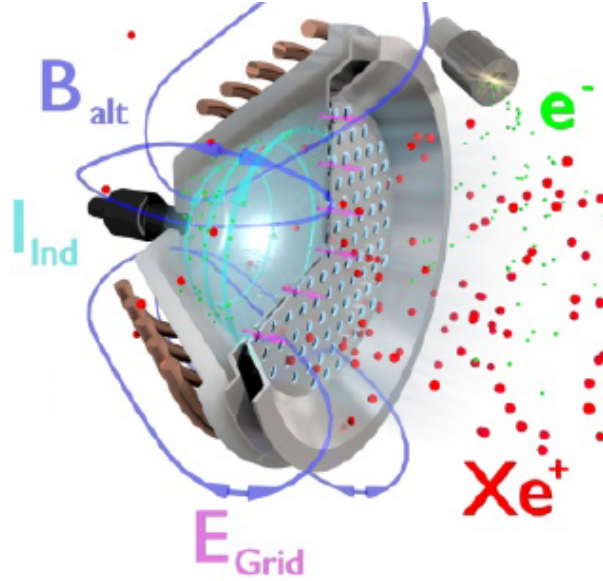
Figure 2.15: Illustration of the main physical processes inside a generic RF gridded ion thruster. The following notations are used: B_{alt} - alternating magnetic field, I_{ind} - induced electron current, E_{grid} - electric field between the grids, e^- - electrons, Xe^+ - positive xenon ions (Lotz, 2013).

It should be noted that there are some additional aspects that need to be considered when analysing the RF plasma. First, a parasitic capacitance can develop between the coil and plasma due to a high coil voltage (Chabert and Braithwaite, 2011). This high voltage then appears in the sheath and acts as a capacitor. The coil power can, therefore, be coupled both inductively and capacitively. In general, however, the inductive mode is observed at high-power and high-density plasmas (Chabert and Braithwaite, 2011). Second, at low pressures when the electron mean path is larger than the thruster's dimensions, the so-called collisionless heating might occur (Godyak et al., 1998). This heating occurs due to the electrons being pushed away from the negative sheath layer in such a way as to give them enough energy to ionise the neutral atoms. The heating can thus occur beyond the skin depth and cause a lot of non-linearities (Lieberman and Lichtenberg, 2005). Such a process is said to generate the anomalous (non-local) skin effect. At low pressure, the power dissipated through the collisionless heating method can be an order of magnitude larger than from the Ohmic (collisional) method (Godyak et al., 1998). Finally, the energy distribution function might be greatly distorted from the Maxwellian, which can immensely complicate the plasma analysis (Lister et al., 1996).

2.4.3   Plasma parameters

Figure 2.16 displays a radial distribution of various plasma parameters as measured in the RIT 10 ion thruster (Loeb et al., 1988). At typical RF thruster working frequencies varying in the range from 1 to 20 MHz, the electric and magnetic fields are concentrated in a thin skin layer at the outer edge of the plasma. The skin layer is therefore where a majority of the plasma heating occurs. As seen in Figure 2.16, the induced electric field E_{ind} decreases nearly linearly from the peak value at the wall to zero near the axis to satisfy the geometrical symmetry. Additionally, the electron temperature T_e is not uniform due to the presence of the skin layer. The highest electron temperature occurs in the skin layer next to the wall and drops exponentially towards the axis.
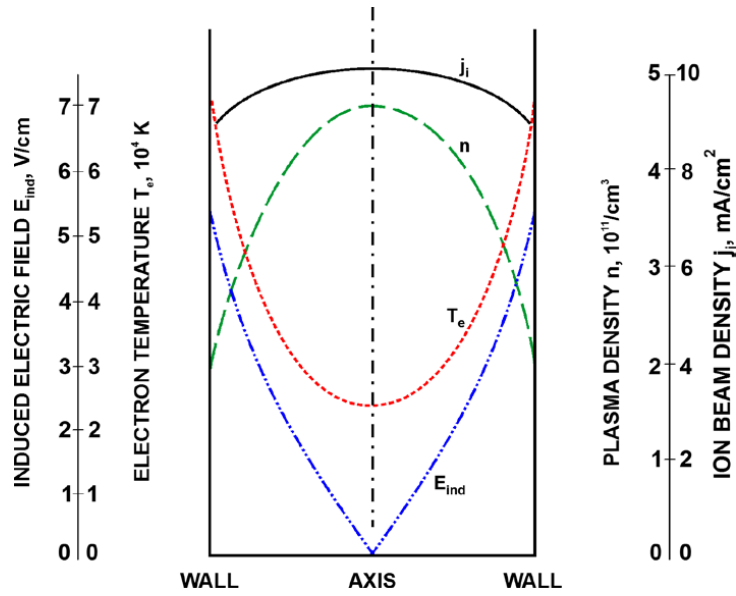
Figure 2.16: Induced electric field, electron temperature, plasma density and ion beam density as a function of the radius, as measured in the RIT 10 ion thruster (Loeb et al., 1988).

Nevertheless, the plasma density n is highest at the centre of the discharge. This is due to the presence of the sheaths near the walls which reduce the plasma density, as was discussed in Figure 2.12. Also, note that the plasma density shape resembles that of a parabola. This behaviour of the plasma density will be used later when developing the RF ion thruster model. Finally, as can be observed in Figure 2.16, the ion beam density J_i is rather flat. This is because the ion beam density is proportional to $n\sqrt{T_e}$. Therefore, a decrease in the ion density n away from the axis is partially offset by an increase in the electron temperature T, as can be seen in Figure 2.16. A flat ion beam density profile has numerous advantages. First, it means that the beam flatness is higher which results in a larger total extracted current. Second, the ion optics apertures can be placed at greater radii, which increases the total extracted beam current as well. Finally, a uniform beam density profile translates into a uniform beam divergence profile, which significantly improves the lifetime of the ion optics and also the produced thrust.

2.4.4 Plasma extraction

Figure 2.17 depicts a potential distribution in the ion optics system. To extract the quasi-neutral plasma from the discharge chamber, a set of at least two perforated grids is needed. The screen grid is biased at the high positive voltage U_{scrn} relative to the ground (or common) potential. The screen grid, therefore, raises the plasma potential to the so-called beam potential $U_b = U_{scrn} + \phi$, where ϕ is the plasma sheath potential equal to about a few tens of volts. A second grid, called the acceleration (accel) grid, is biased negatively with respect to the screen grid (or common) at the potential U_{acc}. First, the accel grid is needed to extract the positive ions from the plasma. Second, the accel grid is required to prevent the very mobile electrons from the neutraliser and background plasma from coming back into a highly positive discharge chamber plasma and overloading the screen power supply (Goebel and Katz, 2008). It is optional to use the deceleration (decel) grid placed downstream of the accel grid and biased at the ground (or common) potential U_{dec}. The main purpose of the decel grid is to shield the accel grid from ion bombardment by charge exchange (CEX) ions produced in the space close to the grids (Goebel and Katz, 2008). Therefore, a three-grid ion optics system has a greater lifetime than a two-grid ion optics system. Furthermore, as can be seen in Figure 2.17, the ion space charge in the beam modifies the grid potential distribution. For instance, the relative accel potential U_{acc} becomes greatly reduced and the relative common potential rises to space potential U_{space}.
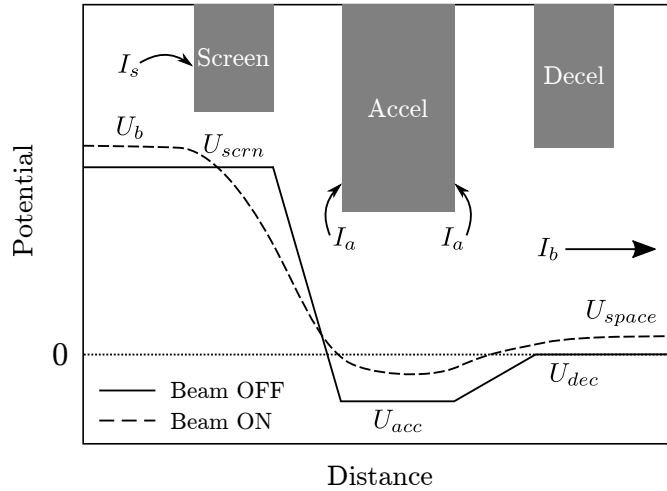
Figure 2.17: Potential distribution on the axis of symmetry of the grid apertures for the cases with and without the ion extraction (beam), and the main grid currents.

As illustrated in Figure 2.17, there are two main currents that can be measured by the grid power supplies. First, the screen power supply measures the ion current that passes through the screen grid, which is referred to as the screen current I_s. Second, the accel power supply measures the ion current that strikes the accel grid either directly from the beam or due to charge exchange, which is referred to as the accel current I_a. The

current of ions that passes through both the screen and accel grids is called the beam current I_b. Usually, the beam current can be calculated as $I_b = I_s - I_a$. However, during nominal operation, $I_a \approx 0.02 I_s$. Therefore, it is often assumed that $I_b \approx I_s$. Finally, the maximum current that an ion optics system can extract and focus can be estimated using the Child-Langmuir law and is called the perveance (Goebel and Katz, 2008)

$$P_{max} = \frac{I_b}{U^{3/2}} = \frac{\pi \epsilon_0}{9} \sqrt{\frac{2e}{M_i}} \frac{D^2}{d^2}, \tag{2.46}$$

where d is the effective grid gap, D is the beamlet diameter and U is the applied voltage.

2.5 Inductive discharges

2.5.1 RF thruster research

The idea of generating plasmas using RF fields was first presented by Hittorf (1884) in 1884. Since then, this idea has been extensively explored for building various radio frequency plasma devices. These include RF ion sources for neutral beam injection systems of fusion devices (Speth et al., 1999), plasma chemistry, plasma processing of materials (Godyak, 2013; Freisinger et al., 1988) and electric propulsion. In 1960, Professor Loeb started performing research on using RF inductive discharges for electrostatic propulsion (Meusemann and Winter, 2005). In 1992, due to Loeb's pioneering research work, the RIT 10 thruster was launched on the EURECA satellite. Whereas, in 2001, the RIT 10 was used for the propulsion of the ESA's ARTEMIS satellite (Killinger et al., 2007). Following an Ariane-5 upper stage malfunction, the RIT 10 thruster, part of a RITA (radio frequency ion thruster assembly) system, was operated for around one year as the principal means of propulsion to shift the ARTEMIS spacecraft to the desired mission orbit (Killinger et al., 2007), thus saving the mission. This proved the RF thrusters' versatility and reliability. A historical overview of the RF ion source development and their applications for electrostatic space propulsion missions can be found in the work by Neumann et al. (2007).

One of the main advantages of RF thrusters is that they can sustain an electrodeless discharge, which means that the lifetime of the thruster can be immensely increased compared to an electron bombardment ion thruster. This is because the electron bombardment ion thrusters suffer from cathode erosion (Goebel and Katz, 2008). During the initial research efforts, the coil was inserted in the plasma to increase the skin depth and thus improve the power transfer efficiency (Lee and Nakanishi, 1981). However, the coil suffered from erosion due to high energy ions. Loeb chose to wrap the coil around an insulating quartz chamber, thus eliminating the erosion problem. Loeb helped develop the RIT 10 ion thruster which at first demonstrated an ion production cost of 350 eV/ion using a mercury propellant (Koschade et al., 1972). At that time, such an ion

production cost was about 50% higher than that of electron bombardment thrusters. Nevertheless, due to continuous research efforts by Loeb and Airbus, the RF thruster efficiency has increased dramatically. For instance, the latest RIT-XT thruster, that uses xenon propellant, developed by Airbus has an ion production cost of only around 220 eV/ion and a specific impulse of around 3,000 s, with a thrust of up to 80 mN (Leiter et al., 2003). These values are comparable to the state-of-the-art electron bombardment thrusters (Goebel and Katz, 2008).

An additional advantage of RF gridded ion thrusters is that they are easily throttleable by varying the RFG power. This is because the ion production and acceleration mechanisms are separate, which allows RF thrusters to be scaled down. Recent space missions such as Darwin (Kilter and Karlsson, 2004), LISA (Leiter et al., 2011) and NGGM (Feili et al., 2015a) require thrusters to work in the μN range and to be easily throttleable. Therefore, RF ion thrusters have been considered as one of the primary candidates in fulfilling these mission requirements. However, working of an RF thruster involves many different physics phenomena, as was shown in Figure 2.15 and Figure 2.16, making a holistic approach to the performance analysis difficult. Furthermore, due to the small size of the scaled-down thrusters and due to high frequencies, plasma measurements are challenging to perform. Additionally, to make the scaled-down thrusters applicable to the above-mentioned space missions, they must consume small amounts of power, have a high efficiency, and must be prevented from overheating. As a result, comprehensive modelling tools are needed.

2.5.2 Transformer model

Thompson (1890) was one of the first to analyse the physics behind the RF or so-called inductive discharges. In performing the analysis, Thompson (1890) considered the discharge to be the secondary of an air-core transformer. Later, using this idea, Piejak et al. (1992) did a comprehensive analysis of the inductive discharges through the use of electrical circuit parameters such as an RF current, voltage and power to characterise the coil and plasma behaviour. The advantage of such a method is that it does not require an explicit knowledge of the spatial field and plasma density distributions. Other researchers, however, concentrated on determining the electromagnetic field and electron density distribution profiles either analytically or computationally. Comprehensive reviews of these modelling efforts and main assumptions were published in the works by Gudmundsson and Lieberman (1997) and Lister et al. (1996). In summary, a majority of these models used the transformer assumptions and solved analytical Maxwell's equations, ignoring the proximity and end coil effects, in a cylindrically symmetric coil and plasma systems. Additionally, electrons were assumed to follow a Maxwellian distribution, and a pre-defined radial variation in the plasma density was introduced.

The circuit used in analysing the plasma-coil system as a transformer is shown in Figure 2.18. The plasma is represented as a one-turn secondary coil of an air-core transformer. The secondary circuit is composed of the plasma inductance $L_p = R_p/\nu$ and the resistance R_p, where ν is the elastic collision frequency between electrons and neutral atoms. Assuming a low-pressure regime where $\nu << \omega$, and a cylindrical geometry with the radius r_0 and length l, the plasma resistance can be expressed as (Chabert and Braithwaite, 2011)

$$R_p = \frac{\pi r_0}{\sigma_r l \delta}, \tag{2.47}$$

where σ_r is the real part of plasma conductivity, which defines the actual plasma loss, and δ is the skin depth. The way these parameters can be obtained will be discussed in Chapter 3 and Chapter 4. Note that the inductance L_p comes from the phase lag between the current and voltage and acts as an electron inertia term (Chabert and Braithwaite, 2011). Whereas, the plasma resistance R_p results from the elastic electron-neutral collisions.

To accurately represent the plasma, another inductance term denoted as L_{mp} is introduced in the secondary. The inductance L_{mp} comes from the fact that induced eddy currents inside the plasma generate a magnetic field that resists the magnetic field produced by the coil. In the high plasma density regime, the electron current is concentrated in a narrow skin depth next to the discharge chamber walls. Therefore, assuming a cylindrical geometry, the inductance L_{mp} can be estimated as (Chabert and Braithwaite, 2011)

$$L_{mp} = \frac{\mu_0 \pi r_0^2}{l}. \tag{2.48}$$

Note that there is also the plasma current I_p flowing in the secondary. This current is needed to represent the induced azimuthal electron current in the plasma.
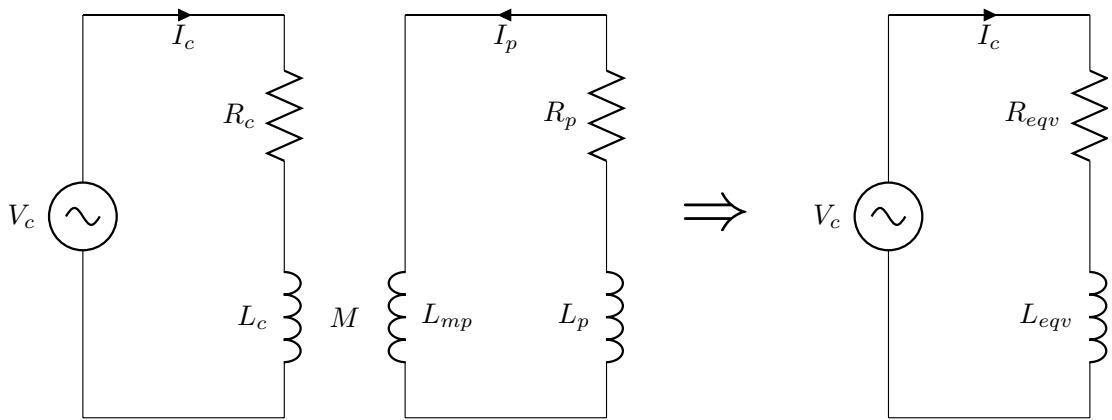
Figure 2.18: Description of the transformer model used to model RF inductive discharges. On the left - a transformer circuit where the plasma is represented as the secondary of the transformer. On the right - an equivalent transformer circuit.

The primary of the transformer is composed of the coil resistance R_c and the inductance L_c. Also, the actual coil current I_c flows in the primary due to the coil voltage V_c generated by the RFG. Finally, the mutual inductance M is used to determine the coupling between the coil and the plasma. Based on the ordinary transformer theory (Chabert and Braithwaite, 2011), primary and secondary circuits can be transformed into a single circuit composed of the equivalent resistance R_{eqv} and inductance L_{eqv}. Note that the equivalent resistance R_{eqv} is itself composed of the coil resistance R_c and induced plasma resistance R'_p. By applying Maxwell's equations to the circuit shown in Figure 2.18, the following relations can be obtained

$$V_c = j\omega L_c I_c + R_c I_c + j\omega M I_p, \tag{2.49}$$

$$V_p = j\omega L_{mp} I_p + j\omega M I_c, \tag{2.50}$$

$$V_c = (j\omega L_{eqv} + R_{eqv}) I_c. \tag{2.51}$$

After some manipulations, it can be shown that the mutual inductance can be expressed as (Chabert and Braithwaite, 2011)

$$M^2 \omega^2 = \left[R_p^2 + \left(\omega L_{mp} + R_p \left(\frac{\omega}{\nu_m} \right) \right)^2 \right] \frac{|I_p|^2}{I_c^2}. \tag{2.52}$$

Finally, the equations defining the equivalent resistance R_{eqv} and inductance L_{eqv} can be written as (Chabert and Braithwaite, 2011)

$$R_{eqv} = R_c + R_p \frac{|I_p|^2}{I_c^2}, \tag{2.53}$$

$$L_{eqv} = L_c - (L_{mp} + L_p) \frac{|I_p|^2}{I_c^2}. \tag{2.54}$$

The equations defining the equivalent circuit parameters are very important because they represent the circuit as seen from the RFG terminals. Therefore, the matching can be performed and the circuit can be optimised.

2.5.3   Global and thermal models

Global (or 0D) models use volume-averaged particle and energy balance equations to compute various plasma parameters such as temperature, potential and density. Additionally, global models often assume a Maxwellian electron energy distribution. One of the first such models was introduced by Brophy (1984) for a DC ion thruster. Brophy (1984) used the results from the global model to estimate the DC ion thruster's performance. Similar global models were developed for analysing RF plasmas by Gudmundsson and Lieberman (1997) and Piejak et al. (1992) as well. Recently, global models have been introduced by Goebel (2008), Tsay (2006) and Chabert et al. (2012). Goebel (2008) developed an analytical RF thruster model by using volume-averaged

plasma assumptions to calculate the plasma power losses for a desired beam current and propellant mass flow rate. However, Goebel (2008) did not analyse electromagnetic field distributions and did not present a method for determining the power transfer efficiency from the coil to the plasma. Instead, Goebel (2008) analysed the thruster performance in light of electric propulsion concepts. Therefore, Goebel (2008) introduced such concepts as the beam current, discharge loss and mass utilisation efficiency. However, the fact that Goebel (2008) analysis does not provide means to calculate the total input power to a thruster is a serious drawback.

Chabert et al. (2012) extended the Goebel (2008) model by introducing the above-mentioned transformer assumptions. As a result, Chabert et al. (2012) were able to calculate the power transfer efficiency and the total input power to a thruster. Nevertheless, it can be shown that for the RIT 3.5 thruster, the transformer assumptions are fully accurate only at ion densities of around 10^{19} 1/m^3 (Chabert and Braithwaite, 2011). However, the RIT 3.5 thruster works at ion densities of about 10^{17} 1/m^3, as was calculated by the model in Chapter 4. Chabert et al. (2012) also introduced an additional power balance equation to estimate the neutral gas heating inside a discharge chamber, allowing the possibility to obtain the gas temperature. However, Chabert et al. (2012) analysis showed that the neutral gas temperature effect on thruster's performance is negligible. The most comprehensive effort so far to model an RF ion thruster was done by Volkmar and Ricklefs (2015). Volkmar and Ricklefs (2015) developed a 3D Biot-Savart solver to calculate the coil impedance and used the magnetic diffusion equation to determine the electromagnetic field distribution inside the plasma. The model was still not representing the surrounding thruster components and, therefore, not accounting for the coupling between the coil, the grids and the case. This is important because it changes the effective inductance and resistance of the system as seen by the RFG. This affects the power balance and matching conditions.

Furthermore, Volkmar and Ricklefs (2015) represented the plasma with a uniform ion density and conductivity calculated from a 0D model assuming a Maxwellian electron energy distribution. Neglecting the spatial plasma density variation causes a substantial error in determining the electromagnetic field distribution inside the plasma. This results in an inaccurate representation of the coil and plasma coupling which dictates the power losses in an RF thruster (Gudmundsson and Lieberman, 1997). Additionally, the model assumed that the extracted ion current is space charge limited, and Child-Langmuir law could be used to calculate the extracted beam current. However, many RF thrusters, especially the small ones (discharge chamber diameter $\approx$ 4 cm), operate at current densities much lower than the Child-Langmuir limit (Loeb et al., 2004). For instance, the Child-Langmuir current density limit for the RIT 3.5 is about 20 mA/cm^2, which is similar to that of various other RIT class thrusters (Loeb et al., 2004). However, the RIT 3.5 works only at about 7 mA/cm^2.

There have also been some efforts aimed at describing non-local and non-linear effects. First, in addition to the inductive coupling, the capacitive coupling was described by Chabert et al. (2003) using the global model and lumped circuit approach. In this model, the capacitive resistance was set to account for the capacitive heating. Furthermore, Godyak et al. (1998) presented an experimental evidence of the collisionless (non-local) power absorption in inductively coupled plasmas. Godyak et al. (1998) noticed that such behaviour is especially predominant in low-pressure plasmas where the electron mean free path is comparable to the discharge chamber dimensions. As a consequence, these non-local effects change the electron distribution function in such a way that it no longer follows a Maxwellian distribution. As a result, a kinetic approach that uses a non-Maxwellian energy distribution function is needed. A self-consistent model was presented by Kaganovich and Polomarov (2003) that estimates the electric field penetration and skin depth in the non-local regime. Additionally, Mistoco (2011) used 1D kinetic model equations derived from the Boltzmann equations to account for non-local effects. Mistoco (2011), however, still assumed a Maxwellian energy distribution function. Finally, Turner (1993) introduced the anomalous skin depth to represent the non-exponential field decay inside the plasma. This enabled the power absorbed by the plasma to be calculated. However, the system used by Turner (1993) was idealised without a proper representation of the coil or the thruster.

To date, there is no self-consistent thermal model capable of accounting for the plasma and RF heating and, in turn, for thruster's temperature effect on the plasma properties and RF heating. Full RF thruster thermal models are particularly challenging to construct because the magnitude of RF heating (via eddy currents) is dependent on the thruster's component temperatures due to a change in their electrical conductivity. Gartner et al. (2013) did create a thermal model of the RIT 2.5 thruster. However, the model developed by Gartner et al. (2013) only included the RF heating contribution. The plasma heating was not modelled because Gartner et al. (2013) did not develop a plasma model to account for different boundary heat fluxes. Creating such a plasma model introduces a great deal of complexity since many plasma parameters are unknown or cannot be measured. Therefore, Gartner et al. (2013) model was only applicable for conditions when there is no plasma, and the thruster is heated solely by the eddy currents. Nevertheless, a few thermal models have been developed for ring cusp gridded ion thrusters such as the one by Noord (2007). One of the main goals of the thesis is to introduce a full RF thruster model that could be used to predict the thruster's performance and temperature distribution in a consistent fashion with solution times of about an hour, acting as a fast, efficient and accurate thruster design tool.

2.6   Summary

Background material regarding electric propulsion fundamentals, RF physics, plasma physics and inductive discharges has been presented. The list below summarises the key points obtained by analysing the background material:

- electric thrusters exhibit high specific impulse values, which reduces the propellant needs of high delta-V missions;

- electric thrusters have low thrust and are power limited;

- RF ion thrusters work based on the principles of Maxwell's equations;

- plasma can be represented using bulk properties such as density, pressure, temperature and potential;

- the main components of RF ion thrusters are: a discharge chamber, an ion optics system, a coil, a gas inlet, a neutraliser and an RFG;

- in RF ion thrusters, plasma parameters vary as a function of the discharge chamber radius;

- the performance of RF ion thrusters has improved a lot over the years and is now comparable to that of ion bombardment thrusters;

- a transformer model is often used to simulate inductive RF discharges.

Finally, the chapter has provided a comprehensive literature review regarding the previous research efforts on inductive discharges and RF ion thrusters in general. The list below presents the key conclusions drawn from the literature review:

- global (or 0D) models are a relatively easy way to estimate volume-averaged plasma properties;

- there has been no RF ion thruster electromagnetic/plasma model that includes a full 3D RF ion thruster structure;

- RF ion thruster electromagnetic models often exclude the radial ion density variation and end coil effects, which causes substantial errors when estimating the power transferred from the coil to the plasma;

- assuming that RF ion thrusters always operate at the Child-Langmuir current density limit is not correct;

- there has been no thermal model for RF ion thrusters that includes electromagnetic and plasma heating in a self-consistent fashion;

- non-local effects and collisionless heating must be accounted when analysing RF ion thrusters;

- RF circuits are often excluded from RF ion thruster models.

The following chapter provides the details of an RF ion thruster model that has been created to overcome the shortcomings and inaccuracies of the previous models, as has been shown in the list above and in Section 2.5.3.

3

RF gridded ion thruster model

This chapter presents an engineering model designed to simulate the RF gridded ion thruster performance and thermal behaviour without the shortcomings of the previously developed models. The developed model is based on the RIT 3.5 geometry, operational set-up and physics, as shown in Figure 3.1. However, the model allows analysing other types of RF gridded ion thrusters as well. Figure 3.1 illustrates the main physics phenomena occurring in the RIT 3.5 thruster. Note that tildes (̃) represent the oscillatory (or complex) nature of the variables. The RIT 3.5 thruster works by passing a high current $\tilde{I}_c$ at a frequency of about 3 MHz through a coil wrapped around an insulating gas chamber, which generates the axial magnetic field $\tilde{B}$. Due to Faraday's law, the axial magnetic field induces the azimuthal electric field $\tilde{E}_\theta$. If the induced electric field is strong enough, the electrons e are accelerated to energies sufficient to ionise the neutral gas atoms with the density n in the discharge chamber. This produces a plasma of the density n_i (+) and the azimuthal plasma current $\tilde{I}_{p\theta}$. The plasma is extracted and focused with a positively biased "screen" grid (I) at the potential U_{scrn} and a negatively biased "accel" grid (II) at the potential U_{acc} located at a downstream end of the discharge chamber. There is also a "decel" (III) grid which is set to the local ground potential, as shown in Figure 3.1. All these grids represent the ion optics system. The ion optics design also controls the neutral gas pressure p inside the discharge chamber since the propellant that is not ionised leaks through the grids.
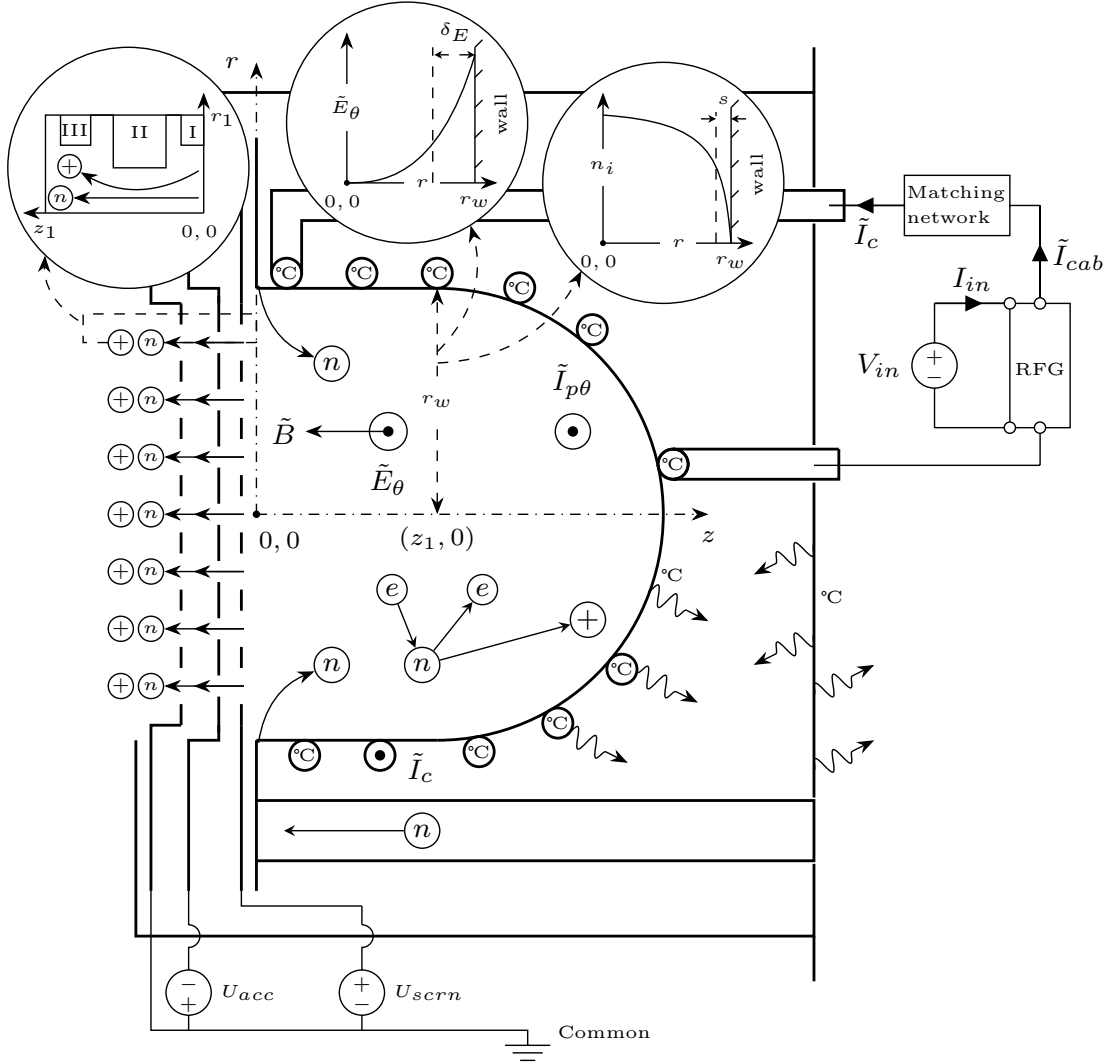
Figure 3.1: Schematic highlighting the main RIT 3.5 (or similar) RF gridded ion thruster geometry, physical components, RFG circuit, beam extraction circuit, heat radiation and other physical processes occurring in the plasma (not to scale).

Since plasma acts as a conductor, the electric (and magnetic) fields decay within a skin depth δ. Depending on the ion density, the electric field skin depth δ_E can vary from being only a few percent to 63% of the thruster's radius (Chabert and Braithwaite, 2011). Similarly, in the case of the magnetic field, the skin depth δ_B can be equal to only a few percent of the thruster's radius or it can be much larger than the thruster's radius (Chabert and Braithwaite, 2011). This strongly influences the power absorbed by the plasma. Additionally, because plasma is quasi-neutral, the ion density n_i is not constant but varies radially in a decaying manner towards the wall with the sheath thickness s. The coil is powered by an RFG that converts the DC voltage input signal V_{in} at the current I_{in} to a high-frequency output sinusoidal current $\tilde{I}_{cab}$ flowing in the coaxial cable connected to the coil. Between the RFG and the coil, there is also a matching network that transforms the thruster's input impedance to the impedance of the RFG.

The aim when designing a thruster for space applications is to transfer as much power as possible from the RFG to the plasma. An ideal thruster, therefore, would transfer all input power to the plasma. However, a significant amount of the input power goes into the coil itself, the cable, the RFG and the surrounding thruster's components. Also, a substantial amount of power is lost from the plasma to the discharge chamber walls or is radiated to the environment. Furthermore, there are losses associated with the electromagnetic eddy current production in the thruster's components. All these contribute to the heating of the thruster - requiring a thermal analysis. Therefore, to have a complete model of the thruster, thermal effects have to be consistently included. This is because the thruster's temperatures affect the plasma properties through the neutral gas pressure and the eddy current losses through a change in the component electrical conductivity. In turn, the plasma properties affect the thruster's temperatures as well. As has been shown, the RF thruster operation encompasses many different areas of physics. As a result, a self-consistent, holistic modelling approach is needed in order to accurately predict the RF ion thruster behaviour and performance.

3.1   Model description

The model presented in the thesis is based on a full 3D RIT 3.5 thruster geometry and operating parameters. Only minor modifications in the geometry that have a negligible influence on the final solution have been performed. The model deals only with the steady-state conditions. The plasma is assumed to be quasi-neutral ($n_i \approx n_e$) within the bulk of the discharge, meaning that the ion density n_i and the electron density n_e are approximately equal. Note, however, that the quasi-neutrality condition does not apply in the plasma sheaths and in the space between the grids. Additionally, it is assumed that only singly-charged ion species are present in the plasma. What is more, the plasma is represented using bulk, volume-averaged quantities such as the ion density n_i, neutral gas density n_0 and electron temperature T_e, which is indicative of global (0D) models. Finally, note that for simplicity, in this chapter, the electron (T_e) and ion (T_i) temperatures are expressed in the units of electronvolts (eV).

The aim of the model is to predict all the main RIT 3.5 (or similar) RF gridded ion thruster performance parameters. This is because small RF thrusters (discharge vessel diameter ≈ 4 cm), for instance, the RIT 3.5, suffer from poor efficiency. The poor efficiency, compared to larger thrusters, is a direct result of an increase in the ion production cost (W/A). The rise in the ion production cost is caused by an increase in the discharge chamber wall surface area A_c to volume V_d ratio (A_c/V_d) (Goebel and Katz, 2008; Loeb et al., 2004). Additionally, smaller thrusters are run at higher pressures, resulting in a lower mass utilisation efficiency (Loeb et al., 2004). Therefore, a thorough understanding of the small thruster behaviour and a capability to optimise them are vital if such thrusters are to be applicable for low power, low thrust space missions.

Software	Physical phenomenon	Output parameters	Domain size	Equations and methods
IBSimu	Plasma extraction through an opening	Ion optics transparency, beam divergence	2D axisymmetric	Poisson's equation, Vlasov iteration
COMSOL	Neutral gas free molecular flow through a cavity	Clausing factor	2D axisymmetric	Molecular dynamics equations, angular coefficient method
COMSOL	Neutral gas free molecular flow inside a volume	Neutral gas pressure and density	3D	Molecular dynamics equations, angular coefficient method
COMSOL	Electron transport inside a plasma	EEDF, Reaction rate coefficients, effective collision frequency, power losses	1D	Boltzmann equation, two-term approximation
Matlab	Plasma generation inside a volume	Plasma density, potential and temperature, discharge loss	0D	Particle and energy balance, volume averaging
Matlab	Plasma generation inside a volume	Plasma density distribution function	1D	Bohm criterion, empirical observations
COMSOL	Electromagnetic fields inside plasma, thruster components and free space	Electromagnetic field magnitude, phase, eddy current power losses, thruster impedance	3D	Maxwell's laws
COMSOL	Temperature distribution	Temperatures and heat fluxes	3D	Stefan-Boltzmann and Fourier's laws
COMSOL	Electric circuits	Electric currents, voltages, power losses, impedance	0D	Kirchhoff's laws

Table 3.1: Descriptions of different sub-models used to construct the holistic RF gridded ion thruster model. The software type, physical phenomenon, output parameters, domain size, equations and methods are indicated for each sub-model.

The model developed in the thesis investigates all five major branches of RF thruster operation: the electromagnetic field generation, plasma production, ion extraction, RF circuit operation and temperature distribution. These branches are represented using a combination of different sub-models, as shown in Table 3.1. Table 3.1 also indicates the software tool that was used to construct the sub-model and the main output parameters solved for. Additionally, the domain size which is used by the model to solve equations and apply boundary conditions is indicated. Note that even though the electromagnetic fields are solved in three dimensions (z, r, θ), other plasma properties are solved only in

(z, r) dimensions and then revolved 360°. Finally, Table 3.1 indicates the main equations and the methods used to obtain the output parameters.

3.2   Solution method

A schematic description of the way the model is solved is shown in Figure 3.2. All sub-models are coupled together through Matlab (The MathWorks Inc., 2014) to easily control the input variables and output parameters for a self-consistent solution. First, the thruster and grid dimensions are given to the model. To make it easier to compare the model results to the RIT 3.5 experimental data, the positive screen voltage U_{scrn} and the negative accel voltage U_{acc} are given as operational inputs to the model. Then, the desired thrust point is defined by providing the input mass flow rate $\dot{m}_{in}$ and the input RFG voltage V_{in}. The system is solved for three unknowns (blocks indicated in bold): the electron temperature T_e, the discharge chamber wall temperature T_w and the bulk ion density n_i. Therefore, at the beginning of each iteration, the guess values to these unknown parameters are provided. The system of equations is solved by having three iteration branches; the first solves for the electron temperature T_e and the second solves for the discharge chamber wall temperature T_w. The third branch solves for the ion density n_i by comparing the RFG input voltage V_{in} to the RFG input voltage V_{in}^{out} obtained from the model for a given input mass flow rate $\dot{m}_{in}$.

All this information is passed to the sub-models in a consecutive order. That is, the output from each sub-model is used as the input for the next one and so on, as indicated by the arrows in Figure 3.2. At the end of the first iteration branch, a value for the electron temperature T_e^{out} is obtained using conservation of power. This value is compared to the guessed value T_e^g. If they are not equal within 1%, the iteration is repeated and a new electron temperature guess value T_e^g is chosen. Once the electron temperature is obtained, a radially varying plasma electrical conductivity $\sigma_p(r)$ is calculated, and the power balance within the plasma is performed. By performing the power balance, the total power P_d needed to sustain the plasma discharge and the individual power fluxes P_k to thruster's surfaces/environment are estimated. The plasma electrical conductivity $\sigma_p(r)$ is then used to solve for the electromagnetic fields in the full 3D geometry of the thruster. The electromagnetic model is utilised to obtain the induced plasma resistance R_p', the thruster's resistance without the plasma R_0' and the thruster's inductance L_{thr}. In the next step, using Ohm's law, the required coil current I_c to sustain the discharge is calculated, as given in Figure 3.2.

Having obtained the coil current, and using Ohm's law again, the model calculates the RF heating values W_k. Finally, the heat fluxes P_k and the RF heating values W_k are used to represent the heat sources in the 3D thermal model of the thruster. From the thermal model, the temperature distribution is obtained. In particular, a special focus

is placed on the discharge chamber wall temperature T_w^{out}. If the guessed discharge chamber wall temperature T_w^g does not match the output temperature T_w^{out} within 5%, T_w^g is changed and a new iteration is started. Once a self-consistent temperature distribution is obtained, the coil resistance R_c, the reflected screen resistance R'_{scrn} and other reflected resistances are determined. These resistances are used in the RF circuit model to determine the matching resonant frequency f_r, the coaxial cable current I_{cab}, the RFG input voltage V_{in}^{out}, the circuit losses and the total input power P_{in}. If the RFG input voltage V_{in}^{out} obtained as the output does not match the RFG input voltage V_{in} that was used in defining the thrust point within 2%, the model changes the ion density guess value n_i^g in incremental steps until a solution is obtained.
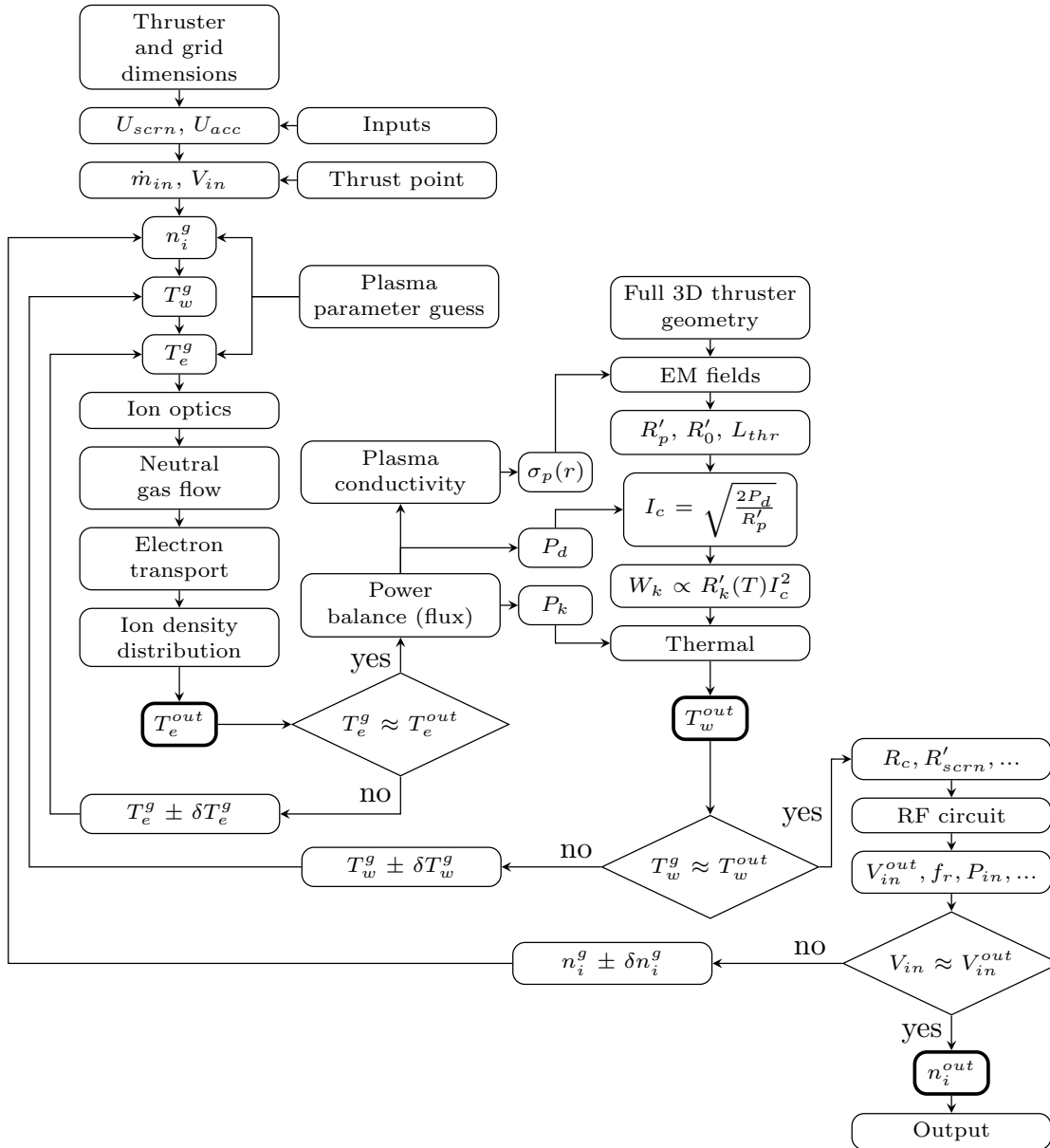
Figure 3.2: Solution method and main parameters of the model. Variables that the model solves for are indicated in bold. Arrows represent the way in which the model is solved.

Iterations in both branches are performed using Matlab's built-in global optimisation functions. Once a consistent solution is reached in all three branches, the iterations are stopped and the model outputs the results. In particular, the model provides the plasma, electrical, thermal, electromagnetic and RF circuit parameters obtained at the correct ion density, discharge chamber wall temperature and plasma temperature values. Normally, the model determines the bulk ion density n_i for a given operational point within 4 iterations. Furthermore, for each ion density iteration, it takes about three iterations to determine the correct electron temperature T_e, and two iterations to determine the discharge chamber wall temperature T_w. Note that the modelling results presented in this thesis were obtained by solving the model using a PC that has a 2.8 GHz, 4-core CPU and 16 GB of RAM.

Using the aforementioned PC, each iteration to calculate the electron temperature T_e takes about 1 min. This 1 min is mostly needed to solve the 3D neutral gas flow sub-model. The ion optics and electron transport sub-models are solved within a few seconds. To obtain the discharge chamber wall temperature T_w, the 3D thermal and 3D electro-magnetic (EM) sub-models need to be solved. The thermal model is solved within about 6 min, while the EM model takes about 4 min to solve. Finally, the RF circuit model is solved within a few seconds. Therefore, the total time needed to obtain a solution can be estimated as $4[n_i] \times \{3[T_e] \times (1 \text{ min}) + 2[\text{EM}] \times (4 \text{ min}) + 2[\text{Thermal}] \times (6 \text{ min})\}$, which results in approximately 90 min. This, however, depends on the chosen mesh quality and on the mass utilisation efficiency. For instance, it was noticed that as the mass utilisation efficiency increases, the solution time goes up. Also, the thermal model can be turned off, which reduces the solution time by more than 40 min. In the following sections, the physics behind each sub-model and the underlying assumptions will be explained. The discussion is started with the ion optics sub-model.

3.3 Ion optics model

A general-purpose open source ion optics code IBSIMU developed by Kalvas et al. (2010) capable of solving electric fields in 1D, 2D and full 3D geometries is utilised to simulate the ion optics. The code is integrated into the main model and is used to simulate 2D axisymmetric positive ion extraction from the RF ion thruster plasma. In the model, the plasma is represented by a surface with the total upstream plasma sheath potential U_t^u, often referred to as the beam voltage V_b, (Lieberman and Lichtenberg, 2005)

$$U_t^u = \phi_s + U_{scrn}, \tag{3.1}$$

where ϕ_s is the floating plasma sheath potential, generally about $20 - 30$ V, and U_{scrn} is the screen grid potential. The total downstream plasma potential U_t^d is determined by the software itself based on the initial upstream boundary conditions.

Figure 3.3 depicts the simulation geometry and boundary conditions. As displayed in Figure 3.3, r_0 represents the open area radius, while r_b is interpreted as the radius of the beam extraction area. In other words, r_0 is used to calculate the aperture area A_0, and r_b is used to define the beam extraction area A_b, as shown in Figure 3.4. Note that the beam extraction area A_b also includes the aperture area A_0. The loss area depicted in Figure 3.4 represents the grid area that excludes the beam extraction area A_b. It is assumed that ions that arrive at the loss area have 0% chance of being extracted. Whereas, ions that arrive at the beam extraction area A_b have a percentage T_{eff} of being extracted, which is calculated by the ion optics model based on the plasma and boundary conditions.
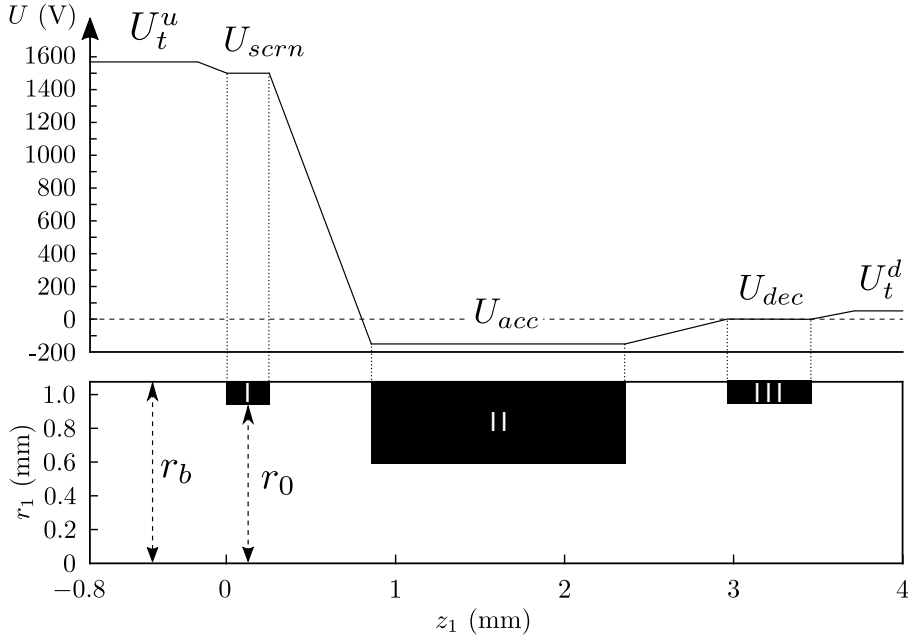
Figure 3.3: 2D axisymmetric half-beamlet simulation geometry and boundary conditions representing the RIT 3.5 ion optics. In the case depicted, $U_{scrn} = 1,500$ V, $U_{acc} = -250$ V and $U_{dec} = 0$ V.

As a boundary condition, it is assumed that ions flow towards the sheath at the beam extraction area A_b with the Bohm current magnitude I_B equal to (Lieberman and Lichtenberg, 2005)

$$I_B = n_s^u u_B A_b e, \tag{3.2}$$

where n_s^u is the upstream ion sheath edge density, $u_B = \sqrt{eT_e^u/M_i}$ is the Bohm velocity used to mimic the pre-sheath behaviour, T_e^u is the upstream electron temperature and A_b is the beam extraction area, as defined in Figure 3.4. Note that the Bohm sheath criterion in the form expressed above is only valid for $T_e >> T_i$ (Goebel and Katz, 2008), where T_i is the ion temperature. This relationship holds in RF discharges since the ion temperature is equal to the discharge chamber wall temperature T_w, which is, generally, about 400 K (Chabert et al., 2012). While the electron temperature T_e is equal to a few eV (or tens of thousands of Kelvin).
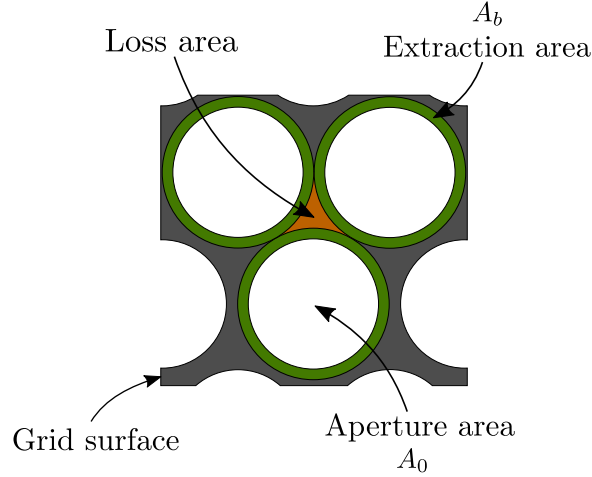
Figure 3.4: Schematic of the grid geometry defining the extraction, aperture and loss areas as used in calculating T_{eff}. Ions arriving at the loss area have 0% chance of being extracted, while ions arriving at the extraction area have T_{eff} chance of being extracted. Note that A_b = green + white.

Some of the Bohm current arriving at the beam extraction area does not get extracted and hits the screen grid. This depends on the shape of the sheath which is resolved by IBSIMU. Therefore, as mentioned before, the percentage (or the ratio) of the extracted beam current is quantified using the effective transparency of the ion optics system T_{eff}. The parameter T_{eff} is calculated as the ratio of the total extracted ion current I_b (determined by IBSIMU) to the total Bohm current I_B arriving at the beam extraction area A_b (Goebel and Katz, 2008)

$$T_{eff} = I_b/I_B. \tag{3.3}$$

Figure 3.5 displays how T_{eff} varies as a function of the beamlet current, where f_{os} represents the screen grid open area fraction, which for the RIT 3.5 ion optics is about 0.63. Whereas f_b represents the beam extraction area fraction equal to about 0.84. Note that f_b sets the maximum value for T_{eff}. For instance, $T_{eff} = f_b$ would mean that all ions arriving at the beam extraction area get extracted into the beam. Figure 3.5 shows that T_{eff} reaches the peak value of about 0.74 at 45 μA. This point is called the cross-over limit. This is because as the beamlet current is decreased below the cross-over limit, the sheath shape in front of the screen grid becomes curved so much that ions are over-focused and directly strike the accel grid (Farnell, 2007). Therefore, T_{eff} decreases. As the beamlet current is increased past the cross-over limit, T_{eff} starts to go down as well. Upon reaching about 280 μA, T_{eff} begins to fall sharply. At this point, it is said that the ion optics has reached its perveance limit because the sheath in front of the screen grid becomes flat and therefore ions directly hit the accel grid (Farnell, 2007).
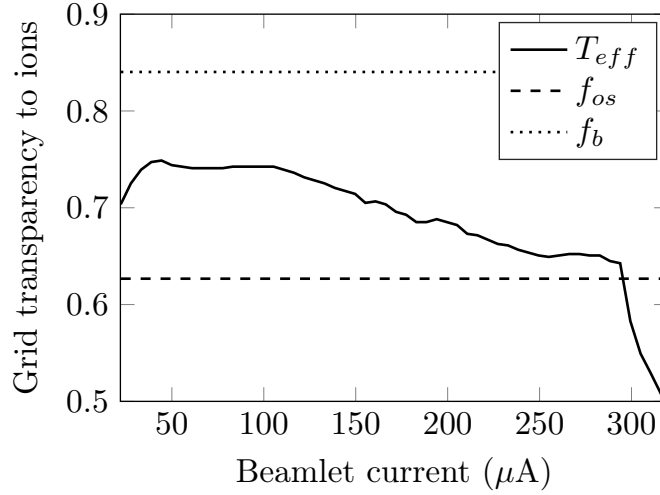
Figure 3.5: RIT 3.5 ion optics transparency to ions at different beamlet currents: $U_{scrn} = 1,000$ V, $U_{acc} = -150$ V, $f_{os} = 0.63$ and $f_b = 0.84$.

An example of multiple ion beam trajectories as predicted by the model for a set of the RIT 3.5 ion optics grids at 2 mN of thrust is shown in Figure 3.6. The operational parameters of 2 mN thrust point are given in Appendix A. Note that the ion optics model is also used to estimate the beam divergence half-angle θ_d which, as was shown in Equation 2.11, affects the produced thrust (Goebel and Katz, 2008). This is achieved by calculating an angle of the streamline which encompasses 95% of the ion current, as defined in Figure 3.6. In the case depicted in Figure 3.6, T_{eff} is about 0.73, while θ_d is roughly 10°.
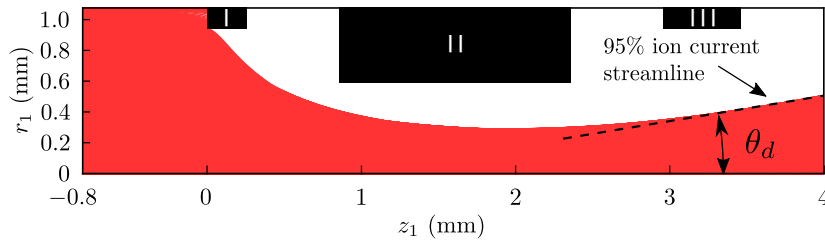
Figure 3.6: 2D axisymmetric half-beamlet ion trajectories for the RIT 3.5 ion optics at 2 mN thrust point. The case depicted has the following parameters: T_{eff} - 0.73 and θ_d - 10°.

3.4   Neutral gas model

3.4.1   Clausing factor

It is important to accurately determine the neutral gas density n_0 in the discharge chamber because it defines the magnitude of the electron temperature and collision frequency between electrons and neutrals. In constructing the model, it is assumed that neutral gas molecules are injected inside the discharge chamber and a fraction of them is ionised. The ones that have not been ionised leak through the grids with a resistance defined by the Clausing factor η_c (Clausing, 1971). The Clausing factor determines the molecule transmission probability through the ion optics and is expressed as the ratio of the incident molecular flux G integrated over the decel grid surface (III) divided by the total incoming flux J integrated over the screen grid surface (I)

$$\eta_c = \frac{\int G \, \mathrm{d}A}{\int J \, \mathrm{d}A}. \tag{3.4}$$

To calculate the Clausing factor, a single ion optics aperture, represented in a 2D axisymmetric geometry, is modelled using the molecular flow module in COMSOL by employing the angular coefficient method. Since the Clausing factor is non-dimensional, it depends solely on the geometry of the grid system, regardless of the upstream neutral gas density. Using the model it was found that the Clausing factor for the RIT 3.5 ion optics grids is about 0.17. COMSOL also allows the neutral gas density distribution inside the ion optics apertures to be determined, as shown in Figure 3.7. This is useful to better understand as to how the ion optics arrangement constricts the neutral gas flow. As Figure 3.7 illustrates, the neutral gas density decreases only slightly through the grid I aperture, but then drops sharply over the grid II, with only about 15% of the initial gas density remaining at the grid III.
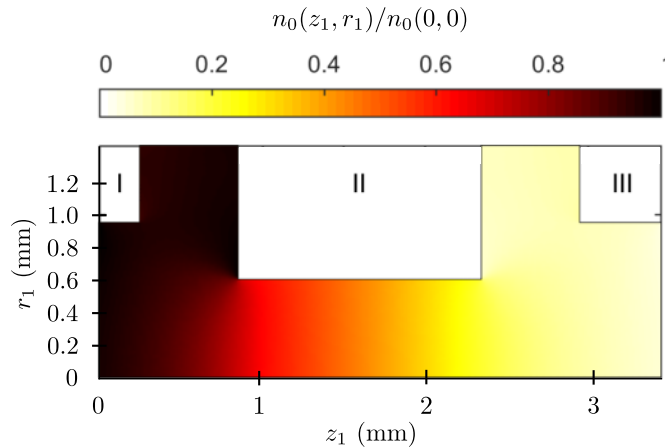
Figure 3.7: 2D axisymmetric neutral gas density distribution normalised to the maximum (upstream) value for the RIT 3.5 ion optics at 2 mN thrust point. For the case depicted, the Clausing factor is about 0.17.

3.4.2 Pressure and density

A neutral gas model is employed to determine the neutral gas pressure p and density n_0 inside the discharge chamber. To do so, the previously calculated Clausing factor, the actual 3D discharge chamber geometry and discharge chamber wall temperature T_w are used as inputs to a 3D free molecular flow module in COMSOL. The 3D simulation geometry and mesh used in constructing the molecular flow module are shown in Figure 3.8. Figure 3.8 also indicates the screen grid area and the locations of where the propellant (gas) enters the discharge chamber.
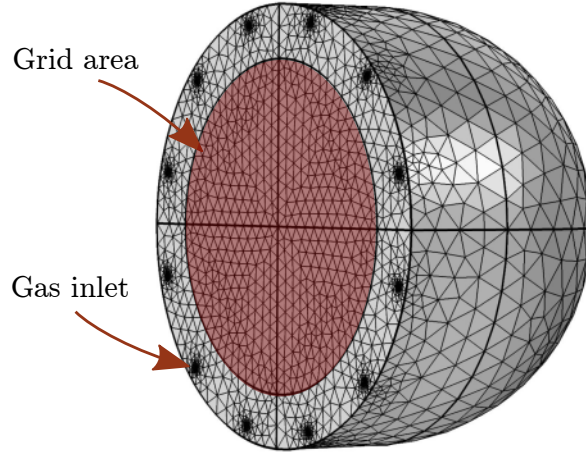
Figure 3.8: 3D geometry and mesh used in the COMSOL molecular flow module for calculating neutral gas pressure and density.

A mesh sensitivity analysis was performed by varying the mesh size from coarse to extra fine and recording the neutral gas pressure p and density n_0 values, as illustrated in Table 3.2. Note that the fancy mesh represents a mesh where the gas inlet and the grid area are meshed with an extra fine mesh, while the remaining boundaries are meshed with a fine mesh. Table 3.2 shows that the neutral gas pressure changes from about 0.82 mTorr to 1.2 mTorr as the mesh size is varied from coarse to extra fine. However, the neutral gas pressure and density values converge to a stable solution starting from the fancy mesh. Since the difference in parameter values between the fancy and extra fine meshes are negligible and the fancy mesh results in much faster solution times (≈ 1 min), it was decided to choose the fancy mesh for all further simulations.

Parameter	Mesh size					
	Coarse	Normal	Fine	Finer	Fancy	Extra fine
p (mTorr)	0.81972	0.80223	0.793	1.0945	1.1962	1.1915
n_0 ($\times 10^{19}$ 1/m^3)	2.282	2.233	2.21	3.05	3.329	3.316
t (min)	0.16	0.17	0.22	0.55	1	23

Table 3.2: Free molecular flow model mesh sensitivity analysis. The analysis was performed with $\dot{m}_{out} = 0.2574$ sccm, $T_w = 350$ K, $\eta_c = 0.167$, $f_{os} = 0.63$.

Note that due to low ionisation levels present in RF ion thrusters ($\approx 0.1-3\%$) the model excludes electrons and ions from affecting the neutral gas pressure inside the discharge chamber. Furthermore, to save computational time, the screen grid apertures are not modelled directly, but, rather, they are represented as a surface with a mathematical open area fraction f_{os}. Therefore, using the Clausing factor, a boundary condition is applied on the screen grid aperture area that reflects the flux K of the total incoming flux J back to the discharge chamber

$$K = (1 - \eta_c f_{os})J. \tag{3.5}$$

In order to calculate the neutral gas pressure inside the discharge chamber, the model also needs to know the fraction of neutral atoms that becomes ionised and forms an electrically-charged beam. To achieve this, the neutral gas mass flow rate $\dot{m}_{out}$ that leaks through the grids and is not part of the ion beam is estimated by subtracting the equivalent mass flow rate required to obtain a specific ion beam current I_b from the input mass flow rate $\dot{m}_{in}$ (Goebel and Katz, 2008)

$$\dot{m}_{out} = \dot{m}_{in} - I_b g_0, \tag{3.6}$$

where g_0 is the conversion factor from amperes to sccm equal to 13.938 sccm/A. The conversation factor g_0 is calculated assuming that each neutral gas atom is a potential ion (Goebel and Katz, 2008). Then, the neutral gas flow rate $\dot{m}_{out}$ (in sccm units) is set as a boundary condition on the discharge chamber gas inlet surface area. The neutral gas molecules are assumed to be diffusively emitted from the gas inlet area with a Maxwell-Boltzmann velocity distribution that depends on the surface temperature.
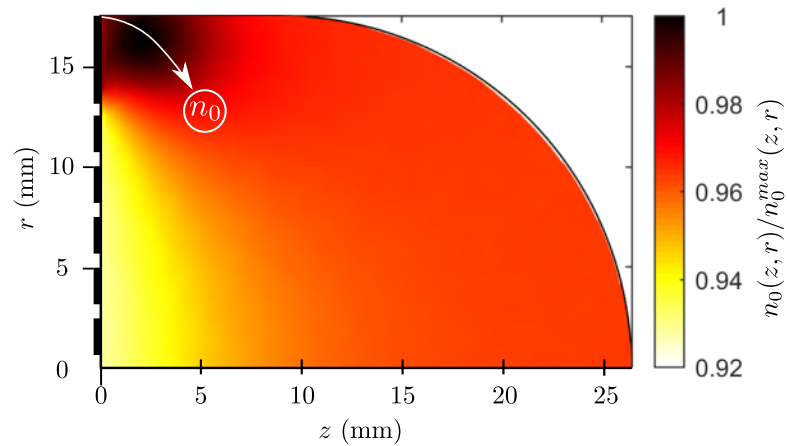
Figure 3.9: Neutral gas density distribution normalised to the maximum value shown on a 2D slice taken through the RIT 3.5 discharge chamber volume at 2 mN thrust point.

From Equation 3.6, it can be seen that the ion extraction model described in the previous section is needed in order to have the extracted beam current always consistent with

the plasma conditions. This is because $I_b = T_{eff}I_B$, and T_{eff} depends on the plasma meniscus shape which in turn depends on the plasma properties. Figure 3.9 shows an example of the neutral gas density distribution in the RIT 3.5 discharge chamber. The upper left corner of the discharge chamber represents the neutral gas entry location, whereas the left edge marks the location of the ion optics grids. The plot indicates that the neutral gas density distribution is quite uniform with only around 8% in variation. Finally, note that since plasma is represented using a 0D model, bulk, volume-averaged neutral gas pressure p and density n_0 values as obtained by COMSOL are used for all subsequent calculations.

3.5   Plasma model

3.5.1   Electron transport

Lister et al. (1996) have shown that it is important to account for oscillating fields and the shape of the electron energy distribution function (EEDF) while calculating high frequency (HF) plasma properties. This is especially true in determining the electron-neutral collision frequency ν_{en} which, under HF conditions, becomes the effective electron-neutral collision frequency ν_{eff}. To determine the EEDF, the electron Boltzmann equation (BE) has to be solved. Using spherical coordinates in the velocity space, the BE for electrons is (Hagelaar and Pitchford, 2005)

$$\frac{\partial f}{\partial t} + v\cos\theta\frac{\partial f}{\partial z} - \frac{e}{m_e}E\left(\cos\theta\frac{\partial f}{\partial v} + \frac{\sin^2\theta}{v}\frac{\partial f}{\partial\cos\theta}\right) = C[f], \qquad (3.7)$$

where f is the electron function that depends on the velocity v, m_e is the electron mass, θ is the angle between the velocity and the field direction and z is the position along this direction, C represents the rate of change in f due to collisions. The f dependence on θ can be simplified by expanding f in terms of Legendre polynomials (spherical harmonic expansion) of $\cos\theta$ (Hagelaar and Pitchford, 2005). Furthermore, only the first two-terms of the spherical harmonic expansion can be used without a substantial loss in accuracy, which is known as the two-term approximation.

For oscillating fields, the two-term approximation for f can be represented as (Hagelaar and Pitchford, 2005)

$$f(v, \cos\theta, z, t) = f_0(v, z, t) + f_1(v, z, t)\cos\theta e^{j\omega t}, \qquad (3.8)$$

where f_0 is the isotropic part of f and f_1 is an anisotropic perturbation. The energy-dependence of f can be separated from its dependence on time and space using the

following relationship (Hagelaar and Pitchford, 2005)

$$f_{0,1}(\epsilon, z, t) = \frac{1}{2\pi\gamma^3} F_{0,1}(\epsilon) n(z, t), \qquad (3.9)$$

where $\gamma = \sqrt{2e/m_e}$, ϵ is the electron energy, n is the electron density and $F_{0,1}$ is the EEDF which is normalized to make the following relationship hold

$$\int_0^\infty \sqrt{\epsilon} F_0 \, \mathrm{d}\epsilon = 1. \qquad (3.10)$$

For more information on the two-term approximation Boltzmann equation the reader should look into the work by Hagelaar and Pitchford (2005).

In this thesis, a COMSOL Boltzmann module is employed to solve the two-term approximation Boltzmann equation for oscillating fields. As the main inputs, the model takes the ionisation degree $\beta = n_i/(n_i + n_0)$, the reduced angular frequency ω/n_0 and the neutral gas temperature T_g, which is assumed to be equal to the discharge chamber wall temperature T_w. Additionally, the collision cross-sections σ_k for each collision process k are provided as well. In the case of xenon gas, these were taken from the SIGLO database (2015) and are presented in Appendix B. Finally, note that in the following plots, for illustrative purposes, the EEDFs are divided by $\sqrt{\epsilon}$.
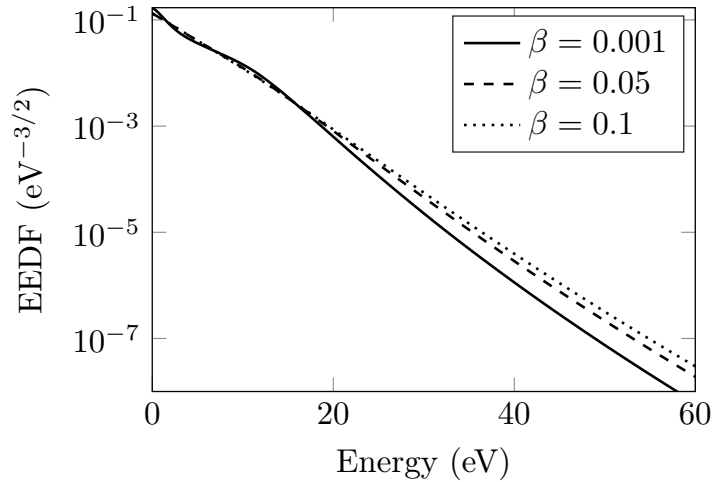
Figure 3.10: Simulated EEDF for $\beta = 0.001$, $\beta = 0.05$ and $\beta = 0.1$ ionisation degrees for the mean electron energy of 6 eV and the reduced angular frequency ω/n_0 of 2×10^{-12} m^3/s.

Figure 3.10 shows simulated EEDFs for ionisation fractions β of 0.001, 0.05 and 0.1 at the mean electron energy of 6 eV. The first two ionisation fractions, as well as the mean electron energy, were chosen to represent the range in which the RIT 3.5 and other similar ion thrusters operate (Closs, 2001; Takao et al., 2011). The last ionisation fraction was added to show that the difference in terms of the EEDFs between $\beta = 0.05$ and $\beta = 0.1$ is insignificant. As illustrated in Figure 3.10, as the ionisation degree β increases, the curve

starts to resemble a straight line, which is an indication that the EEDF approaches a Maxwellian distribution. This is because as the ionisation degree increases, the electron-electron collisions tend to drive the distribution towards the Maxwellian (Hagelaar and Pitchford, 2005). Nevertheless, considering that the RIT 3.5 operates at β of around 0.02, the EEDF encountered should be close to the Maxwellian at low energies, with a considerable deviation in the high energy tail of the distribution, as can be observed from Figure 3.10.
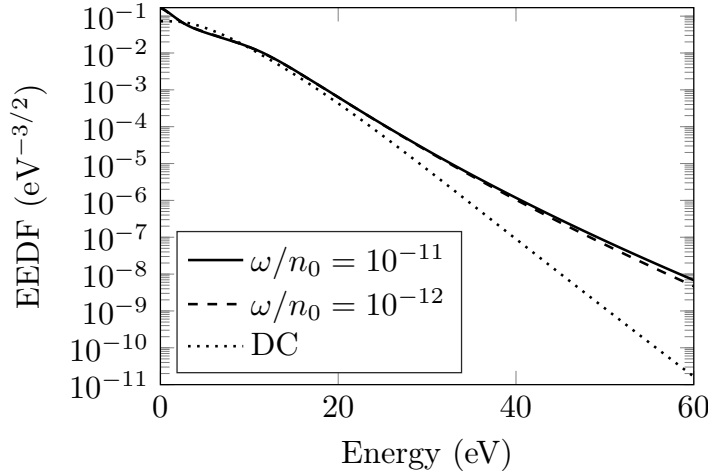
Figure 3.11: Simulated EEDF for $\omega/n_0 = 0$ (DC), $\omega/n_0 = 10^{-12}$ m^3/s and $\omega/n_0 = 10^{-11}$ m^3/s reduced angular frequencies for the mean electron energy of 6 eV and the ionisation degree $\beta = 0.001$.

Similarly, Figure 3.11 was included to depict the simulation results that show how EEDFs change as a function of the reduced angular frequencies ω/n_0 typical of the RIT 3.5 and other RF ion thrusters (Closs, 2001; Takao et al., 2011). Additionally, to show that the AC treatment of the EEDF should be used, a DC case was included as well. Figure 3.11 shows that the EEDF for the DC case ($\omega/n_0 = 0$) is substantially different from the AC cases, especially at higher electron energies. Therefore, as mentioned above, the electron-neutral collision frequency ν_{en} calculated using the AC rather than DC fields must be used, resulting in the so-called effective electron-neutral collision frequency ν_{eff}. This comes from the fact that the heating mechanisms in DC and AC fields are different. Namely, in the DC fields, the collisions impede the heating process, while in the AC fields they enhance it (Hagelaar and Pitchford, 2005). That is why in Figure 3.11 there has been observed a higher number of more energetic electrons in the tail of the distribution in the AC cases compared to the DC case.

The effective electron-neutral collision frequency ν_{eff} can be determined from the HF electron mobility μ which is calculated using the EEDF F_0 and the effective total momentum transfer collision cross-section σ_m for HF fields, as defined by Hagelaar and Pitchford (2005)

$$\mu = -\frac{\gamma}{3n_0} \int_0^\infty \frac{\epsilon}{\sigma_m} \frac{\partial F_0}{\partial \epsilon} \, \mathrm{d}\epsilon. \tag{3.11}$$

However, ν_{eff} can also be expressed using a well-known mobility equation (Shkarofsky et al., 1996)

$$\mu = \frac{e/m_e}{\nu_{eff} + j\omega_{eff}}, \tag{3.12}$$

where ω_{eff} is the effective angular frequency. The difference between the effective angular frequency ω_{eff} and the applied frequency ω depends largely on the neutral gas pressure and electron temperature (Lister et al., 1996). However, considering that the RIT 3.5 and other RF ion thrusters operate at pressures in the range of a few mTorr (Loeb et al., 2004), it can be shown that $\omega_{eff} \approx \omega$ (Lister et al., 1996).

The rate coefficient K_k for each collision process k is (Hagelaar and Pitchford, 2005)

$$K_k = \gamma \int_0^\infty \epsilon \sigma_k F_0 \, \mathrm{d}\epsilon. \tag{3.13}$$

Using the previously calculated rate coefficients, the reaction rate α_k for the collision process k between two species with densities n_1 and n_2 is (Hagelaar and Pitchford, 2005)

$$\alpha_k = K_k n_1 n_2. \tag{3.14}$$

Employing a global energy balance approach, the model obtains the power lost in ionising the gas (Chabert and Braithwaite, 2011)

$$P_i = \alpha_i V_d U_i e, \tag{3.15}$$

where V_d is the discharge chamber (or plasma) volume, U_i is the ionisation potential and α_i is the ionisation reaction rate. Also, using the Boltzmann module in COMSOL, the fractional power losses f_k for each collision process k are obtained. As given in Appendix B, the model accounts for the following electron-neutral collision processes while considering xenon as the propellant (COMSOL Group, 2016): elastic scattering, single charge ionisation with energy 12.12 eV and excitation with 8.31 eV, 8.44 eV, 9.69 eV, 10 eV, 11 eV and 11.7 eV energy levels. Finally, the total collisional power P_{coll} expanded in creating a plasma is $P_{coll} = P_i/f_i$, where f_i is the fraction of total power expanded to ionisation. Similarly, the power losses for other collision processes are calculated as $P_k = f_k P_{coll}$. Therefore, the power lost to each collision process can be determined.

3.5.2 Ion density distribution

During preliminary simulations, it was observed that in order to correctly account for the plasma electromagnetic heating, an accurate representation of the ion density distribution is extremely important. From the RIT 10 ion density distribution measurements and from literature it was discovered that the ion density varies as a function of the

radial distance r from the discharge vessel centre (Schäfer, 1971; Chabert and Braithwaite, 2011). In the model, this variation in the ion density is introduced through the h parameter

$$h(z, r) = \frac{n_i(z, r)}{n_i(z, 0)}, \tag{3.16}$$

where $n_i(z, 0)$ is the ion density at the centre of the discharge and $n_i(z, r)$ is the ion density at the location r from the centre for a given z value. For simplicity, the z variable is omitted. As a result, the following relationships are used: $n_i(z, 0) = n_i$, $n_i(z, r) = n_i(r)$ and $h(z, r) = h(r)$. Furthermore, it is important to define the h_r parameter. In the model, h_r is represented as the ion density ratio $h(r)$ at $r = r_w - s$, where r_w is the discharge chamber radius and s is the plasma sheath thickness, as defined in Figure 3.1. Lieberman and Lichtenberg (2005) derived the following expression for estimating the ion density profile as a function of the radial distance for low pressure discharges

$$\left(\frac{n_i(r)}{n_i}\right)^2 + \left(\frac{r}{r_w}\right)^2 = 1. \tag{3.17}$$

Note that Equation 3.17 represents a circle with $n_i(r) = n_i$ at the centre of the discharge where $r = 0$ and $n_i(r) = 0$ at the radial edge boundary of the discharge where $r = r_w$. However, researchers have discovered that the ion density profile also varies depending on the pressure, size of the system and magnetic field (Lieberman and Lichtenberg, 2005; Chabert and Braithwaite, 2011). Therefore, a more general solution was derived to estimate the h_r parameter assuming an infinite length cylindrical geometry (Lieberman and Lichtenberg, 2005)

$$h_r = \frac{0.8}{\left[4 + \frac{r_w}{\lambda_i} + (0.8 r_w u_B / (\chi_{01} J_1(\chi_{01}) T_e / T_i D_a))^2\right]^{1/2}}. \tag{3.18}$$

Similarly, the h_l parameter, which accounts for the ion density variation in the axial z direction, was estimated assuming infinite radii plates separated by the distance l

$$h_l = \frac{0.86}{\left[3 + \frac{l}{2\lambda_i} + (0.86 l u_B / (\pi T_e / T_i D_a))^2\right]^{1/2}}, \tag{3.19}$$

where D_a is the ion diffusion coefficient, χ_{01} is the first zero of the Bessel function of the first kind, J_1 is the Bessel function of the first kind. The λ_i variable is the ion mean free path equal to $\lambda_i = 1/(n_0 \sigma_s)$, with σ_s being the total ion scattering cross-section. Therefore, both h_r and h_l parameters strongly depend on the neutral gas pressure p through the neutral gas density n_0.

To simplify the problem, the model still uses the circular ion density profile as defined in Equation 3.17, but the h_r factor from Equation 3.18 is introduced as well. Additionally, it can be shown that for the plasma found in RF ion thrusters, the sheath thickness s is

generally a few Debye lengths in size and the Debye length is less than 0.1 mm (Lieberman and Lichtenberg, 2005; Chabert and Braithwaite, 2011). Therefore, the model neglects the sheath size altogether by setting $s \approx 0$, which results in $h_r = n_i(r_w)/n_i$. The parameter $h(r)$ then can be expressed using an elliptical profile

$$h(r) = \sqrt{1 - \left(\sqrt{1 - h_r^2} \frac{r}{r_w} \right)^2}. \tag{3.20}$$

Figure 3.12 compares the ion density variation as measured in the RIT 10 thruster (Schäfer, 1971) and that predicted by the model using Equation 3.20. As can be observed, the deviations between the experimental and model values are only a few percent in magnitude. In plotting the graph, it was assumed that the ion density distribution is independent of the z location since the RIT 10 discharge chamber is cylindrical. Additionally, the RIT 10 ion density profile was taken at around 1 mTorr, which is roughly the same pressure at which the RIT 3.5 operates. Therefore, the theory says that the ion density profiles should be very similar in both the RIT 3.5 and RIT 10 thrusters even though the discharge chamber diameters are different. For instance, the h_r value from the RIT 10 experimental data and the h_r value from the RIT 3.5 model are approximately the same and equal to 0.42.
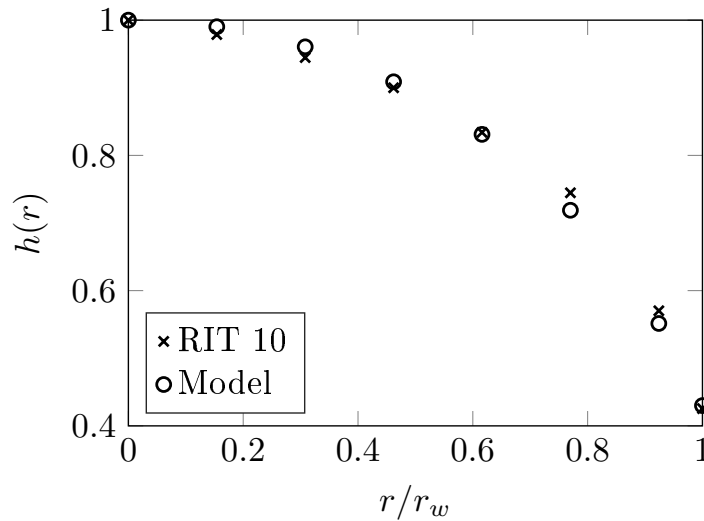
Figure 3.12: Ion density variation as predicted by the model compared to the RIT 10 experimental data at 1 mTorr.

Goebel (2008) presented a theory detailing how the magnetic field results in an ion confinement and thus lower losses to the boundaries. In developing the model, it was decided to investigate this effect through the ion diffusion phenomenon since the presheath ion density values h_r and h_l directly depend on the ion diffusion coefficient D_a, as shown in Equation 3.18 and Equation 3.19. However, the ion diffusion coefficient D_a depends on the magnetic field magnitude. A reduction of h_r and h_l parameters would directly lead to lower boundary losses and therefore better plasma confinement.

Assuming the ambipolar diffusion solely in the radial r direction across a uniform time-averaged magnetic field B, the ambipolar diffusion coefficient D_a becomes (Chabert and Braithwaite, 2011)

$$D_a{}^* \approx \frac{eT_e}{M_i\nu_i}(1+\tau_B)^{-1}. \tag{3.21}$$

In addition, Equation 3.21 was derived assuming that electrons were magnetised but ions were not. The τ_B parameter can be considered as a confinement factor since it strongly depends on the magnetic field B through

$$\tau_B = \frac{\omega_{ci}\omega_{ce}}{\nu_i\nu_e}, \tag{3.22}$$

where ν_i and ν_e are the ion and electron collision frequencies with neutrals, respectively. The ω_{ci} and ω_{ce} variables are ion and electron cyclotron frequencies equal to $\omega_{ci} = eB/M_i$ and $\omega_{ce} = eB/m_e$, respectively. The limiting factor of such a theory is that it assumes that plasma is infinite in the axial or z direction. This means that ions are only allowed to diffuse in the radial direction, which is not the case. To capture this phenomenon, a 2D approach as described by Lieberman and Lichtenberg (2005) is needed. Finally, the model also does not include the neutral depletion, as discussed by Liard et al. (2007).
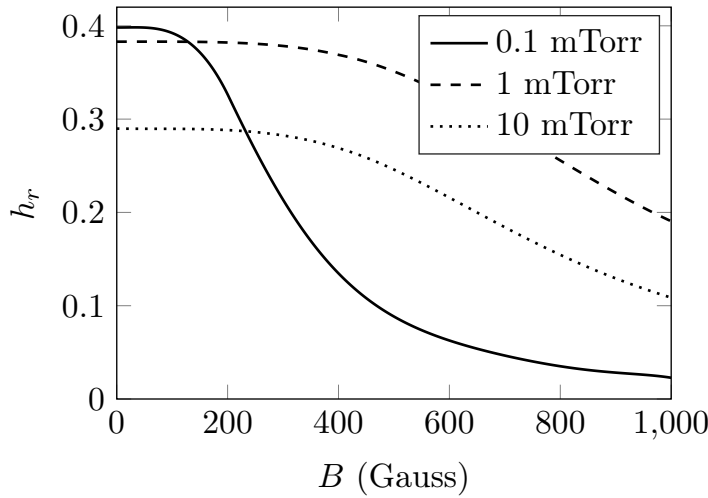
Figure 3.13: The h_r parameter variation with the magnetic field for 0.1 mTorr, 1 mTorr and 10 mTorr neutral gas pressures for the RIT 3.5 thruster geometry at a location $z = 5$ mm.

The effect of the magnetic field strength on h_r is shown in Figure 3.13. First, a case is considered when there is no magnetic field, that is, $B = 0$ Gauss. In the range of the RIT 3.5 working pressures from 0.1 to 1 mTorr, h_r is about constant and equal to 0.4. However, if the pressure is increased from 1 mTorr to 10 mTorr, h_r sharply decreases to around 0.28. If 1 mTorr is taken as the approximate pressure value at which the RIT 3.5 is likely to operate, it can be observed that the magnetic field starts to become significant only from about 400 Gauss. For the 0.1 mTorr case the magnetic field effect is more pronounced; h_r begins to decrease at about 100 Gauss. However, the maximum

magnetic field expected in the RIT 3.5 plasma is only about 25 Gauss. Furthermore, the magnetic field distribution inside the plasma is not uniform, as can be observed in Figure 3.14. This results in the majority of the plasma volume having a field strength of only around 10 Gauss. Therefore, the confinement factor τ_B is negligible at such plasma conditions.
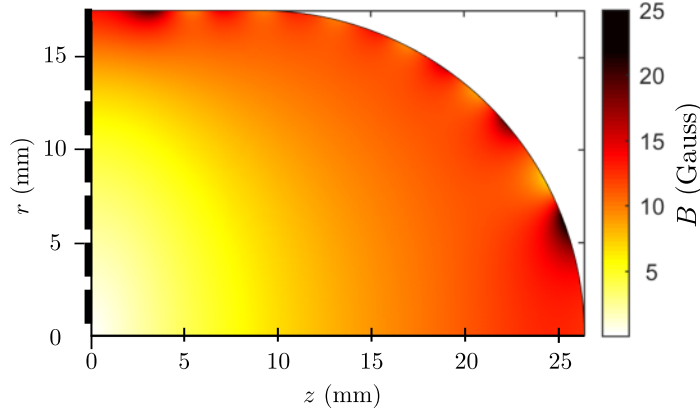
Figure 3.14: Magnetic field distribution in the plasma shown on a 2D slice taken through the RIT 3.5 discharge chamber volume at 2 mN thrust point.

3.5.3 Plasma conductivity

The plasma acts as a conductor and can be represented using familiar properties generally used to define conductors. The first of these is the electrical conductivity. At applied frequencies in the range of tens of MHz the displacement current can be neglected (Chabert and Braithwaite, 2011), and the plasma conductivity can be represented as (Shkarofsky et al., 1996)

$$\sigma_p(z,r) = \frac{n_i(z,r)e^2}{m_e(\nu_{tot} + j\omega_{eff})}, \tag{3.23}$$

where ν_{tot} is the total collision frequency composed of different collision frequencies associated with various heating mechanisms. First, the electron-ion collision heating mechanism can be expressed by (Huba, 2016)

$$\nu_{ei} = 2.91 \times 10^{-12} \frac{n_i \ln \Lambda}{T_e^{3/2}}, \tag{3.24}$$

where $\ln \Lambda$ is the Coulomb logarithm (Huba, 2016)

$$\ln \Lambda = 23 - 0.5 \ln \frac{10^{-6} n_i}{T_e^3} \qquad \text{for} \qquad T_i m_e/M_i < T_e < 10 \text{ eV}. \tag{3.25}$$

As was discussed in Chapter 2, some authors have observed that at low pressures the collisional heating is not the dominant process, but rather the stochastic heating dominates (Godyak et al., 1998; Turner, 1993; Aliev et al., 1997; Weibel, 1967; Schulze et al.,

2008). This happens because if an electron traverses a localized skin layer faster than the RF period, then it gains energy from the field (Lieberman and Lichtenberg, 2005; Chabert and Braithwaite, 2011). In such a case, the spatial distribution of the electric field and current is not the usual exponential decay within the skin depth (Lieberman and Lichtenberg, 2005; Chabert and Braithwaite, 2011). However, the error in using the exponential decay function for the electric field has been shown to be small (Lieberman and Lichtenberg, 2005; Vahedi et al., 1995). Therefore, in the model, it was decided to express the electric field skin depth δ_E as (Lieberman and Lichtenberg, 2005)

$$\delta_E^{-1} = \frac{\omega}{c} \text{Im} \left[\epsilon_p^{1/2} \right],$$
(3.26)

where ϵ_p is the effective plasma permittivity

$$\epsilon_p = 1 - \frac{\omega_{pe}^2}{\omega(\omega - j\nu_{tot})},$$
(3.27)

with the plasma frequency given by $\omega_{pe} = \sqrt{n_i e^2 / m_e \epsilon_0}$, where c is the speed of light and ϵ_0 is the permittivity of free space. Lieberman and Lichtenberg (2005) have introduced the equivalent stochastic frequency ν_{stoc} to represent the stochastic heating mechanism

$$\nu_{stoc} = \frac{\bar{v}_e}{4\delta_E} \left(\frac{1}{\Psi(\chi) + \chi/4} \right),$$
(3.28)

where

$$\Psi(\chi) = \frac{1}{\pi} \left[e^\chi (1 + \chi) \int_\chi^\infty \frac{e^{-\xi}}{\xi} \mathrm{d}\xi - 1 \right],$$
(3.29)

and

$$\chi = \frac{4\omega^2 \delta_E^2}{\pi \bar{v}_e^2},$$
(3.30)

where $\bar{v}_e$ is the thermal electron velocity given as $\bar{v}_e = \sqrt{(8eT_e)/(\pi m_e)}$. Finally, the total collision frequency ν_{tot} can be determined as the sum of the effective collision frequency ν_{eff}, the electron-ion collision frequency ν_{ei} and the stochastic collision frequency ν_{stoc}

$$\nu_{tot} = \nu_{eff} + \nu_{ei} + \nu_{stoc}.$$
(3.31)

The above equations are solved by first providing a guess value for the plasma skin depth δ_E. Then, Equation 3.26 to Equation 3.31 are solved to determine the plasma permittivity ϵ_p. The plasma permittivity ϵ_p is then substituted back into Equation 3.26 to obtain a new skin depth value. After that, the guessed and the newly obtained skin depth values are compared to each other. The process is iterated until both of these values match within an error of a few percent.

3.5.4   Power and particle balance

From Equation 3.14, it can be shown that the ion production rate $\alpha_i(T_e)$ is a function of the electron temperature T_e. Therefore, the electron temperature can be found by performing a power balance within the plasma. In particular, the power expended to produce the plasma (left side of Equation 3.32) must be equal to the power lost from the plasma to the discharge chamber walls (right side of Equation 3.32). Furthermore, it is assumed that ions flow with the flux $\Gamma_i = h n_i u_B$ to the discharge chamber wall A_c and screen A_s areas where, if not extracted, they recombine to produce a neutral atom. After plugging in the variables and noting that the ion density n_i cancels out, the final equation becomes (Chabert and Braithwaite, 2011)

$$n_0 \alpha_i(T_e) V_d = u_B (h_r A_c + h_l A_s). \tag{3.32}$$

The plasma sheath potential is obtained by assuming that the electron and ion fluxes to the boundaries are ambipolar (or equal). Therefore, the plasma sheath potential is given by a well-known floating potential equation (Lieberman and Lichtenberg, 2005; Goebel and Katz, 2008)

$$\phi_s = T_e \ln \sqrt{M_i/(2 m_e \pi)}. \tag{3.33}$$

In order to account for the plasma's effect on the thruster's heating, the particle currents within the discharge chamber are determined. Using the conservation of particles and energy (Chabert and Braithwaite, 2011; Lieberman and Lichtenberg, 2005), and the ambipolar flux assumption, the total ion (or electron) current flowing towards the discharge chamber wall area A_c is

$$I_{ci} = h_r n_i u_B A_c e. \tag{3.34}$$

As discussed before, the beam current I_b is

$$I_b = T_{eff} h_l n_i u_B A_s e \Gamma_b, \tag{3.35}$$

where Γ_b is the flatness of the beam used to define the radial variation in the h_l parameter. If the RIT 3.5 ion optics system is taken as an example, it can be shown that the beam flatness Γ_b is around 85%. This is because the grid apertures are made only in a high-density plasma region to give a flat beam. The ion current to the screen grid area A_s is equal to the remaining current that is not extracted through the grids to form the ion beam

$$I_{si} = (1 - T_{eff}) h_l n_i u_B A_s e \Gamma_b. \tag{3.36}$$

Assuming ambipolar losses again, the electron current to the screen grid is $I_{se} = I_b + I_{si}$.
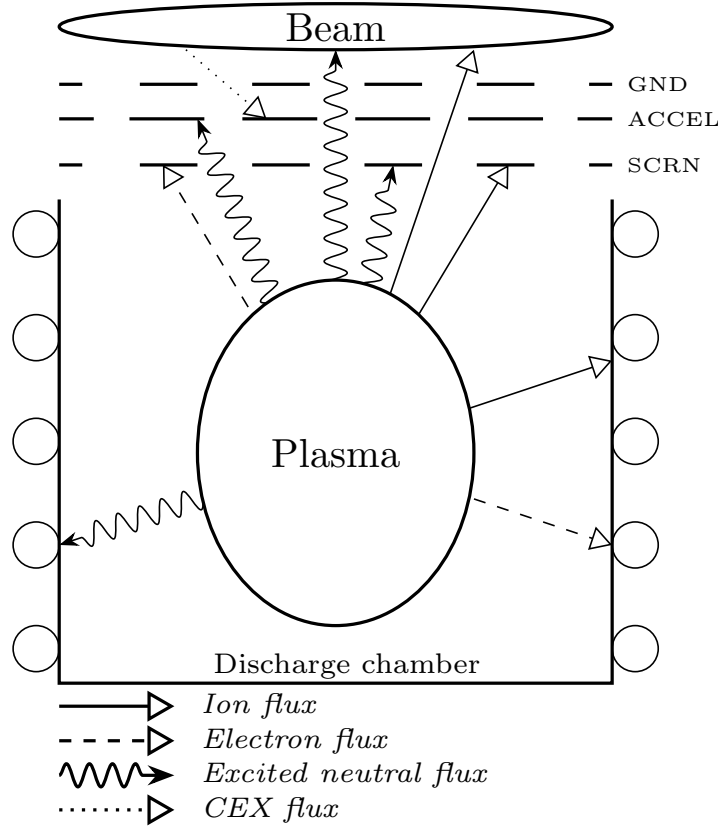
Figure 3.15: Ion, electron, excited neutral and CEX fluxes as observed inside the radio frequency gridded ion thruster.

As defined previously, there are power losses associated with the production of plasma itself. One of the losses is the collisional power loss P_{coll} composed of the ionisation P_i, excitation P_x and elastic scattering P_{scat} losses, as have been introduced earlier. However, a substantial power loss is additionally incurred due to various particle fluxes, as indicated in Figure 3.15. One particle loss mechanism occurs when, upon reaching the wall, these particles are accelerated by the electrostatic fields in the plasma and then deposit their energy to the wall, causing it to heat up. Additionally, the heat can also be transferred by the excited neutral particles that radiate energy to the thruster's boundaries or out of the discharge chamber into the beam. In the model, the heating to a particular boundary from the excited neutral flux is determined based on the boundary's surface area size relative the total boundary surface area size A_w (Noord, 2007).

The discharge chamber wall heating by ions and electrons is

$$P_c = I_{ci}(\phi_s + \frac{5}{2}T_e + U_i), \tag{3.37}$$

whereas the heating from excited neutrals is

$$P_{cx} = \frac{A_c}{A_w}P_x. \tag{3.38}$$

The screen grid heating due to electrons is

$$P_{se} = I_{se}(w_s + 2T_e), \tag{3.39}$$

where w_s is the screen grid work function. The screen grid heating due to ions is

$$P_{si} = I_{si}(\phi_s + \frac{1}{2}T_e + U_i - w_s). \tag{3.40}$$

Finally, the screen grid heating due to excited neutrals is

$$P_{sx} = \frac{(1 - f_{os})A_s}{A_w}P_x, \tag{3.41}$$

where f_{os} and f_{oa} represent the screen and accel grid open area fractions, respectively. The heating of the accel grid comes mainly from the excited neutral radiation given by

$$P_{ax} = \frac{(f_{os} - f_{oa})A_s}{A_w}P_x, \tag{3.42}$$

and charge exchange (CEX) ions

$$P_{CEX} = I_{cex}(U_{acc} + U_i - w_a), \tag{3.43}$$

where I_{cex} is the CEX particle current, usually less than 2% of the beam current, and w_a is the accel grid work function. The power processed by the RFG power supply also includes the excited neutral radiation power that escapes through the grid system to the beam

$$P_{xout} = \frac{f_{oa}A_s}{A_w}P_x, \tag{3.44}$$

and the power that escapes with the ions in the beam

$$P_b = I_b(\phi_s + \frac{1}{2}T_e + U_i). \tag{3.45}$$

The total discharge power P_d that is needed to generate a plasma for a particular beam current at a specified mass flow rate is the sum of all the aforementioned losses, i.e.

$$P_d = P_{scat} + P_c + P_{cx} + P_{se} + P_{si} + P_{sx} + P_{ax} + P_{xout} + P_b - I_b w_s. \tag{3.46}$$

3.6   Electromagnetic model

An electromagnetic model has been developed in order to determine the electromagnetic field distributions inside the coil, the surrounding thruster's structure and the plasma itself. In particular, the model allows determining the power transferred from the coil to the plasma and thus the power transfer efficiency. Additionally, the model is used to calculate the voltage/current and impedance values of the coil and the plasma. Finally,

the electromagnetic model provides the eddy current heating magnitudes inside various thruster's components. These heating values are later used as inputs for the thermal model to find the temperature distribution.

3.6.1   Geometry and boundary conditions

The electromagnetic fields were simulated in COMSOL using the full 3D RIT 3.5 thruster geometry. The geometry and mesh employed in the simulations, with the thruster's cover hidden for clarity, are shown in Figure 3.16. As can be seen from Figure 3.16, all the major components of the thruster such as the coil, discharge chamber, case and grids were represented in the model. Complicated components such as some parts of the gas inlet, bolts or other tiny features were simplified or removed. Also, note that only the screen grid geometry was used to represent the ion optics. This is because the electromagnetic field is screened by the screen grid. Therefore, the accel and decel grids play no effect in the electromagnetic simulations and thus can be removed.
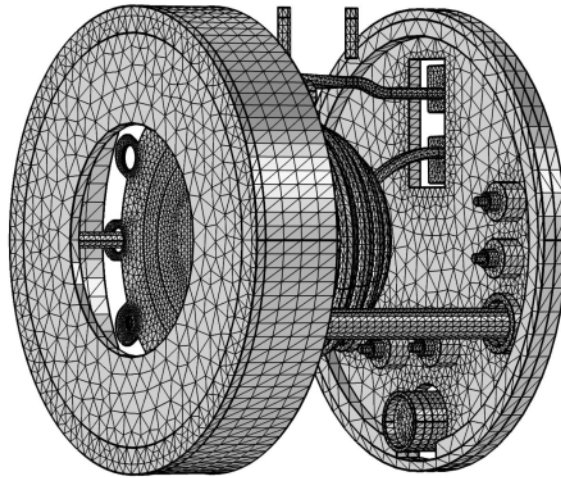
Figure 3.16: 3D RIT 3.5 thruster geometry and mesh used in the electromagnetic simulations.

In creating the mesh, the aim was to have the fewest number of elements without lowering the model's accuracy. This was necessary to reduce the computational time to a few minutes. The created mesh consists of 455580 elements with an average quality of 0.61. Normally, the quality of an element represents how "flat" it is. Therefore, a quality factor of 0 would mean that all corners of the element are in one plane or that the element is completely flat. A mesh sensitivity analysis was performed to gauge the mesh size effect on the solution parameters (defined later). In the analysis, three different mesh sizes were investigated: coarse, normal and fine. The results from the mesh sensitivity analysis at a particular operational condition are summarised in Table 3.3. As can be seen from Table 3.3, the mesh size has a negligible effect on the solution parameters, the largest difference in the parameter values between the mesh cases is only a few percent.

However, the solution time increases from 1.68 min to 3.56 min with the mesh size. Taking into account the solution accuracy and time it takes to obtain the solution, the normal mesh size was chosen as the most optimum.

	Mesh size		
Parameter	**Coarse**	**Normal**	**Fine**
P_{in} (W)	24.967	24.985	24.881
W_p (W)	18.582	18.7	18.687
W_c (W)	4.9515	4.8439	4.7183
W_{scrn} (W)	0.68016	0.68288	0.69721
W_{str} (W)	0.75334	0.75822	0.77849
k_f	0.3417	0.34198	0.34215
B_{avg} (G)	12.88	12.892	12.872
L_{thr} (μH)	0.79218	0.79356	0.79417
t (min)	1.68	2.63	3.56

Table 3.3: Electromagnetic model mesh sensitivity analysis. The analysis was performed with $\sigma_r = 170$ S/m, $\sigma_i = -65$ S/m and $I_c = 10$ A.

It is critical to accurately mesh the coil because it determines the electromagnetic field distribution and magnitude inside the thruster. The RIT 3.5 thruster's coil mesh is shown in Figure 3.17. The 3D mesh was designed by sweeping a triangular 2D mesh face throughout the length of the coil. This helped reduce the number of computational domains and thus the computation cost. Note that the model solves Maxwell's equations in all components of the thruster except in the coil itself. The coil is excluded because the skin depth in the coil at the operational frequency of around 3 MHz is less than 1 mm. As a result, it is very computationally expensive to resolve the electromagnetic field gradients in such a narrow space. Therefore, it was assumed that all current is concentrated on the very surface of the coil (the higher the frequency, the more accurate this assumption).
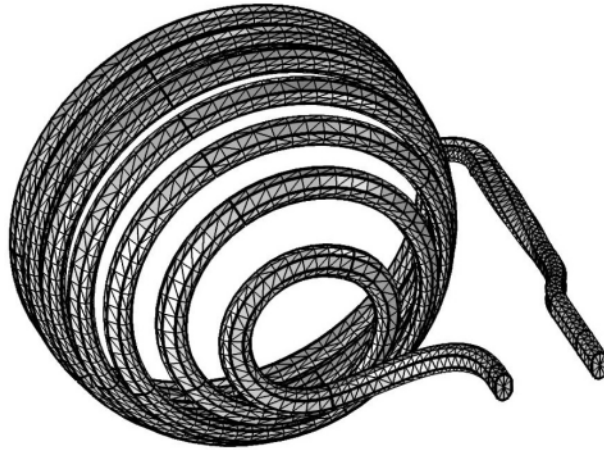
Figure 3.17: RIT 3.5 coil mesh made of triangular and structured quadrilateral boundary elements.

The assumption that all current flowing through the coil is concentrated on the coil's surface was implemented using the impedance boundary condition in COMSOL. The impedance boundary condition forces all losses to be estimated based on the surface properties of the magnetic field. This is similar to evaluating the Poynting vector at the coil's surface, as defined by Poynting (1884). To excite the coil, the electromagnetic COMSOL model uses the port boundary condition, as shown in Figure 3.18. The model accepts either the coil current I or voltage V as inputs. COMSOL then determines the complex impedance Z of the port which accounts for the total impedance of the thruster. The complex impedance includes the induced eddy currents in the thruster's components, capacitive coupling, plasma's effect and screening.
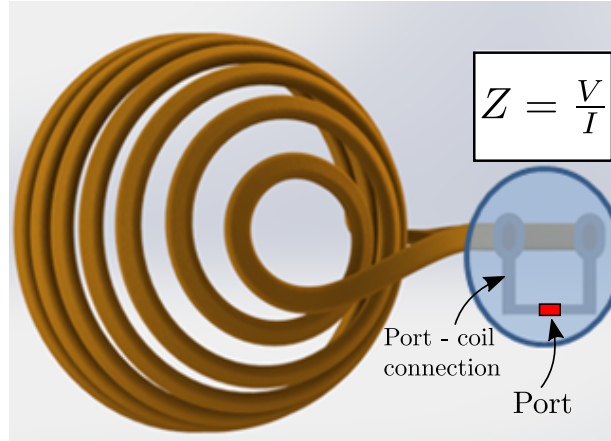
Figure 3.18: Implementation of the port boundary condition which is used to excite the coil in the electromagnetic model.

Finally, the magnetic insulation boundary condition was applied on the port-coil connection's surface, as shown in Figure 3.18. This was done to avoid any losses in the port itself and in the port-coil connection because these parts are fictitious and should not generate any losses. In COMSOL, the magnetic insulation condition was expressed as

$$n' \times A = 0, \tag{3.47}$$

where n' is the unit vector normal to the coil's surface and A is the magnetic vector potential. The application of the magnetic insulation boundary condition also helped improve the stability and accuracy of the model.

3.6.2 Main equations and principles

The electromagnetic model treats the plasma as a pure solid with the complex electrical conductivity obtained from Equation 3.23, which was expressed as

$$\sigma_p(z, r) = \sigma_r(z, r) - j\sigma_i(z, r). \tag{3.48}$$

Representing the plasma conductivity in such a way introduces a phase lag between the electric field and current through the imaginary part σ_i. This was done to account for the finite electron inertia, as was mentioned when discussing the transformer model in Chapter 2.

Note that the plasma electrical conductivity depends directly on the ion density. Therefore, it is critical to account for the spatial variation of the ion density to accurately determine the power transferred from the coil to the plasma. As a result, in the proposed model, the plasma conductivity was defined as $\sigma_p(z,r) \propto h(z,r)n_i(z,0)$, which states that the plasma conductivity is directly proportional to the ion density distribution through the $h(z,r)$ parameter, as discussed earlier. As before, in the following discussion $\sigma_p(z,r)$ is set to $\sigma_p = \sigma_p(z,0)$ to represent the plasma conductivity at the centre of the discharge chamber where $r = 0$.
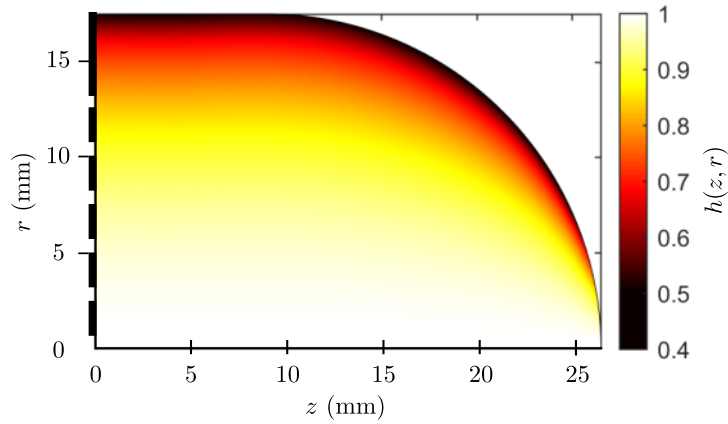
Figure 3.19: Plasma density variation inside the RIT 3.5 discharge chamber normalised to the centre value for $h_r = 0.4$.

For the RIT 3.5 thruster, the spatial distribution of the $h(z,r)$ parameter is shown in Figure 3.19. As can be seen from Figure 3.19, the ion density is highest near the central axis of the discharge chamber and decreases to h_r at the radial boundary. There is also a density variation in the axial direction through the h_l parameter. However, the h_l parameter was excluded from the model. This is because the electromagnetic fields are screened by the plasma at the radial edge of the discharge chamber. As a consequence, away from the radial edge boundaries there is virtually no electromagnetic power absorption. However, the h_l parameter was still used in calculating the currents I to the axial boundaries, as was shown in Equation 3.35 and Equation 3.36.

Figure 3.20 depicts the way in which the main thruster-plasma system parameters are calculated/represented in COMSOL. Expressing the thruster and plasma behaviour with electrical components is very helpful in analysing the overall thruster's performance. As Figure 3.20 illustrates, the coil and the thruster's structure are described using the resistance R_0' and inductance L_0. Similarly to the transformer model, the plasma can be thought of as a combination of the inductance L_p and resistance R_p, as shown in

Figure 3.20. Note that the plasma inductance L_p comes from the complex nature of the plasma conductivity. This complex part introduces a phase lag between the voltage and current. As mentioned already, the complex thruster impedance is obtained directly from COMSOL as $Z = R + jX$. The real part R of the complex impedance represents the thruster's resistance and is associated with the actual power loss. The complex part X accounts for the reactive component, or the phase lag, as a result of the inductive and capacitive couplings.
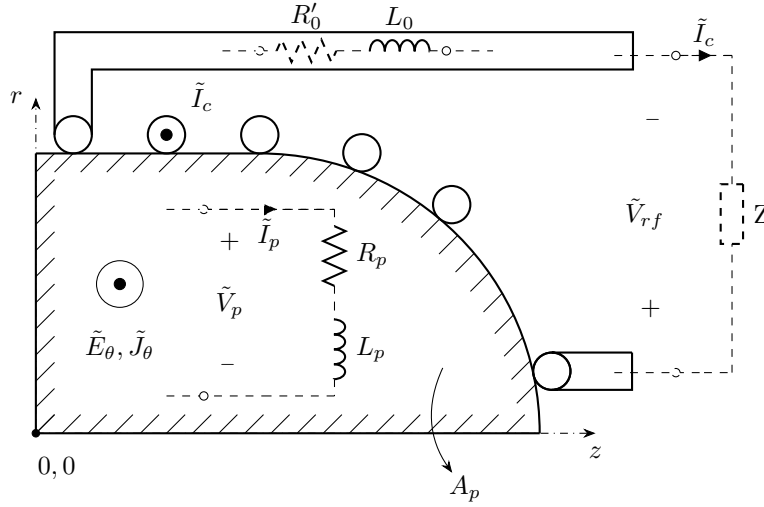
Figure 3.20: Schematic interpretation of the main plasma and coil/thruster parameters as obtained from the electromagnetic model developed in COMSOL.

The time-averaged power loss in the plasma (or the thruster's components) due to induced electromagnetic fields is obtained using the following equation (Griffiths, 1999)

$$W_p = \frac{1}{2} \iiint \Re(\sigma_p \cdot |\tilde{E}|^2) \, \mathrm{d}V_d. \tag{3.49}$$

Equation 3.49 can also be used to find the power loss in the thruster's components as well by replacing σ_p with the electrical conductivity σ_k of a particular component k. Additionally, the power lost in the thruster's component/plasma can be calculated using Ohm's law

$$W_k(T) = \frac{1}{2} R_k'(T) \tilde{I}_c^2, \tag{3.50}$$

where $R_k'(T)$ is the reflected (induced) component/plasma resistance, or the resistance as seen from the RFG terminals, and $\tilde{I}_c$ is the coil current. The parameter R_k' depends solely on the component/plasma electrical conductivity, geometry and relative distribution with respect to the coil (or the E field strength), as seen in Equation 3.49. Therefore, for each reflected resistance $R_k'(T)$ value, the power lost due to eddy currents $W_k(T)$ in this component can be determined using the applied coil current $\tilde{I}_c$. Therefore, in the thermal model, $W_k(T)$ values are used as the heat sources. Additionally, it is important to mention that the thruster's component reflected resistances $R_k'(T)$ are functions of the temperature T because the electrical conductivity $\sigma_k(T)$ is a function of the temperature

as well. Figure 3.21 shows how the reflected resistances vary with temperature for the thruster's structure, screen grid and coil.

(a) Screen and structure.

(b) Coil.
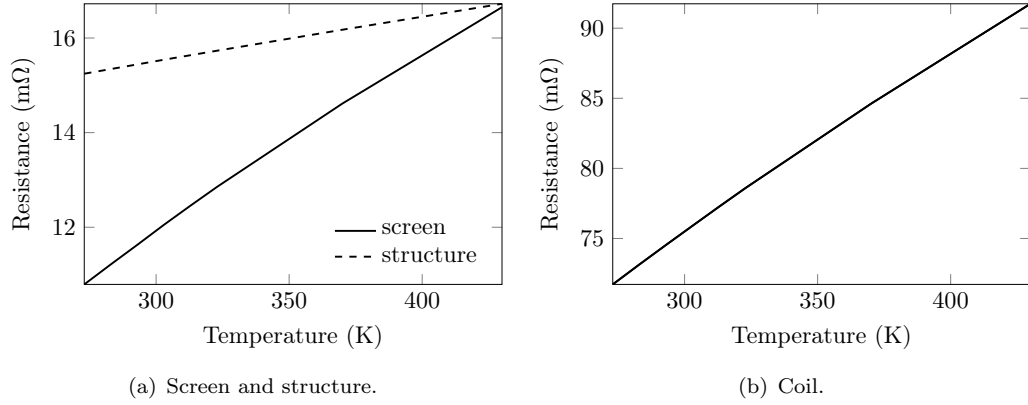
Figure 3.21: Reflected resistance variation with temperature for various RIT 3.5 thruster components.

In the model, the voltage drop over the coil $\tilde{V}_{rf}$ is obtained from the thruster's impedance Z as $\tilde{V}_{rf} = |Z|\tilde{I}_c$, where $\tilde{I}_c$ is the coil current given as the input to the electromagnetic model by the user. Furthermore, note that if the plasma electrical conductivity is set to zero, the electrical parameters R_p and L_p representing the plasma contribution disappear. Therefore, the thruster's impedance Z directly gives the reflected thruster's resistance R'_0 and inductance L_0 values without the plasma's effect. Next, the plasma voltage $\tilde{V}_p$ is determined by taking a 2D surface slice through the plasma, as represented by the plasma area A_p in Figure 3.20. Then, the model calculates the area-averaged potential drop over the plasma $\tilde{V}_p$ using the equivalent azimuthal electric field $\tilde{E}_\theta$

$$\tilde{V}_p = \frac{\iint \tilde{E}_\theta 2\pi r \,\mathrm{d}A_p}{A_p}. \tag{3.51}$$

The total plasma current $\tilde{I}_p$ is obtained by integrating the equivalent azimuthal current density $\tilde{J}_\theta$ on the 2D plasma surface slice

$$\tilde{I}_p = \iint \tilde{J}_\theta \,\mathrm{d}A_p. \tag{3.52}$$

The model also performs a 360° volume averaging of the potential drop across the plasma $\tilde{V}_p$ and current $\tilde{I}_p$ due to the 3D nature of the electromagnetic simulation domain. The plasma resistance R_p is estimated by using the previously calculated power absorbed by the plasma as $R_p = 2W_p/|\tilde{I}_p|^2$. The plasma inductance L_p comes directly from the imaginary part of the plasma conductivity given from Equation 3.23, noting that the reactance X is equal to $X = L_p/\omega$. The inertial plasma inductance is then calculated as $L_p = R_p/\nu_{tot}$.
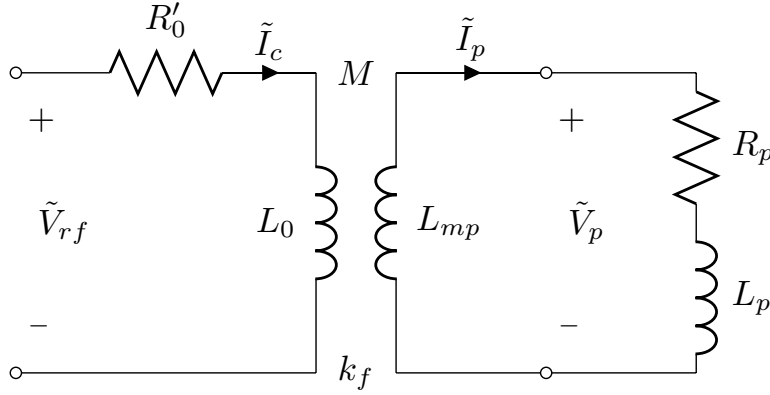
Figure 3.22: The thruster and plasma circuits coupled as in a transformer.

Finally, note that the plasma-thruster system can be represented as two equivalent circuits, as shown in Figure 3.22. Such a treatment of the plasma and thruster is referred to as the transformer method which was mentioned previously. This is because the two circuits shown in Figure 3.20 can be represented as linked through the mutual inductance M and the field coupling coefficient k_f, just as found in transformer circuits. The mutual inductance M and the inductance L_{mp} are obtained by rearranging the transformer equations presented in Chapter 2

$$M = (\tilde{V}_{rf} - j\omega L_0 \tilde{I}_c - R'_0 \tilde{I}_c)/(j\omega \tilde{I}_p), \qquad (3.53)$$

and

$$L_{mp} = (\tilde{V}_p - j\omega M \tilde{I}_c)/(j\omega \tilde{I}_p). \qquad (3.54)$$

Note that L_0 and R'_0 include not only the coil, but also reflected resistances and inductances of other thruster's components. However, L_0 and R'_0 do not include the effect of the plasma. Finally, the field coupling coefficient k_f between the coil and the plasma is calculated as (Griffiths, 1999)

$$k_f = \frac{M}{\sqrt{L_{mp}L_0}}. \qquad (3.55)$$

3.7   Thermal model

A thermal model based on the 3D RIT 3.5 thruster geometry has been designed in order to determine the thruster's surface temperature distribution. Primarily, the model was used to observe what effect the thruster's temperatures have on the electromagnetic heating losses in the conductors and on the plasma properties. What is more, the model was needed to analyse and help solve any potential thermal issues present in the RIT 3.5 thruster due to, for example, the thermal stresses which cause the ion optics and coil thermal expansions. Also, it was critical to make sure that the matching network capacitors installed on the RIT 3.5 did not overheat.

3.7.1   Geometry and meshing

The first step in creating the model was to simplify the RIT 3.5 geometry so it can be imported and successfully meshed in COMSOL. This meant that many small features such as bolts, screws and holes had to be removed. Furthermore, surfaces that come in contact tangentially or have very small radii had to be modified as well. However, it proved to be very computationally expensive to keep the original ion optics geometry, as shown in Figure 3.23(a). This was mainly due to a high number of apertures that needed to be meshed and resolved in solving the radiative heat transfer equations.

(a) Original ion optics geometry (121 apertures).   (b) Modified ion optics geometry (19 apertures).
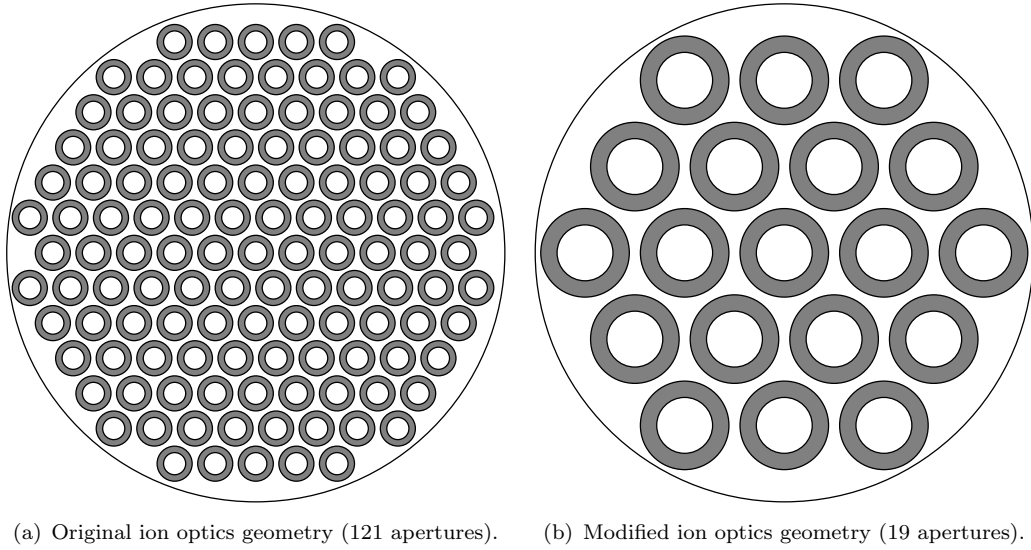
Figure 3.23: Original and modified RIT 3.5 ion optics geometries. Note that white + grey = scrn, white = accel, grey = scrn - accel.

An accurate representation of the heat radiation through the ion optics system is crucial to the overall heat balance. This is because the accel grid apertures are smaller than those of the screen grid and therefore some of the heat radiated by the discharge chamber (and the screen grid itself) to the environment is blocked. As a result, this greatly influences the overall heat balance and thus the temperature distribution. In particular, since some of the heat flux is blocked, temperatures of the accel grid, as well as the rest of the thruster's components, go up. The grid system was simplified by reducing the number of apertures from 121 to just 19, as shown in Figure 3.23(b). However, note that the accel grid open area (white area) and the screen grid open area blocked by the accel grid (grey area) were kept the same. This was done to keep the same radiative heat transfer balance as in the original grid design. Various studies performed while developing the thermal model have shown that such a simplification of the ion optics system causes only a minor effect on the overall temperature distribution inside the thruster.

The full 3D mesh of the thruster used in the thermal simulations is shown in Figure 3.24. Note that to display the inside view of the thruster, one part of the thruster's case has been hidden. The final 3D mesh consisted of a combination of swept hexahedral and tetrahedral mesh elements. Additionally, the mesh was composed of 147190 elements with an average quality of 0.53. As can be observed, Figure 3.24 also indicates the main components that are present in the thruster. While developing the model, a particular emphasis was placed on analysing the contact conductance between the RIT 3.5 attachment surfaces and the attachment flange. Simulations have shown that the contact conductances between these surfaces greatly influence the temperature distribution. Therefore, the thermal model was designed to represent the installation of the thruster as precisely as possible. Note that the exact way the thruster was installed during the RIT 3.5 experimental campaign will be shown in Chapter 6.
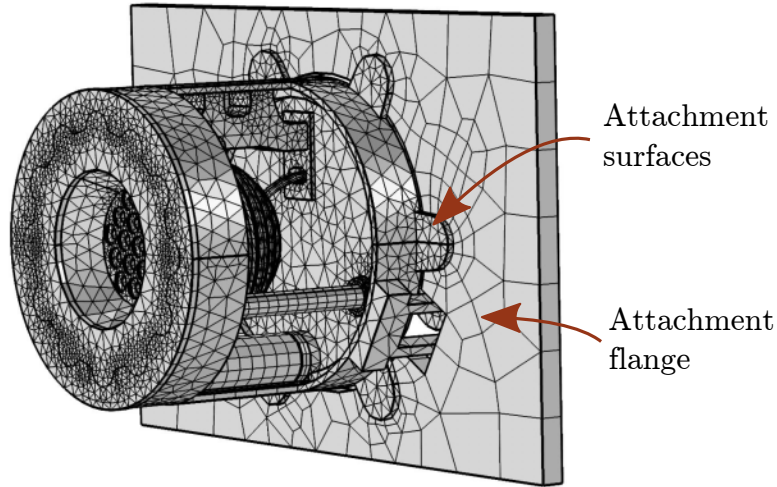
Figure 3.24: 3D RIT 3.5 thruster geometry and mesh used in the thermal simulations with the attachment surfaces and the attachment flange indicated by the arrows.

Figure 3.25 represents marked locations from 1 to 8 at which temperature measurements were recorded in the model. Additionally, Figure 3.25 illustrates the main RIT 3.5 thruster geometry features and the RF circuit with the RFG and the matching capacitor C_1. These temperature measurement points represent the locations where the temperature sensors (TS) were installed during the experimental campaign. Note that a detail discussion of the temperature sensor locations and description of the temperature sensors themselves, and the way the temperature sensors were installed is given in Section 6.2.7. In Chapter 4, the temperature sensor measurements from the experiments and the temperatures simulated in the model will be compared to validate the thermal model. Finally, the modelled temperature sensor temperatures were used to investigate the thermal model sensitivity to the mesh size, as will be shown in the following paragraph.
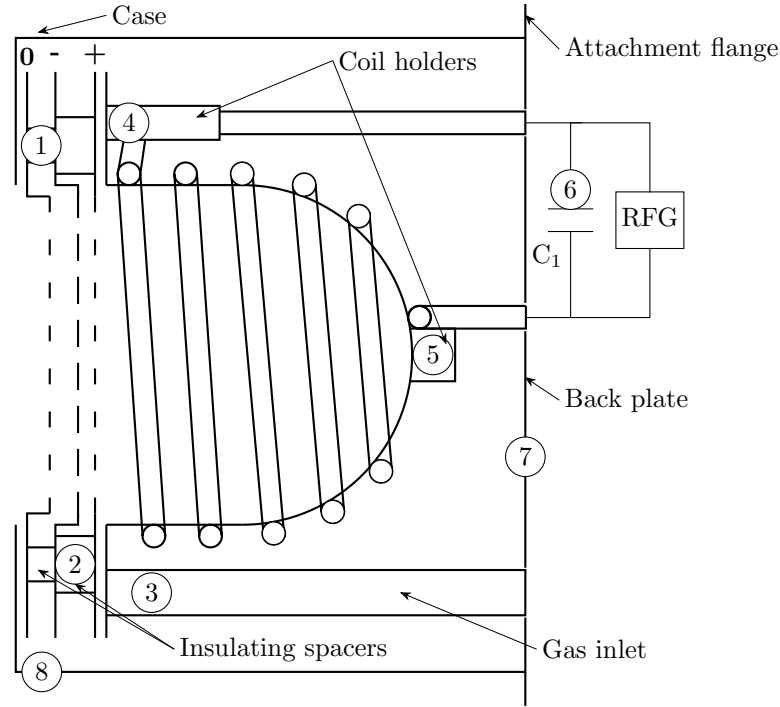
Figure 3.25: RIT 3.5 geometry and temperature sensor locations.

A thermal model mesh sensitivity analysis regarding the temperature sensor values was performed to aid in choosing the mesh size. The results from the analysis are depicted in Table 3.4. Table 3.4 shows that the greatest difference between the temperature values while varying the mesh size from coarse to fine is only about 1%. Nevertheless, the solution time varies widely. For instance, using the coarse mesh, it takes about 7 min to obtain a solution, while using the fine mesh, it takes 45 min to solve the model. Since the accuracy of the model almost does not change with decreasing mesh size, it was decided to use the coarse mesh for the simulations. This was mainly influenced by a substantial reduction in the solution times compared to other mesh sizes.

	Mesh size		
Parameter	**Coarse**	**Normal**	**Fine**
T_1 (℃)	115.65	115.75	115.88
T_2 (℃)	125.21	125.28	125.42
T_3 (℃)	94.692	94.394	94.991
T_4 (℃)	91.253	91.572	92.163
T_5 (℃)	214.01	214.23	214.48
T_6 (℃)	179.8	179.71	180.19
T_7 (℃)	56.482	56.359	56.537
T_8 (℃)	68.019	67.912	68.121
T_w (℃)	186.32	186.87	187.08
t (min)	7	15	45

Table 3.4: Thermal model mesh sensitivity analysis. The simulations were performed with $P_c = 14$ W, $P_s = 3$ W, $P_a = 0.5$ W and $I_c = 10$ A.

3.7.2 Main equations and principles

To find the thruster's temperature distribution, a 3D thermal model was developed in COMSOL by solving the steady-state heat equation (COMSOL Group, 2016)

$$\Delta(-\kappa \Delta T) = Q_i, \tag{3.56}$$

where Q_i represents the heat sources within the system and κ is the thermal conductivity. In RF ion thrusters, neglecting the contribution from the environment, there are two main heat sources: the plasma heating P_k and RF heating W_k. The plasma heating P_k due to the charged particle fluxes and excited neutral radiation was described in Section 3.5.4. The RF heating W_k due to eddy currents in the thruster's components was defined in Section 3.6.2.

In the thermal model, it was assumed that the thruster loses heat to the vacuum chamber either by conductance through the contact surface with the thruster's attachment plate or by surface radiation. The thruster was modelled as being attached to an infinitely large body at a set temperature T_{amb}, which was used to mimic the behaviour of the vacuum chamber. To complete the heat balance equations, surface-to-surface and ambient radiation mechanism were included as (COMSOL Group, 2016)

$$Q_{rad} = \epsilon(S - \sigma T^4), \tag{3.57}$$

where T is the surface temperature, σ is the Stefan-Boltzmann constant and ϵ is the emissivity of the material, which was set equal to the absorptivity across the full wavelength spectrum due to the grey-body assumption (Yogesh and Kenneth, 1986). The S parameter represents the incoming heat flux composed of the ambient S_{amb} and mutual heat fluxes S_m between the components (COMSOL Group, 2016)

$$S = S_m + S_{amb}. \tag{3.58}$$

In order to save computational time, radiation groups were defined. A radiation group was defined as a collection (or a set) of components, including the environment, that have considerably large view factors with respect to each other (Yogesh and Kenneth, 1986). Therefore, this allowed solving the radiation equations only within a particular radiation group.

Thermal analysis has shown that the contact conductances between components are very important in accurately predicting the temperature distribution. However, due to many unknown parameters these were difficult to estimate. Nevertheless, the contact conductance values were obtained using the data and methods available in literature (Holman, 2010; Toh and Ng, 1997). In the model, the contact conductance U_c between two adjacent component surfaces was represented using the Mikic's elastic model (Bejan

and Kraus, 2003)

$$U_c = \frac{1.54\kappa_c m_{asp}}{\sigma_{asp}} \left(\frac{\sqrt{2}p_c}{m_{asp}E_c} \right)^{0.94}, \tag{3.59}$$

where m_{asp} and σ_{asp} are the effective root-mean-square (RMS) contact surface asperities' slope and roughness, respectively, p_c is the contact pressure and κ_c is the average (harmonic mean) thermal conductivity of the surfaces with thermal conductivities κ_1 and κ_2 in contact (Bejan and Kraus, 2003)

$$\kappa_c = \frac{2\kappa_1\kappa_2}{\kappa_1 + \kappa_2}. \tag{3.60}$$

The equivalent contact elastic modulus E_c was calculated using the elastic moduli E_1 and E_2, as well as the Poisson's ratios ν_1 and ν_2 of the surfaces 1 and 2 in contact (Bejan and Kraus, 2003)

$$\frac{1}{E_c} = \frac{1 - \nu_1^2}{E_1} + \frac{1 - \nu_2^2}{E_2}. \tag{3.61}$$

Note that the material emissivities ϵ and thermal conductivities κ were taken from the data sheets provided by the manufacturers of the thruster's components and literature (Haynes, 2016). Also, to get a more accurate temperature distribution, the thermal conductivities were set as functions of the surface temperature as $\kappa(T)$ (Haynes, 2016).

(a) Full coupling.   (b) Reduced coupling.
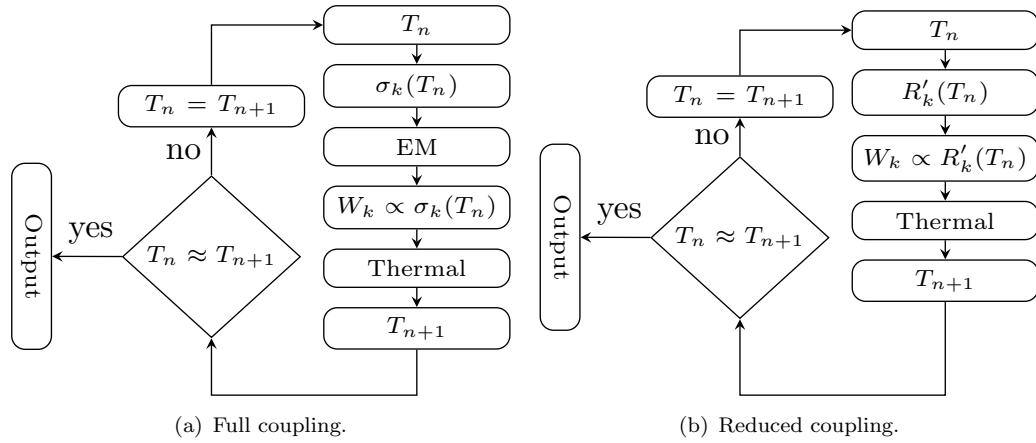
Figure 3.26: Flow chart depicting two possible solution methods that can be used to determine the eddy current heating magnitude in a thermal model. The "reduced coupling" solution method is much more stable and faster compared to the "full coupling" solution method.

Figure 3.26 shows two solution methods that were investigated while developing the thermal model. Both solution methods present a way to self-consistently calculate the eddy current heating magnitude in a thermal model. The discussion is started with the "full coupling" method depicted in Figure 3.26(a). First, note that the temperatures T_n obtained from the thermal model affect the thruster's component electrical conductivities $\sigma_k(T_n)$. As a result, this influences the RF heating magnitudes W_k that are obtained from the electromagnetic (EM) model. This is because W_k depends on $\sigma_k(T_n)$, as was

shown in Equation 3.49. However, when the heating values W_k at the temperature T_n are plugged back into the thermal model, the model calculates new temperature values T_{n+1}. In the "full coupling" system, this process has to be repeated until the thruster's temperatures become self-consistent with the RF heating magnitudes. This will happen when $T_n \approx T_{n+1}$.

	Full coupling	Reduced coupling
T_1 (℃)	115.69	115.65
T_2 (℃)	125.21	125.21
T_3 (℃)	94.184	94.692
T_4 (℃)	91.562	91.253
T_5 (℃)	213.99	214.01
T_6 (℃)	179.78	179.8
T_7 (℃)	56.33	56.482
T_8 (℃)	67.875	68.019
t (min)	120	7

Table 3.5: Temperature sensor values for "full coupling" and "reduced coupling" cases. The simulations were performed with $P_c = 14$ W, $P_s = 3$ W, $P_a = 0.5$ W and $I_c = 10$ A.

It was observed that it is very difficult and time-consuming to obtain convergence using the "full coupling" method because of a high degree of coupling. Therefore, when solving the thermal model it was decided to use the "reduced coupling" solution method depicted in Figure 3.26(b). The "reduced coupling" method is similar to the "full coupling" method. However, the RF heating values W_k are not calculated directly from the electromagnetic model based on the component electrical conductivities $\sigma_k(T_n)$. Rather, the RF heating magnitudes are represented as $W \approx R'_k(T_n)$, as was shown in Equation 3.50. The reflected resistances R'_k are pre-calculated in advance and plotted versus temperature, as was depicted in Figure 3.21. By using the "reduced coupling" method, the solution was achieved much faster and in a more stable manner. As indicated in Table 3.5, both solution methods give almost identical temperature sensor values. However, the "reduced coupling" method is about 110 min faster compared to the "full coupling" method.

3.8   RF circuit model

An RF circuit model was developed in COMSOL to determine the power losses in the coaxial cable and the RFG, which allowed the total input power to the thruster to be calculated. What is more, the RF circuit model was used to find the matching frequency and the R, L, C values of the matching circuit. In the model, the transformer circuit from Figure 3.22 was transformed using Maxwell's equations to an equivalent

thruster's circuit composed of the coil resistance R_c, the multiple reflected component resistances R'_k, the reflected plasma resistance R'_p and the equivalent thruster inductance L_{thr}, as seen in Figure 3.27. Notice that all these circuit parameters are obtained from the electromagnetic (EM) model. Also, note that, as discussed before, the reflected (or induced) resistance values (denoted by R') are not the actual resistance values of the component/plasma. Rather, the reflected resistances are the resistance values as seen from the RFG terminals. For instance, the reflected plasma resistance R'_p can be calculated using Ohm's law

$$R'_p = 2W_p/\tilde{I}_c^2, \tag{3.62}$$

where W_p is the actual power absorbed by the plasma. Remember that in Equation 3.62, the factor of 2 is needed to express the time-averaged value of the coil current $\tilde{I}_c$.

As in the actual RIT 3.5 experimental set-up, the circuit depicted in Figure 3.27 also includes an RFG, a matching network composed of capacitors C_1 and C_2, and a coaxial cable. As shown in Figure 3.27, the RIT 3.5 thruster operation involves the following principles. First, the DC voltage V_{in} is set on the power supply of the RFG. Based on the thruster and plasma parameters, the circuit draws the DC current I_{in}. Therefore, the total input power P_{in} that is being supplied to the thruster can be calculated as $P_{in} = V_{in} \times I_{in}$. Then, the RFG converts the DC voltage V_{in} into the high-frequency rectangular voltage $\tilde{V}_{out}$ which is then transformed into the sinusoidal coil current $\tilde{I}_c$. Furthermore, the RFG and thruster are connected through the coaxial cable in which the current $\tilde{I}_{cab}$ flows. Finally, the capacitors C_1 and C_2 are used to cancel the predominantly inductive reactance of the circuit so that the RFG operates at a predefined frequency in a resonance mode; that is, the phase angle of the circuit is zero.
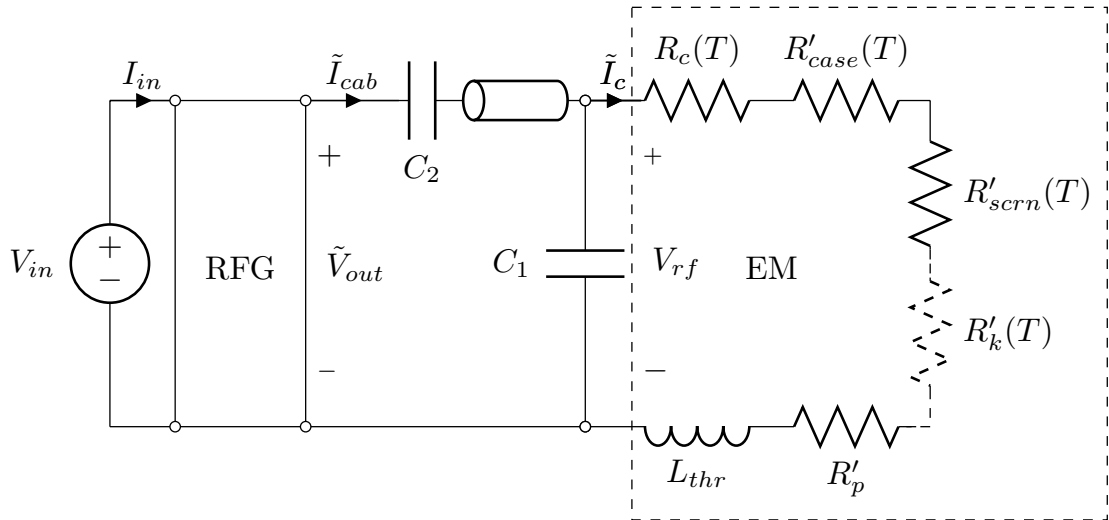
Figure 3.27: Schematic representation of the plasma and the RF circuit in the RF circuit model developed in COMSOL. "EM" represents the parameters obtained from the electromagnetic model.

Additionally, the capacitors influence the relative difference between the coil and the cable currents $\tilde{I}_c$ and $\tilde{I}_{cab}$, respectively. For the RIT 3.5, the resonance frequency was chosen to be at about 3 MHz. During the thruster's operation, the reflected plasma resistance R'_p and the reflected component resistances R'_k, as well as the total thruster inductance L_{thr} change due to a variation in the plasma parameters and temperature. Therefore, to keep the circuit in resonance, the RFG adjusts the applied frequency in a phase-controlled loop to reduce the phase angle to zero. This ensures that the maximum amount of power is delivered to the plasma. In the RF circuit model, the resonant frequency is obtained by performing a frequency sweep. Then, the resonant frequency is chosen at the frequency where the input power P_{in} reaches a minimum value. Note that the matching could in principle also be done by adjusting the capacitances C_1 and C_2 based on the knowledge of the R'_0 and L_{thr} values. However, it was discovered that changing the frequency to perform matching is more efficient and faster.

In the RF circuit model, it is imperative to accurately determine the current I_{in} supplied by the RFG since it directly influences the cable $\tilde{I}_{cab}$ and coil $\tilde{I}_c$ currents. Furthermore, the RFG and cable have small, but not negligible resistances R_{rfg} and R_{cab}, respectively. Therefore, a fraction of the total power supplied to the thruster is lost in these components due to the Ohmic losses that depend on $\tilde{I}_c$. The RF circuit model determines the input current I_{in} by simulating the circuit depicted in Figure 3.27 in the following manner. First, for given operational parameters, the required coil current $\tilde{I}_c$ to generate the plasma that produces the beam current I_b is calculated using the electromagnetic model. This is achieved by setting the time-averaged power loss in the plasma W_p due to EM fields equal to the discharge power loss P_d, which must be true under the steady-state conditions (Chabert and Braithwaite, 2011). Also, the model uses the fact that the induced plasma resistance R'_p does not change with the coil current, but is solely a function of the plasma geometry and the electrical conductivity. Finally, using these two assumptions, the coil current is calculated using Ohm's law

$$\tilde{I}_c = \sqrt{\frac{2P_d}{R'_p}}. \tag{3.63}$$

To have a self-consistent solution corresponding to the thruster's behaviour, the RF circuit model varies the input current I_{in} until the coil current $\tilde{I}_c$ as calculated from Equation 3.63 is attained. Once the correct input current is obtained, the RF circuit model determines all the other information of interest such as the cable current $\tilde{I}_{cab}$, the Ohmic power losses in the circuit's components, matching frequency, voltages and various current-voltage phase angles. As a final step, the model calculates the power transfer efficiency η_w. The power transfer efficiency to the plasma is calculated by dividing the power W_p that reaches the plasma (or is transferred to the plasma) by the

total input power to the system P_{in}

$$\eta_w = W_p/P_{in}. \tag{3.64}$$

Neglecting the RFG and coaxial cable resistances, Equation 3.64 can be simplified using the circuit components found in Figure 3.27

$$\eta_w \approx \frac{R'_p}{R'_0 + R'_p} \approx \frac{1}{R'_0/R'_p + 1} \approx \frac{1}{R_c/R'_p + 1}, \tag{3.65}$$

where $R'_0 = R_c + R'_{case} + R'_{scrn} + ... + R'_k$. Equation 3.65 is of great importance since it shows how the electrical parameters can be used to understand the RF thruster behaviour and optimise its performance. In general, it can be seen that to increase the power transfer efficiency η_w, the R'_0/R'_p ratio has to be minimised. In other words, the reflected thruster's resistance R'_0, which in magnitude is almost equal to the coil resistance R_c, must be made as small as possible, while the reflected plasma resistance R'_p must be made as high as possible. The implications of this will be discussed in Chapter 4.

3.9   Summary

In this chapter, an engineering model has been designed to simulate the RF gridded ion thruster's performance and thermal behaviour without the shortcomings of the previously developed models, as described in Chapter 2. The model was based on the RIT 3.5 geometry, experimental set-up and operational parameters. Nevertheless, the model can be successfully applied to simulate other RF thrusters as well, as will be shown in Chapter 5. To account for various physical phenomena occurring inside RF ion thrusters, the RF thruster model has been composed of the plasma discharge, 2D axisymmetric ion extraction, 3D electromagnetic, 3D thermal and RF circuit models. The plasma discharge model itself has been developed using the 0D global, 2D axisymmetric and 3D molecular neutral gas, and Boltzmann electron transport sub-models. In the plasma model, the non-local effects have been accounted for by introducing the collisionless heating frequency and the equivalent collisionless skin depth. The 3D thermal model has been employed to self-consistently determine the temperature distribution for various throttle points based on the electromagnetic heating values and heat fluxes from the plasma. For instance, the RF thruster model allows determining the following parameters: the ion optics effective transparency T_{eff}, neutral gas pressure p, EEDFs, plasma density n_i, radial ion density distribution $n_i(z,r)$, plasma conductivity $\sigma_p(z,r)$, total discharge power P_d, RF heating values W_k, coil current I_c, total RFG input power to the thruster P_{in}, temperature distributions and power transfer efficiency η_w to name a few. The RF thruster model developed in this chapter is the first model of this kind to self-consistently include all the operational parameters of RF thrusters. In the next

chapter, the RF thruster model validation will be performed and the RIT 3.5 perfor-
mance, as simulated by the model, will be analysed.

4

RF gridded ion thruster model: results

In this chapter, the simulation results from the RF thruster model described in Chapter 3 are presented. First, the RF thruster model is validated against an analytical model. This is done to make sure that the electromagnetic model developed in COMSOL is correct. Then, the RF thruster model is also validated against the RIT 3.5 experimental performance and thermal data that were measured as a part of this thesis. Once the validation results are summarised, the model is used to simulate the RIT 3.5 behaviour. Finally, using the simulated data, the RIT 3.5 performance is analysed.

4.1   Validation

The model was validated by comparing the results of the electromagnetic model developed in COMSOL to the results obtained by solving analytical (idealised) Maxwell's equations using Bessel functions, as derived by Chabert and Braithwaite (2011). Note that the analytical equations were solved using Matlab. The geometry which the model validation was based on is shown in Figure 4.1. The geometry features a 2D-axisymmetric discharge chamber with the radius r_0 and length l. The coil is represented by the number N of uniformly distributed conductive rings at the distance r_c from the axial centre where the peak sinusoidal current $\tilde{I}_c$ flows. While developing the COM-SOL electromagnetic validation model, it was assumed that the plasma can be solely

described using a uniform complex conductivity σ_p. The plasma conductivity/permittivity was assumed uniform to have comparable results between the COMSOL and the analytical model, as will be discussed next. Furthermore, the mesh was designed to take into account the fact that in the plasma there are electric E and magnetic B fields that decay within the characteristic skin depth δ.
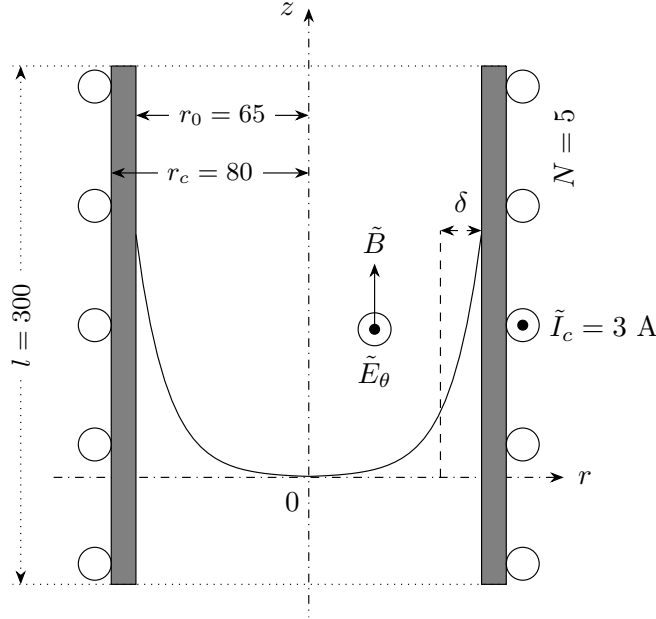
Figure 4.1: Discharge chamber geometry used to validate the electromagnetic model developed in COMSOL against Maxwell's equations represented through Bessel functions.

In the analytical model, the electromagnetic fields inside the plasma were calculated using Maxwell's equations expressed through Bessel functions J. The analytical model uses the following assumptions: the plasma is uniform with a complex permittivity ϵ_p, $l >> r_0$, geometry is perfectly cylindrical, and end coil and proximity effects can be ignored. Using these assumptions, for the geometry depicted in Figure 4.1, the power absorbed by plasma can be expressed as (Chabert and Braithwaite, 2011)

$$P = i\frac{\pi N^2 I_c^2}{l}\left[\frac{k_w r_0 J_1(k_w r_0)}{\omega\epsilon_0\epsilon_p J_0(k_w r_0)} + \frac{1}{2}\omega\mu_0(r_c^2 - r_0^2)\right], \qquad (4.1)$$

where $k_w = \omega/c\sqrt{\epsilon_p}$ is the complex wave number, c is the speed of light, J_0 is the 0th Bessel function of the first kind and J_1 is the 1st Bessel function of the first kind. The time-averaged power dissipated in the plasma P_{abs} is obtained by taking the real part of the complex power P

$$P_{abs} = \text{Re}\,[P]. \qquad (4.2)$$

Using a similar approach as before, the inductance of the system L_{ind} can be expressed as (Chabert and Braithwaite, 2011)

$$L_{ind} = L_c \left[1 - \frac{r_0^2}{r_c^2} \right] + \frac{2\pi N^2}{l\omega^2 \epsilon_0} \text{Im} \left[\frac{ik_w r_0 J_1(k_w r_0)}{\epsilon_p J_0(k_w r_0)} \right]. \tag{4.3}$$

The coil inductance is calculated using a well-known analytical equation (Chabert and Braithwaite, 2011)

$$L_c = \frac{\mu_0 \pi r_c^2 N^2}{l}. \tag{4.4}$$

Furthermore, the plasma current I_p is obtained as (Chabert and Braithwaite, 2011)

$$I_p = N I_c \left[\frac{1}{J_0(kr_0)} - 1 \right], \tag{4.5}$$

while the plasma resistance R_p is

$$R_p = \frac{2P_{abs}}{|I_p|^2}. \tag{4.6}$$

It is also important to determine the coupling coefficient k_f, as was mentioned when discussing the transformer assumptions. In this section, k_f is defined as

$$k_f = \frac{M}{\sqrt{L_c L_{mp}}}. \tag{4.7}$$

The mutual inductance M is obtained from the transformer equations discussed in Chapter 2. As mentioned before, L_{mp} is an inductance generated by the loop current flowing in the plasma, which produces a magnetic field. Therefore, the inductance L_{mp} can be expressed as (Chabert and Braithwaite, 2011)

$$L_{mp} = \frac{R_p n_i e^2 \mu_0 r_0 \delta}{\nu m_e}, \tag{4.8}$$

where δ is the skin depth approximated as $\delta = c/\omega_{pe}$ and ν is the collision frequency between electrons and neutrals.

4.1.1 Results and discussion

This section compares the result from the analytical model to those of the electromagnetic (COMSOL) model. This is done to gauge the discrepancies and similarities between the two models. Figure 4.2 displays the power absorbed by the plasma P, as obtained from Equation 4.2, against the ion density for different ν/ω values. Note that the ν/ω ratio represents the inverse of the phase difference between the RF current density and the RF electric field. This can be checked by dividing the complex part of the plasma conductivity given in Equation 3.23 by the real part. In addition, the ν/ω ratio

is strongly dependent on the neutral gas pressure inside the discharge chamber through the electron-neutral collision frequency ν. Figure 4.2 shows that as the ion density increases, the discrepancy between the COMSOL and the analytical models varies. At the ion densities of up to about 1×10^{17} 1/m^3, the COMSOL model predicts the power absorbed by the plasma that is approximately 49% lower compared to the COMSOL model for all ν/ω cases. This means that compared to the analytical model, the COMSOL model underestimates the power for the case $\nu/\omega = 0.1$ by about 4 W at the ion density of 3×10^{16} 1/m^3, by about 35 W for the case $\nu/\omega = 1$ at 6×10^{16} 1/m^3 and by about 76 W for the case $\nu/\omega = 10$ at 3×10^{17} 1/m^3. However, as the ion density goes past about 3×10^{17} 1/m^3, the difference between the models decreases dramatically. As a result, at the ion density of about 6×10^{18} 1/m^3, the discrepancies are only about 15%. The COMSOL model should be taken as being more accurate because it includes the end coil and proximity effects, which are not represented by the analytical equations. Note that typically RF ion thrusters work in the range of 10s to a few hundred of watts of RF power and at ion densities of about 1×10^{17} 1/m^3 (Loeb et al., 2004; Smirnova et al., 2016a; Schäfer, 1971).
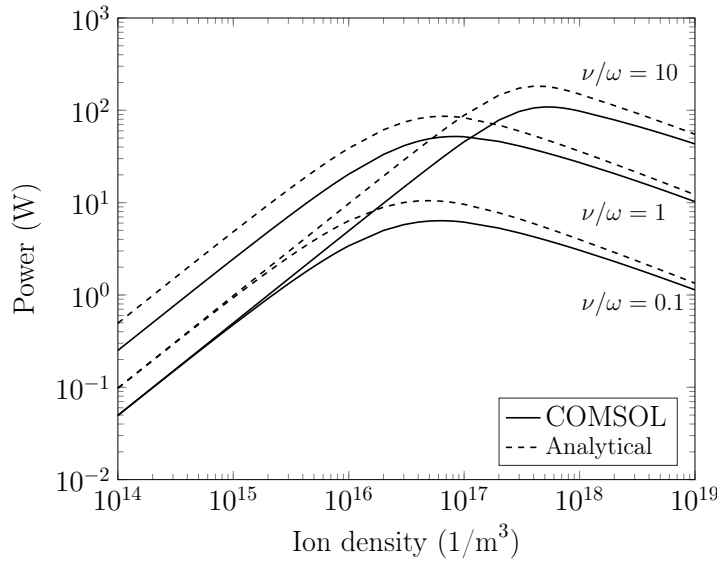
Figure 4.2: Validation of the electromagnetic model (COMSOL) against the analytical model: power absorbed by the plasma vs ion density for $\nu/\omega = 0.1$, $\nu/\omega = 1$ and $\nu/\omega = 10$.

As far as the trends shown in Figure 4.2 are concerned, it can be seen that the absorbed power increases linearly with the ion density n_i at low densities, reaches a maximum and then starts dropping as $n_i^{-1/2}$ at high densities (Chabert and Braithwaite, 2011). Such a behaviour occurs because at low ion densities the magnetic field penetrates most of the plasma's volume and therefore the skin depth is large. However, at high densities, the magnetic field becomes concentrated in a very thin skin layer and thus the capability of the coil to transfer power to the plasma diminishes. That is, the plasma volume that can absorb power becomes small due to the narrow skin depth.

Therefore, the absorbed power reaches a peak when the ion density is high enough for a sufficient electron acceleration and gas ionisation by the electromagnetic fields, but not too high to start shielding the plasma from the fields. Furthermore, the absorbed power increases linearly with ν/ω due to an increase in the collision frequency ν, which itself is proportional to the neutral gas pressure. However, once ν/ω becomes much larger than 1, the absorbed power starts to decrease at lower ion densities and to increase at higher ion densities, as shown in Figure 4.2.
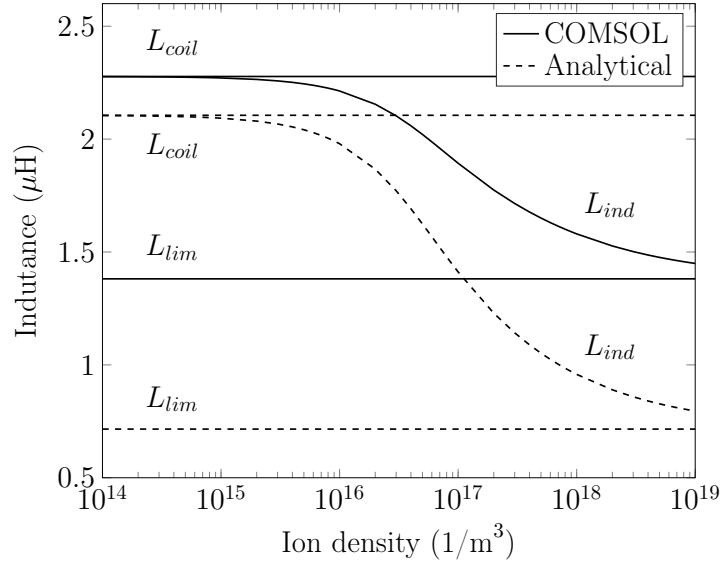
Figure 4.3: Validation of the electromagnetic model (COMSOL) against the analytical model: plasma inductance vs ion density for $\nu/\omega = 1$.

Figure 4.3 shows how the induced inductance L_{ind} varies with the ion density for $\nu/\omega = 1$, as calculated using Equation 4.3. As can be seen in Figure 4.3, there are relatively high discrepancies between the COMSOL and the analytical models. However, the same trends are followed. It should be observed that the whole plot representing the COMSOL results is shifted upwards. This is because the COMSOL model predicts the coil inductance L_c that is about 8% higher compared to the analytical coil inductance obtained from Equation 4.4. Such a discrepancy is caused because the analytical model excludes the proximity and skin effects (Grover, 1946). Also, while calculating the coil inductance, the analytical model assumes that the coil is infinite in the axial direction (Nagaoka, 1909). Therefore, the inductance value as calculated by COMSOL is more accurate because COMSOL does not use the aforementioned simplifying assumptions. The parameter L_{lim} represents the inductance value when the current inside the plasma is concentrated in a very thin loop so it behaves as a one-turn coil. Remember that such a description of the plasma was used when equating the plasma to a one-turn coil in the secondary of a transformer. Also, note that in the high-density regime $L_{lim} = L_c(1 - r_0^2/r_c^2)$, as indicated in Figure 4.3. What is more, Figure 4.3 shows that L_{lim} estimated using the analytical approach is about half of that obtained from the COMSOL model.

Figure 4.3 depicts that at low ion densities L_{ind} is equal to the L_c because there are no opposing electromagnetic fields inside the plasma. In such conditions, the electromagnetic fields decay as in a vacuum. However, as the ion density increases, an ever larger opposing magnetic field is produced by the plasma, cancelling the primary magnetic field generated by the coil according to Faraday's and Lenz's laws. Therefore, a majority of the plasma's volume becomes field-free. As a result, L_{ind} starts to decrease steeply. When the ion densities of $1 \times 10^{19}\,1/m^3$ and above are reached, the plasma behaves like a one-turn coil and the whole system can be simulated using the transformer model. The transformer model becomes valid because L_{ind} starts approaching the L_{lim} magnitude. In theory, as the density is increased even further, L_{ind} should stop changing and reach a constant value defined by L_{lim}. Finally, note that this behaviour is observed in both the COMSOL and the analytical models, as can be seen in Figure 4.3.
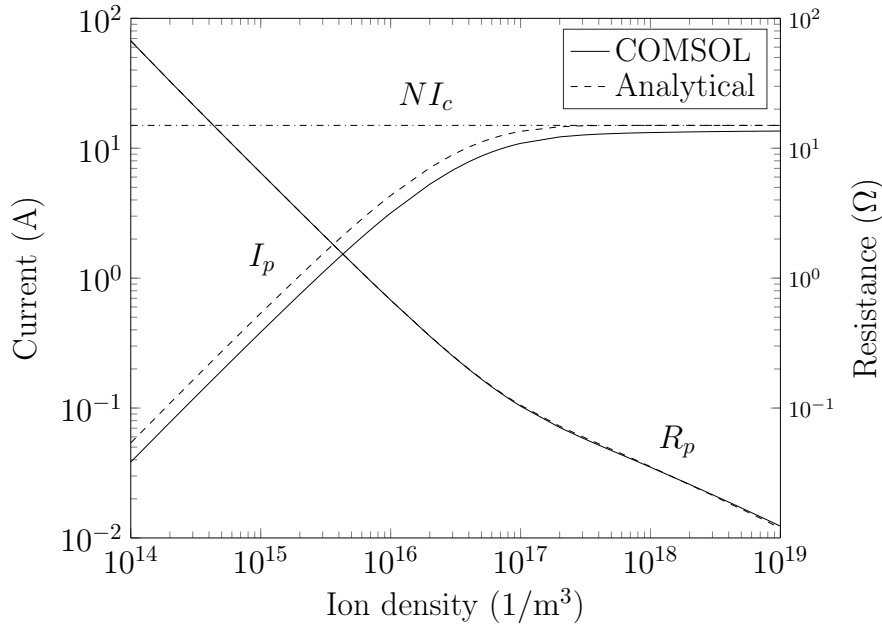
Figure 4.4: Validation of the electromagnetic model (COMSOL) against the analytical model: plasma current and resistance vs ion density for $\nu/\omega = 0.1$.

Figure 4.4 illustrates that as the ion density increases, the plasma resistance R_p decreases from $80\,\Omega$ to less than $0.1\,\Omega$, as was calculated by Equation 4.6. However, the relationship is non-linear. The shift in the gradient occurs because the induced current starts becoming concentrated in a thin skin layer at the ion density of about $1 \times 10^{17}\,1/m^3$, as was mentioned before. On the contrary, the azimuthal plasma current, calculated using Equation 4.5, increases with the ion density and flattens out at a maximum value equal to NI_c. This again happens due to the electromagnetic field saturating in the narrow skin depth. When the saturation happens, the coil and plasma behave as if though they were coupled through a transformer circuit and therefore normal transformer equations can be used to analyse the system. For instance, the plasma density in the RIT 3.5 thruster is around $1 \times 10^{17}\,1/m^3$. Therefore, assuming that the RIT 3.5 thruster plasma

is similar to the one being investigated, the plasma density in the RIT 3.5 is too low to consider the transformer assumptions fully applicable. This is one of the reasons why the full 3D electromagnetic model was created to represent the plasma-thruster system. Additionally, the RIT 3.5 discharge chamber's geometry is not cylindrical, which would make solving the analytical equations challenging and the results would be inaccurate.
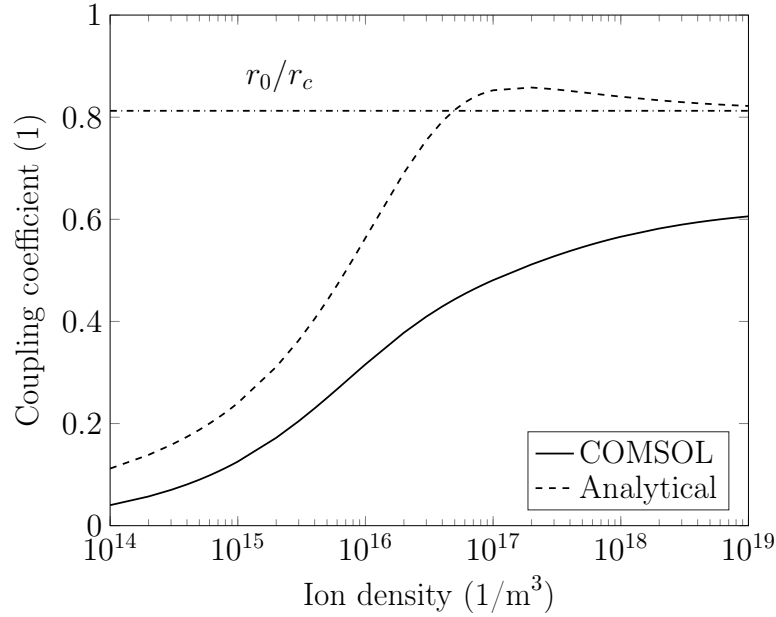
Figure 4.5: Validation of the electromagnetic model (COMSOL) against the analytical model: coupling coefficient vs ion density for $\nu/\omega = 0.1$.

The coupling coefficients, as obtained from the COMSOL and the analytical model using equation Equation 4.7, are illustrated in Figure 4.5. It can be seen that at low ion densities, the coupling coefficient is less than 0.2 for both cases analysed. However, the COMSOL model predicts the coupling coefficient that is 50% lower compared to the analytical model. Note that in both models, such low coupling coefficients are observed because the coil does not feel the presence of the plasma. As the ion density increases, the coupling coefficient increases as well. At the density from about 1×10^{18} 1/m^3, the analytical coupling coefficient starts to plateau at around 0.8. Notice that this value is simply the coupling coefficient equal to r_0/r_c of two solenoids coupled as a transformer, as shown in Figure 4.5 (Chabert and Braithwaite, 2011). Therefore, this once again confirms that the whole circuit behaves as a transformer at the ion density of about 1×10^{19} 1/m^3. The coupling coefficient as predicted by COMSOL also increases with the ion density but the maximum value it reaches is only about 0.6 at 1×10^{19} 1/m^3. The coupling coefficient is lower in the COMSOL model because, due to the finite length of the coil and due to a small number of turns, a substantial part of the total magnetic field "leaks" around the edges of the coil and does not penetrate the plasma. It was noticed that as the length of the coil (or the length of the discharge chamber) and the number of turns increase, the coupling coefficient approaches the value calculated using

the analytical equations and, ultimately, the value defined by the r_0/r_c ratio. At the RIT 3.5 working ion densities, the coupling coefficient should be only about $0.3 - 0.5$, which is indicative of a loosely coupled transformer behaviour. Therefore, full Maxwell's equations have to be solved to accurately represent the RIT 3.5 thruster.

4.1.2 Summary

It can be concluded that the COMSOL model accurately represents the plasma and the coil system. Even though there are some significant discrepancies between the analytical and the COMSOL models, these are explainable by analysing the plasma behaviour and the assumptions made in the analytical model. For instance, the analytical model excludes the proximity effect, the skin effect and assumes that the coil is infinite in the axial direction and there are no end coil effects. Note that the errors are especially significant if short coils with a few turns, which is the case for RF thruster coils, are simulated using analytical models. All the aforementioned shortcomings of the analytical model are fully accounted for in the COMSOL model using a finite-element method (FEM). Therefore, it can be expected that the COMSOL model is more accurate than the analytical model at representing the plasma, especially in a lower ion density regime where the transformer assumptions cannot be fully applied. Since the RIT 3.5 works at relatively low densities and has a non-cylindrical discharge chamber geometry with only 7 turns, it was decided that a full treatment of Maxwell's equations using the FEM is necessary to accurately represent the thruster's behaviour. For these reasons, the full 3D electromagnetic model has been developed in COMSOL, as has been discussed in Chapter 3.

4.2 Performance parameters

4.2.1 RFG input power and current

This section presents the RF thruster model results and compares them to the RIT 3.5 experimental data to gauge the accuracy of the model. Figure 4.6 depicts the RFG input power P_{in} and RFG input current I_{in} variations for different mass flow rates as a function of the mass utilisation efficiency η_m, as was defined in Chapter 2. Note that in this thesis, the beam current I_b is defined as $I_b = I_{scrn} - I_{acc}$, where I_{scrn} is the electron current collected by the screen grid and I_{acc} is the electron current drawn by the accel grid. Observe that above each experimental point in Figure 4.6, the screen voltage U_{scrn} (in volts) at which the experimental point was measured is also depicted. Also, the accel voltage U_{acc} is the same for all points and equal to -150 V. For the reference, a table containing a full set of the RIT 3.5 operational points as measured during the experimental campaign is given in Appendix A. Finally, note that each experimental

point was measured multiple times. However, the error bars are not plotted since the spread in measured values is negligible at the scale depicted in Figure 4.6. It was decided to judge the accuracy of the model based on two criteria. First, the model was judged by how well it can predict the shape of the trend curve observed in the experiments. This was achieved by doing the best curve fit for the experimental data and finding the coefficient of determination R^2, which was then compared to the R^2 value found in the model trends. Second, the percentage error deviations between the experimentally measured and simulated individual parameter values were compared.
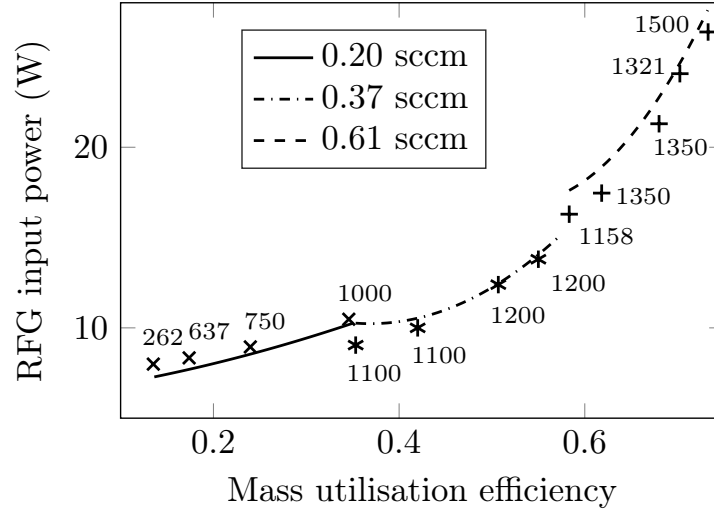
(a) RFG input power.
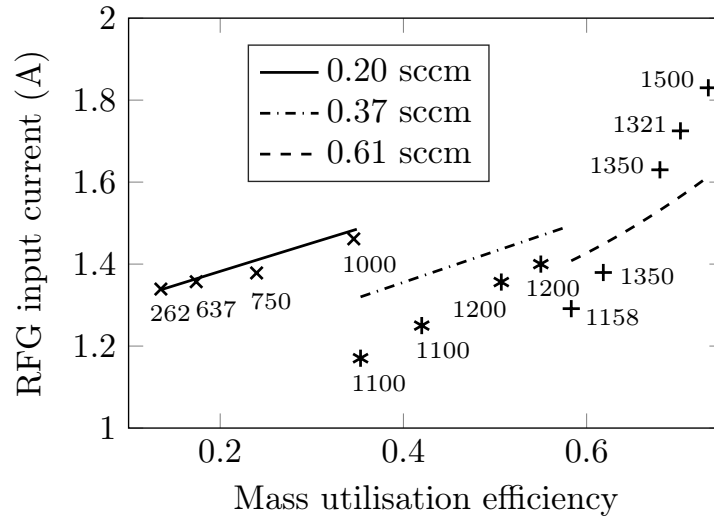
(b) RFG input current.

Figure 4.6: RFG parameters for 0.2 sccm, 0.37 sccm and 0.61 sccm propellant flow rates compared with the experimental data $\times$, $*$, $+$, respectively. U_{scrn} values are shown above each experimental point in volts. U_{acc} is set to -150 V for all points.

Table 4.1 summarises the modelled RFG input power P_{in} and RFG input current I_{in} percentage deviations from the experimental results using the data from Figure 4.6, which was used to judge the accuracy of the model. The deviations from the experimentally measured data points are provided in the range from the minimum to the maximum values in percentages. Additionally, the percentage deviations in the R^2 parameter are provided as well. As can be seen in Table 4.1, the model predicts the RFG input power P_{in} values with an error between 1% and 12% for the mass flow rates investigated. Similarly, the model predicts the RFG input current I_{in} with an error between 0.1% and 13%. In general, the P_{in} value indicates how well the whole thruster-plasma system is modelled. Additionally, the P_{in} parameter is of great importance since this is the value that is often being minimised. Therefore, the error in P_{in} should be as small as possible. Similarly, the I_{in} value also indicates how well the whole thruster-plasma system is modelled. In addition, I_{in} also shows how accurately the model predicts the coil current $\tilde{I}_c$ since $\tilde{I}_c \propto I_{in}$.

Measured parameter	Mass flow rate, sccm	Min. model deviation, %	Max. model deviation, %	R^2 model deviation, %
	0.20	3	9	1
P_{in}	0.37	1	12	6
	0.61	3	9	0.5
	0.20	0.1	2	3
I_{in}	0.37	5	11	0.2
	0.61	5	13	0.2

Table 4.1: RFG input power P_{in} and RFG input current I_{in} percentage deviations in individual values and trends between the RIT 3.5 experimental data and the model results for 0.2 sccm, 0.37 sccm and 0.61 sccm flow rates.

However, for the model to be used for the analysis and optimisation of the thruster's behaviour, the model results also have to exhibit the same trends as observed in the experiments. This is why the R^2 parameter was introduced. Remember that the R^2 parameter is a statistical measure of the difference between the data and the fitted regression line. In general, the higher the R^2 value, the better the fit between the data and the model. However, the percentage difference between the R^2 values obtained from the experimental and model data should be as small as possible. As Table 4.1 indicates, the maximum R^2 parameter error in predicting the P_{in} trend is 6%, whereas that in predicting the I_{in} trend is 3%. Based on the aforementioned analysis, Table 4.1 and Figure 4.6 results, and the fact that all errors were consistent over a wide range of operating conditions, it was deemed that the model is accurate enough to be trusted. Therefore, it was decided to use the model to further investigate and better understand the RIT 3.5 thruster behaviour.

By looking at Figure 4.6, it can be seen that the RFG input power increases with the mass utilisation efficiency. This is because, according to Equation 2.8, to increase the

mass utilisation efficiency, the thruster has to produce a larger beam current I_b for a given mass flow rate $\dot{m}_{in}$. To produce a larger beam current I_b, the ion density must increase, which in turn results in a rise in the RFG power. Ideally, one would like to operate at the highest possible mass utilisation efficiency because it translates in a high specific impulse I_{sp} since $I_{sp} \propto \eta_m \sqrt{U_{scrn}}$. However, as can be seen from Figure 4.6, there is a power penalty associated with the high mass utilisation efficiency. Additionally, as the RFG input power is increased, the RFG input current increases as well. This, in turn, increases the coil current.

A large coil current results in significant losses in the RF circuit and the thruster's structure. However, having the coil current too low means that the power delivered to the thruster will be small and the RFG input voltage V_{in} will be high because $V_{in} = P_{in}/I_{in}$. Generally, such a low power and high voltage condition results in a low mass utilisation efficiency and poor RFG performance. Therefore, to be able of operating the thruster at a high mass utilisation efficiency and low RFG input power, an optimisation analysis is needed. Such an optimisation analysis can now be performed using the model developed in this thesis. Usually, the optimisation is performed by generating many plots as the ones found in Figure 4.6 for various mass flow rates or beam currents. Then, the thruster and mission designer can choose the most optimum values for a given mission. By using models to simulate the thruster's performance, the length of the design process and the experimental campaign can be reduced significantly; saving time, cost and resources. Such an approach will be implemented in Chapter 5 to design and optimise a double-sided ion thruster.

4.2.2 Circuit parameters

It is also beneficial to analyse the RIT 3.5 thruster's performance through the circuit parameters, as defined in Chapter 2 and Chapter 3. Figure 4.7(a) analyses the power transfer efficiency η_w because it is an important factor used in evaluating the overall thruster and RF circuit design. As can be seen from Figure 4.7(a), the power transfer efficiency η_w increases from 0.48 until it starts to plateau at the value of around 0.65 at 20 W of input power. To understand this behaviour, the way the induced plasma resistance R'_p varies with the input power has to be analysed, as depicted in Figure 4.7(b). First, R'_p increases gradually with the input power. However, similarly to the power transfer efficiency η_w, R'_p starts levelling off at around 20 W at a value of about 0.4 Ω. Once R'_p becomes constant, as the input power (or the coil current) is increased further, the power transfer efficiency will not change because $\eta_w \approx 1/(R'_0/R'_p + 1)$, where the thruster's resistance without plasma R'_0 is about constant as well. To change R'_p, the propellant flow rate would have to be increased.

Next, Figure 4.7(a) illustrates that the field coupling efficiency k_f is only around 0.35, which is indicative of a loosely coupled air core transformer. Therefore, this confirms the
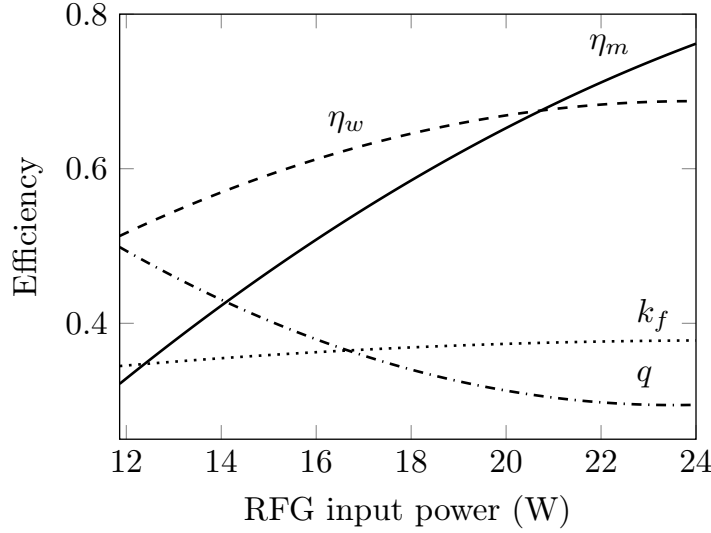
(a) Efficiency parameters.
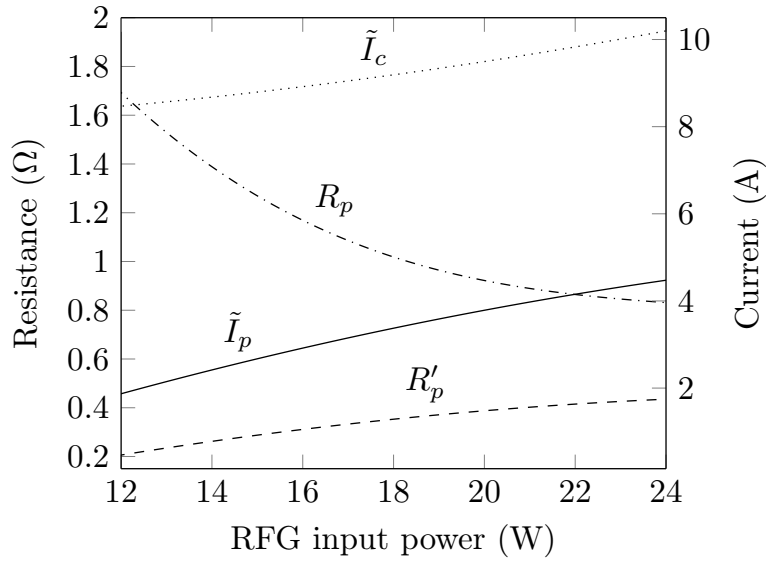
(b) Electrical parameters.

Figure 4.7: Modelled RIT 3.5 thruster electrical (resistance R, current I) and performance (coupling coefficient k_f, power transfer efficiency η_w, mass utilisation efficiency η_m and normalized Q factor q) parameters as a function of the RFG input power for 0.5 sccm and $U_{scrn} = 1$ kV.

discussion from the previous section which concluded that the RIT 3.5 thruster should have the coupling efficiency of about 0.4 while operating. As Figure 4.7(a) indicates, the coupling efficiency increases only slightly for a constant propellant flow rate. To increase the coupling coefficient more, the mass flow rate should be increased as well or the discharge chamber and coil geometries changed. Figure 4.7(a) also displays the Q-factor normalised by 100, which is referred to as q. The q factor keeps decreasing from about 0.5 at 12 W to around 0.25 at 24 W. Since the q factor strongly depends on the thruster's inductance L_{thr}, it can be thought of as an indication of the coupling between

the coil and the plasma. Therefore, the larger the decrease in the thruster's q factor is, the bigger the effect the plasma has on the coil, or the better the coupling is. This happens because the current induced in the plasma generates an opposing magnetic field that tries to cancel the coil's magnetic field and therefore L_{thr} goes down.

However, the mass utilisation efficiency η_m does not plateau as the previous parameters and keeps increasing past 20 W, as shown in Figure 4.7(a). Therefore, an optimisation analysis has to be performed between the mass utilisation efficiency, power transfer efficiency and coil current. The goal is to produce the highest possible beam current with the smallest possible amount of input power for a given mass flow rate. Furthermore, Figure 4.7(b) shows that the plasma resistance R_p keeps sharply decreasing down to around 0.9 Ω at 20 W of input power and then starts to plateau. In contrast, the plasma current $\tilde{I}_p$ increases up to 4 A at around 22 W of input power, before starting to level off. The reduction in the plasma resistance R_p and increase in the plasma current $\tilde{I}_p$ are due to the rise in the ion density with the input power. Finally, it can be observed that the coil current $\tilde{I}_c$ increases constantly to around 10 A at 24 W of input power.

4.2.3   Plasma properties

To explain the trends displayed in the previous section, the plasma behaviour, as expressed in various plots in Figure 4.8, has to be analysed. Figure 4.8(a) shows that as the input power goes up, the ion density n_i increases until it plateaus at around 3×10^{17} 1/m^3 at 20 W of RFG input power. Also, the neutral density n_0 decreases at a constant rate to about 1×10^{19} 1/m^3 at 20 W. The decrease in n_0 is due to the following reasons. First, as can be seen from Equation 3.6, the neutral mass flow rate leaving the system $\dot{m}_{out}$ decreases as the beam current, which is directly proportional to the ion current, increases. As a consequence, the pressure goes down, as can be seen in Figure 4.8(b). For instance, the pressure decreases from about 1.6 to 0.5 mTorr as the RFG input power increases from approximately 11 to 25 W. The decrease in pressure causes the neutral density to go down as well.

Figure 4.8(d) displays that the real σ_r and imaginary σ_i parts of the plasma conductivity follow the ion density trend and level off at around 20 W. The real part of the plasma conductivity reaches about 180 S/m, while the imaginary part goes down to about -80 S/m at 25 W. Therefore, parameters in Figure 4.7 level off at around 20 W because the plasma conductivity plateaus at this power. The ion density itself levels off due to the fact that as the RFG input power increases, the neutral gas pressure p decreases, as seen in Figure 4.8(b). The decrease in pressure results in an exponentially increasing electron temperature T_e. Figure 4.8(b) shows that the electron temperature T_e increases from about 4 to 6.5 eV as the RFG input power increases from about 11 to 25 W. Consequently, the power losses to the boundaries increase dramatically, which, for a given input power, affects the ion density.
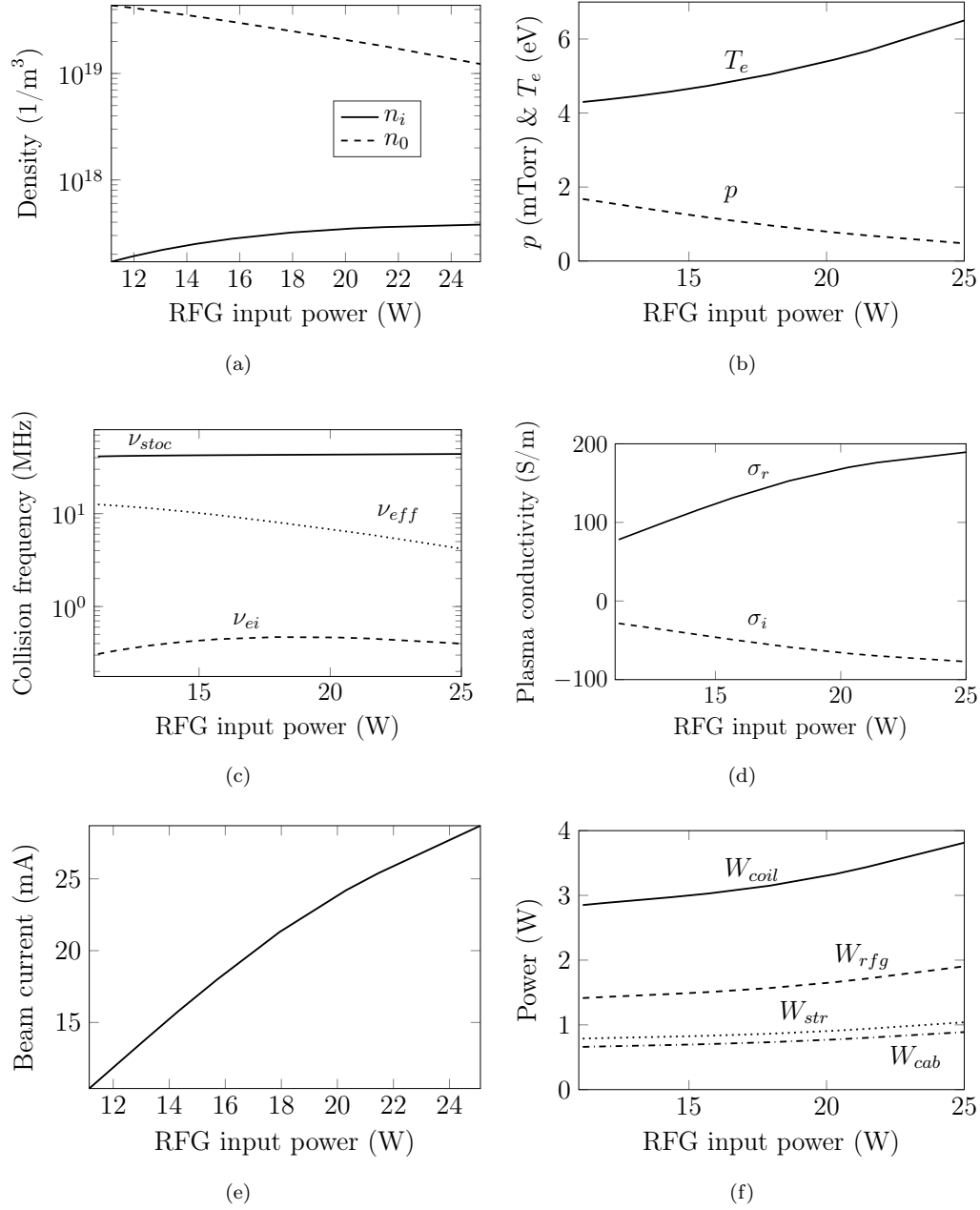
Figure 4.8: Modelled RIT 3.5 plasma properties, beam current and power losses as functions of the RFG input power for a constant 0.5 sccm flow rate. In the simulations, the screen grid voltage $U_{scrn} = 1$ kV.

However, Figure 4.8(e) indicates that the extracted beam current still keeps increasing past 20 W, even though the ion density has plateaued. This is due to the fact that the extracted beam current is also proportional to the Bohm velocity which, in turn, is proportional to the electron temperature T_e (rising exponentially). In order to better quantify the power loss distribution within the thruster, Figure 4.8(f) shows the magnitude of the RFG input power that is not transferred to the plasma but is lost to the coil W_{coil}, the RFG W_{rfg}, the thruster's structure W_{str} and the coaxial cable W_{cab}. It can be seen that the majority of the power is lost in the coil, which is about 3 W at 20 W of the

RFG input power. There is also up to 2 W of power lost in the RFG. The cable's and thruster's structure losses contribute to about 0.8 W each. Figure 4.8(c) plots the three main collision frequency variations with the RFG input power. As can be seen from Figure 4.8(c), the electron-ion collision frequency ν_{ei} is nearly negligible, equalling to around 0.8 MHz. The electron-neutral effective collision frequency ν_{eff} goes down from around 10 to 4 MHz mainly because of the decrease in the neural gas pressure, as was shown in Figure 4.8(b). Finally, the majority of the heating comes from the stochastic processes expressed through a nearly constant stochastic collision frequency ν_{stoc} equal to about 40 MHz.

4.3   Ion optics

The RIT 3.5 ion optics system was simulated using IBSIMU for different beamlet currents, as displayed in Figure 4.9. Figure 4.9(a) and Figure 4.9(b) show two examples of the under-perveance conditions. When the under-perveance occurs, the sheath is curved too much because the ion current is too low for the applied screen voltage, or the screen voltage is too high for the extracted ion current (Farnell, 2007; Goebel and Katz, 2008). Therefore, the ions are over-focused and directly intercept the accel or decel grids. Such a condition cannot be sustained because it will lead to a rapid grid erosion (Goebel and Katz, 2008). Figure 4.9(c) and Figure 4.9(d) illustrate the optimal perveance conditions. As can be observed from the figures, under these conditions the beam divergence is low and the ions are well focused (Farnell, 2007; Goebel and Katz, 2008), meaning that the accel and decel grids are not hit by the ions. This is an optimum condition in which thrusters normally aim to operate. However, the optimum-perveance condition might be hard to sustain over a wide range of operating conditions due to changing screen grid voltage and ion density. Therefore, the grid behaviour must be analysed at each thrust point either experimentally or by modelling.

Finally, Figure 4.9(e) and Figure 4.9(f) depict the over-perveance conditions. At the over-perveance condition, the sheath is nearly flat because the ion current is too high for the applied screen voltage, or the screen voltage is too low for the extracted ion current (Farnell, 2007; Goebel and Katz, 2008). As a result, the focusing is negligible and ions directly impinge on the accel grid. This condition also has to be avoided if the grid lifetime is to be increased. Figure 4.9 also shows the effective ion optics transparency parameter T_{eff}. As can be seen from Figure 4.9, T_{eff} increases from 0.7 to 0.74 as the beamlet current goes up from 22 μA to 110 μA. However, as the beamlet current is increased further to 310 μA, T_{eff} drops to 0.53, which is indicative of a poor focusing efficiency. Note that the variation in the T_{eff} parameter is directly influenced by the change in the sheath shape caused by a combination of the beamlet current and screen voltage, as mentioned above.

(a) Beamlet current = 22 μA; $T_{eff} = 0.7$.

(b) Beamlet current = 110 μA; $T_{eff} = 0.74$.

(c) Beamlet current = 166 μA; $T_{eff} = 0.7$.

(d) Beamlet current = 221 μA; $T_{eff} = 0.66$.

(e) Beamlet current = 277 μA; $T_{eff} = 0.65$.

(f) Beamlet current = 310 μA; $T_{eff} = 0.53$.
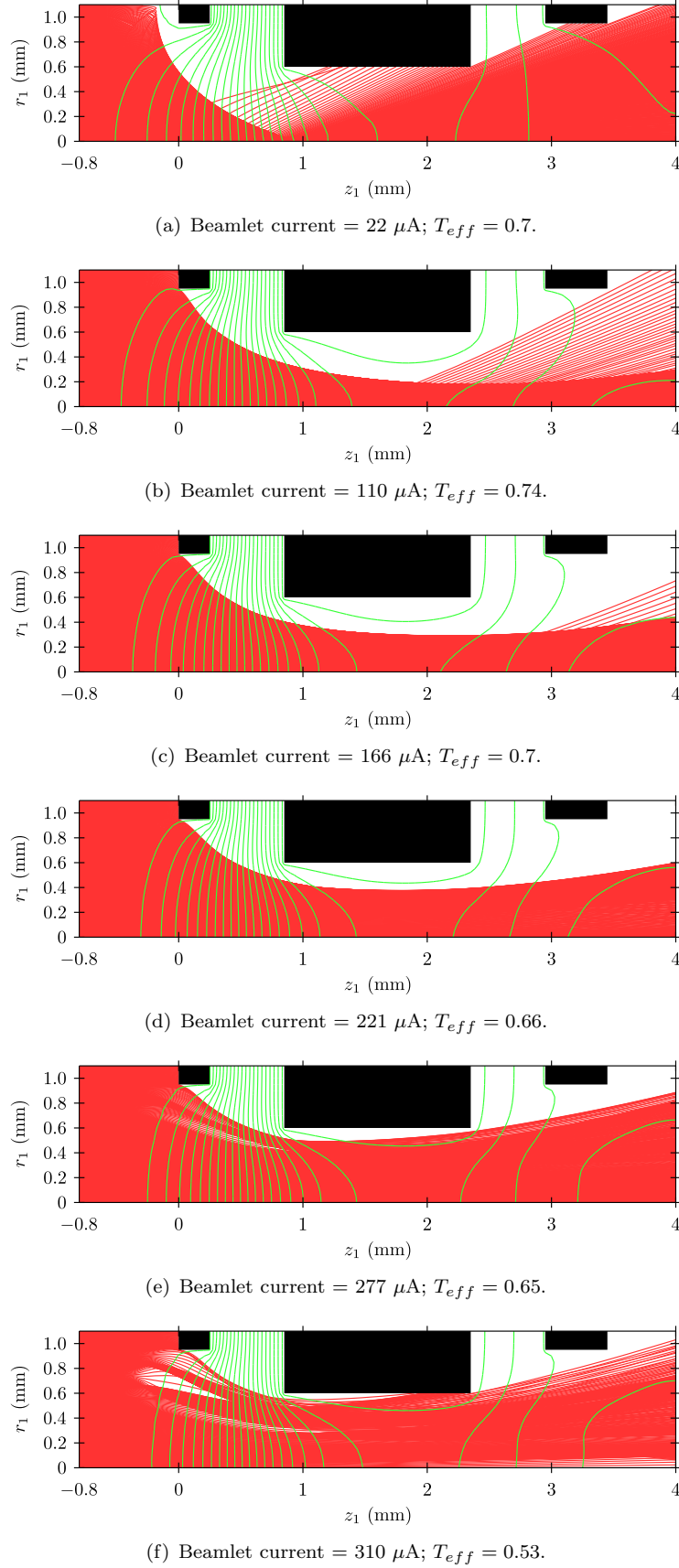
Figure 4.9: Ion trajectories as modelled by IBSIMU for the RIT 3.5 ion optics system for different beamlet currents: (a)-(b) under-perveance, (c)-(d) optimal perveance and (e)-(f) over-perveance; red - ion trajectories, black - grids, green - equipotential lines.

4.4 Electromagnetic fields

Figure 4.10(a) highlights the power transfer mechanism itself inside the RIT 3.5 thruster's plasma. In particular, Figure 4.10(c) depicts how the h parameter, or the plasma density distribution, affects the power absorption W. Note that the plots in Figure 4.10(c) and Figure 4.10(d) were produced by making radial section cuts through the discharge chamber's volume, as indicated by the dashed lines in Figure 4.10(a) and Figure 4.10(b). Figure 4.10(c) shows that a majority of the plasma heating occurs around 2 mm away from the wall in the vicinity of the plasma pre-sheath where the plasma density is around 60% of that in the centre. This occurs due to the two following factors. First, at 2 mm from the wall, the plasma density is about 25% higher than that at the wall. Second, as indicated in Figure 4.10(b) and Figure 4.10(d), the electric field E at this location is about 80% of the initial value. Furthermore, Figure 4.10(d) and Figure 4.10(b) depict that away from the wall, the electric field E drops from 200 V/m in almost a linear fashion to nearly 0 V/m at the centre. Such a linear trend is indicative of an electric field decay in a vacuum due to low ion densities and the small dimensions encountered in the RIT 3.5 thruster (Chabert and Braithwaite, 2011). As a result, the electric field skin depth δ_E is about 10 mm (60% of the chamber radius), as given in Figure 4.10(d). Therefore, the power transfer is nearly negligible further away than the skin depth.

(a) Normalised power absorption.

(b) Absolute electric field.

(c) Normalised plasma power absorption W and ion density distribution h.

(d) Magnetic field B and electric field E.
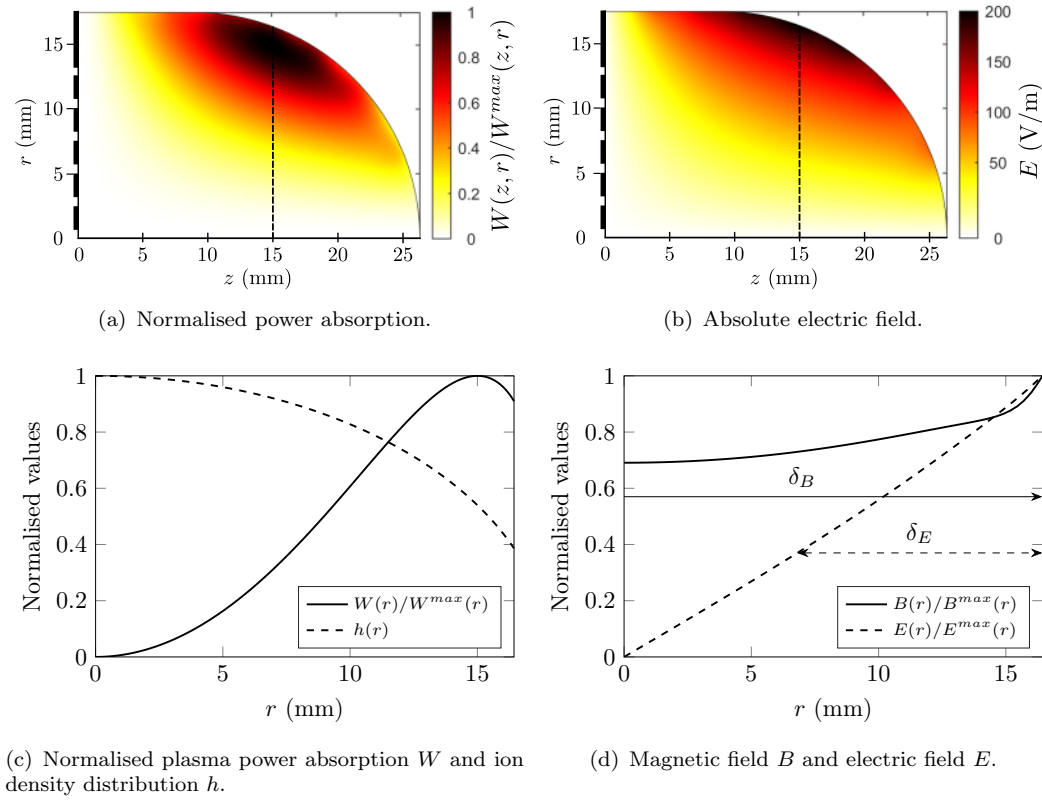
Figure 4.10: Modelled electromagnetic field behaviour inside the RIT 3.5 plasma at 2 mN of thrust.

Furthermore, as shown in Figure 4.10(d), the magnetic field B is about 75% of the magnetic field value near the wall throughout a majority of the plasma volume. Therefore, the magnetic field skin depth δ_B is much larger than the discharge chamber radius. Finally, due to the end coil effects, a majority of the power is transferred towards the middle of the discharge chamber's length (z-axis), as depicted in Figure 4.10(a). In Figure 4.11, the power absorption mechanism is also illustrated in three dimensions at different planes distributed throughout the length of the discharge chamber. Figure 4.11 confirms that most of the power is absorbed in the middle of the discharge chamber's length ($z \approx 10 - 20$ mm) due to the end coil effects. Near the plasma centre and axial discharge chamber edges, there is virtually no power absorption from the coil, which is indicated by the dark regions in the plots. Furthermore, Figure 4.11 shows that the induced current density vectors are directed azimuthally and follow the power absorption trend, with the highest current density present in the middle of the plasma, next to the coil. Also, as discussed above, the current density is nearly zero at the centre.
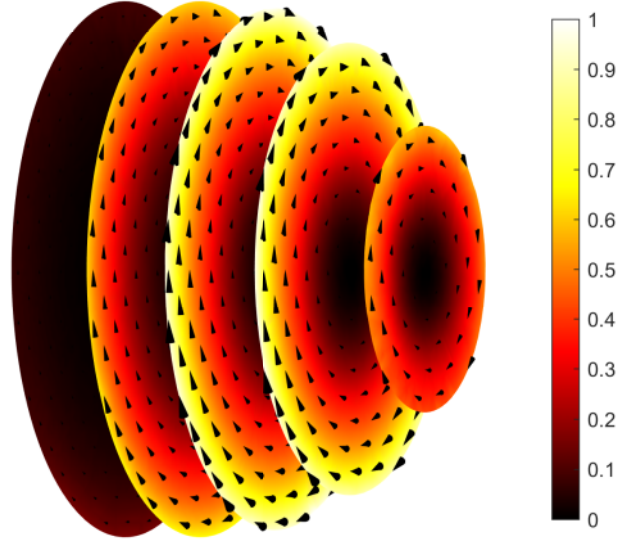
Figure 4.11: Normalised power absorption magnitude and the vectorial induced current density distribution inside the RIT 3.5 plasma at 2 mN of thrust.

4.5 Thermal behaviour

4.5.1 Temperature distribution without plasma

First, to validate the thermal model, the thruster's temperatures without the plasma present (i.e. only with the RF eddy current heating) were simulated, as can be seen in Table 4.2. This allowed to check that the thermal resistances, thermal conductances, surface emissivities and boundary conditions are correct, without the possibility of having an incorrect plasma model. Also, note that in this section, a new power transfer efficiency parameter is defined as $\eta_w' = P_{thr}/P_{in}$. It indicates the percentage of the

RFG input power P_{in} transferred to the thruster P_{thr}. Such a definition is necessary, since the previously defined power transfer efficiency η_w would be zero when there is no plasma. As observed in Table 4.2, around 77% of the total input power to the RFG P_{in} goes to the coil (W_{coil}), while approximately 20% is lost to the screen (W_{scrn}) and 3% to the case (W_{case}). Table 4.2 also indicates that only around 68% of the total RFG input power P_{in} reaches the thruster (P_{thr}), as given by the power transfer efficiency η'_w. Table 4.2 depicts that the power transfer coefficient η'_w is about constant, regardless of the input power, because when there is no plasma, the total thruster resistance stays about constant as well. Note that the rest of the input power ($\approx 30\%$) is lost due to Ohmic losses inside the coaxial cable and the RFG itself.

P_{in} (W)	18.0	16.0	14.0	12.0	10.0	8.0	7.0
W_{coil} (W)	9.5	8.5	7.4	6.4	5.4	4.3	3.7
W_{scrn} (W)	2.3	2.0	1.7	1.5	1.3	1.0	0.9
W_{case} (W)	0.35	0.3	0.26	0.22	0.19	0.15	0.13
P_{thr} (W)	12.2	10.8	9.4	8.1	6.9	5.45	4.7
η'_w (%)	68.0	68.0	67.0	68.0	69.0	68.0	67.0

Table 4.2: RF heating magnitudes for different RFG input power values without the plasma, as simulated for the RIT 3.5 thruster.

Having obtained the RF heating values, thermal simulations were performed in order to determine the TS1 to TS8 sensor temperatures. In Table 4.3, the modelled sensor temperatures for different RFG input powers are compared against the experimental RIT 3.5 data without the plasma. The experimental temperature values were recorded after leaving the thruster to run for about one hour in steady-state conditions at a set thrust point. It was deemed that the temperatures had reached equilibrium when the temperature trends vs time would level off and would not change by more than ± 0.2 ℃. Remember that the detailed discussion regarding the locations of the temperature sensors and the way the temperatures were measured will be presented in Chapter 6.

P_{in} (W)	18.0		16.0		14.0		12.0		10.0		8.0		7.0	
	Mod.	Exp.	Mod.	Exp.	Mod.	Exp.	Mod.	Exp.	Mod.	Exp.	Mod.	Exp.	Mod.	Exp.
T_1 (℃)	66	71	58	66	53	60	50	55	46	49	40	43	39	41
T_2 (℃)	71	74	62	69	58	63	54	56	48	50	42	45	40	42
T_3 (℃)	59	65	54	61	51	56	45	50	42	45	37	41	33	38
T_4 (℃)	58	58	67	54	45	49	46	45	42	40	38	36	36	34
T_5 (℃)	79	80	71	74	60	67	58	60	51	53	45	47	41	44
T_6 (℃)	106	113	94	104	83	93	76	83	68	72	57	62	51	57
T_7 (℃)	38	42	43	40	40	37	32	34	30	31	28	30	28	29
T_8 (℃)	43	41	38	39	36	36	36	34	33	31	30	29	30	28

Table 4.3: Modelled vs experimental RIT 3.5 thruster's temperature distribution for various RFG input powers without plasma.

Table 4.3 shows that the agreement between the experimental results and the model is satisfactory, the largest discrepancies are observed in the temperatures measured on the C_1 capacitor by the sensor TS6, reaching up to 10%. To better understand the overall temperature distribution and to check the accuracy of the model, a 3D surface temperature plot was produced, as shown in Figure 4.12.
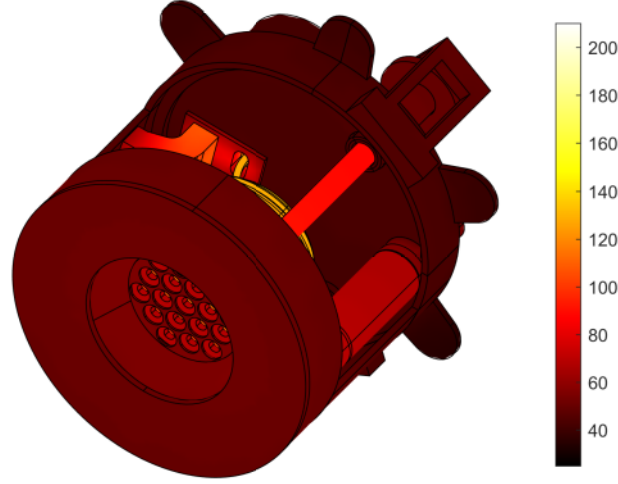
Figure 4.12: Modelled RIT 3.5 thruster's surface temperature distribution for an RFG input power of 18 W without plasma. Temperatures are in °C.

4.5.2   Temperature distribution with plasma

Based on the percentage deviations in both the predicted thruster's performance parameters and temperatures, it was assumed that the model is accurate enough to perform thermal simulations of the thruster with the plasma present. First, based on the screen voltage U_{scrn} and extracted beam current I_b, the RF heating W and plasma heating P values for different throttle points were estimated, as shown in Table 4.4. Table 4.4 indicates the total power absorbed by the plasma P_d and the amount of this power lost to the discharge chamber walls P_c, screen P_s, accel grid P_a and beam P_b, as was shown in Section 3.5.4. Similarly, Table 4.4 shows the total power loss due to the eddy current RF heating W_{tot} and the amount of this power lost to the screen W_{scrn}, coil W_{coil} and case W_{case}. Combining these power losses, the power that is lost in the thruster altogether P_{thr} is estimated. Then, by adding losses in the RFG itself and the coaxial cable, the total RFG input power to the thruster P_{in} is determined, which allows the power transfer efficiencies η_w and η_w' to be calculated.

From Table 4.4, it can be observed that when the plasma is present, the power transfer efficiency η_w' is much higher compared to the case without the plasma. This happens because the presence of plasma dramatically increases the total thruster's resistance since there is an additional reflected plasma resistance R_p' component. However, η_w is lower than η_w', which means that not all power that reaches the thruster goes into the

P_{in} (W)	29.7	29.4	28.5	22.1	15.0	9.4	7.5
U_{scrn} (V)	1625	1500	1350	1000	1200	1000	262
I_b (mA)	38.0	31.6	26.6	19.3	13.2	4.8	1.85
P_c (W)	14.2	13.2	12.2	8.5	4.9	1.9	1.0
P_s (W)	3.2	3.1	2.9	1.95	1.1	0.42	0.26
P_a (W)	0.47	0.35	0.3	0.22	0.14	0.05	0.03
P_b (W)	1.54	1.43	1.25	0.95	0.59	0.2	0.07
P_d (W)	19.4	18.1	16.6	11.7	6.7	2.5	1.4
W_{coil} (W)	5.0	5.4	5.6	4.1	3.9	3.2	2.9
W_{scrn} (W)	1.2	1.3	1.35	1.1	0.9	0.77	0.69
W_{case} (W)	0.16	0.17	0.17	0.14	0.12	0.1	0.09
W_{tot} (W)	6.36	6.87	7.12	5.22	4.92	4.07	3.68
P_{thr} (W)	25.7	24.9	23.7	16.9	11.7	6.6	5.1
η'_w (%)	87.0	85.0	83.0	77.0	78.0	70.0	68.0
η_w (%)	65.0	62.0	58.0	53.0	45.0	26.0	19.0

Table 4.4: Plasma P and RF heating W magnitudes for different throttle points based on the screen voltage U_{scrn} and beam current I_b, as simulated for the RIT 3.5 thruster.

plasma. Rather, some of the power is lost in the thruster's components. Furthermore, the power transfer efficiency η'_w goes up as the RFG input power increases, reaching 87% at around 30 W. This happens mainly due to a rise in the plasma's density and electron temperature, which increase the reflected plasma resistance R'_p. As the power is decreased, the plasma density goes down as well. Therefore, the power transfer efficiency η'_w decreases to 68%, which is the same as in the case where there was no plasma at all, as was shown in Table 4.2. Therefore, as far as the RFG operation is concerned, a low-density plasma acts just as a vacuum. Similarly, the power transfer efficiency η_w goes up from 19% to 65% as the input power increases from 7.5 W to 29.7 W.

P_{in} (W)	29.7		29.4		28.5		22.1		15.0		9.4		7.5	
U_{scrn} (V)	1625		1500		1350		1000		1200		1000		262	
I_b (mA)	38		31.6		26.6		19.3		13.2		4.8		1.85	
	Mod.	Exp.	Mod.	Exp.	Mod.	Exp.	Mod.	Exp.	Mod.	Exp.	Mod.	Exp.	Mod.	Exp.
T_1 (°C)	111	113	108	108	104	104	82	88	66	76	49	57	46	54
T_2 (°C)	120	120	117	115	112	111	90	92	70	79	51	58	48	55
T_3 (°C)	90	93	88	89	85	86	68	73	57	64	42	49	42	48
T_4 (°C)	86	86	84	83	82	80	66	66	55	58	41	45	41	44
T_5 (°C)	112	117	110	113	108	110	88	92	72	79	53	59	50	55
T_6 (°C)	142	151	140	147	135	144	112	122	90	104	66	77	62	72
T_7 (°C)	53	58	53	56	51	55	42	47	37	43	31	36	31	36
T_8 (°C)	63	58	63	55	60	55	49	47	42	43	34	36	34	36

Table 4.5: Modelled vs experimental RIT 3.5 thruster's temperature distribution for different throttle points.

Table 4.5 gives the temperature distribution based on the throttle points from Table 4.4. If the first throttle point given as $U_{scrn} = 1,625$ V and $I_b = 38$ mA is taken, it can be seen that the discrepancy between the modelled and measured temperatures for the TS6 sensor is still the same 6% as was observed in the case without the plasma. This is very important, not only because it confirms that the thermal model is correct, but also that the plasma model is correct as well. If the plasma model was incorrect, the simulated temperatures would not correspond to the measured ones due to the wrong plasma heating values. Therefore, the thermal model can also be used to check the accuracy of the plasma model. By analysing the rest of the data from Table 4.5, it can be observed that the maximum error does not go above 14%, with a majority of the predicted temperature values falling within 10% of the measurements. What is more, a 3D surface temperature distribution for the $U_{scrn} = 1,625$ V and $I_b = 38$ mA throttle point is shown in Figure 4.13. As Figure 4.13 indicates, the temperatures are much higher than in the case without the plasma. For instance, with the plasma present, the coil temperature reaches more than 200 ℃, which is an increase of about 50% compared to the case without the plasma. This makes the coil the hottest component in the thruster. Furthermore, the matching capacitors reach about 140 ℃, which is within their operational range. The screen and accel grids reach temperatures of about 120 ℃.
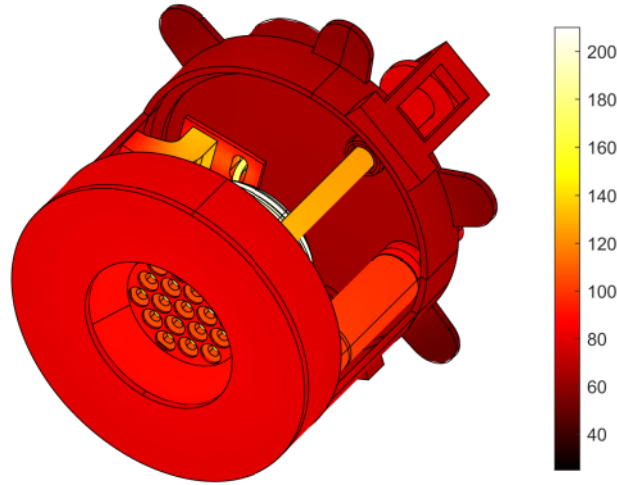
Figure 4.13: Modelled RIT 3.5 thruster's surface temperature distribution for the $U_{scrn} = 1,625$ V and $I_b = 38$ mA throttle point. Temperatures are in ℃.

4.5.3   Temperature effect on performance

To better understand how the thruster's temperatures affect the plasma properties and performance, a case was analysed where the input mass flow rate $\dot{m}_{in}$ was set as a constant and the RFG input power was varied. Note that varying the input power changes the ion density and in turn alters the mass utilisation efficiency η_m through the beam current I_b, as defined in the equation $\eta_m = (I_b g_0)/\dot{m}_{in}$. Figure 4.14 shows how the coil T_{coil}, discharge chamber wall T_w, screen grid T_{scrn} and case T_{case} temperatures vary with

the mass utilisation efficiency. As Figure 4.14 depicts, the coil and discharge chamber temperatures are very similar to each other, with only a few percent difference. Furthermore, as the mass utilisation efficiency increases, the screen grid temperature changes from being about 8% lower to 20% lower than the chamber wall temperature. Finally, Figure 4.14 illustrates that the case temperature is just above the room temperature.
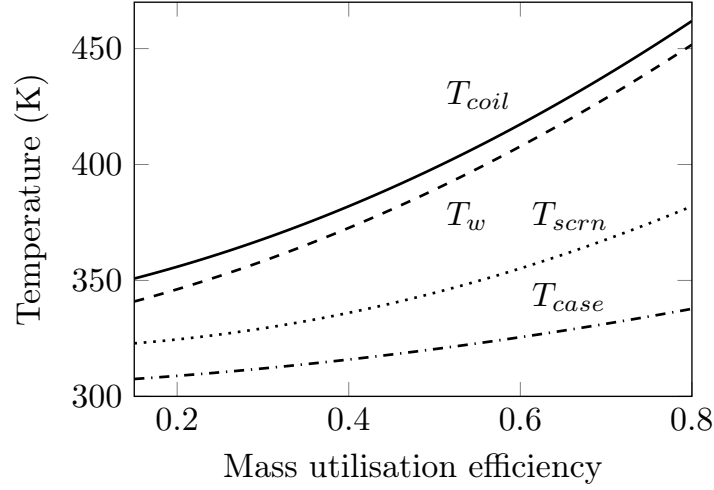
Figure 4.14: RIT 3.5 thruster's temperature distribution for different mass utilisation efficiency values η_m for a constant mass flow rate of 0.5 sccm.

The thruster's performance was investigated further by plotting the RFG input power variation with the mass utilisation efficiency. This was done for three different cases. As depicted in Figure 4.15, Case I represents a situation in which the thruster's temperatures are consistent with the plasma parameters and the RF heating, which is what actually occurs in the real-life situations. Case II represents a condition where the plasma parameters are consistent with the thruster's temperatures, but the RF heating is not. Finally, Case III simulates a situation in which the thruster's temperatures are set constant and not consistent with neither the plasma parameters nor the RF heating. Case III is commonly used when analysing RF thrusters, where the discharge chamber wall temperature is set to a constant predefined value, which is usually around 400 K (Chabert et al., 2012; Goebel, 2008). Therefore, in Case III, the wall temperature of the thruster was set to 400 K as well.

As can be seen from Figure 4.15, at low mass utilisation efficiencies, Case III results in the RFG input power that is $3 - 4\%$ larger compared to the other cases. This is because Case III over-estimates the thruster's temperatures, mainly due to higher eddy current losses. As the mass utilisation efficiency of around 0.5 is approached, all three cases merge. This occurs due to the fact that the thruster's temperatures are approximately equal to the constant temperatures that were set. However, as the mass utilisation efficiencies of 0.7 and 0.8 are approached, the discrepancies between the cases increase. In particular, Case III under-estimates the RFG input power compared to Case I by up to 10%, which is approximately a $2 - 3$ W difference. Note that the thruster's

temperatures affect not only the eddy current heating. The thruster's temperatures also impact the plasma properties through the discharge chamber wall temperature, which influences the neutral gas pressure, as will be shown in the following section.
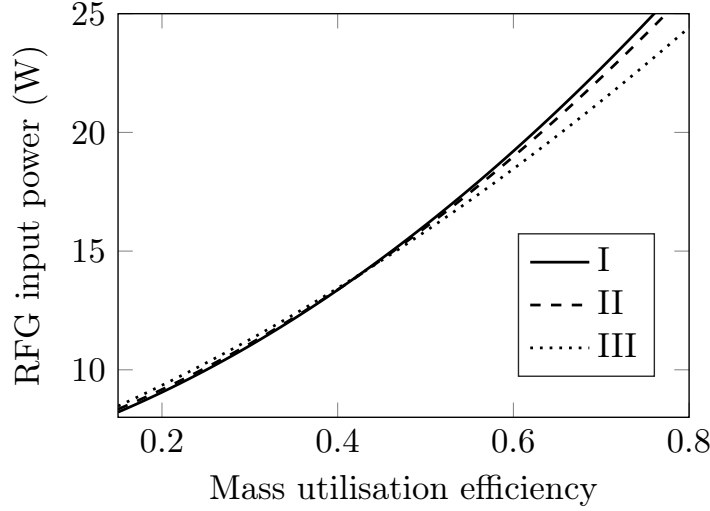
Figure 4.15: RFG input power variation with the mass utilisation efficiency for three different thruster's temperatures - plasma properties - RF heating coupling cases, as simulated for the RIT 3.5 thruster.

4.5.4   Temperature effect on plasma properties

To finish off the discussion about the temperature effects on the plasma properties and thruster's performance, the following hypothetical situation is analysed. First, the extracted beam current I_b is set to 20.3 mA and the mass flow rate $\dot{m}_{in}$ is set to 0.5 sccm. Both these parameters are assumed to be constant. Then, it is supposed that the thruster starts heating up, which could be due to a neutraliser starting to operate or due to a change in the thermal load from the spacecraft. This could also happen because the thruster is exposed to different heat fluxes from the environment when, for instance, the thruster starts facing the Sun side. It could also simply mean a modification in the thruster's design, causing the temperatures to change. The goal of this analysis is to see how the thruster's temperatures affect the plasma parameters and the performance. The results of the analysis are plotted in Figure 4.16. All the plots are done against the discharge chamber wall temperature T_w, but it should be noted that all thruster's temperatures change.

First, Figure 4.16(a) shows that as the temperatures increase, the neutral gas density n_0 decreases following an inversely proportional relationship given as $n_0 \propto 1/T_w$. In contrast, Figure 4.16(b) depicts that the electron temperature goes up in a linear fashion. Remember that the electron temperature is inversely proportional to the neutral gas pressure. The ion density, on the other hand, decreases linearly since a rise in the electron temperature results in an increase in the Bohm velocity, as can be seen from

Figure 4.16(c). Therefore, a lower ion density is needed to achieve a set beam current. Figure 4.16(d) illustrates that the reflected thruster's structural resistance R'_0, which is the thruster's resistance excluding the plasma's resistance, increases nearly linearly with the temperatures due to an increase in the thruster's component electrical conductivities. However, the reflected plasma resistance R'_p actually goes down since the plasma's electrical conductivity decreases due to the decreasing ion density.
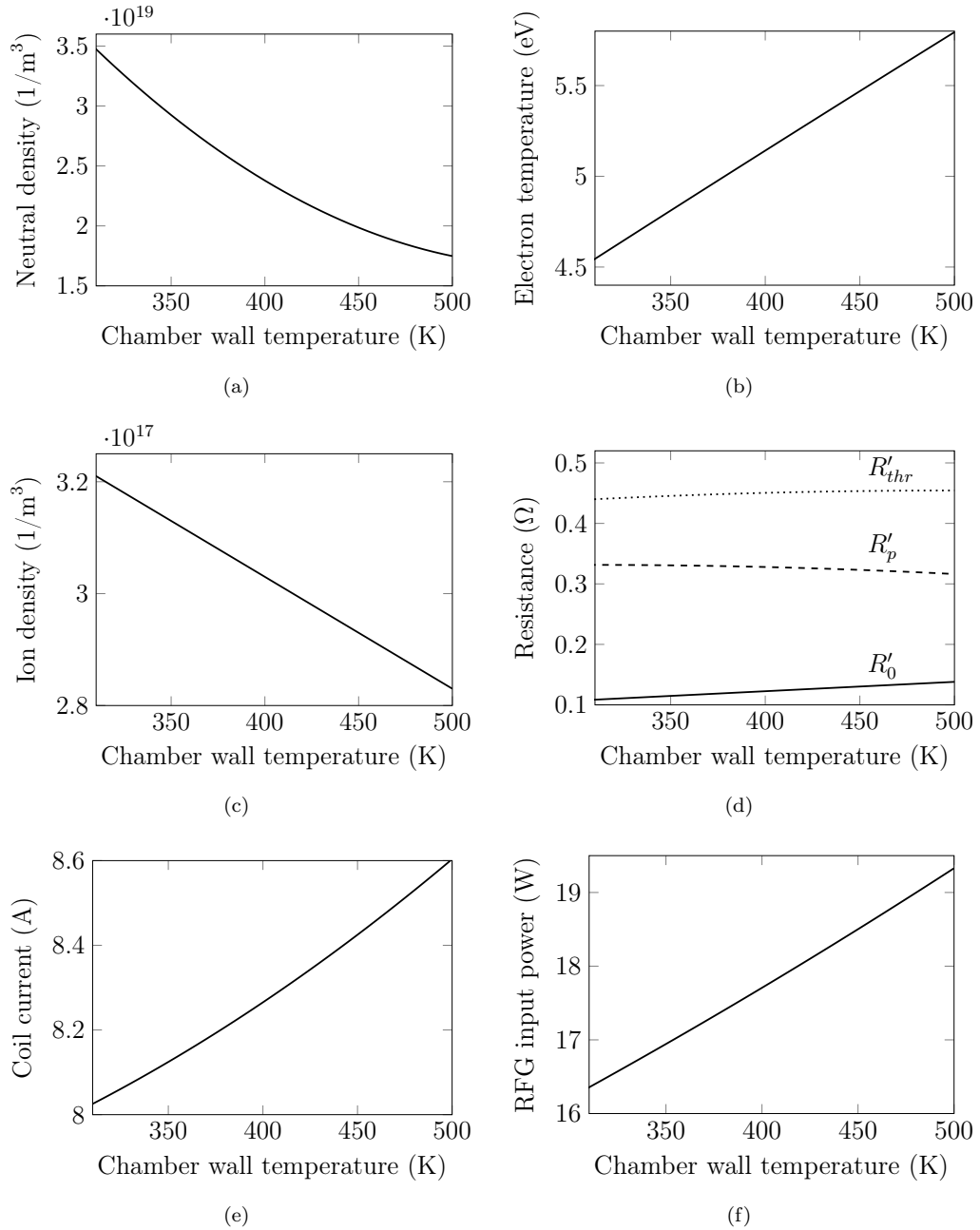
Figure 4.16: Simulated RIT 3.5 thruster's plasma properties as functions of the discharge chamber wall temperature for a constant mass flow rate of 0.5 sccm and a beam current of 20.3 mA.

Therefore, due to the combination of these effects, the total reflected thruster's resistance R'_{thr} goes up slightly. As shown in Figure 4.16(e), the coil current increases quite sharply because of two factors. First, due to an increasing electron temperature, there are higher boundary losses incurred, requiring more power (proportional to the coil current) to be transferred to the plasma. Second, due to the decrease in the plasma's electrical conductivity, a higher coil current is required to transfer the same amount of power to the plasma. Finally, due to the increase in both the coil current and thruster's resistance, the RFG input power goes up by about 20% when the wall temperature changes from 310 K to 480 K, as can be observed in Figure 4.16(f). Therefore, to increase the thruster's performance, it is beneficial to run the thruster at the lowest temperatures possible.

4.5.5   3D thermal plots

Figure 4.17 displays various 3D temperature distribution plots as obtained by simulating the RIT 3.5 thruster. As can be seen in Figure 4.17(a), the maximum temperature reached by the coil is about 200 ℃. The temperature of the discharge chamber is very close to that of the coil as well due to a strong thermal contact between the coil and discharge chamber surfaces. Since the coil supporting structures are electrical insulators, they also have a very low thermal conductivity and thus reach temperatures of only about 100 ℃. Additionally, the coil supporting structures are connected to cold surfaces such as the case or the back plate. As depicted in Figure 4.17(b), each grid has a distinctively different temperature. The screen grid is the hottest at about 140 ℃, the accel grid is at about 100 ℃ and the decel grid is at about 70 ℃. This difference between the grid temperatures is caused by the ceramic grid spacers being inserted between the grids, which have poor thermal conductivities. Additionally, each grid is being exposed to the different levels of plasma heating and environmental cooling. For instance, the decel is exposed to the vacuum and thus can radiate a lot of heat. The screen grid, however, absorbs a substantial amount of heat from the plasma, and is not able to radiate the heat easily to the environment. It has to be mentioned that since the grids experience dissimilar temperatures, they expand differently as well. This can cause alignment problems, and can also result in grids being shorted out.

As mentioned above, the grid spacers have poor thermal conductivities because they are manufactured out of Al2O2 (alumina oxide). Therefore, as Figure 4.17(c) depicts, their temperature varies from about 70 ℃ to 130 ℃. The fact that the some of the grid spacers are directly in contact with the discharge chamber (hot) and others are in contact with the case (cold) plays a significant role as well. Figure 4.17(d) displays the back plate side that is exposed to the vacuum. As can be observed in Figure 4.17(d), the back plate is at about 50 ℃, which is much cooler than other thruster's components. This is due to a few reasons. First, the back plate is exposed directly to the vacuum. Second, the back plate is attached to the case, which in turn is secured to the vacuum facility that

(a) Coil and chamber.

(b) Ion optics system.

(c) Grid spacers (isolators).

(d) Back plate view I.

(e) Back plate view II.

(f) Electrical contact shielding and gas inlet.
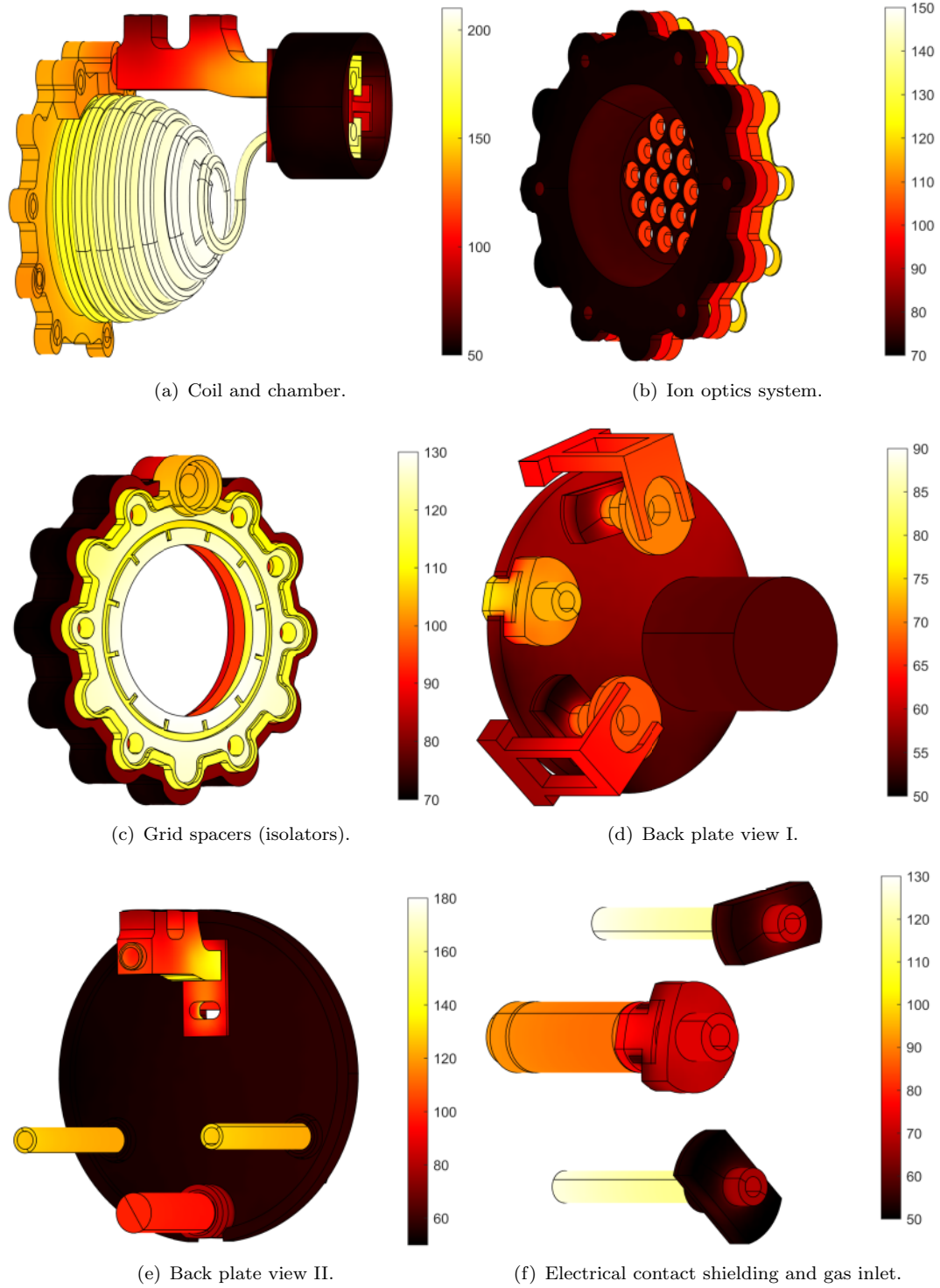
Figure 4.17: Thermal plots (in °C) of various RIT 3.5 thruster's components/parts and assemblies as obtained by simulating the thruster at 2 mN thrust point.

is at the room temperature. The electrical contacts and the gas inlet that are connected to the back plate are at roughly 100 °C, as shown in Figure 4.17(e) and Figure 4.17(f). There is such a big difference in the temperatures because the electrical contacts and

the gas inlet are isolated from the case by low thermal conductivity parts. In addition, as can be seen in Figure 4.17(e), the coil holder is at a temperature approximately 50 ℃ higher compared to the inner part of the back plate.

4.6   Summary

The RF ion thruster model developed in Chapter 3 has been successfully validated against the experimental RIT 3.5 data and the analytical model. It has been shown that there are substantial discrepancies between the analytical and the electromagnetic (COMSOL) models at low ion densities where the transformer assumptions do not apply. This is because the analytical model does not account for the skin, proximity and end coil effects. However, the discrepancies between the models decrease dramatically at high ion densities where the transformer assumptions fully apply. Also, the COMSOL model has shown that the RIT 3.5 thruster should have the coupling coefficient of about $0.3 - 0.5$ while operating. Normally, such a low coupling coefficient is attributed to a loosely coupled transformer behaviour. Furthermore, while comparing the RF ion thruster model to the RIT 3.5 experimental data, errors of up to 13% have been observed between the experimental and modelled RFG voltage and current values. Additionally, discrepancies in the modelled results while predicting the experimental trends have been shown to be below 6%.

It has been demonstrated that the model can predict the RIT 3.5 temperature distribution within an error of approximately 10%. After the model has been successfully validated, the performance parameters of the RIT 3.5 thruster have been simulated. Additionally, the ion optics focusing efficiency and thermal behaviour have been analysed. In particular, various 2D/3D plots have been produced to show how the ion optics performance and thruster's temperatures change as the RIT 3.5 is throttled. What is more, the electromagnetic field distribution inside the plasma has been plotted. In particular, the electromagnetic plots were used to indicate the points of maximum power absorption and the magnetic/electric field skin depths. Finally, it has been shown that the developed model is capable of determining various plasma parameters (ion density, neutral gas density/pressure, electron temperature, collision frequency), beam parameters (half-divergence beam angle, extracted beam current) and temperatures without the need of measuring them directly. Therefore, significant time and cost savings are possible using the model.

5

Investigation into a DST concept for IBS missions

As mentioned in Chapter 2, there are around 6,000 tonnes and 15,000 trackable debris objects in the orbit (Bombardelli and Pelaez, 2011b). The Ion Beam Shepherd (IBS) has been suggested as one of the possible methods to target the debris problem. As a result, the LEOSWEEP (Improving Low Earth Orbit Security with Enhanced Electric Propulsion) mission plans to use the IBS method to de-orbit a 1.5-ton launcher upper stage from a nearly polar low Earth orbit (LEO) (Ruiz et al., 2014). To successfully perform the mission, two thrusters are needed. In addition, the mission requires that the thrust delivered to the target is more than 30 mN and the total power of both thrusters is less than 3 kW (Cichocki et al., 2015). However, such a two-thruster design introduces a lot of complexity regarding the power and propellant management systems.

To help mitigate these issues associated with the two-thruster design, a novel ion thruster concept for the IBS type missions is presented in this chapter. This concept, instead of using two thrusters, requires only one thruster capable of generating two distinct ion beams for the impulse transfer (IT) and impulse compensation (IC) purposes. The advantage of such a design is that it potentially requires about two times less RF power than two single-ended thrusters. Additionally, it is expected that such a system would have a much simpler sub-system architecture, lower cost, and lower total mass. In the thesis, the concept thruster is referred to as the Double-Sided Thruster (DST). The

DST thruster has been designed and optimised using the RF gridded ion thruster model developed in Chapter 3 while keeping the LEOSWEEP mission concept requirements as constraints. Once designed, the DST was manufactured, assembled and tested. The discussion is started by a detailed investigation of the IBS type mission concept.

5.1 IBS mission concept

The IBS mission concept is depicted in Figure 5.1. As illustrated in Figure 5.1, the Impulse Transfer Thruster (ITT) produces a collimated quasi-neutral ion beam and generates the thrust F_{IT}. The target represents a piece of debris that is being bombarded by the high-velocity ions coming from the thruster positioned $10 - 20$ meters away. The ions impart their momentum, thus producing the force F_D on the debris. If enough momentum is transferred, the debris orbit would decrease until the debris burns in the Earth's atmosphere. Such a debris removal concept is often referred to as contactless since there is no direct contact between the debris and the shepherd satellite. Another option is to propel the debris to a graveyard orbit and thus reduce the risk of collision with operational satellites.
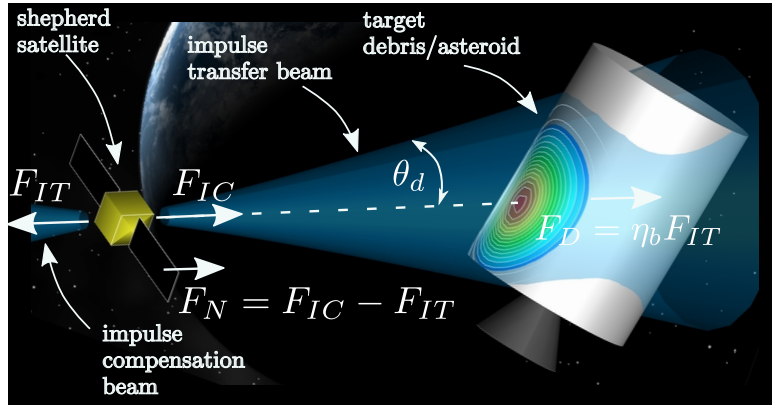
Figure 5.1: Schematic of the Ion Beam Shepherd (IBS) concept with the shepherd satellite, target debris object and the main mission parameters indicated.

Not all momentum generated by the ITT is transferred to the debris. The force transferred to the debris F_D can be expressed using the momentum transfer efficiency η_B (Bombardelli and Pelaez, 2011b)

$$F_D = \eta_B F_{IT}. \tag{5.1}$$

The momentum transfer efficiency η_B depends on the beam divergence half-angle θ_d, the target debris object size and the distance between the shepherd satellite and the target. However, note that there is also a second thruster called the Impulse Compensation Thruster (ICT) which is needed to offset the thrust produced by the ITT; in particular, the thrust difference F_N must be achieved to keep the satellite and debris in the same

orbit. If it is assumed that the shepherd satellite and the target debris object are in a circular orbit, the impulse compensation force F_{IC} that needs to be generated by the ICT is (Bombardelli and Pelaez, 2011b)

$$F_{IC} = \left[1 + \eta_B \frac{m_{IBS}}{m_{TG}}\right] F_{IT},$$ (5.2)

where m_{IBS} and m_{TG} are the shepherd satellite and target debris masses, respectively.

It can be shown that the minimum beam divergence half-angle θ_d^{min} achievable by an electric propulsion thruster strongly depends on the longitudinal ion velocity v_i (Reiser, 2008)

$$\theta_d^{min} = \tan^{-1}\left[\frac{\sqrt{2eT_i/M_i}}{v_i}\right],$$ (5.3)

where e is the electron charge, T_i is the ion temperature (in eV) in the plasma and M_i is the ion mass. A high velocity of ions can be obtained by having a large acceleration potential which can be achieved by applying a large screen grid voltage. However, having a high screen grid voltage results in a large beam power, as will be shown in the following sections. Therefore, an optimisation analysis is necessary.

5.2 Propulsion subsystem requirements

The goal of the LEOSWEEP mission is to de-orbit a rocket launcher upper stage weighing 1.5 tonnes from a nearly polar low Earth orbit (LEO) at 300 km in 170 days (Cichocki et al., 2015). This means that the debris object has to change the altitude by about 2 km per day. Table 5.1 summarises the requirements of the electric propulsion subsystem (EPS) needed to fulfil the LEOSWEEP mission goals.

EPS requirements	Values
Force on the debris target F_D (mN)	30
Total input power to both thrusters (kW)	2.6
Distance between the debris and ITT (m)	> 7

Table 5.1: Requirements for the propulsion subsystem imposed by the LEOSWEEP mission.

An optimisation analysis was performed by Feili et al. (2015b) aimed at choosing the most optimum EPS parameters to achieve the mission goals. Feili et al. (2015b) concluded that to keep the total thruster input power below 2.6 kW, the screen voltage must be around 3.5 kV. Also, at such a voltage the beam divergence of about 6° would be achieved, which is necessary to stay within the power constraints, as will be discussed in the following sections.

To be able to apply such a high screen voltage, Feili et al. (2015b) have decided to use an RF ion thruster for the IT purposes. It is important to remember that the energy to

which the ions are accelerated depends mainly on the screen grid voltage. Furthermore, as described above, the screen voltage greatly influences the divergence angle of the beam. The advantage of RF thrusters compared to other electric thrusters is that the ion production and acceleration mechanisms are separate. To produce the ions, the RFG power needs to be transferred from the coil to the plasma. Whereas, to extract the ions, the beam power has to be supplied to the screen grid. This allows a very high voltage to be applied to the screen grid without the fear of inhibiting the plasma production mechanism. It should be noted that RF ion thrusters also require an electron source (neutraliser) to be installed in order to neutralise the positive ion beam. The neutraliser prevents the thruster from reaching a high positive potential.

Figure 5.2 depicts the Impulse Transfer Thruster (ITT) with a discharge chamber diameter of 17 cm that was designed specifically for the LEOSWEEP mission by Smirnova et al. (2016b). As can be seen in Figure 5.2, the thruster exhibits a feature that is different from standard RF thrusters, that is, the neutraliser is located in the middle of the discharge chamber. Smirnova et al. (2016b) decided to do this to reduce the beam-neutralising electron temperature and thus help confine the ions to a beam that has a very low divergence angle (Cichocki et al., 2015). Additionally, Figure 5.2 shows that the extraction aperture pattern does not fully encompass all the grid area. This is because the ion density varies radially, which, for a set screen grid voltage, creates a varying divergence beam (Feili et al., 2009). To have a flat, uniform and low divergence beam, Smirnova et al. (2016b) chose to place the apertures only where the plasma is uniform.

Figure 5.2: ITT thruster having a discharge chamber diameter of 17 cm, as designed for the LEOSWEEP mission.

The list below summarises the main performance parameters predicted for the ITT thruster (Smirnova et al., 2016b; Feili et al., 2015b):

- force on the debris - 30 mN;

- distance between the thruster and debris - 7 m;

- thrust - 31 mN;

- beam current - 317.7 mA;

- screen grid voltage - 3,500 V;

- beam power - 1,130 W;

- beam divergence - 6°;

- RFG power - 240 W;

- total ITT power - 1,370 W;

- specific impulse - 5,260 s.

Remember that the requirements on the beam divergence angle imposed on the ICT are much more relaxed compared to the ITT. Therefore, a Hall thruster with a beam divergence angle of over 40° can be used as the ICT (Merino et al., 2011). Furthermore, in the case of a gridded ion thruster, a larger beam divergence angle would translate into a lower screen grid voltage and thus lower beam power. For instance, the ITT would exhibit a beam divergence angle of about 28° at around 1.2 kV (Smirnova et al., 2016a).

5.3 DST concept

This section presents the main DST concept characteristics and geometry. The DST thruster has been developed as a part of this thesis to act as an alternative for the LEOSWEEP (and other IBS) type missions. The main features of the DST concept are presented in Figure 5.3. The proposed thruster uses RF electromagnetic waves generated by a multi-turn coil to produce a plasma inside a ceramic discharge chamber. The plasma is then extracted to produce two ion beams from each side of the thruster. At both ends of the discharge chamber, there are different ion optics systems specially designed to produce the F_{IT} and F_{IC} thrusts. As a result, instead of the initially proposed two thrusters, one providing the impulse transfer (ITT) and one compensating the impulse (ICT), the DST concept allows having only one thruster. The aim of the DST concept is to reduce the sub-system complexity associated with a two-thruster design while having similar (or better) power and propellant requirements. An additional advantage

of the DST concept is that (ideally) the RFG power remains approximately the same, regardless of the production of the second beam. Therefore, taking the LEOSWEEP mission as an example, a gain of around 250 W can be achieved in comparison to the two-thruster design.
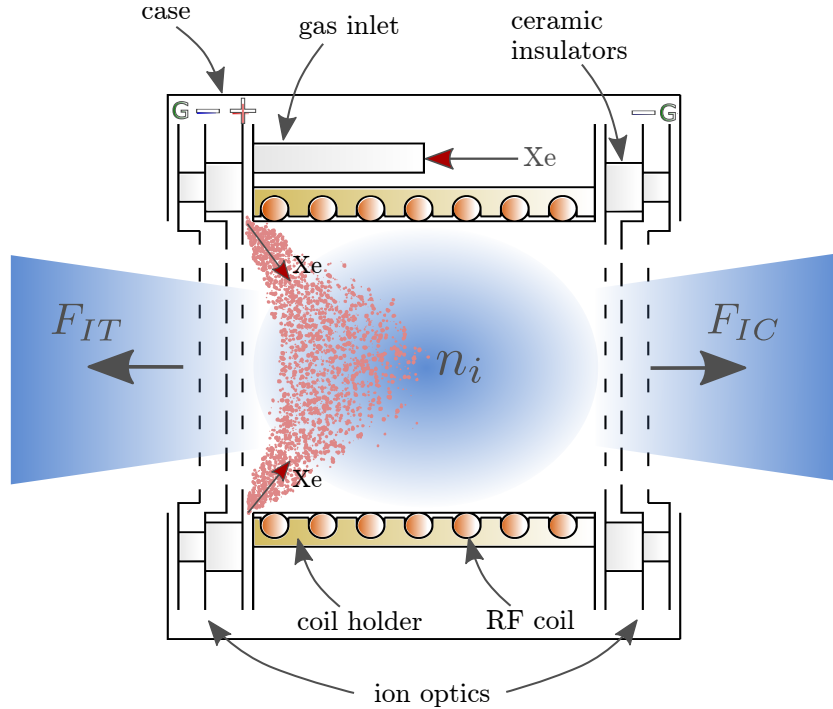
Figure 5.3: Double-sided ion thruster concept with main geometry features, electrical potentials, performance parameters and working principles.

The concept of shooting two ion beams from the same thruster is not entirely new. A similar concept was investigated by Collingwood (2011) as a means for producing very small thrust magnitudes through a differential thrust control method. However, the thruster designed by Collingwood (2011) was made of two discharge chambers, two separate coils and a gas inlet through the middle of the discharge chamber. Furthermore, the discharge chambers were separated with a ceramic shutter. This allowed an independent control of the neutral gas and ion densities inside each discharge chamber. Therefore, the thrust could be controlled independently from each side of the thruster. However, such a design suffered from large plasma power losses due to a large discharge chamber surface area. Also, there were issues due to the complexity of the two separate coil/chamber designs. Finally, there were problems associated with the neutral gas distribution uniformity due to a large aspect ratio of the thruster.

This PhD thesis is aimed at developing a thruster mainly for the IBS type missions. It has been chosen to design the thruster with only one coil and one discharge chamber, making the design efficient and compact. Therefore, in the proposed design, the total length of the discharge chamber is similar to that of a one-sided thruster. This should significantly reduce the eddy current power losses in the coil and the plasma losses to the

discharge chamber walls. However, similarly to what was done by Collingwood (2011), the thruster was designed in such a way that it could also be used to generate a very low thrust in the micro-Newton range. A very low net thrust can be produced by varying the IT and IC side thrust values so they are nearly equal. Due to the dual grid system, the DST concept can also be used to understand the RF gridded ion thruster behaviour in a more comprehensive way.

5.3.1   Performance parameters

Figure 5.4 shows a more detailed view of the DST concept. In particular, Figure 5.4 indicates the main power supplies required for the thruster, the electrical scheme and the main performance parameters/relations. As mentioned above, one side of the thruster is used to produce the impulse transfer thrust F_{IT}, while the other side is used to produce the impulse compensation thrust F_{IC}. To create the plasma, the power P_{in} is fed to the coil using the RFG and the propellant is supplied into the discharge chamber. The plasma is extracted by applying the potential U_s on the screen grid and the negative potential U_{a1} on the acceleration (accel) grid. Since the applied screen voltage on the IT side shows up in the plasma sheath itself, it means that the same floating potential will be present on the screen grid at the IC side of the thruster as well. Therefore, to extract the beam from the IC side, it is enough to apply the voltage U_{a2} on the accel grid at the IC side. The total power to the thruster P_{tot} is then composed of the RFG power P_{in} and the two beam powers P_{b1} and P_{b2}.

$$P_{tot} = P_{in} + P_{b1} + P_{b2}$$
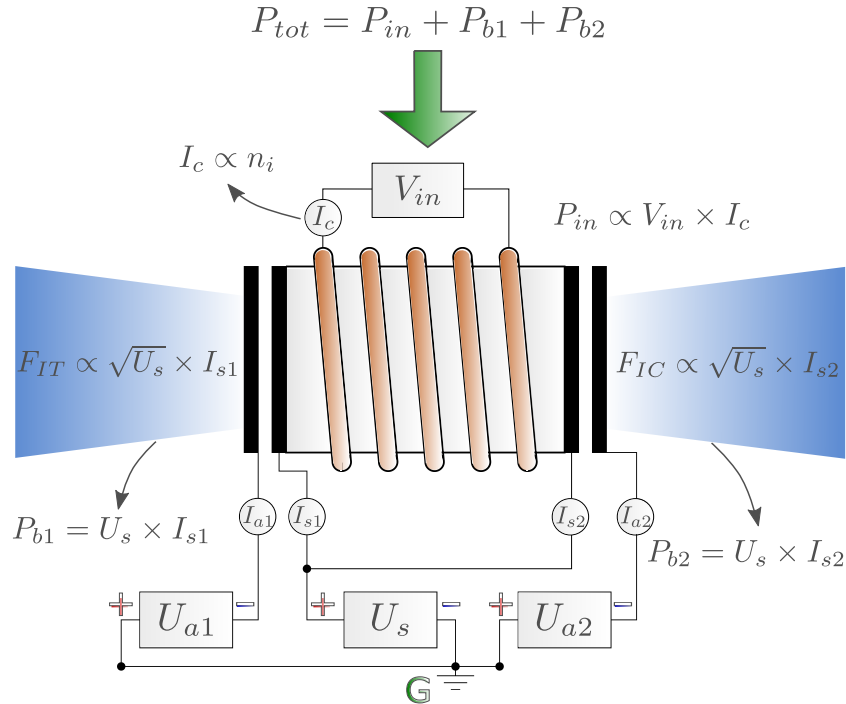
Figure 5.4: Double-sided ion thruster electrical circuit schematic, main performance parameters and relations.

Note that even though the screen voltage is the same for both sides, the beam powers differ based on the extracted currents I_{s1} and I_{s2} from the IT and IC sides, respectively. Furthermore, as seen in Figure 5.4, the thrust magnitudes F_{IT} and F_{IC} are proportional to the screen grid voltage U_s. This means that the thrusts generated from each side of the thruster are coupled. That is, for a constant RFG power and propellant flow rate, the thrust magnitude produced by each set of grids is dependent on the screen grid voltage U_s. This is because the plasma potential is common to both ion extraction systems. Therefore, it becomes challenging to independently control the thrust values from the IT and IC sides. For instance, this could cause various issues if a large (and variable) difference between the F_{IT} and F_{IC} values is required. Nevertheless, the next section will look at the possible ways to control the thrust magnitudes from the IT and IC sides independently, which is necessary in order to meet the LEOSWEEP mission requirements.

5.3.2 Thrust control

There are two main ways to control the thrust produced by the IT and IC sides independently. The first way is to adjust the I_{s1} and I_{s2} currents extracted from the IT and IC sides, respectively. This can be done by manufacturing the ion optics systems with the pre-defined number N of apertures with the area S, as illustrated in Figure 5.5. The thrust values can be controlled using the following relations

$$\frac{F_{IC}}{F_{IT}} \propto \frac{I_{s2}}{I_{s1}} \propto \frac{N_{IC}S_{IC}n_iU_s}{N_{IT}S_{IT}n_iU_s} \propto \frac{N_{IC}S_{IC}}{N_{IT}S_{IT}}, \tag{5.4}$$

where N_{IT} and N_{IC} are the number of apertures in the ion optics systems of the IT and IC sides, respectively. Whereas, S_{IT} and S_{IC} are the aperture areas in the ion optics systems of the IT and IC sides, respectively. As can be seen from Equation 5.4, since the ion density n_i and the screen grid voltage U_s are common to both ion optics systems, they cancel each other out. Therefore, the thrust ratio F_{IC}/F_{IT} can be controlled by adjusting the total grid extraction area of each ion optics system. Note that the ion density does vary along the length of the discharge chamber. However, this variation is usually symmetric around the centre of the discharge chamber, meaning that ion densities at both ends of the discharge chamber are roughly equal (Chabert and Braithwaite, 2011).

Another way to independently control the thrust values is by modifying the plasma meniscus shape at the either ion optics system, as depicted in Figure 5.6. This can be achieved by varying the accel voltages U_{a1} and U_{a2}. The change in the plasma meniscus shape modifies the ion optics effective transparency T_{eff}, which in turn affects the extracted currents I_{s1} and I_{s2}. As was proven in Equation 5.4, this causes a change in the F_{IT} and F_{IC} thrust values. However, the change in the extracted current due to the change in the meniscus shape is expected to be very small. Therefore, this method of thrust control is only suitable for very fine thrust adjustments that might be required

during the mission. Both methods of the thrust control were investigated experimentally, and the results from the investigation are presented in Chapter 7.
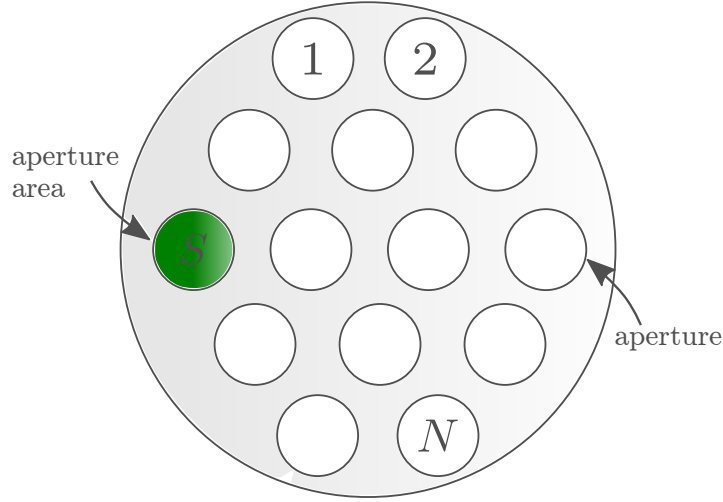
Figure 5.5: Schematic depicting parameters of a generic ion optics geometry.
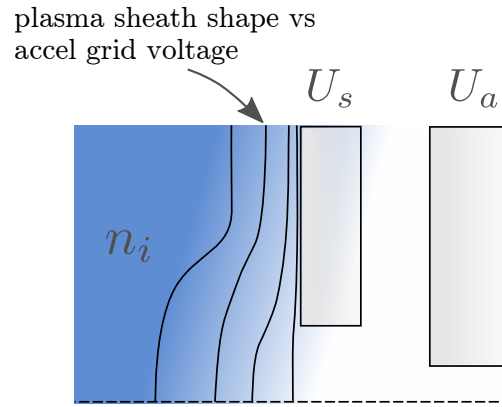
Figure 5.6: Effect of the accel grid voltage on the plasma sheath shape.

5.4 DST design

The double-sided ion thruster has been designed, manufactured and assembled. The design and optimisation of the thruster were driven by the computational tools developed in the thesis, as described in Chapter 3. In performing the optimisation analysis, the coil number of turns N and discharge chamber length l were varied with the goal to reduce the total input power, as depicted in Figure 5.7. The parameters of the LEOSWEEP mission were taken as constraints while performing the optimisation. In particular, it was assumed that 30 mN of thrust must be transferred to the debris target, the mass flow rate is 15 sccm and the screen grid voltage is 3 kV. Note that the screen grid voltage optimisation will be shown in Section 5.5.1. Furthermore, it was assumed that the discharge chamber diameter is fixed at about 17 cm. This is because it was decided to use the ITT ion optics system, which has an active diameter of about 16 cm, for the

IT side of the DST. Also, the coil diameter was set to 4.5 mm due to the capability of obtaining a copper tube of this diameter. As a result, geometrical parameters that could be optimised were the number of turns (N) and the discharge chamber length (l).
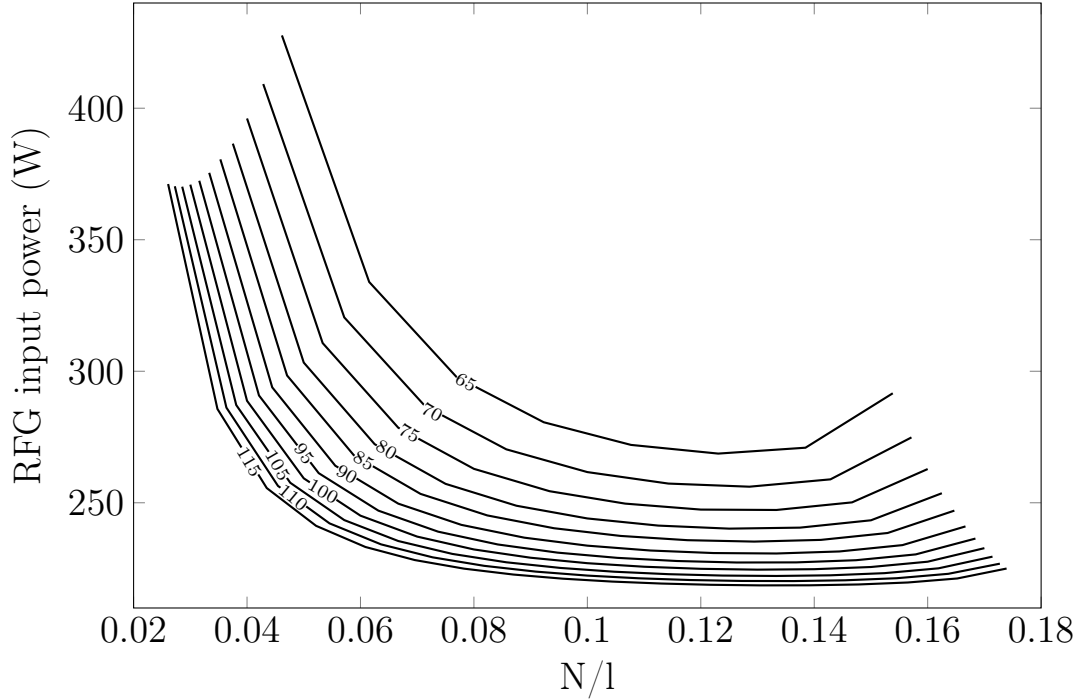
Figure 5.7: DST optimisation. RFG input power vs number of turns (N) to discharge chamber length (l) ratio N/l for discharge chamber lengths varying from 65 to 115 mm in 5 mm increments. Operational parameters: mass flow rate = 15 sccm, screen grid voltage = 3 kV, thrust to the target = 30 mN.

Figure 5.7 depicts that, at first, as the number of turns for a given discharge chamber length increases, the RFG input power decreases sharply. However, past N/l values of about 0.08, the RFG power plateaus. Finally, when N/l increases above approximately 0.14, the RFG power begins to increase again. The values at which the curve plateaus and then again increases shift slightly with the discharge chamber length. In particular, as the discharge chamber length increases, the N/l values where the RFG input power plateaus decrease, while the N/l values where the RFG input power starts going up increase. What is more, as the discharge chamber length increases, the RFG input power goes down. This is mainly driven by the increase in the discharge chamber volume to area ratio, which results in lower plasma losses to the boundaries. Also, as the number of turns increases, the coupling and power transfer efficiencies go up, and the losses in the RF circuit decrease. However, these are offset by a rise in eddy current losses in the coil itself. Therefore, the rate at which the RFG input power goes down with the chamber length decreases. Finally, at the chamber length of about 115 mm, the RFG input power plateaus. Upon increasing the discharge chamber length further, the RFG input power starts going up.

Based on the results from Figure 5.7, it was decided to choose a chamber length of about 80 mm and the coil with N/l of about 0.1, which would translate in 8 turns. The chamber length of 80 mm was chosen because even though the RFG input power decreases by about 20 W as the discharge chamber length increases to 115 mm, the extra discharge chamber length would result in an increase in the cost, size and mass of the thruster. Also, with a longer discharge chamber, more coil turns would be required, increasing the complexity of the thruster even more. Furthermore, a longer discharge chamber length might reduce the neutral gas uniformity. Finally, CAD drawings of the cross-sectional views of the DST with final dimensions are shown in Figure 5.8. As can be seen from Figure 5.8, the discharge chamber length is 76.7 mm and the coil has 8 turns. What is more, the thruster was designed in such a way that it could be set up in two configurations depending on the type of the ion optics system used for the IC side.

(a) Configuration A (IC1). (b) Configuration B (IC2).
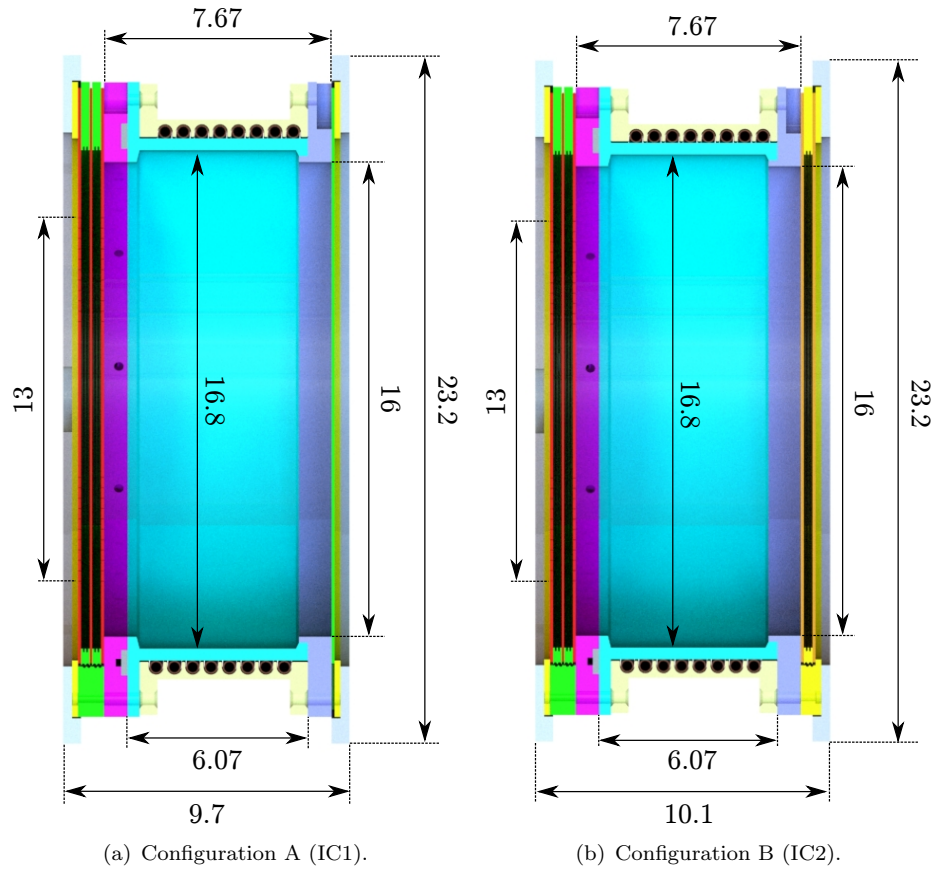
Figure 5.8: CAD drawings of the cross-sectional views of the DST thruster for Configuration A and Configuration B. All dimensions are in cm.

In Configuration A, an IC1 ion optics system composed of a single grid was used for the IC side. Whereas, in Configuration B, an IC2 ion optics system composed of two grids was employed for the IC side. In both A and B Configurations, for the IT side, an IT ion optics system having three grids was used. As Figure 5.8 depicts, both configurations have a single discharge chamber and a single coil. What is more, the IT ion optics and

the IC1 ion optics systems are located on the left and right sides of the discharge chamber, respectively, as illustrated in Figure 5.8. Furthermore, Configuration B has the IC2 ion optics system on the right side of the discharge chamber. Notice that both configurations are nearly identical in terms of thruster's dimensions, as displayed in Figure 5.8. Nevertheless, in Configuration B, the thruster is 0.4 cm wider to accommodate for the additional grid on the IC side. In the following sections, the design of the double-sided thruster will be discussed in more detail.

5.4.1   Configurations A and B

Figure 5.9 shows the DST thruster in Configuration A from both the IT and IC ion optics sides. Figure 5.9 also indicates the main components of the thruster and the materials. Note that the IT ion optics has three grids that are all made out of carbon-carbon (C-C) material. Also, observe that the IT ion optics system has an area at the centre that has no apertures and there is a hole at the centre as well. To be able to use the IT ion optics system in the DST thruster, the hole was taped with an aluminium (Al) tape, as seen in Figure 5.9(a). This is because the IT ion optics system was taken from the ITT thruster, and the hole was used to house the neutraliser, as was shown in Figure 5.2 depicting the ITT. As depicted in Figure 5.9(b), the IC1 ion optics has apertures throughout the area of the grid. The grid itself is made out of SILUX (Sico, 2017) and has a layer of aluminium taped on the accel side. Observe that the gas inlet locations are different between the two configurations. This is because, initially, the gas inlet was located as shown in Figure 5.9(b). However, to prevent sparks from forming between the gas inlet and the beam, the gas inlet was installed as depicted in Figure 5.9(a).

Finally, observe from Figure 5.9 that in Configuration A, the thruster has four electrodes: IT screen (I_{s1}), IT accel (I_{a1}), IT GND and IC accel (I_{a2}). Figure 5.9(b) illustrates that all electrode connections are made using safe high voltage (SHV) connectors. Similarly, Figure 5.10 depicts the DST thruster in Configuration B. As was discussed preciously, Configuration B has a different IC ion optics system represented with two titanium (Ti) grids and denoted as IC2. Furthermore, there is also an additional IC accel electrode (I_{a2}) that is connected to the power supply directly through a cable, as indicated in Figure 5.10(b). What is more, on the IT side, the SHV connector is no longer used as the IC accel (I_{a2}) electrode. It is now employed to provide the screen potential, and it acts as the IC screen (I_{s2}) electrode. Note that all other geometrical parameters between the two configurations are nearly exactly the same, as was discussed in the previous section. In the following sections, each part of the thruster will be described and discussed individually.

Gas inlet
(final location)

Decel
(C-C)

Opening
(taped with
Al tape)

SHV
connector
(I_{a2})

(a) IT ion optics.

Gas inlet
(initial location)

Case
(stainless steel)

SHV
connector
(I_{a1})

SHV
connector
(I_{s1})

RF coil exit
location

SHV
connector
(GND)

Screen/Accel
(SILUX/Al)
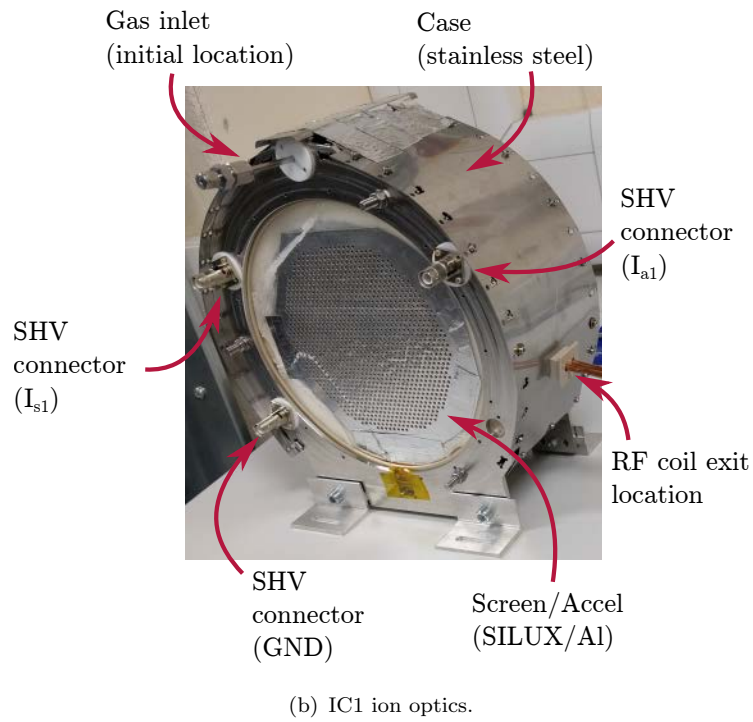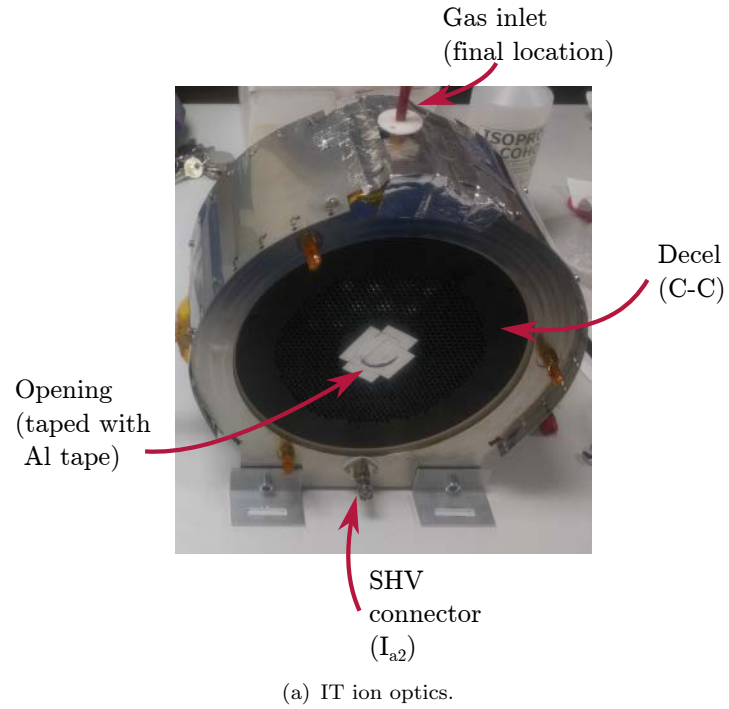
(b) IC1 ion optics.

Figure 5.9: IT and IC ion optics sides in Configuration A.

Gas inlet
(final location)

Decel
(C-C)

SHV
connector
(I_{s2})

(a) IT ion optics.

Gas inlet
(final location)

Al tape
for RF
shielding

Accel
(Ti)

Cable connection (I_{a2})

(b) IC2 ion optics.

Figure 5.10: IT and IC ion optics sides in Configuration B.
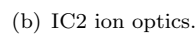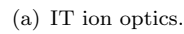
5.4.2   Discharge chamber

The discharge chamber is depicted in Figure 5.11. It is made out of Al2O2 (aluminium oxide) and has a wall that is 4 mm thick. The wall thickness was kept to a minimum allowed by the manufacturing standards to have the best possible coupling coefficient

between the coil and the plasma. Additionally, the chamber has openings at both sides to allow for an attachment of the IT and IC ion optics systems.

Figure 5.11: Al2O2 discharge chamber.

At one end of the discharge chamber, there is a flange that is used to press the gas inlet flange against, as denoted in Figure 5.11. The gas inlet flange itself is shown in Figure 5.12(a). Whereas, at the other end of the discharge chamber, there is a few millimetres wide surface to press the discharge flange against. The discharge flange is depicted in Figure 5.12(b). The gas inlet flange is used to secure the IT ion optics system, while the discharge flange is used to hold the IC ion optics system. Additionally, as the name suggests, the gas inlet flange is used to transmit the gas from the gas inlet into the discharge chamber. Both flanges also act as supporting structures for the coil holders and electrodes.
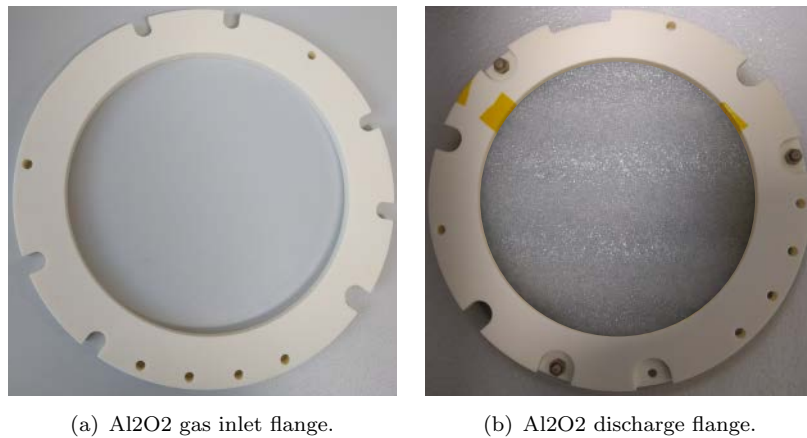
(a) Al2O2 gas inlet flange.

(b) Al2O2 discharge flange.

Figure 5.12: Al2O2 flanges that are secured to the ends of the discharge chamber.

5.4.3   RF coil

The RF coil was designed to have a high power transfer efficiency from the RFG to the plasma and minimum eddy current losses in the thruster's components and the coil itself. Figure 5.13 depicts the coil and the supporting holders secured onto the discharge chamber. The coil holders are made out of a high-temperature plastic (PEEK) and are needed to hold the coil onto the discharge chamber. Upon heating, due to the thermal stresses, the coil starts flexing and expanding. Therefore, the coil holders are also needed to maintain the shape of the coil and to keep the distance between the coil and the plasma to a minimum. Due to the same thermal issues, the coil holders also prevent the coil turns from touching and thus shorting out the circuit.
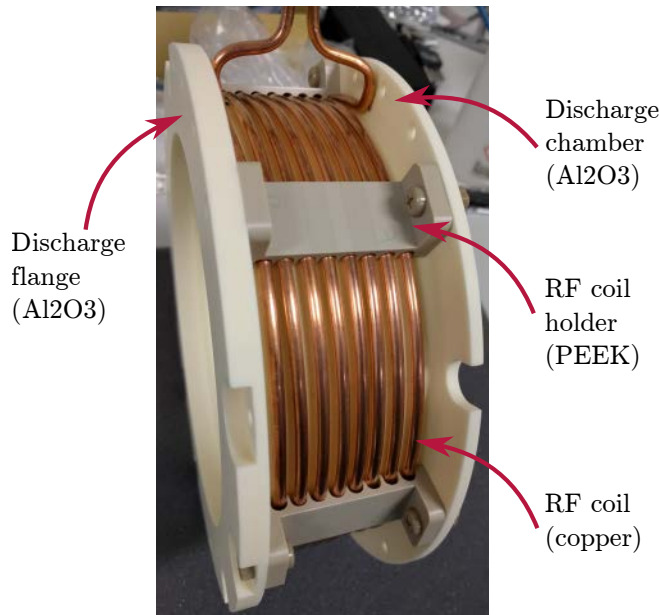
Figure 5.13: RF copper coil and PEEK holders secured onto the discharge chamber.

The coil is manufactured out of a hollow 4.5 mm diameter copper tube. The coil diameter itself is 18 cm, the width is 5 cm and it has 8 turns. Such a coil design, especially the number and spacing of the turns, was driven by the optimisation analysis performed using the RF ion thruster model developed in the thesis, as was shown in the previous section. The coil is connected to the RFG using a 30 cm long 50 Ω coaxial cable with a LEMO connection, as illustrated in Figure 5.14. The cable is attached to the coil by drilling two holes into the coil and using bolts to secure the core and shield of the coaxial cable, as shown in Figure 5.14.
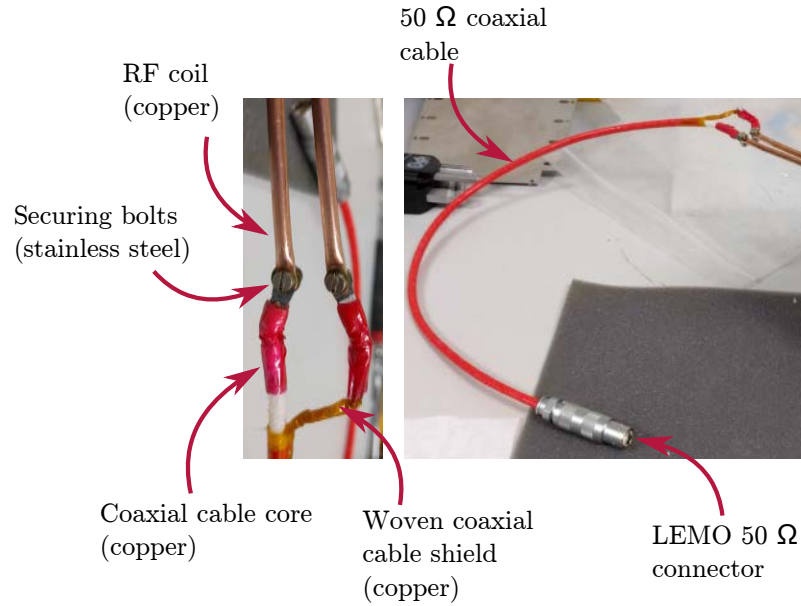
Figure 5.14: Coaxial cable used to transfer power from the RFG to the coil and the method by which the coaxial cable is secured to the coil.

5.4.4 Propellant distribution system

Figure 5.15 shows a detailed illustration of the propellant flow system designed to transfer the propellant from the gas inlet into the discharge chamber. First, the propellant enters the discharge chamber through a gas inlet depicted in Figure 5.16. Then, the propellant flows into the gas inlet flange where it circulates in a specially cut 240° annulus, as indicated by the arrows. To prevent the gas from escaping, the annulus is covered with an Al2O2 O-ring. The O-ring is then secured using ceramic, high-temperature glue. Also, the gas inlet flange is pressed against the main flange of the discharge chamber to prevent any leaks.
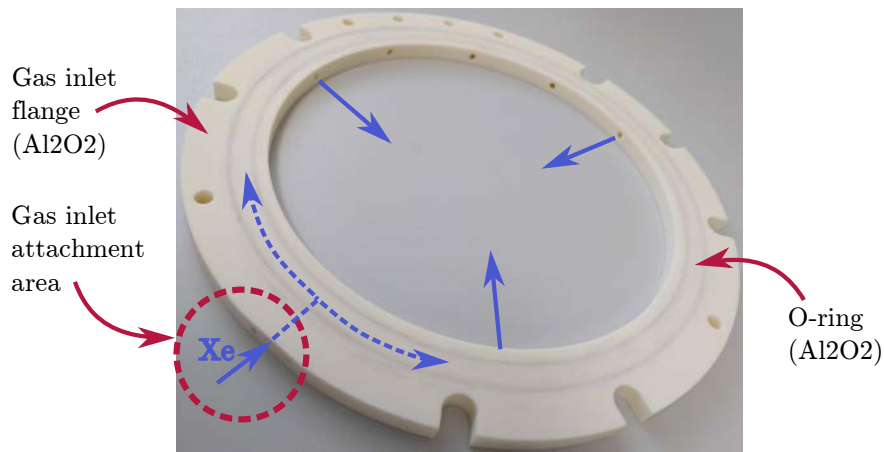
Figure 5.15: Al2O2 gas inlet flange and the Al2O2 O-ring installed to prevent the propellant from escaping. Blue arrows indicate propellant flow directions.

As Figure 5.15 depicts, three 70° angled holes, each 3 mm in diameter, are drilled into the flange to let the gas flow from the annulus into the discharge chamber. The propellant flow is specifically directed at 70° angles at the walls. This is done to increase the neutral gas residence time and thus its uniformity inside the discharge chamber. The gas inlet itself is secured using two PEEK screws at the top of the gas inlet flange, as shown in Figure 5.16. The gas inlet has a 1/8 to 1/16 inch Swagelok reducing section in order to connect the main propellant line. Since during the thruster operation the gas inlet charges up to nearly the plasma potential, it is isolated from the grounded thruster's case using a Teflon isolation bushing.
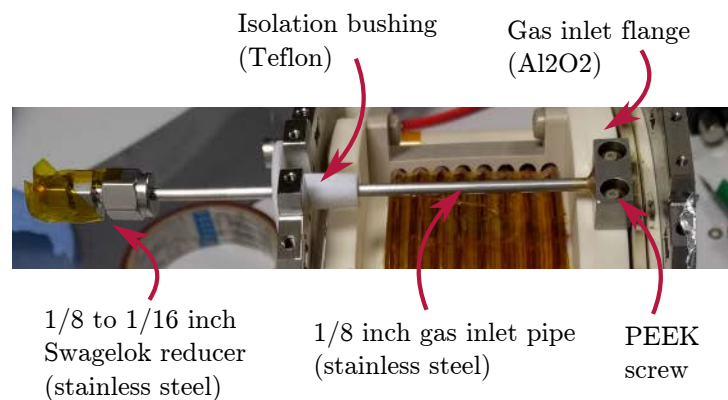
Figure 5.16: Gas inlet secured onto the thruster's structure. Not the final configuration. The final configuration is identical to the one depicted, except the gas inlet pipe is bent 90° upwards.

5.4.5 Electrodes

Since the thruster works within the range of a few kV voltage, an appropriate electrode design is vital. The electrode designed for the DST is shown in Figure 5.17. Figure 5.17 also depicts the different components of the electrode and the way in which they are assembled. The key element of the electrode is the Tekon spring-loaded connector. The Tekon connector is soldered onto a copper holder which is then connected by a copper wire to a SHV connector. Finally, the holder is screwed into a stainless steel adapter which is then secured into the discharge chamber flange or the discharge flange. Since the connector is spring loaded, by screwing it is pushed against the grid surface thus making a secure, low resistance electrical connection. Finally, the connector is isolated by an Al2O3 tube to prevent short-circuiting.

Connector holder
(copper)

Spring-loaded
connector

Isolation bushing
(Teflon)

Isolation tube
(Al2O3)

Connector adapter
(stainless steel)

Electrode-grid
contact point

SHV
connector
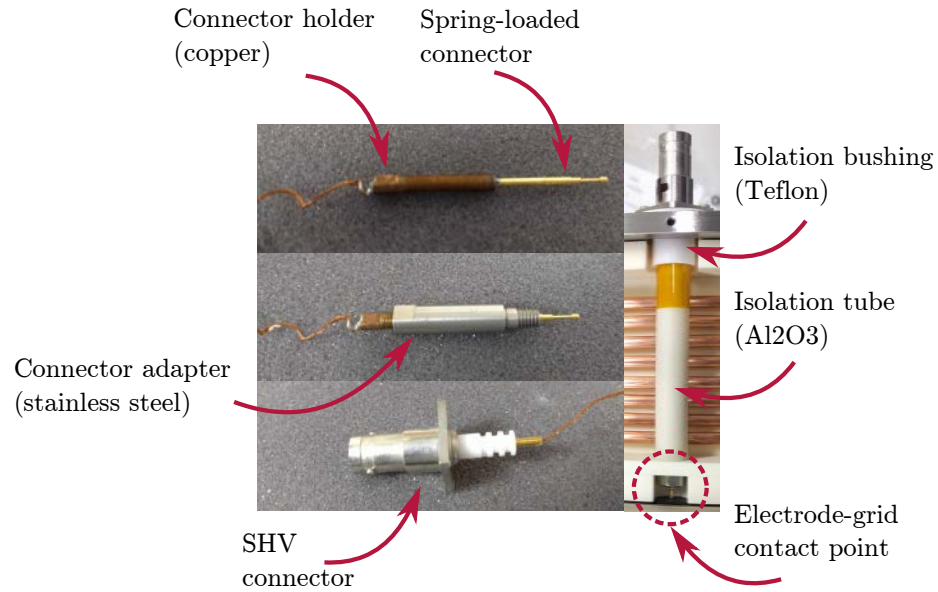
Figure 5.17: Electrode assembly and main individual components.

5.4.6 IT ion optics

As was discussed previously, the IT side of the thruster is used to accelerate ions towards the debris object. In order to do so efficiently, it is critical to have a low beam divergence angle. Therefore, the IT ion optics system incorporates a three-grid design that generates a flat, low-divergence beam, but at the same time has a low beam power. Each grid is manufactured out of carbon-carbon (C-C) to achieve the best possible thermal stability, minimising the thermal expansion problem. The IT ion optics dimensions are shown in Figure 5.18. Such dimensions were chosen to obtain an optimum focusing efficiency at the screen grid potential of around 3 kV and the plasma parameters that are expected at about 250 W of RFG power. Note that each grid has 948 axially aligned apertures that form the same number of beamlets.

Screen
(C-C)

Accel
(C-C)

Decel
(C-C)

1

0.75

1

2.8

1.8

2.8

3

3
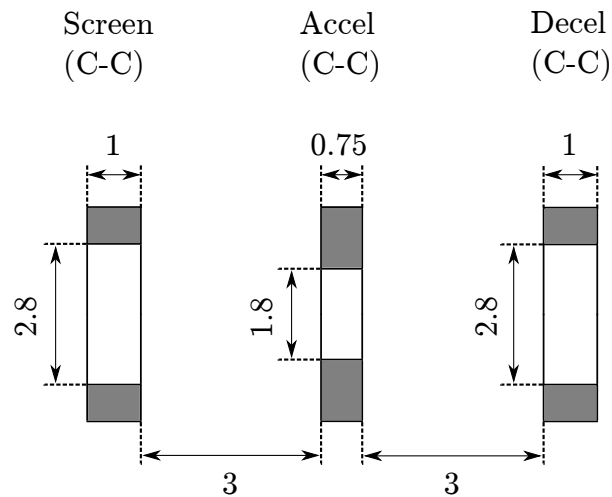
Figure 5.18: IT ion optics dimensions in mm.

Figure 5.19 shows all three grids and the way they were assembled to form the IT ion optics system. One of the main issues with any ion optics system is obtaining a proper alignment of the apertures. In the IT ion optics system, the grid alignment is achieved by using three Al2O2 grid aligners that are inserted (with very tight tolerances) into the cuts made in the grids. The aligners themselves are then secured onto the compression bolts, as indicated in Figure 5.19. Finally, in order to prevent the formation of sparks and shorting out, the grids are separated using Al2O2 ring-shaped spacers.
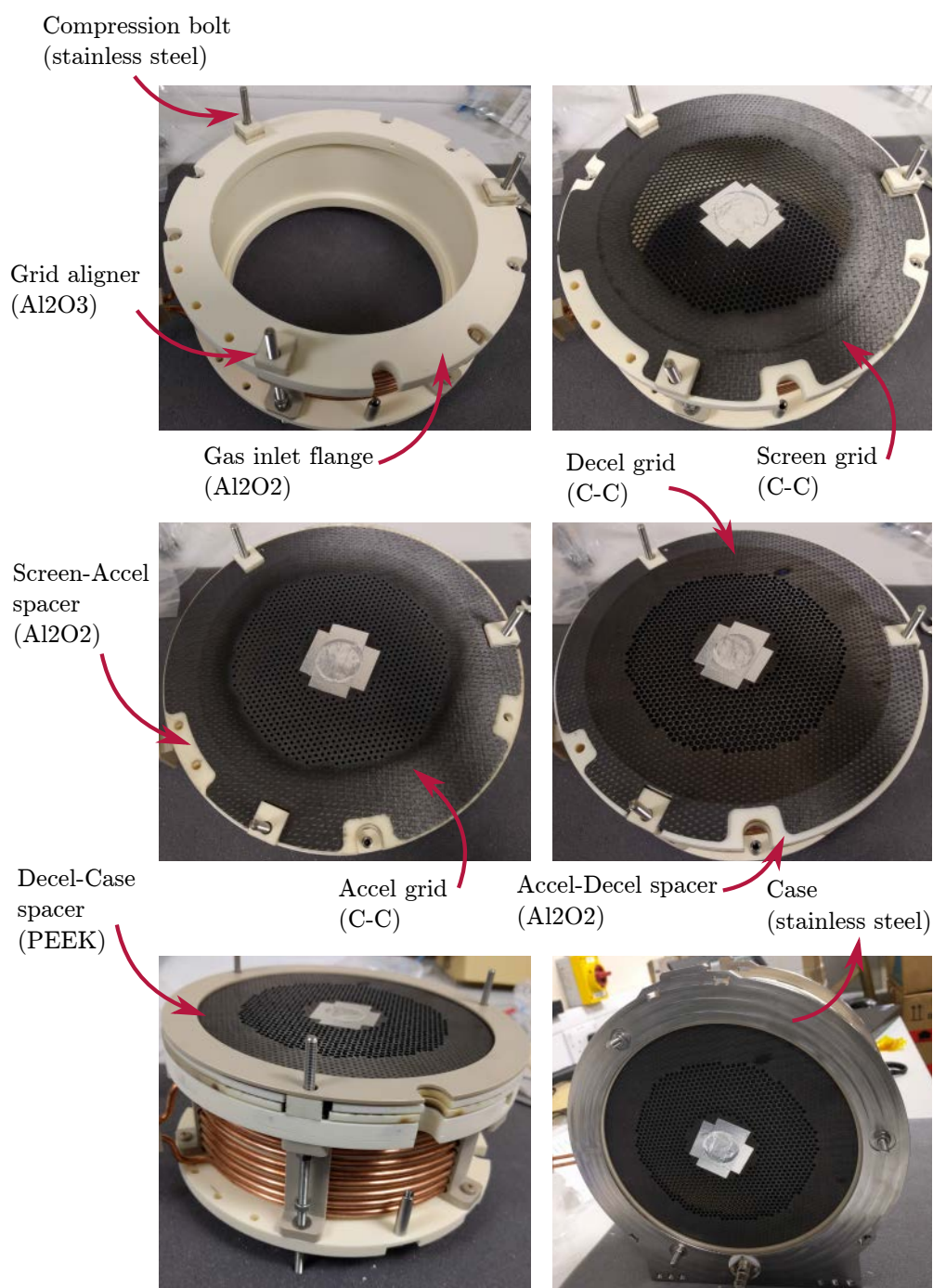
Figure 5.19: Detailed assembly of the IT ion optics system.

5.4.7 IC1 ion optics

Contrary to the IT ion optics system, the IC ion optics system does not have strict requirements regarding the beam divergence angle. Therefore, the IC ion optics system was optimised for the thrust compensation and satellite orbit control. What is more, since the plasma potential is set by the screen grid on the IT side, there is no need to have a conductive screen grid in contact with the plasma on the IC side. As a consequence, it was decided to use a non-conductive screen grid made out of SILUX (ceramic) which has similar properties to those of glass, as illustrated in Figure 5.20.
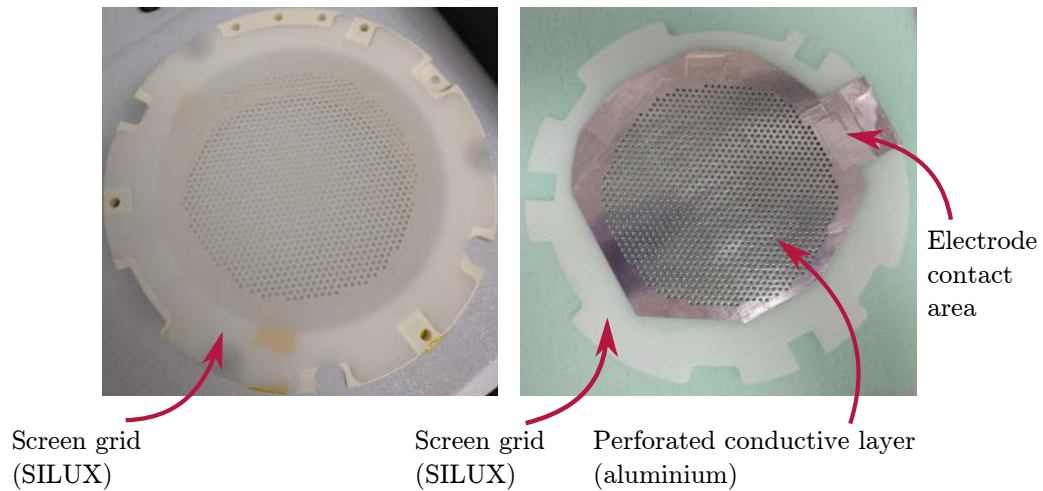
Figure 5.20: IC1 grid in the original form (left) and in the final form with an aluminium layer providing the accel potential (right).

One of the advantages of a non-conductive grid is that there are no eddy current losses in the grid itself. Additionally, misalignment issues due to the thermal expansion and improper alignment are non-existent for a single grid design. However, to focus the ion beam, a conductive layer must be applied on the grid surface facing away from the plasma. This was achieved by first sticking a layer of aluminium tape onto the grid and then piercing holes in the tape that coincide with the main grid apertures, as shown in Figure 5.20. To date, this is one of the first times such a single-grid design has been used.

The IC1 ion optics dimensions are shown in Figure 5.21. As can be seen from Figure 5.21, there is only one grid with an aluminium layer. The grid has 1171 2 mm diameter apertures. The aperture number and diameter were chosen by taking into account the results from Equation 5.4. That is, as will be shown in the following section, the IC ion optics side has to provide around 30% more thrust compared to the IT side. Therefore, the IC side needs to have about 30% more apertures than the IT side. However, since there is only one grid, to prevent the gas from escaping the thruster and to create a sufficient pressure in the discharge chamber, the aperture diameter was reduced to 2 mm, which is 0.8 mm less compared to the aperture diameter of the IT ion optics

system. Nonetheless, depending on the applied screen voltage and RFG power, it is expected that the IC ion optics system, on average, will produce $20 - 30\%$ more thrust compared to the IT ion optics system. Such a difference should be sufficient to satisfy the LEOSWEEP mission requirements.
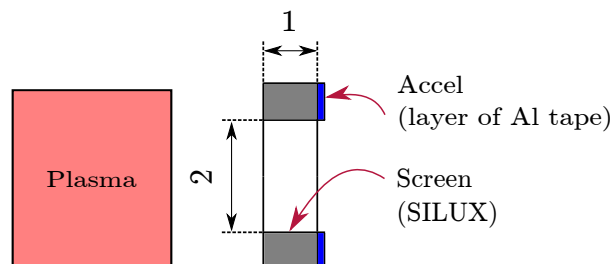
Figure 5.21: IC1 ion optics dimensions in mm. The aluminium layer is facing away from the plasma, while the SILUX grid is in contact with the plasma.

The IC1 ion optics assembly is depicted in Figure 5.22. Observe that since there is only one grid, the assembly is rather different compared to the IT side. The key point is that for the IC side there is no need to have the grid aligners and ceramic ring-shaped separators (isolators), which greatly simplifies the design. However, in order to isolate the aluminium side of the grid from the case, a PEEK ring-shaped spacer was installed.
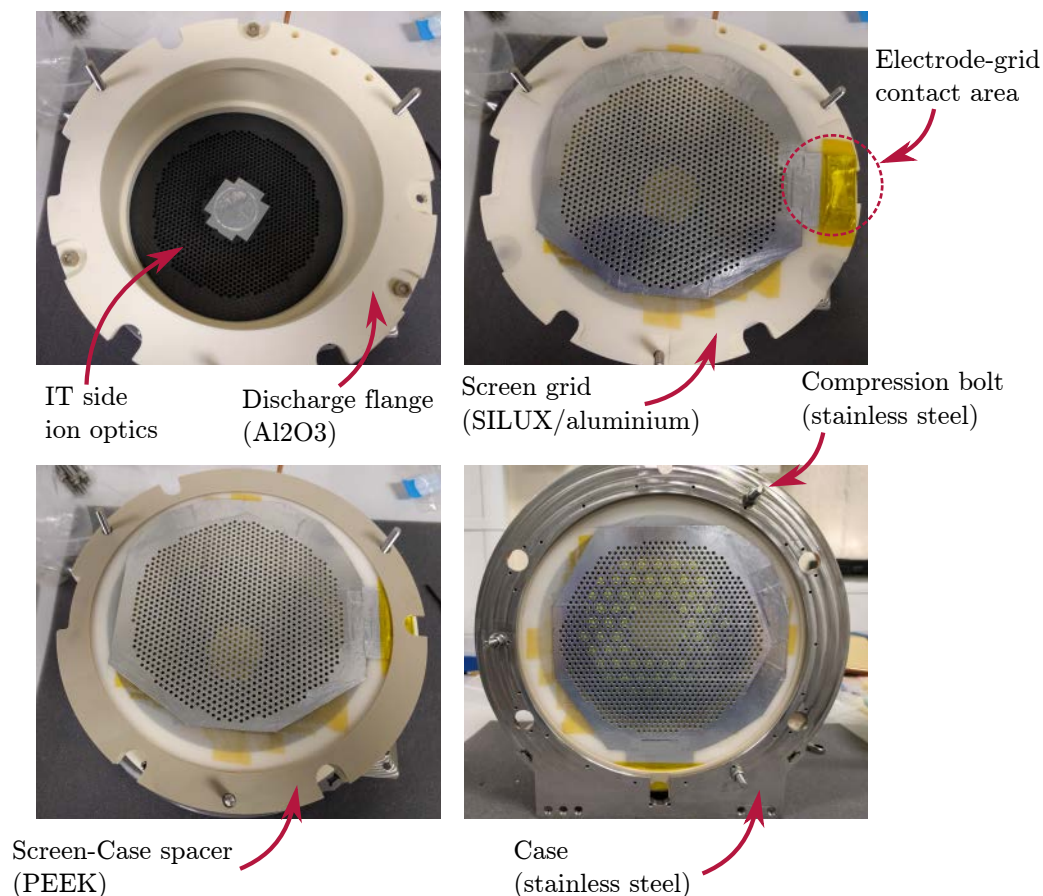
Figure 5.22: Detailed assembly of the IC1 ion optics system.

5.4.8 IC2 ion optics

Figure 5.23 depicts the IC2 ion optics assembly. Remember that the IC2 ion optics system is composed of two titanium grids. As can be observed from Figure 5.23, similarly to the IT ion optics side, the titanium grids were separated using a non-conductive PEEK ring. The alignment itself was achieved using three grid aligners made out of PEEK. Furthermore, an additional electrode had to be designed to connect the IC2 accel grid to the U_{a2} potential, as shown in Figure 5.23.
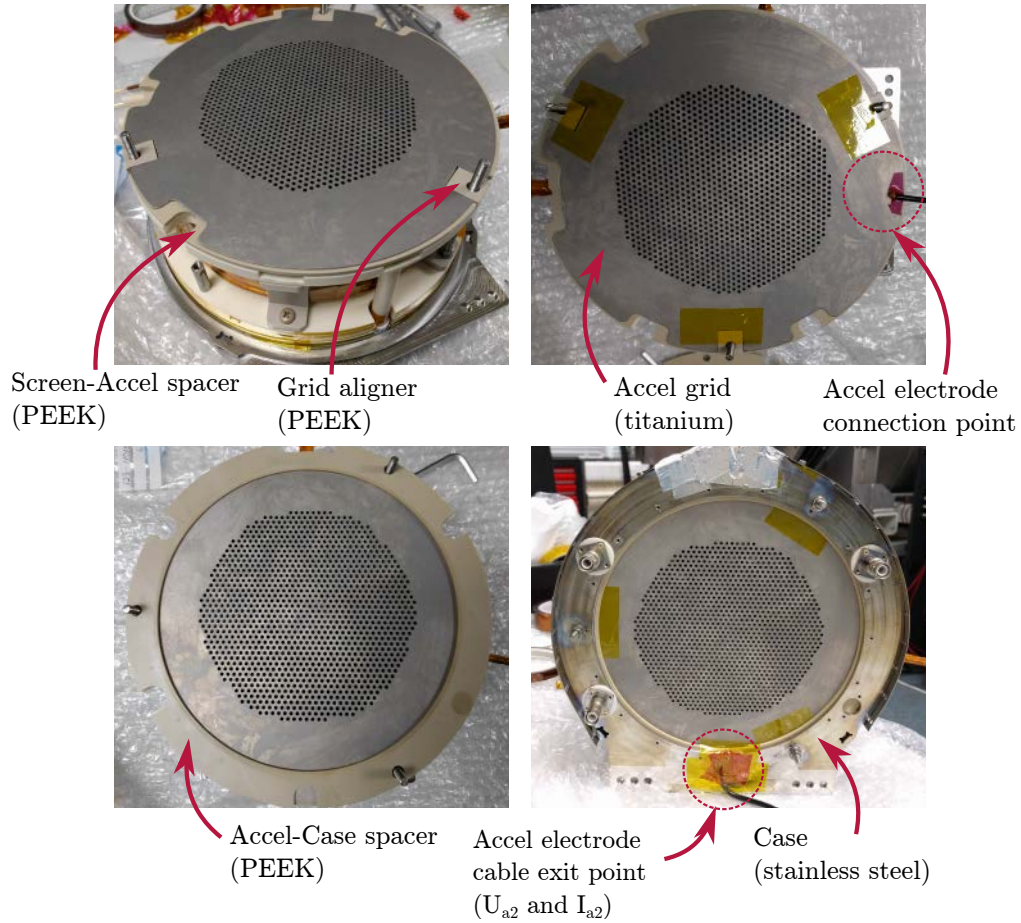
Figure 5.23: Detailed assembly of the IC2 ion optics system.

Furthermore, notice that both grids have 1171 2 mm apertures, as depicted in Figure 5.24. The titanium grids were manufactured with exactly the same dimensions and at the same time to reduce costs associated with machining. This manufacturing method also ensured that the grid apertures are properly aligned. Additionally, note that the IC2 ion optics aperture diameter and the aperture number are exactly the same as those of the IC1 ion optics system. However, since the IC2 ion optics system has two grids, the grid thickness was reduced to 0.7 mm. Finally, note that the grid thickness was also dependent on the availability of material.
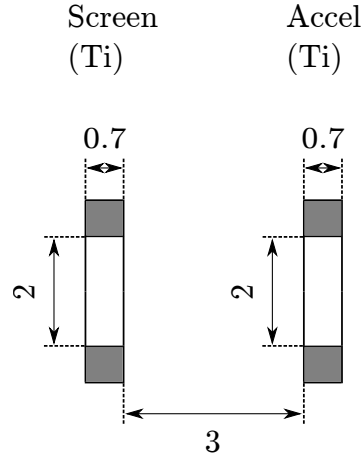
Figure 5.24: IC2 ion optics dimensions in mm.

5.5   DST simulations

The RF ion thruster model, as described in Chapter 3, was employed to simulate the double-sided ion thruster's performance while keeping the LEOSWEEP mission requirements as inputs. In particular, the modelling results were used to choose the optimum screen grid voltage. In addition, the modelling results allowed to compare the DST performance to other thrusters. Finally, the DST simulation results were taken into account when designing and testing the thruster.

5.5.1   Optimisation analysis

First, the model was used to calculate the IT side beam divergence angle as a function of the screen voltage, as displayed in Figure 5.25(a). Then, using the published results from the work by Cichocki et al. (2017), the momentum transfer efficiency η_b for the IT ion optics system, as a function of the screen voltage, was determined, as seen in Figure 5.25(b). These parameters were necessary in order to determine how efficiently the ion energy is transferred to the debris object. Moreover, the beam divergence angle and the momentum transfer efficiency were critical in performing the optimisation analysis. As indicated in Figure 5.25(b), as the screen voltage increases, the momentum transfer efficiency goes up in a nearly linear fashion from the value of 0.6 at the screen voltage of 2 kV. However, at about 4 kV, the momentum transfer efficiency plateaus at the value of approximately 0.95. Additionally, Figure 5.25(a) shows that the beam divergence angle decreases from about 10° at 2 kV to about 4° at 4.5 kV.

The optimisation analysis was performed in order to choose the most optimum screen grid voltage. Such an analysis was necessary since the IT and IC sides are coupled through a common screen grid voltage and RFG power. The results of the analysis are displayed in Figure 5.26. Figure 5.26(a) indicates that the RFG input power decreases
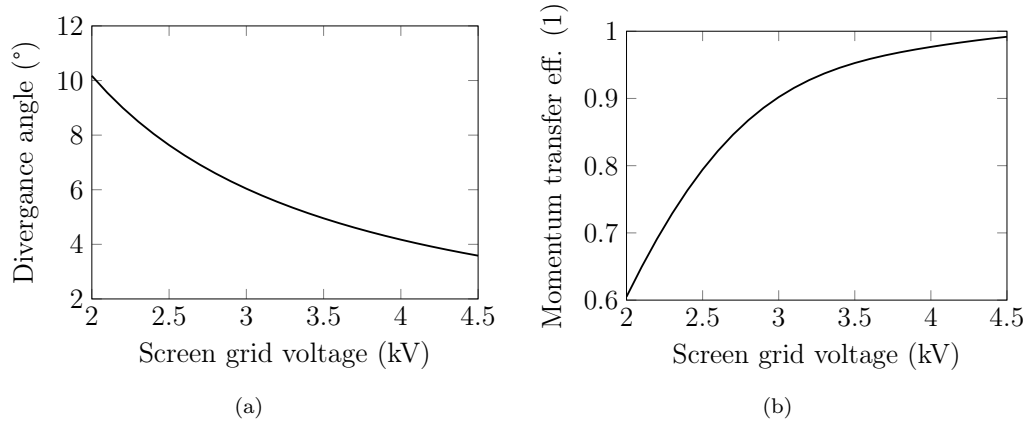
Figure 5.25: IT ion optics divergence angle and momentum transfer efficiency vs the screen grid voltage.

with the screen voltage. This happens because a rise in the screen voltage results in an increase in the momentum transfer efficiency η_B, as was shown in Figure 5.25(b). This in turn, as given by Equation 5.1, decreases the IT thrust (as well as the IC thrust) that needs to be generated to impart a force of 30 mN on the debris object. Therefore, a lower screen current is needed, which results in a lower RFG power that needs to be supplied to the plasma. Next, Figure 5.26(b) illustrates that the beam power reaches a minimum magnitude at around 2.8 kV. The reason for this is that the beam power is a product of the screen voltage and the screen current. Additionally, as the screen voltage increases, the required screen current decreases. However, as already mentioned, at the screen voltage values above approximately 4 kV, the momentum transfer efficiency plateaus. As a result, the thrust T that needs to be generated by the thruster reaches a minimum value. Therefore, the rate at which the screen voltage U_s increases overtakes the rate at which the screen current I_s decreases since $T \approx I_s \sqrt{U_s}$. As a consequence of the above, the beam power P_b, being equal to the product $P_b = I_s U_s$, starts going up.

As can be inferred from Figure 5.26(c), the way in which the total input power varies with the screen voltage mimics the total beam power trend behaviour observed in Figure 5.26(b). This occurs because, compared to the RFG power, the beam power adds a much greater contribution to the total power of the thruster. As illustrated in Figure 5.26(c), the screen voltage that results in a minimum input power is around 3 kV. Nevertheless, as depicted in Figure 5.26(d), the total propellant mass needed for the mission decreases constantly as the screen voltage goes up due to the decreasing screen current required to achieve the 30 mN of thrust. A lower screen current means that the ion density that needs to be generated is smaller and therefore less propellant is needed. Finally, Figure 5.26(d) shows that at 3 kV the total propellant mass is about 21 kg.
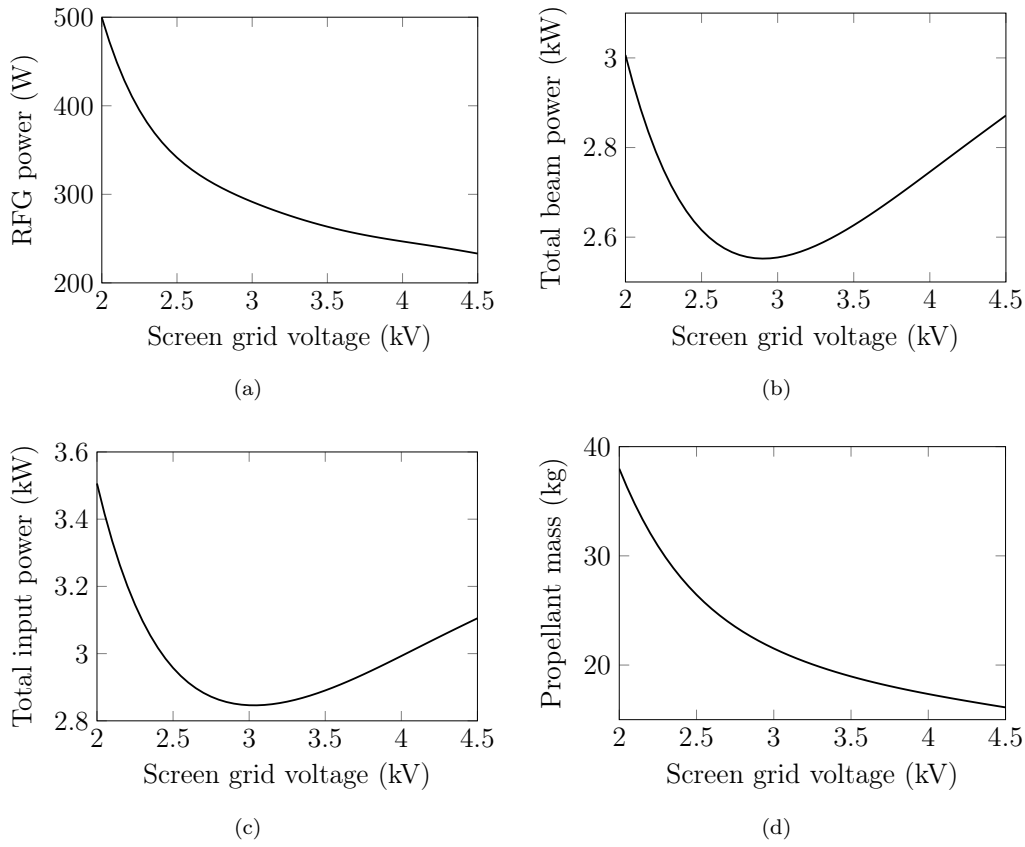
Figure 5.26: Power and propellant requirement optimisation for the DST thruster vs the screen grid voltage.

5.5.2   Performance and plasma parameters

As discussed previously, the DST thruster generates two distinct ion beams. Therefore, for clarity and ease of comparison to other single-sided ion thrusters, the performance values for the IT and IC sides are shown separately, as seen in Table 5.2. Observe that Table 5.2 also provides the performance values of the single-sided ITT thruster designed for the LESOWEEP mission, as was mentioned earlier in the chapter. Also, note that, as per LEOSWEEP requirements, both thrusters are required to transfer 30 mN of force on the debris target. As can be seen in Table 5.2, in the case of the DST thruster, the IC ion optics side has to produce 30% more thrust compared to the IT ion optics side. This requirement comes from Equation 5.2, assuming the debris mass of 1,500 kg and the shepherd satellite mass of approximately 500 kg. Note that for the double-sided thruster, the optimisation analysis, as performed in the previous section, has shown that applying 3,000 V on the screen grid results in the lowest total power. However, for the ITT, the lowest total power is predicted to occur at the voltage of 3,500 V.

Notice that for the DST thruster, since 30% more thrust has to be generated from the IC side, the extracted beam current from the IC ion optics system has to be 30% higher as well compared to the IT side. This is because the screen voltage on both

		IT	IC	ITT
Force on debris (mN)		30		30
Distance between thruster and debris (m)		7		7
Thrust (mN)		33	43	31
Beam current (mA)		370	480	320
Screen voltage (V)		3000	3000	3500
Beam power (W)		1110	1440	1130
Beam divergence (°)		6	6	5
RFG power (W)		270		240
Propellant flow (sccm)		14.9		5.6
Specific impulse (s)		5205		5260

Table 5.2: DST performance for the IT and IC sides compared to the ITT.

the IT and IC sides is the same due to the common plasma potential with respect to the ground. As described earlier, to achieve 30% more thrust from the IC side, the IC ion optics system was designed with 24% more apertures compared to the IT ion optics system. Additionally, as Table 5.2 indicates, the DST needs only 30 W more RFG power compared to the ITT even though the beam current extracted by the DST is more than two times larger than that extracted by the ITT. Also, remember that the discharge chamber diameters of the DST and ITT are similar in size. Finally, Table 5.2 shows that the DST needs 14.9 sccm of propellant, which is much higher than the 5.6 sccm required by the ITT thruster. However, the DST produces two ion beams instead of one. This results in the specific impulse values of both thrusters being nearly identical.

Neutral gas pressure (mTorr)	0.35
Neutral gas density ($1/m^3$)	7.5×10^{18}
Plasma density ($1/m^3$)	3.5×10^{17}
Beam current density (mA/mm^2)	70
Plasma potential (V)	24.5
Electron temperature (eV)	4.65
Electron-neutral eff. collision freq. (MHz)	2.4
Stochastic collision freq. (MHz)	15.9
Real part of plasma conductivity (S/m)	468
Imaginary part of plasma conductivity (S/m)	-155

Table 5.3: Simulated plasma parameters of the DST thruster.

Table 5.3, on the other hand, gives the main plasma parameters of the DST thruster for the thrust point given in Table 5.2. Table 5.3 indicates that the neutral gas pressure in the discharge chamber is 0.35 mTorr, while the neutral gas density is 7.5×10^{18} $1/m^3$. To produce the required thrusts, the plasma density in the discharge is estimated to be 3.5×10^{17} $1/m^3$. Finally, the plasma temperature and potential are expected to be 4.65 eV and 24.5 V, respectively. Table 5.4 shows additional DST performance parameters at

a frequency of 1 MHz for the thrust point shown in Table 5.2 and the plasma conditions from Table 5.3. At this operational point, apart from other parameters, the model predicts that the coil current is 10.4 A, the power transfer efficiency to the plasma is about 82%, while the field coupling value is 0.4 and the mass utilisation efficiency is 80%.

Operational frequency (MHz)	1
Coil inductance (μH)	14.3
Coil resistance (Ω)	0.22
Coil Q-factor	411
Thruster inductance w/o plasma (μH)	8
Thruster resistance w/o plasma (Ω)	0.48
Thruster Q-factor w/o plasma	240
Thruster inductance w/ plasma (μH)	7.3
Thruster resistance w/ plasma (Ω)	5.1
Thruster Q-factor w/ plasma	9.4
Plasma resistance (Ω)	4.7
Coil current (A)	10.4
RFG current (A)	3.35
RFG power (W)	270
RFG power transferred to thruster (W)	258
RFG power transferred to plasma (W)	220
Mass utilisation efficiency	0.8
Power transfer efficiency	0.82
Field coupling coefficient	0.4

Table 5.4: Simulated performance and efficiency parameters of the DST thruster.

One has to realise that the LEOSWEEP mission requires two separate single-ended thrusters or one double-sided thruster. The ITT thruster's parameters currently chosen for the mission have already been discussed. However, the best thruster option for the IC purpose has not been selected yet. When choosing the thruster for the IC such aspects as the total power requirement, the weight/complexity of the entire system and the total propellant consumption have to be considered. Table 5.5 illustrates different thruster options that could potentially be used together with the ITT thruster. Observe that the DST thruster is included as well to check whether it is a viable candidate compared to the other thrusters. As can be observed from Table 5.5, regarding the lowest total power, the best thruster for the IC would be the SPT-70 (Goebel and Katz, 2008) or another similar Hall thruster. However, the Hall thrusters also need the largest amount of propellant for the mission. For instance, Table 5.5 shows that the SPT-70 and the ITT combination requires more than two times the amount of propellant compared to the DST.

IT	IC	Total power (W)	Total propellant mass (kg)
DST		2840	21
ITT	ITT	2928	30
ITT	RIT 15	2531	29
ITT	SPT-70	2050	47
ITT	NEXT	2350	38

Table 5.5: Comparison of different propulsion systems in terms of the total propellant and power requirements to fulfil the LEOSWEEP mission goals.

What is more, Table 5.5 indicates that the ring-cusp gridded ion engine NEXT (Patterson and Benson, 2007) and the ITT combination needs 15% more power and 20% less propellant compared to the combination with the Hall thruster. Furthermore, the DST uses 100 W less power than the combination of two single-sided ITT thrusters. Moreover, the DST requires about 300 W more power compared to the combination in which the RIT 15 (Leiter et al., 2000) is employed. However, it should be noted that the DST thruster presented in this analysis has not been optimised regarding the power and propellant requirements. Therefore, the DST results shown in Table 5.5 do not represent the best possible performance achievable by the thruster. Also, note that this study did not take into account the total system mass. It is expected that the DST would have the lowest total system mass of any two single-sided thruster systems, giving it a clear advantage. First, the reduction in mass would occur due to a simpler propellant feed system. Second, the DST is expected to be capable of operating with a single neutraliser. Third, the DST needs fewer power supplies compared to a two-thruster design. Finally, the mass of the DST thruster itself is estimated to be smaller than the sum of two thruster masses.

5.5.3   2D electromagnetic field distribution in plasma

To better understand how the DST thruster works and how it can be improved, 2D electromagnetic field and plasma interaction plots were produced, as shown in Figure 5.27. Note that the dashed lines represent the locations of the ion optics systems. The normalised ion density distribution h, as predicted for the DST, is depicted in Figure 5.27(a). As Figure 5.27(a) shows, the ion density ratio is maximum at the centre and decays to about 0.5 at the radial edge of the discharge chamber. Using the plasma density distribution from Figure 5.27(a) and the plasma properties from Table 5.3, Figure 5.27(b) illustrates the normalised electromagnetic heating magnitude W inside the plasma. Figure 5.27(b) shows that most of the power is transferred to the plasma next to the coil, while the power transfer to the rest of the plasma is negligible due to a finite skin depth and screening effects. Also, the maximum power transfer occurs in the middle of the discharge chamber's length due to the end coil effects.

(a) Ion density distribution.

(b) Normalised power absorption.

(c) Magnetic field.

(d) Normalised current density.
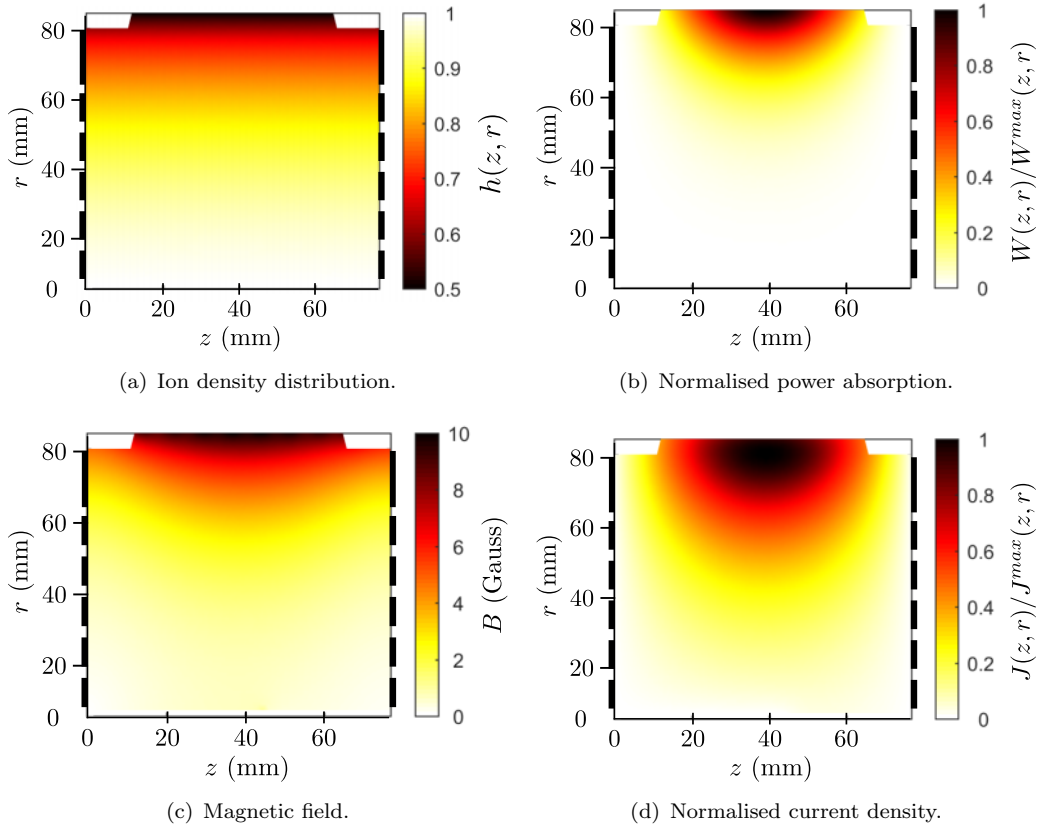
Figure 5.27: 2D electromagnetic simulations of the DST thruster plasma.

Figure 5.27(c) shows the magnetic field B distribution inside the plasma of the DST thruster. As Figure 5.27(c) illustrates, the maximum magnetic field value is about 10 Gauss, which occurs next to the coil. Also, the magnetic field decays rapidly away from the coil, with the majority of the plasma's volume being exposed to an approximately uniform magnetic field of about 2 Gauss. Finally, the current density distribution J normalised to the maximum value is shown in Figure 5.27(d). Figure 5.27(d) depicts that the maximum current density occurs approximately 6 mm away from the coil. This happens because in this region the electromagnetic heating is still high and the ion density is also much higher than that next to the wall.

5.5.4   2D neutral gas distribution

The propellant inlet system of the DST thruster is designed in such a way that the propellant enters through a flange on the IT side of the thruster. It was decided to investigate whether this would cause any substantial variation in the neutral gas density uniformity throughout the discharge chamber. This is important because variations in the neutral gas density might lead to ion densities being different at the axial extremes of the discharge chamber (IT and IC sides), which would make it difficult to predict the thrust magnitudes from each side and invalidate the assumptions that were made about

the thrust control in Section 5.3.2. Additionally, a neutral gas non-uniformity next to the ion optics system could lead to grid erosion and poor focusing due to the resulting variation in the ion density. Figure 5.28 displays the simulation results of the neutral gas density distributions in Configurations A and B. Note that in Figure 5.28, the neutral gas density is normalised to the maximum value. Also, the black regions in Figure 5.28 are indicative of the normalised neutral gas density that is higher than the maximum shown on the colour bar.

(a) Configuration A.
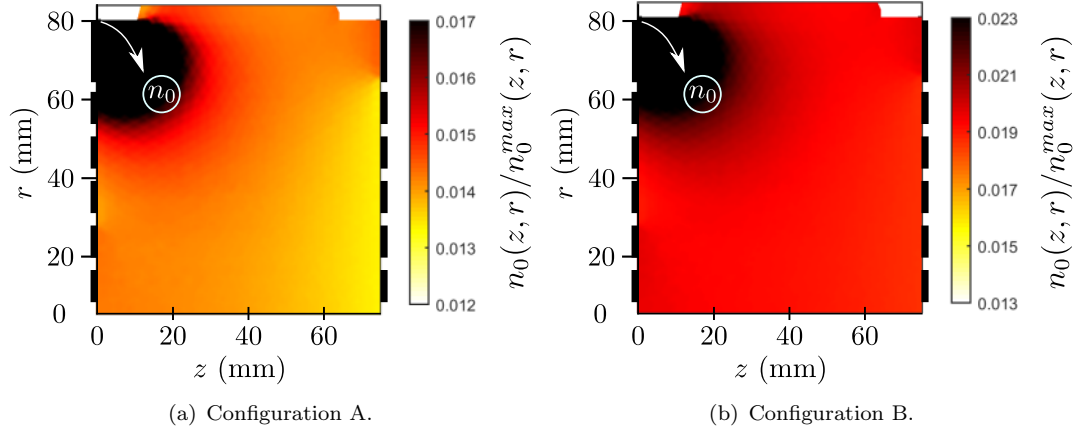
(b) Configuration B.

Figure 5.28: 2D neutral gas distribution in Configurations A and B. Simulated parameters: input mass flow rate = 15 sccm, total extracted ion current = 0.85 A, discharge chamber wall temperature = 450 K.

First, observe that the neutral gas density is at a maximum next to the location where the propellant enters the discharge chamber, as indicated by black spots in Figure 5.28. However, further away from the location of entry, the neutral gas density drops sharply and becomes about uniform. For instance, in Configuration A, the normalised neutral gas density varies from roughly 1.7% to 1.2% in the bulk of the discharge chamber volume, as depicted in Figure 5.28(a). Furthermore, in Configuration B, the normalised neutral gas density varies from 2.3% to 1.3%. The neutral gas density in Configuration B is higher than in Configuration A because the Clausing factor of the IC1 ion optics system is 0.67, while that of the IC2 ion optics system is 0.4. Also, the Clausing factor of the IT ion optics system is 0.18. Therefore, the IC1 ion optics system allows more gas to leak through the grids compared to the IC2 ion optics system, causing a decrease in the neutral gas pressure and density. Nevertheless, based on the results from Figure 5.28, a conclusion can be drawn that the neutral gas density is uniform in both configurations, except at a location directly next to the gas inlet opening. As a consequence, the ion density is expected to be uniform as well.

5.6   Summary

This chapter has presented a novel Double-Sided Thruster (DST) concept for the Ion Beam Shepherd (IBS) type missions. The main feature of the DST concept is that the thruster produces two ion beams from each end of the discharge chamber. The main advantage of the DST concept, compared to the originally proposed two-thruster design for the IBS missions, is a much simpler sub-system architecture with similar (or better) power and propellant requirements. In this chapter, a DST thruster has been designed and optimised to satisfy the LEOSWEEP mission requirements. Simulation results have shown that the DST thruster has to produce about 30% more thrust from the impulse compensation (IC) side compared to the impulse transfer (IT) side to meet the LEOSWEEP mission requirements. Also, simulations have indicated that the performance of the DST thruster is comparable to that of the ITT thruster which was specifically designed for the LEOSWEEP mission. For instance, the simulations have predicted that the most optimum screen grid voltage for the DST to work at is about 3 kV. Also, it has been predicted that the DST would need about 2.8 kW of power and 21 kg of propellant for the LEOSWEEP mission.

Finally, this chapter has presented a methodology behind the design of the DST thruster. In particular, the geometry, dimensions and materials of various thruster's components have been presented and discussed. The DST thruster features a 17 cm diameter discharge chamber that has the IT and IC ion optics systems installed at each of its openings. Also, the discharge chamber length is 7.67 cm and the coil has 8 turns. These geometrical parameters were determined by performing an optimisation analyses using the RF thruster model developed in this thesis. Furthermore, the DST thruster has been designed so it can be run in Configuration A and Configuration B. In Configuration A, the IT ion optics system composed of three carbon-carbon (C-C) grids is used, while the IC ion optics system employs a single SILUX (ceramic) grid (IC1). In Configuration B, the IT ion optics system is the same as in Configuration B. However, the IC ion optics system is composed of two titanium grids (IC2). Based on the theory presented in this chapter, for the IC side to achieve 30% more thrust compared to the IT side, the IC side has been designed with 24% more apertures. The next chapters will describe the experimental set-up and the experimental results of the DST thruster. The experimental campaign was aimed to prove that the thruster can extract two ion beams from each end of the discharge chamber and achieve about 30% more thrust from the IC side.

6

Experimental arrangements and procedures

This chapter presents the experimental arrangements and procedures that were used in testing both the DST and RIT 3.5 thrusters. In addition, the information about the equipment which was used and the way it was set-up is provided as well. The chapter starts with a discussion on the DST test campaign that was performed at the University of Southampton vacuum facilities. Next, the RIT 3.5 test campaign that was held in Germany, Giessen at the TransMIT vacuum facilities is described.

6.1 DST experimental campaign

6.1.1 Configurations and electrical set-ups

The DST was designed in such a way that it could be tested in multiple configurations. The figures below describe the type of the ion optics system used and the electrical set-up of each configuration. The first configuration is denoted as Configuration A. In Configuration A, the thruster uses a combination of the IT and IC1 ion optics systems, which were described in Chapter 5. Additionally, depending on which ion optics side is active, Configuration A can be run in three different modes. The first mode is called AIT, as indicated in Figure 6.1. In this mode, the IC side of the ion optics is blocked

with Kapton tape. Therefore, the ion beam is extracted only from the IT side. Such a configuration is useful when testing the performance of the IT ion optics side only. This helps gauging the thruster's, especially the ion optics, design and efficiency. Figure 6.1 also illustrates the electrical set-up of Configuration A. First, observe that the current I_c, supplied using the RFG, flows in the coil. Additionally, the screen grid is connected to the SCREEN (U_s) power supply, while the accel grid is connected to the ACCEL1 (U_{a1}) power supply. The decel grid is grounded. Furthermore, there are current measuring devices (A) installed in the SCREEN and ACCEL1 lines to measure the I_s^{it} and I_a^{it} currents, respectively.
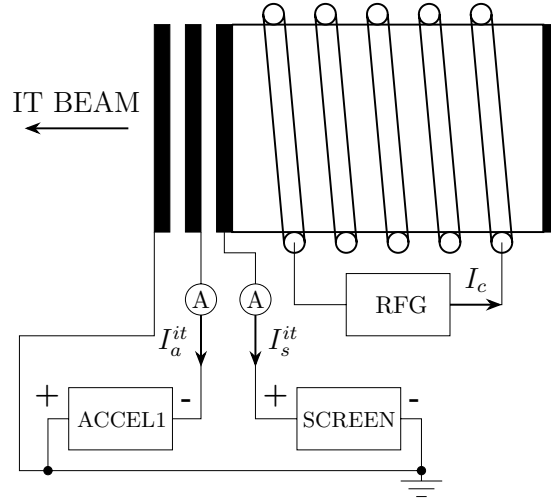
Figure 6.1: Configuration AIT: IT and IC1 ion optics systems are used, only IT is active. SCREEN – U_s, ACCEL1 – U_{a1}.

Similarly, in Configuration AIC, the IT side of the ion optics is blocked with Kapton tape while the beam is extracted from the IC1 ion optics system, as depicted in Figure 6.2. Notice that since the IC1 ion optics does not have a screen grid, the screen potential is provided using the SCREEN power supply connected to the screen grid of the IT ion optics system. Also, the aluminium tape on the IC1 grid is connected to the ACCEL2 (U_{a2}) power supply. Technically speaking, the current I_s^{ic} that is measured by the SCREEN power supply is not the actual current falling on the screen grid of the IC1 ion optics system since, as mentioned before, the IC1 ion optics system does not have a screen grid. Instead, I_s^{ic} is the electron current equivalent to the ion current that is extracted by the IC1 ion optics system. However, for clarity, the term "screen current" is still used when taking about the IC1 ion optics system throughout the thesis. What is more, note that since the IT and IC sides can be tested individually, it is possible to compare the performance parameters from each side independently. This is especially interesting since each ion optics system features a different design; that is, the number of apertures and the aperture dimensions of each ion optics system are different.

Finally, in order to check if the thruster could be run in the double-sided mode, both ion optics systems were opened. Such an operational condition is called Configuration
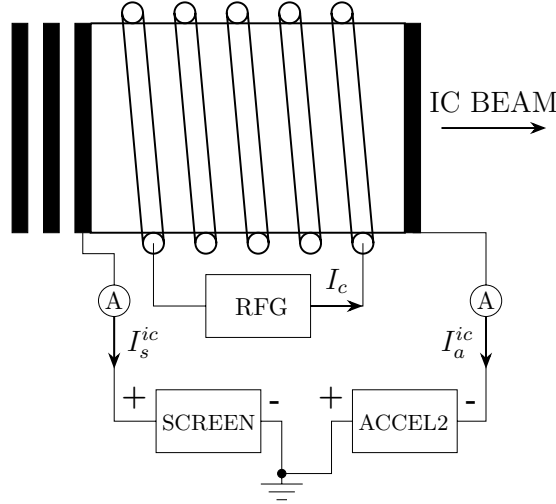
Figure 6.2: Configuration AIC: IT and IC1 ion optics systems are used, only IC is active. SCREEN – U_s, ACCEL2 – U_{a2}.

ADST, as shown in Figure 6.3. In Configuration ADST, as before, only a single RFG power supply is used. However, now there are three power supplies employed to provide voltages to the grids. On the IT side there are the SCREEN and ACCEL1 power supplies, while on the IC side there is the ACCEL2 power supply used. Note that since there is no screen grid on the IC side, the extracted currents from the IT side (I_s^{it}) and the IC side (I_s^{ic}) are processed by the SCREEN power supply. Therefore, the SCREEN power supply shows a sum $I_s^{it} + I_s^{ic}$ of the two currents. As a result, it is not possible to know the exact currents I_s^{it} and I_s^{ic} that are extracted from each side individually without performing the beam plume measurements using probes. Moreover, the current I_a^{it} shows the ion current falling on the accel grid of the IT ion optics, while the current I_a^{ic} represents the ion current hitting the conductive aluminium layer on the IC1 grid.
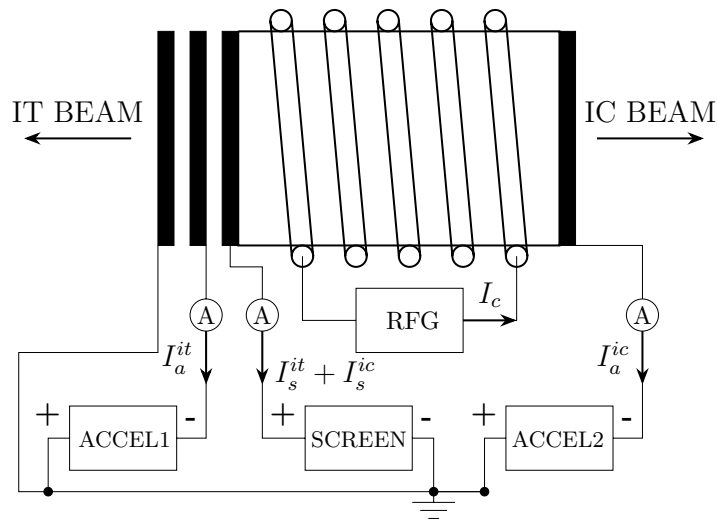
Figure 6.3: Configuration ADST: IT and IC1 ion optics systems are used, IT and IC are active. SCREEN – U_s, ACCEL1 – U_{a1}, ACCEL2 – U_{a2}.

Furthermore, Configuration B represents the DST thruster with a combination of the IT and IC2 ion optics systems. However, in Configuration B, the thruster is tested only in the double-sided mode. That is, both ion optics systems are active and two ion beams are simultaneously extracted from the IT and IC sides, as shown in Figure 6.4. The IC2 ion optics system does have a screen grid. Therefore, the current I_s^{ic}, that represents the actual electron current hitting the screen grid, is measured in the line connected to the SCREEN power supply. However, note that the SCREEN power supply still displays the sum of both currents. Configuration B allows tracking precisely how the I_s^{it} and I_s^{ic} currents change while varying the SCREEN/ACCEL voltages, RFG power and gas flow rate. This, in turn, enables the thrust values from each side to be determined.
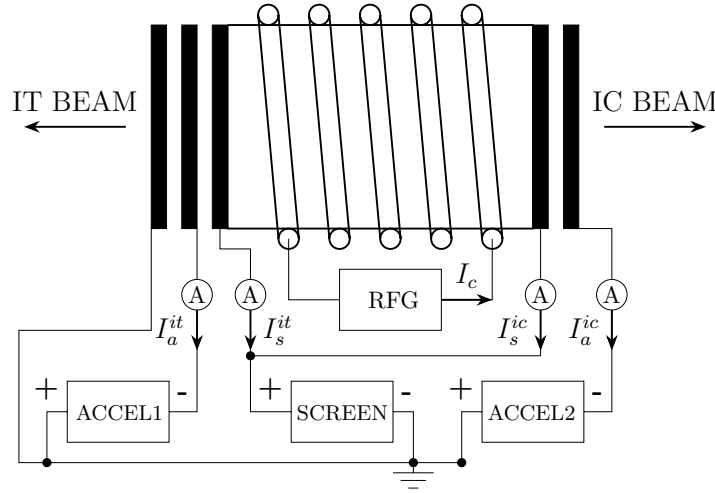
Figure 6.4: Configuration BDST: IT and IC2 ion optics systems are used, IT and IC are active. SCREEN – U_s, ACCEL1 – U_{a1}, ACCEL2 – U_{a2}.

6.1.2 Southampton University vacuum facility

University of Southampton vacuum facility consists of a test chamber and a loading chamber separated by a pneumatic, high vacuum isolation gate valve, as shown in Figure 6.5 and Figure 6.6. The test chamber has a diameter of about 1.9 m and a total length of about 4 m. Whereas, the loading chamber is approximately 0.75 m in diameter and length. The main test chamber is capable of reaching the base pressure in the range of 10^{-8} mbar using a combination of two turbopumps backed by a rough pump and two cryopanels (CP). Note that the DST thruster was tested only in the main chamber, with the vacuum isolation valve closed. Figure 6.7 depicts the schematic diagram of the facility. This diagram is displayed on a touch screen panel next to the facility, allowing easy control and monitoring of all the main facility's parameters.

Figure 6.5: Outside view of the University of Southampton vacuum test facility.

The generation of vacuum from atmospheric conditions in the test chamber takes place in a two-stage pumping procedure. First, a water cooled, dry compression screw pump FP1 (Oerlikon Leybold LV140C) is utilised to reach a pressure equal to about 10^{-2} mbar. Once a sufficient pressure is achieved, the roughing valve V4 is closed, and the rough pump starts acting as a backing pump. Then, the foreline valves V1 and V2 are opened, and the two magnetically-levitated turbo molecular pumps TP1 and TP2 (Oerlikon Leybold MAG W 2200 iP) are turned on to reach an ultimate pressure of about 10^{-8} mbar (with cryopanels on). The pressure in the test chamber is monitored by the Pirani gauge G1.
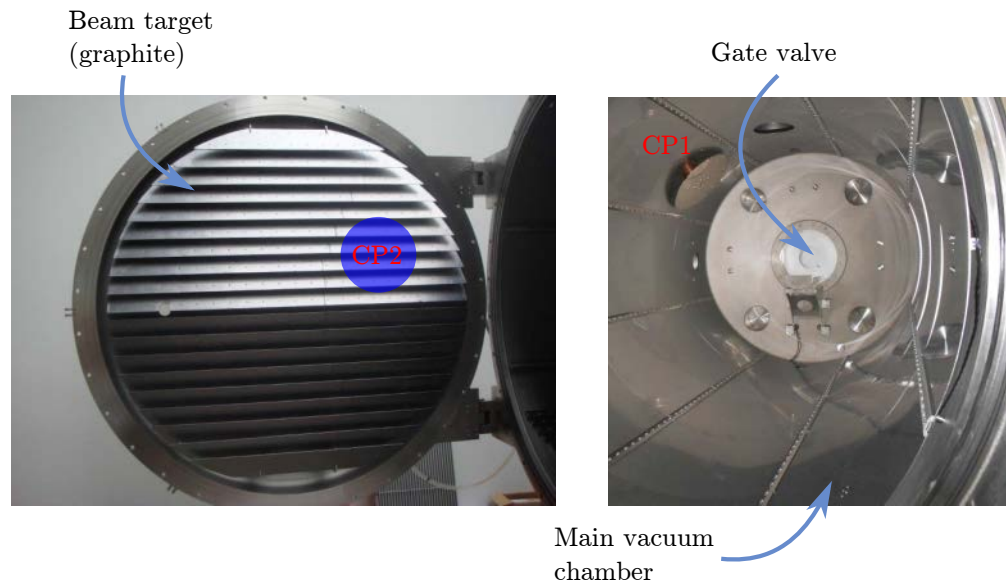
Figure 6.6: Graphite beam target and cryopanel locations inside the test chamber.

To increase the facility's pumping capacity when a thruster is operating, the facility is equipped with two coldheads (Coolpower 140T), the corresponding cryo compressors (Coolpack 6000H) and cryopanels CP1 and CP2. The locations of the cryopanels inside the test chamber are shown in Figure 6.6. The CP1 is attached to a flange facing towards the thruster testing platform. The CP2 is mounted between the graphite beam target and the test chamber door in order to reduce the cryopanel's exposure to the ion beam. The graphite beam target is used to prevent the ion beam from sputtering the test chamber. Therefore, the graphite covering acts as a sacrificial material. The cryopanels are able to reach temperatures down to about 20 K, thus gases condensate upon hitting the cryopanels. The cryopanels are equipped with Si-diodes, which allows the temperatures to be monitored and displayed on the control panel. For instance, the whole vacuum system is capable of operating at a pressure of about 10^{-5} mbar at around 15 sccm flow rate of xenon, which is a similar flow rate to that used while testing the DST.
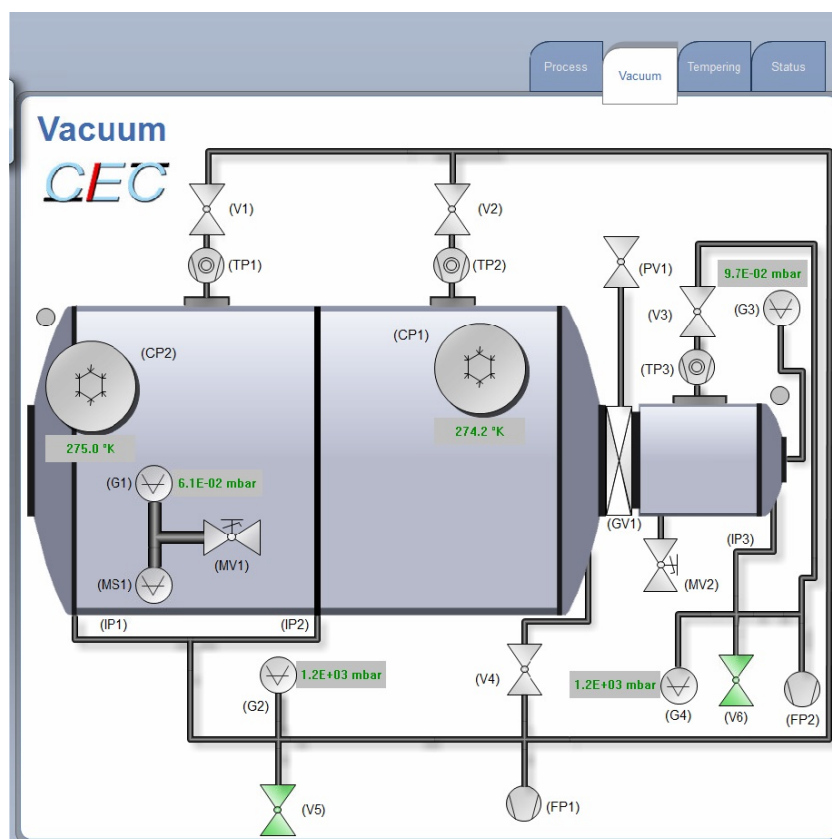
Figure 6.7: Vacuum facility's schematic digram indicating the main components and the control interfaces. The following labels are used: Valves - "V", gauges - "G", fore-pumps - "FP", turbo pumps - "TP", cryopanels - "CP", interstage pumping lines - "IP", manual valves - "MV", mass spectrometer - "MS", pressurised air valve - "PV", gate valve - "GV".

6.1.3 Test set-up

The main equipment that was used in the test set-up for the DST thruster is shown in Figure 6.8. As indicated in Figure 6.8, the test set-up consists of the following components: electrical power supplies for the ion optics, electrical power supplies for the RFG, data measuring/monitoring devices and a propellant management system. In the following sections, each set-up component will be described and discussed in detail.
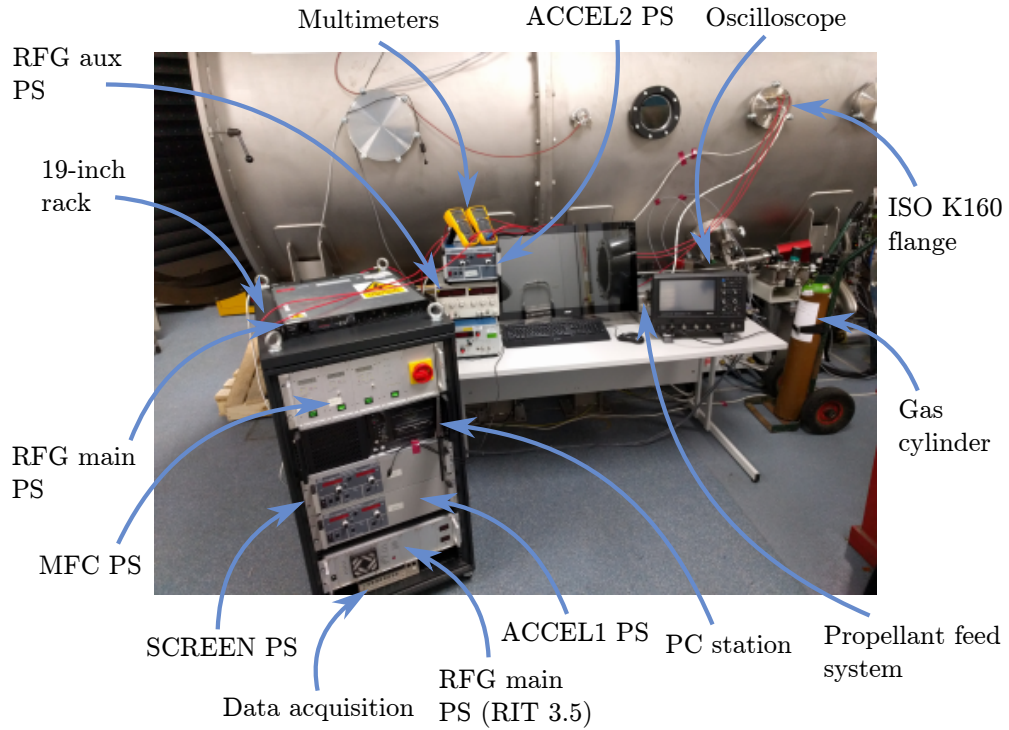
Figure 6.8: Overview of the DST thruster's set-up outside the vacuum facility.

6.1.4 Radio frequency generator

The discussion regarding the set-up is started with the RFG. In the test set-up, RFG-40 developed by Apcon was used to power the DST. RFG-40 is designed to provide up to about 100 W of power. Note that in Chapter 5 the DST was simulated with about 250 W of RFG power. However, at the time of testing, only RFG-40 was available. Nevertheless, it was expected that the goal of the thesis, which was to prove the DST concept, could be successfully achieved with only 100 W of RFG power. To operate the RFG, two power supplies are needed: the main and auxiliary (aux). The main power supply directly transfers power to the RF coil and then to the plasma. The magnitude of the RF power is controlled by varying the voltage V_{in} of the main power supply. This voltage is directly connected with the RFG's power stage. Since the power stage has Ohmic input characteristics, the total RFG power P_{in} supplied to the thruster is $P_{in} = I_{in} \times V_{in}$. Additionally, the RFG has a second DC input. It is used to provide

power to the control electronics, including the driver stage, the phase-locked loop (PLL) circuit and the oscillator.
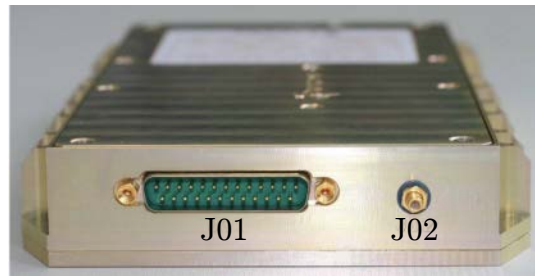
(a)

(b)

Figure 6.9: RFG-40 electrical interfaces.

The electrical interfaces of RFG-40 are shown in Figure 6.9. The details of each interface are summarised in the list below:

- J01 - connector interface to the main and auxiliary power supplies (type: male DAM15PNMB /FR023);

- J02 - isolated output for frequency data acquisition (type: SMB). Can be connected to an oscilloscope through a BNC connection;

- J03 - RF output interface (type: coax, LEMO). Can be loaded with a 50 Ω coaxial cable.

6.1.5   Propellant feed system

The DST thruster was tested using a laboratory grade gas flow control system. The flow control system's diagram is shown in Figure 6.10. As can be observed from the diagram, the propellant is supplied from a xenon bottle at a pressure set by the pressure reducer, which during the experiments was set to about 1.2 bar. The gas flow is controlled through two flow lines using the mass flow controllers MFC1 (line 1) and MFC2 (line 2). The line 1 is designed to be used for a neutraliser. However, since the DST was operated without a neutraliser, the line 1 was closed using the valve V2. The thruster was supplied with the propellant using the line 2.
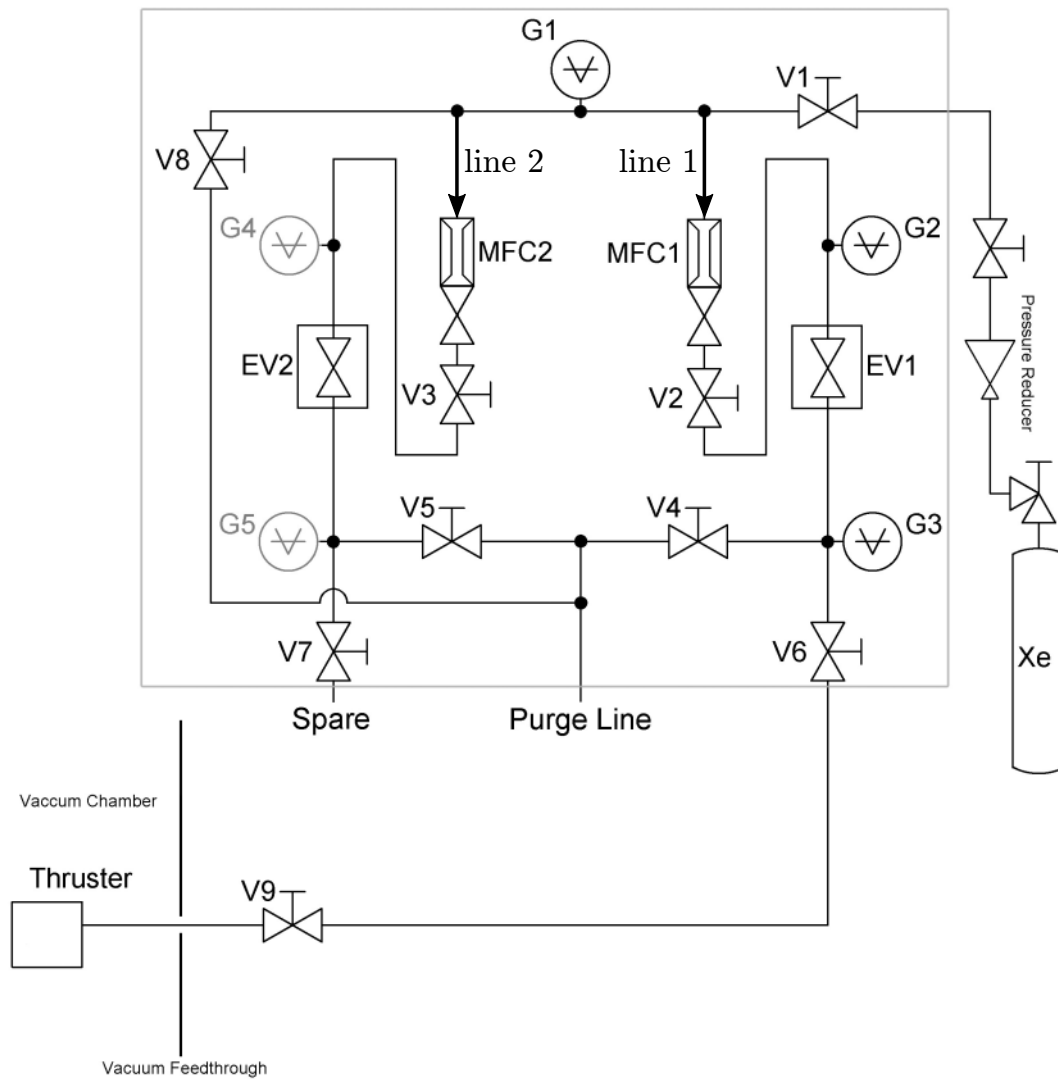
Figure 6.10: Propellant flow control system's diagram. Line 1 - flow through the MFC1, line 2 - flow through the MFC2.

A list of all the components used in building the flow system is given in Table 6.1. The mass flow controller utilised to supply the thruster with propellant was calibrated to be used with xenon. Note that during the experimental campaign, a xenon gas of grade 5.0 was used. Figure 6.11 depicts a fully installed flow control system at the University of Southampton vacuum test facility. Finally, note that propellant to the DST was supplied through a 1/8 inch Swagelok tube made out of Teflon that had 1/8 inch Swagelok connectors at each end. The connectors were installed onto a KF40 feedthrough flange, as illustrated in Figure 6.11.

Device	Component	Description
V1	Isolation Valve (manual)	Swagelok D=1/8 inch
V2	Isolation Valve (manual)	Swagelok D=1/8 inch
V3	Isolation Valve (manual)	Swagelok D=1/8 inch
V4	Isolation Valve (manual)	Swagelok D=1/8 inch
V5	Isolation Valve (manual)	Swagelok D=1/8 inch
V6	Isolation Valve (manual)	Swagelok D=1/8 inch
V7	Isolation Valve (manual)	Swagelok D=1/8 inch
V8	Isolation Valve (manual)	Swagelok D=1/8 inch
V9	Isolation Valve (manual)	Swagelok D=1/8 inch
EV1	Electrical Valve	Wagner, Art.Nr. 20001, Viton
EV2	Electrical Valve	Wagner, Art.Nr. 20001, Viton
MFC1	Mass Flow Controller	Bronkhorst EL-Flow 1.5 sccm
MFC2	Mass Flow Controller	Bronkhorst EL-Flow 15 sccm
G1	Analog Pressure Meter	Swagelok, 0 to 2.5 Bar, absolute
G2	Pressure Sensor P-025	Wagner, 0-250 mBar absolute, 0.25%
G3	Pressure Sensor P-025	Wagner, 0-1600 mBar absolute, 0.25%

Table 6.1: Propellant flow control system's components.
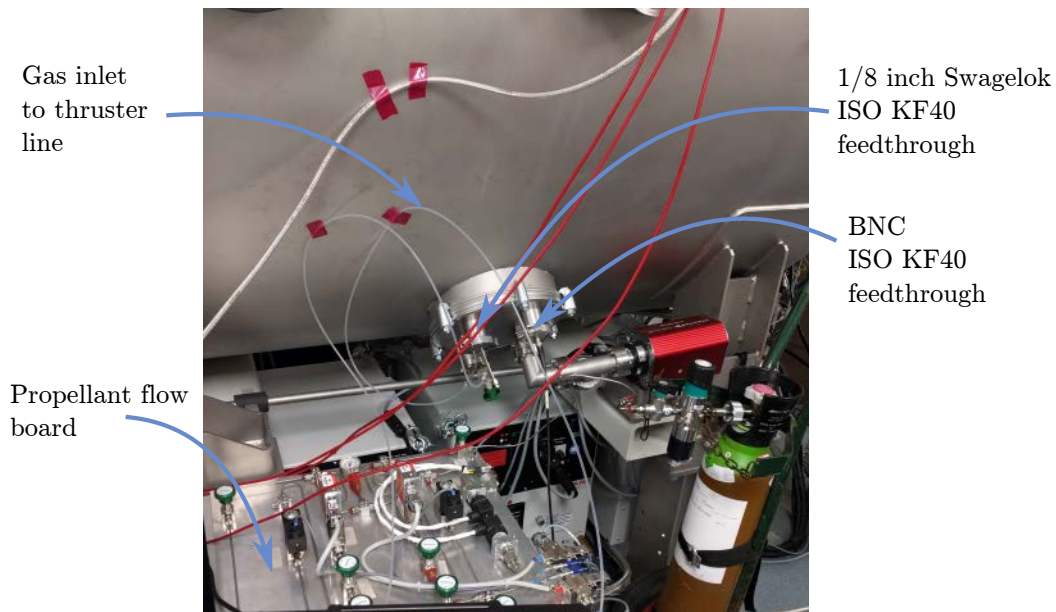
Figure 6.11: Fully installed propellant flow control system.

6.1.6 Power supplies and electrical interfaces

During the experimental campaign, all the main electrical power supplies were placed inside a 19-inch rack, as was shown in Figure 6.8. Other power supplies were located either on the rack itself or next to the rack on the table. A list of the electrical power supplies used during the experimental campaign is given in Table 6.2. Also, Table 6.2 provides properties of the RFG and oscilloscope.

Equipment	Instrument	Description
SCREEN PS	FUG HCP1400-3500	0-3500 V; 0-400 mA; SHV
ACCEL1 PS	FUG HCP350-2000	0-2000 V; 0-125 mA; SHV
ACCEL2 PS	FUG HCP35-3500	0-3500 V; 0-10 mA; SHV
RFG aux PS	AIM-TTI EL302RD	0-30 V; 0-2 A; Banana
RFG main PS	Sorensen XG 300-5.6	0-100 V; 0-5.5 A; Banana
MFC PS	Laboratory model, self-construction	0-24 V; 0-1 A; RS232
RFG	APCON RFG-40 100 W	0-50 V; 0-3 A; 1-4 MHz; LEMO
Oscilloscope	LeCroy Wavesurfer 3024	200 MHz, 4 GS/s; BNC

Table 6.2: List of electrical equipment used while testing the DST.

Figure 6.12 depicts the electrical feedthrough interfaces. As Figure 6.12 illustrates, all the connections were made on the K160 flange. The IT screen line was used to transmit (record) the I_s^{it} current, while the IC screen line was used for transmitting (recording) the I_s^{ic} current. Note that both these lines were at the same potential provided by the SCREEN power supply. Furthermore, except for the IC screen line (I_s^{ic}), all the power supplies were connected to the flange using SHV connectors. Remaining connections were made using push-pull LEMO connectors. Additionally, all lines from the high-voltage power supplies were connected in series to RF filters. This was done to filter out any RF noise that could damage the power supplies.
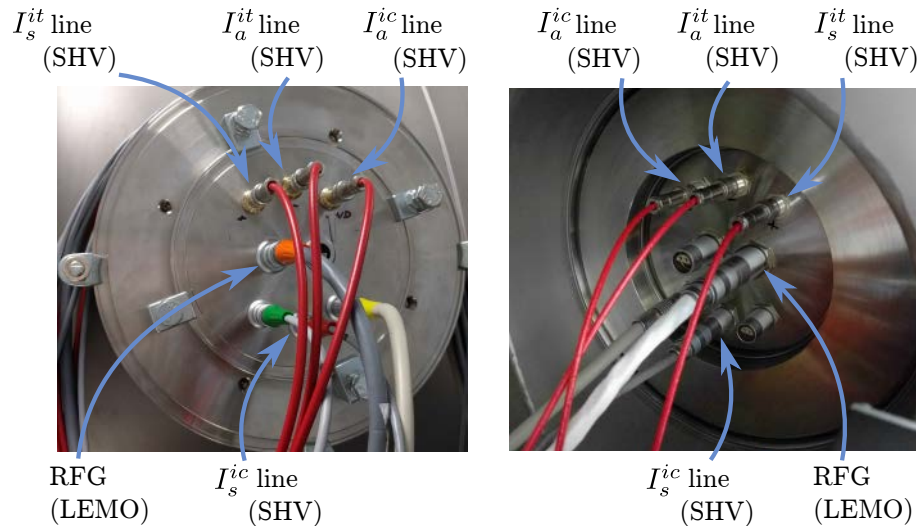
Figure 6.12: Electrical feedthrough interfaces on the K160 flange on the air side (left) and the vacuum side (right), as installed at Southampton University.

6.1.7 Thermal interfaces

To prevent RFG-40 from overheating it was mounted on a thermally conditioned cooling platform (i.e. a cooling plate), as displayed in Figure 6.13. The cooling plate was made out of copper and had integrated M8 copper tubes that were used to circulate water from the chiller. In the test configuration, the cooling plate had a cooling capacity of around 500 W, and temperature of the cooling plate over the full RFG operational envelope did not go above 25 °C (in the vacuum). Also, the copper plate had multiple M4 threads to provide mounting capabilities for different RFG models and various mounting racks. Finally, the copper tubes were connected through a KF40 feedthrough.
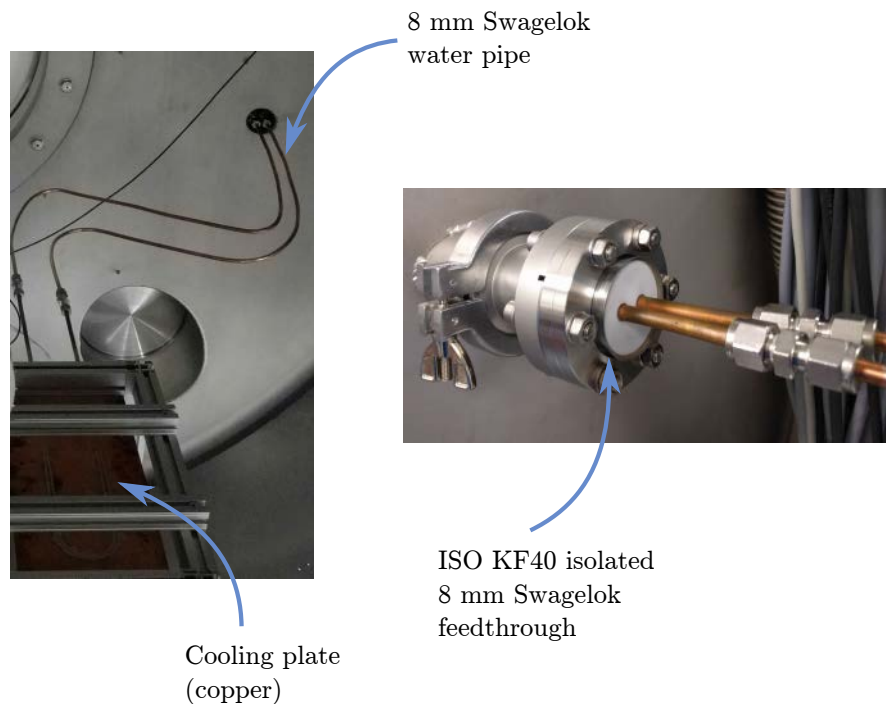
Figure 6.13: Thermally conditioned cooling platform and the cooling line connections.

6.1.8 Installation

The way the DST was installed on the support structure is shown in Figure 6.14. In particular, Figure 6.14(a) depicts the installation from the IC side. As can be seen, the RFG was installed directly underneath the thruster using two rails attached to the support structure. The DST thruster itself was attached using L-shaped aluminium brackets. One side of the bracket was attached to the rail of the support structure, while the other side was secured to the DST thruster's case which had 5 mm diameter holes drilled in. Note that the thruster's support structure was grounded. Therefore, the decel grid was connected directly to the thruster's support structure. Furthermore, the IT side of the thruster is shown in Figure 6.14(b). As Figure 6.14(b) illustrates,

the thruster was placed approximately in the middle of the test chamber since there were two ion beams coming from the thruster. The beam from the IT side was directed towards the graphite beam target, while the beam from the IC side was aimed towards a concave stainless steel sheet, as shown in Figure 6.14(b).
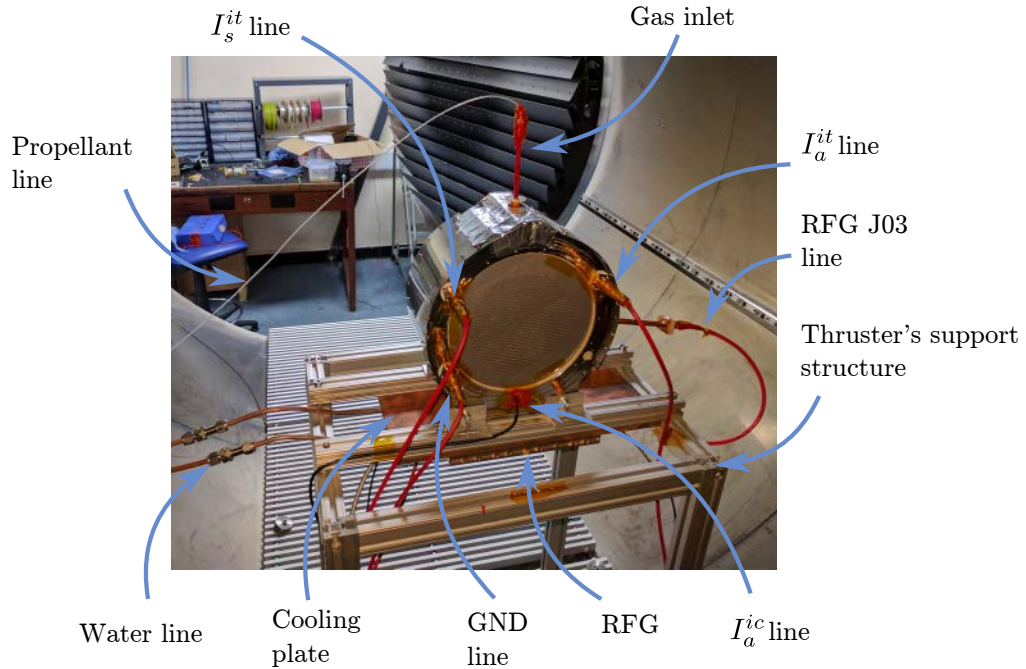
(a) IC side.
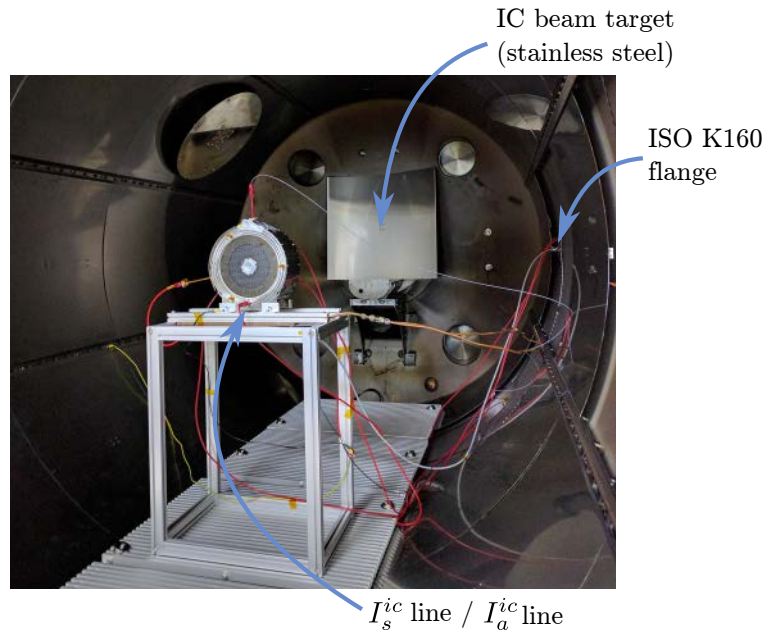
(b) IT side.

Figure 6.14: DST installation from the IT and IC sides inside the main chamber of the vacuum facility.

6.2   RIT 3.5 experimental campaign

The RIT 3.5 thruster was tested in Giessen, Germany at the TransMIT vacuum facility in order to collect experimental data for the RF thruster model, developed in the thesis, validation. A picture of the RIT 3.5 thruster is shown in Figure 6.15. Note that the RIT 3.5 thruster has a 3.5 cm diameter discharge chamber. The thruster itself was developed by Feili et al. (2015a) for the ESA's Next-Generation Gravity Mission (NGGM) to compensate for the drag force and to act as an attitude control device. To satisfy the NGGM requirements, the thruster was designed to operate from μN to mN (up 2 mN) thrust levels. For instance, during the experimental campaign, the RIT 3.5 thruster achieved thrust magnitudes from 50 μN to 2 mN with the total input power ranging from about 9 W to 75 W. Also, the RIT 3.5 thruster demonstrated specific impulse values varying from 300 s at 50 μN to about 3,700 s at 2 mN. Remember that a full list of data points measured during the experimental campaign is provided in Appendix A.
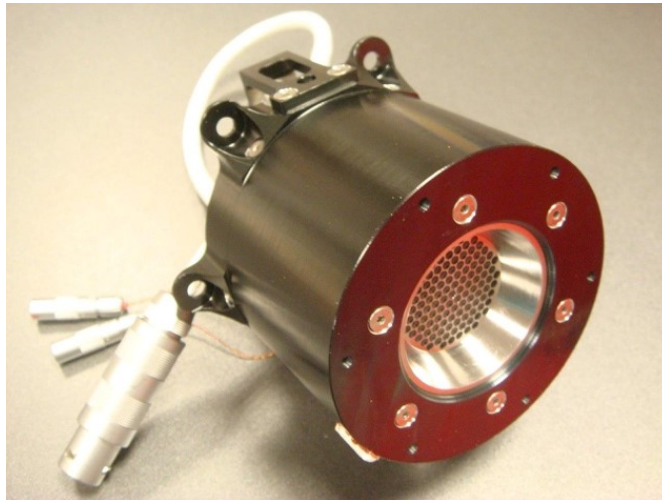
Figure 6.15: RIT 3.5 thruster designed for the NGGM mission. The thruster has a 3.5 cm diameter discharge chamber.

The objectives of the experimental campaign were to perform measurements of the thruster's performance at different RFG powers, propellant mass flow rates and ion optics voltages. Additionally, the thruster was equipped with multiple temperature sensors to measure temperatures of various thruster's components. As mentioned above, all the experimental data was used to validate the RIT 3.5 performance and thermal models developed in the thesis. In the following sections, the equipment that was used to obtain the experimental data will be discussed.

6.2.1   Electrical set-up

Figure 6.16 illustrates the RIT 3.5 thruster's electrical set-up diagram. In the diagram, the screen grid power supply is denoted as PHV, while the accel grid power supply is

denoted as NHV. The diagram also displays a neutraliser with the power supply NTR. However, note that during the experimental campaign, the neutraliser was not used. Similarly, the beam current controller was not used as well. Normally, the beam current controller is employed to regulate the beam current depending on the desired thrust value. Also, note that the thruster could be floated with respect to the facility's ground by referencing the thruster's chassis to the secondary star ground (SSG).
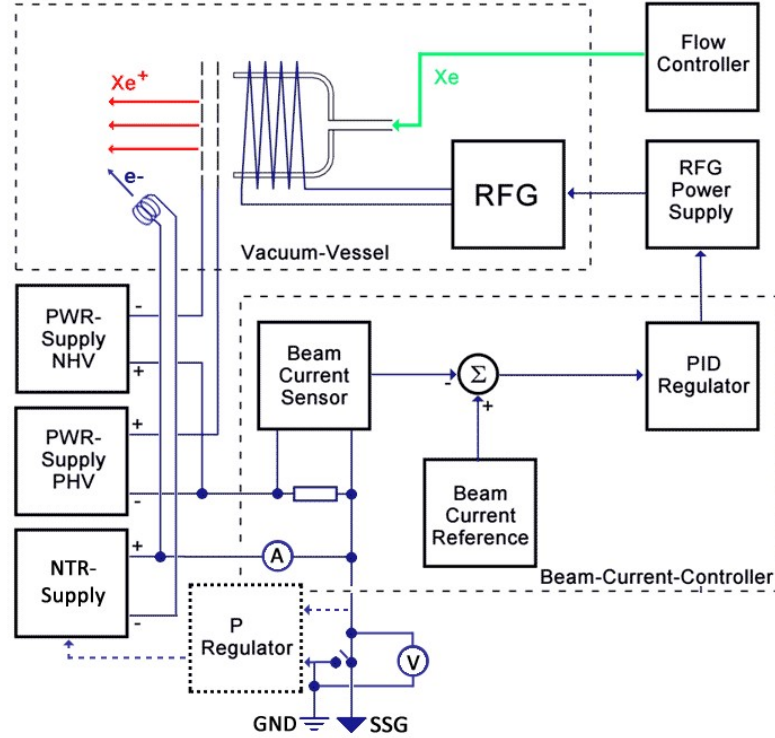
Figure 6.16: RIT 3.5 electrical set-up diagram. The beam current controller and the neutraliser (NTR) were not used during the experimental campaign. SSG stands for the secondary star ground, which was used to float the thruster with respect to the facility's ground.

6.2.2 TransMIT vacuum facility

The RIT 3.5 thruster was tested in the R2D2 vacuum test facility in Germany, Giessen, which is owned by TransMIT. A schematic of the facility and its main components, including the thruster's location, is shown in Figure 6.17. Whereas, an actual image of the facility is provided in Figure 6.18. Note that the facility has a volume of about 4.5 m^3. To pump down the facility, in the first stage, a vane pump and a root pump are used. In the second stage, four turbo molecular pumps backed by a rotary vane pump and a spiro molecular pump are employed. Additionally, two cryo vacuum pumps powered by a helium compressor are used to reach an ultimate vacuum level. Together these pumps have a pumping capacity of 30,000 ltr/s. The facility is able of reaching a

base pressure of 1.4×10^{-7} mbar. During the RIT 3.5 test campaign the pressure inside the vacuum facility did not go above 10^{-5} mbar for the mass flow rates of up to 1 sccm.
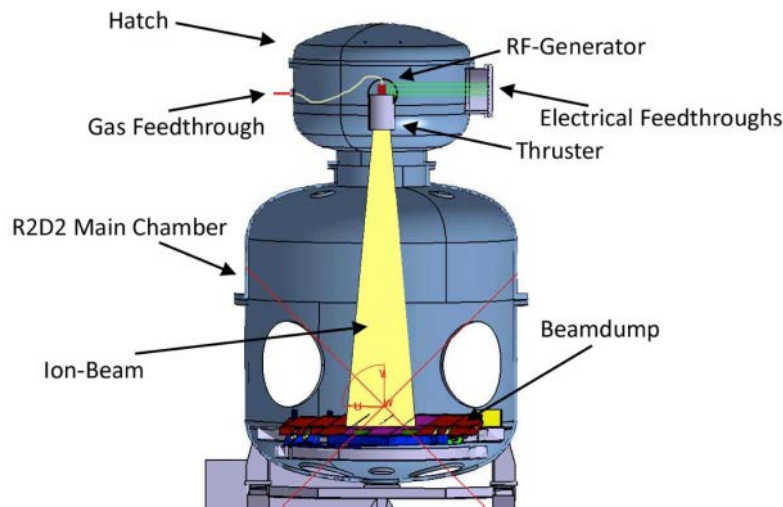
Figure 6.17: R2D2 facility's schematic diagram.

Figure 6.18: Actual image of the R2D2 facility.

6.2.3   Radio frequency generator

The RIT 3.5 experimental campaign was performed using RFG-60, as depicted in Figure 6.19. The RFG connections are the same as was discussed in Section 6.1.4 and therefore will not be reiterated. However, note that RFG-60 was protected with an input noise filter and an input current limiter to ensure a safe operation. Both items were combined in a filter-box located directly beside the RFG in the vacuum chamber.

(a)

(b)
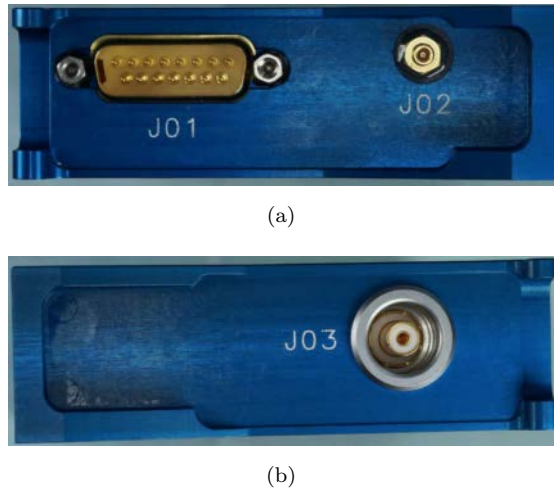
Figure 6.19: RFG-60 electrical interfaces.

6.2.4 Propellant feed system

The flow board system used in testing the RIT 3.5 was nearly exactly the same as the one defined in Section 6.1.5. The way the flow board was installed next to the R2D2 facility is depicted in Figure 6.20. There were, however, a few differences. First, the MFC1 (line 1) instead of the MFC2 (line 2) was used to run the thruster. Second, the line leading from the flow board to the flange was no longer made out of a Teflon tube. Instead, the line was made out of a stainless steel Swagelok tube. Note that as in the DST test campaign, the line pressure was set to 1.2 bar.

Figure 6.20: Propellant feed system installed next to the R2D2 facility.

6.2.5 Power supplies and electrical interfaces

The RIT 3.5 thruster was run using a majority of the power supplies indicated in Section 6.1.6. However, as illustrated in Table 6.3, the main RFG power supply was

different. Additionally, a data acquisition system was used to record the temperature values. All these devices, including the properties of the RFG, are listed in Table 6.3, where DQ stands for data acquisition. Observe that, similarly to the DST test campaign, all electrical connections were made through a K160 flange, as depicted in Figure 6.21.

Equipment	Instrument	Description
RFG main PS	Laboratory model, self-construction	0-35 V; 0-3.5 A; RS232
RFG	APCON RFG-60 60 W	0-20 V; 0-3 A; 1.8-3.2 MHz; LEMO
DQ System	Keithley Integra 2701	20 channels; RS232

Table 6.3: Additional electrical equipment used to test the RIT 3.5 thruster.
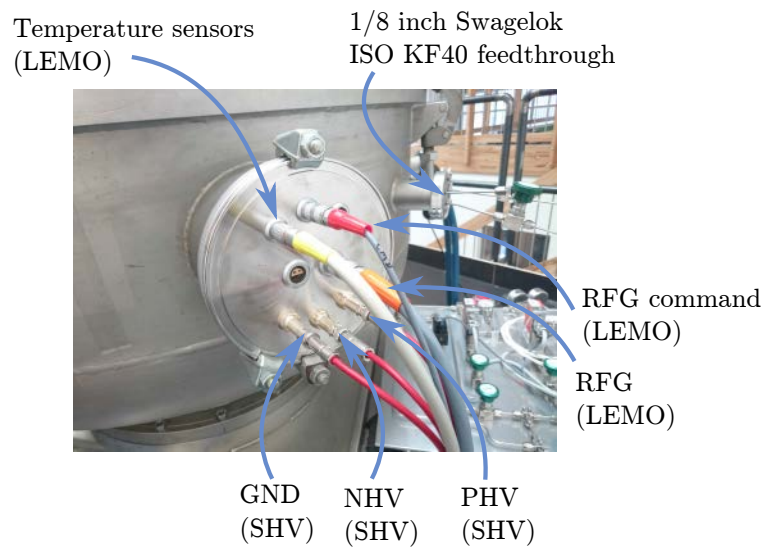
Figure 6.21: K160 flange with electrical interfaces installed on the R2D2 facility.

6.2.6   Installation

The RIT 3.5 thruster was attached to an aluminium mounting plate inside the R2D2 facility through 6 M4 titanium screws, as depicted in Figure 6.22. Furthermore, as can be observed from Figure 6.22, the RFG sits on a water-cooled copper plate inside the chamber. The whole set-up was installed inside the hatch of the R2D2 vacuum chamber. Note that the hatch is connected to the main chamber through a gate valve. While developing the thermal model it was aimed to mimic all the main installation features of the thruster, as depicted in Figure 6.22. In particular, it was critical to correctly model the contact conductances between the thruster and the mounting plate.
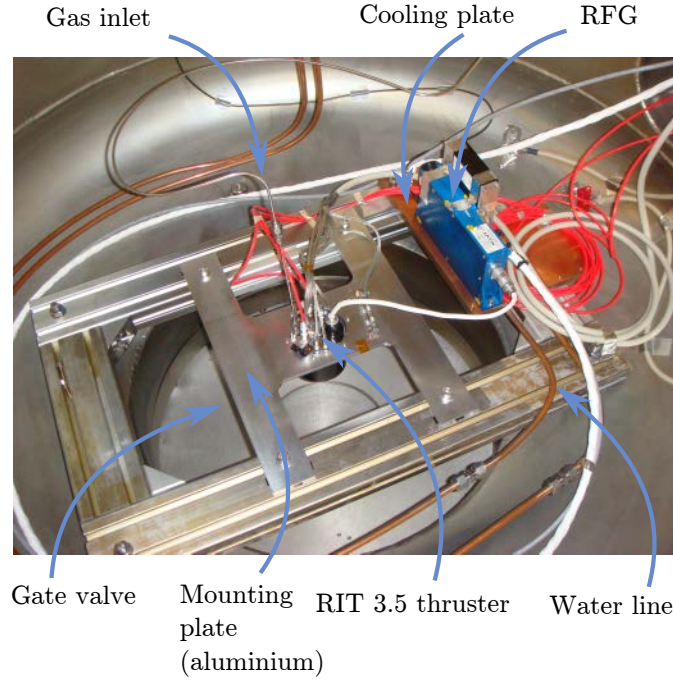
Figure 6.22: RIT 3.5 installation set-up inside the R2D2 vacuum facility.

6.2.7 Temperature sensors

The RIT 3.5 thruster was equipped with 8 PT100 temperature sensors capable of measuring temperatures from -200 to 850 ℃. The temperature values were obtained by processing the resistance magnitudes, as measured by the Keithley data acquisition device, using Labview. The temperature measurements were taken to prevent the thruster from overheating and to validate the thermal model. A schematic diagram illustrating the locations of the temperature sensors (TS) is shown in Figure 6.23. The following list describes the location of each temperature sensor in a more detailed manner: TS1 inserted in the insulation spacer between the second ("-") and third ("0") grids, TS2 inserted in the insulation spacer between the first ("+") and second ("-") grids, TS3 located on the gas inlet, TS4 located on the bracket holding the coil, TS5 placed on the discharge chamber, TS6 attached to the matching capacitor (C_1) connected to the coil, TS7 installed on the back plate of the thruster, TS8 attached to the outer thruster's housing (case).
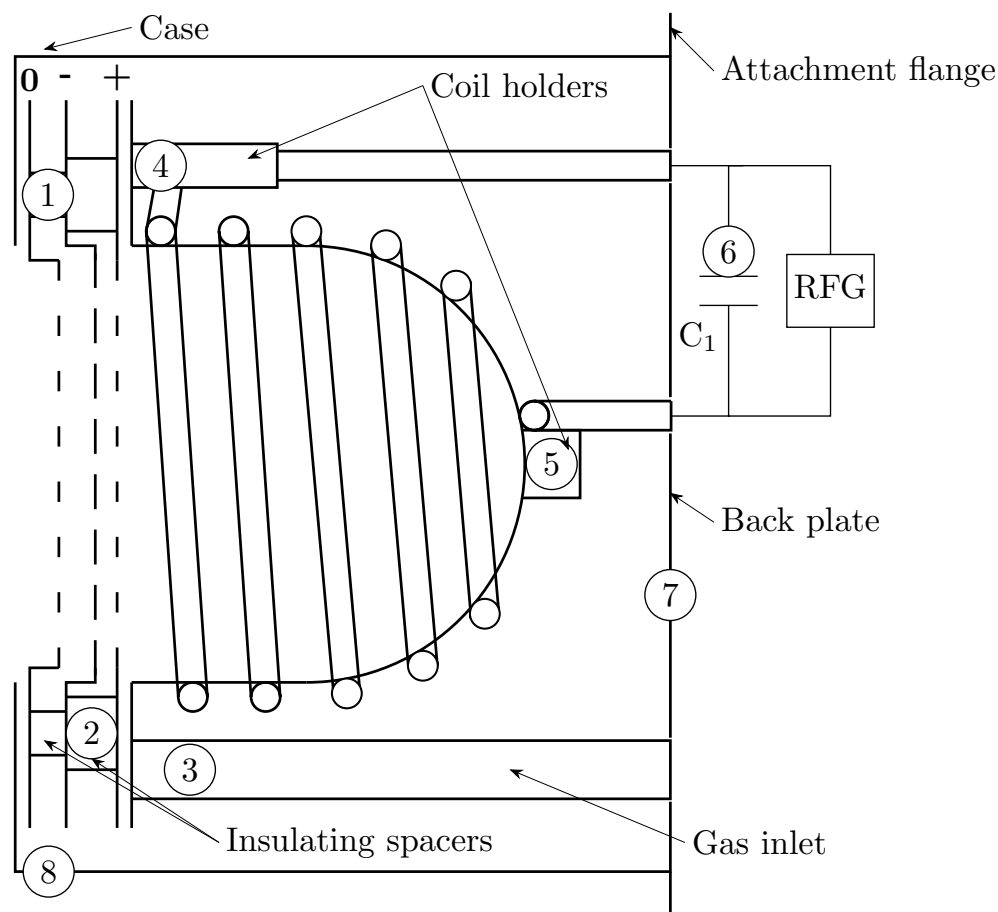
Figure 6.23: RIT 3.5 geometry and TS1 (1) to TS8 (8) temperature sensor locations. The ion optics system is denoted as: screen grid - "+", accel grid - "-", decel grid - "0".

The temperature sensors were glued to their defined positions with high temperature adhesive "Turbocoll Turboflex Thermo" which is resistant to temperatures of up to 350 ℃. The layer of the adhesive was less than 0.5 mm in thickness to ensure high thermal coupling and minimal temperature deviations. All of the sensors were embedded in a housing made out of a heat resistant ceramic medium "Thermokitt Roth" that withstands temperatures of up to 1,100 ℃. The ceramic medium was used to isolate the temperature sensors from electrical influences and provide structural strength to the wire junctions. The wires themselves were coated in Kapton tape and configured in a 4-wire double-twisted pair mode to increase the measurement accuracy. For instance, Figure 6.24 indicates the actual location of the TS7 temperature sensor on the back plate of the RIT 3.5 thruster. Figure 6.24 also shows the way the temperature sensors and other connections were installed.
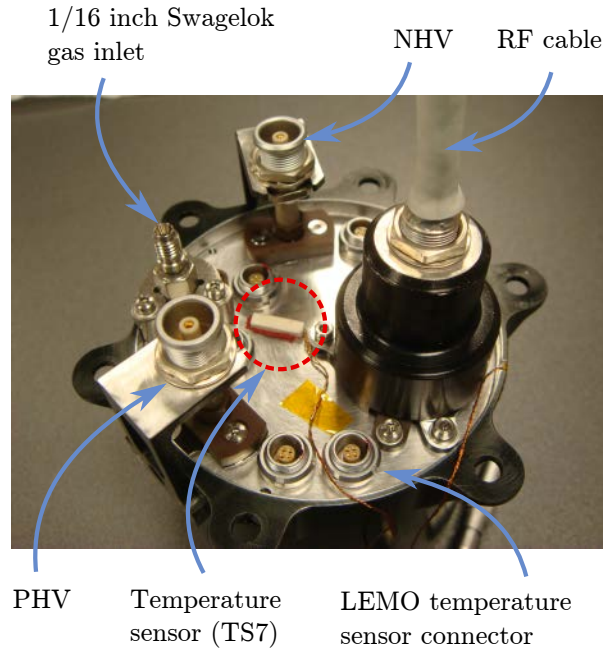
Figure 6.24: Back plate of the RIT 3.5 thruster indicating the set-up of temperature sensors and electrical connections. The TS7 temperature sensor can be seen attached to the back plate using red adhesive paste.

6.3   Summary

The chapter has presented the experimental arrangements and procedures that were used while performing the experimental campaigns of the DST and RIT 3.5 thrusters. In particular, the chapter has provided details of the power supplies, electrical connections, feedthroughs, propellant flow system, thermal interfaces and the installation set-up employed while performing the DST experimental campaign at the University of Southampton vacuum facility. A similar description was provided for the RIT 3.5 experimental campaign at the R2D2 TransMIT vacuum facility in Giessen, Germany. Also, the RIT 3.5 installation inside the R2D2 was discussed regarding the way the thruster was secured to the mounting plate. Finally, the properties and locations of the temperature sensors used to measure the RIT 3.5 temperatures and validate the thermal model developed in the thesis have been described and discussed. The next chapter will focus on presenting and analysing the DST thruster's experimental results.

7

DST experimental campaign: results and discussion

This chapter presents the main experimental results as obtained from the DST thruster test campaign at the University of Southampton. The goal of the experimental campaign was to prove that the double-sided thruster concept can be used for IBS type missions, especially the LEOSWEEP mission. Remember that for the LEOSWEEP mission, the DST thruster has to meet the following requirements. First, the thruster has to be able to produce ion beams from the IT and IC sides simultaneously. Second, the beam current extracted from the IC side has to be about $20 - 30\%$ larger compared to the IT side. Third, the thruster has to show that it can achieve a similar specific impulse regardless if run in the single-sided or double-sided modes. Additionally, the experimental campaign was needed to gauge the difference in the RFG power that needs to be supplied to the thruster while extracting two ion beams and while extracting only one beam. Finally, the experimental data was required to analyse how the variation of the RFG power and the screen/accel voltages affects the extracted beam current (or the thrust). The experimental results for each configuration are summarised in separate sections entitled as performance mapping. In the same sections, a performance analysis of the thruster based on the experimental results is also performed. In addition, there are sections dedicated to comparing and contrasting the results obtained while running the thruster in different configurations, as has been described in Chapter 6.

7.1   RFG configuration and ignition

Before the start of the experimental campaign, the RFG set-up was performed. To tune the RFG's matching network, the resistance and inductance values of the thruster were measured in various configurations using high-precision LCR tweezers at 10 kHz. The measurement results are summarised in Table 7.1. The matching network of RFG-40 was set-up in such a way as to have the thruster working at about 1.23 MHz throughout all operational conditions. Note that the operational frequency does change slightly with the plasma parameters since the RFG changes the frequency to perform matching. However, this change was observed to be only about 2%. Therefore, while analysing the experimental results it will be assumed that the thruster operates at 1.23 MHz exactly.

Parameter	Coaxial cable	Assembly	Value
Inductance	No	Coil and discharge chamber only	15.5 μH
Inductance	Yes	Coil and discharge chamber only	15.7 μH
Inductance	Yes	Fully assembled	11.37 μH
Resistance	No	Coil and discharge chamber only	30 mΩ
Resistance	Yes	Coil and discharge chamber only	80 mΩ
Resistance	Yes	Fully assembled	170 mΩ

Table 7.1: Resistance and inductance measurements for the DST thruster at various configurations.

As mentioned in Chapter 6, the power to the RFG was controlled with the RFG main power supply. Therefore, the total RFG power P_{in} was calculated as $P_{in} = I_{in} \times V_{in}$. Furthermore, the thruster was ignited using a pressure shock. The pressure shock was performed using the following steps. First, the line 2 of the propellant flow system, as has been depicted in Figure 6.10, was filled using the MFC2. The line was deemed to be full once the mass flow rate measured by the MFC2 would drop to zero. Then, the RFG was put in an ignition mode by setting the maximum current to 3 A and voltage to 35 V on the main RFG power supply, which meant that the power supply was working in a current-controlled mode. In the next step, about 1.5 kV was applied to the screen grid and -250 V to the accel grid. This was needed to produce a spark when the gas was released. Note that the spark generates a lot of background electrons helping to sustain the plasma. Finally, if successful, the thruster would ignite upon opening the valve V6.

The ignition method as described above was very reliable. The ignition was achieved at least 9 times out of 10. However, note that the RF class ion thrusters can also be ignited using a neutraliser, which is what is performed in space. The ignition is achieved by turning off the accel grid power supply and leaving the screen grid power supply on. This causes the electrons produced by the neutraliser to be accelerated to the screen grid. Some of the electrons are accelerated to sufficiently high energies to ionize the neutral gas background atoms. The electrons from the neutraliser and the background

electrons are then accelerated by the RF electromagnetic fields thus initiating the plasma discharge.

Once the thruster was ignited, both voltages on the ion optics grids were turned off to prevent the unstable plasma from damaging them. Additionally, since with the presence of the plasma the thruster's resistance goes up significantly, the RFG current would drop and the RFG power supply would go into a voltage-controlled mode. Therefore, to change the RFG power, it was simply enough to change the voltage setting of the main RFG power supply. After a minute or two, the pressure inside the propellant flow lines and thruster would stabilise. This regime with the plasma on is known as a standby mode. Then, the extraction would be started by applying voltages on the grids.

7.2 Configuration AIT

7.2.1 Performance mapping

The performance mapping was performed by running the thruster at different RFG powers while keeping the screen/accel grid voltages and the mass flow rate constant. Then, a different mass flow rate would be chosen and the process repeated. As mentioned in Chapter 6, the DST was operated in different configurations. The discussion is started by first analysing Configuration AIT. In Configuration AIT, the IC ion optics side is blocked. Therefore, the ion beam is extracted only from the IT side. Figure 7.1 shows the DST thruster in Configuration AIT with the extraction turned on. As can be seen in Figure 7.1(a), the IT ion optics system does not extract a beam from the middle of the grids since this area has no apertures and is blocked. By looking at the beam from the side in Figure 7.1(b), it can be seen that the beam divergence is quite low. In the same figure, it can also be observed that the IC1 ion optics system emits a lot of light but there is no beam. This is because the Kapton tape that was employed to block the apertures is nearly transparent. In addition, the SILUX material used to manufacture the screen grid transmits a lot of light from the plasma.

The performance mapping results are presented by plotting the screen grid, accel grid, and the RFG currents as functions of the RFG power at different mass flow rates. The mass flow rates go from 3.0 sccm to 7.0 sccm in 0.5 sccm increments, which encompasses a broad range of operating conditions. In Configuration AIT, the performance mapping was performed at the screen grid voltages of 1 kV, 1.5 kV, 2 kV, 2.5 kV and 3 kV. However, only the results for 1.5 kV are presented in this section. The remaining results are provided in Appendix C. Such a screen grid voltage was chosen because the IC1 ion optics system could not work with more than 1.5 kV without producing sparks. Therefore, while testing the thruster in the double-sided configuration, the voltage of the IT side had to be limited to 1.5 kV as well. This is because, as discussed previously, in the

double-sided mode the IT and IC ion optics systems are subjected to the same screen grid voltage due to the plasma coupling. As a result, when analysing Configuration ADST, the experimental results only for the 1.5 kV case are presented, as will be seen in the following sections.
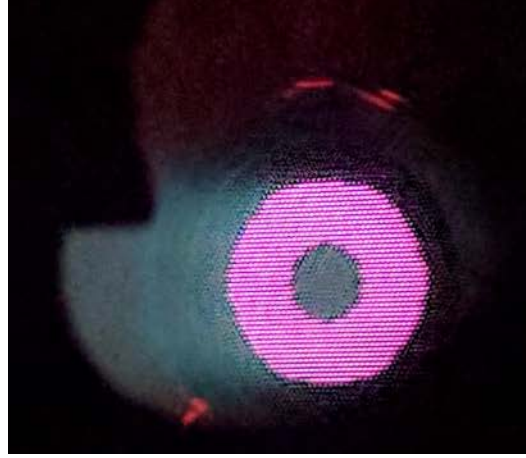
(a) Front.

(b) Side.

Figure 7.1: Extracted ion beam from the IT ion optics side in Configuration AIT as seen through two different view ports.

As already mentioned, the IC1 ion optics system was producing arcs above about 1.5 kV. The arcing occurred because the IC1 grid could not hold off the electric field between the plasma and the aluminium layer. In particular, it was suspected that the aluminium layer was not completely uniform and flat, and had "dirty" spots with a lot of oxides and impurities. All these imperfections degraded the voltage hold-off capability of the grid. Additionally, the voltage hold-off capability of the grid could have been reduced by background neutral gas atoms assisting the secondary electron production. This is because the Clausing factor of the IC1 ion optics system was about 0.67, which is high considering that the Clausing factor of the IT ion optics system was about 0.19. It is possible to improve the voltage hold-off capability of the IC1 grid by increasing the grid thickness and thus reducing the effective electric field. Additionally, aluminium could be replaced with a material that has a better voltage hold-off capability, for instance, molybdenum. Finally, the aperture diameter can be decreased to reduce the Clausing factor.

Figure 7.2: Configuration AIT: IT side screen grid current at various mass flow rates vs RFG power ($U_s = 1.5$ kV, $U_{a1} = -250$ V).

Figure 7.2 shows how the screen current I_s^{it} varies with the RFG power. From Figure 7.2, it can be observed that as the RFG power goes up, the screen current increases as well. At the RFG power of up to about 70 W, the growth in the screen current is nearly linear. However, as the RFG power goes past 70 W, the screen current starts to flatten out. The maximum screen current achieved is about 76 mA at 3.5 sccm and 105 W of RFG power. Additionally, Figure 7.2 indicates that for the same RFG power, as the mass flow rate increases, the screen current rises as well. For instance, it can be estimated that at 80 W the difference in the screen currents between the 3.0 sccm and 7.0 sccm cases is about 5 mA. This difference, however, becomes more significant as the RFG power increases.

The accel current I_a^{it} also increases with the RFG power, as illustrated in Figure 7.3. If the ion focusing is somewhere between the under-perveance and over-perveance limits, there should be no ions hitting the accel grid directly. Therefore, the accel current should be caused mainly by charge exchange ions. However, as the gas flow rate increases, there are more neutral atoms in the gap between the grids, which translates into a higher rate of charge exchange ion generation and thus a larger accel current. Furthermore, the increase in the RFG power rises the number of ions in the beam. The increase in the accel current with the mass flow rate is seen in Figure 7.3. Also, observe that, at the same RFG power, the difference in the accel currents between different mass flow rates grows larger with rising RFG power. For instance, at 90 W and 7.0 sccm, the accel current reaches its maximum value of about 3 mA. This means that at this point the

accel current is about 5% of the screen current, which is indicative of the fact that a majority of the accel current is caused by charge exchange ions. If it were otherwise, the percentage of the screen current collected by the accel grid would be much larger. As a result, it can be concluded that in Configuration AIT, the ion optics system was working near its optimum perveance at the mass flow rates and RFG powers tested.
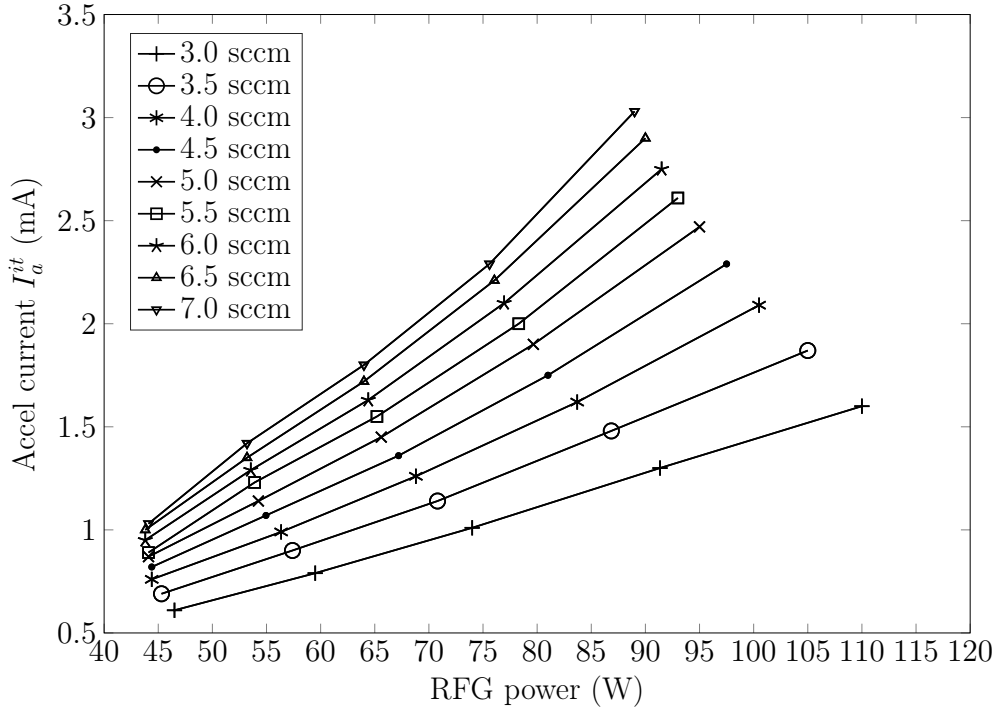
Figure 7.3: Configuration AIT: IT side accel grid current at various mass flow rates vs RFG power ($U_s = 1.5$ kV, $U_{a1} = -250$ V).

Finally, Figure 7.4 depicts the RFG current variation with the RFG power at different mass flow rates. As can be discerned from Figure 7.4, the RFG current goes up with the RFG power in a linear fashion. Note that the way in which the RFG current behaves is strongly influenced by the plasma parameters such as plasma density and pressure. For instance, an increase in the mass flow rate causes a rise in the neutral gas pressure in the plasma. This translates into the plasma density increase which in turn causes the total thruster's resistance to go up. Therefore, due to Ohm's law, the current must go down if the RFG power is to be kept the same. As a result, it can be predicted by looking at Figure 7.4 that since, for the same RFG power, the RFG current decreases as the mass flow rate rises, the ion density must be going up. It should be noted that an increase in the thruster's temperature can also cause a decrease in the RFG current due to the increased induced impedance. However, at the RFG power of up to 100 W, the temperature effect is much less pronounced compared to the change in the ion density.

Figure 7.4: Configuration AIT: RFG current at various mass flow rates vs RFG power ($U_s = 1.5$ kV, $U_{a1} = -250$ V).

7.2.2 Performance analysis

In this section, the data from performance mapping is used to analyse the performance of Configuration AIT. First, the discharge loss is plotted in Figure 7.5. As the figure indicates, the discharge loss decreases as the mass utilisation efficiency rises. This decrease is very steep at low mass utilisation efficiencies. However, at higher mass utilisation efficiencies, the discharge loss starts levelling off. The mass utilisation efficiency at which the levelling off occurs goes up as the mass flow rate decreases. What is more, for a constant mass utilisation, the discharge loss falls as the mass flow rate increases. For instance, at a mass utilisation efficiency of 0.3, at 3 sccm the discharge loss is about 1,500 W/A, whereas at 3.5 sccm it is about 1,400 W/A. Note that the RIT 10 thruster, for example, exhibits a discharge loss of about 460 W/A. Nevertheless, as mentioned before, the DST thruster was not optimised for efficiency, but, rather, its design was driven by the IBS type mission requirements which are a low beam divergence and a high ion energy. Finally, as depicted in Figure 7.5, the mass utilisation efficiencies at the mass flow rates tested do not go above about 0.35. This is because of the 100 W RFG power limit imposed by RFG-40. To increase the mass utilisation efficiency to about 0.9, the RFG power would have to be around 250 W.

Figure 7.5: Configuration AIT: discharge loss at various mass flow rates vs mass utilisation efficiency ($U_s = 1.5$ kV, $U_{a1} = -250$ V).

The specific impulse, on the other hand, increases in a linear fashion with the RFG power and goes down as the mass flow rate rises, as depicted in Figure 7.6. In Configuration AIT, it was possible to reach a specific impulse of about 1,600 s at 3 sccm and 107 W of RFG power. The RIT 10 thruster, for example, can achieve a specific impulse of about 3,400 s. Again, in order to get to higher specific impulse values, more RFG power would be needed. The total efficiency behaves in a nearly the same fashion as the specific impulse, as shown in Figure 7.7. The maximum total efficiency achieved is approximately 16% at 107 W of RFG power and 3 sccm.
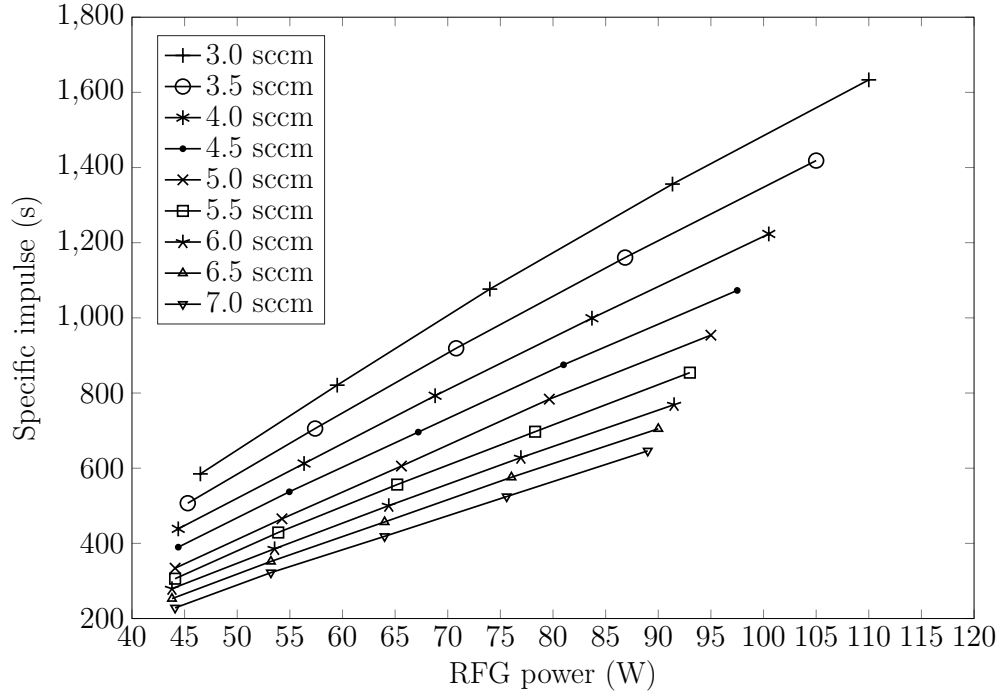
Figure 7.6: Configuration AIT: specific impulse at various mass flow rates vs RFG power ($U_s = 1.5$ kV, $U_{a1} = -250$ V).

In Figure 7.8, a variation in the total power (RFG + beam power) needed to achieve a particular thrust magnitude is plotted. Note that the thrust values were obtained using Equation 2.11 and plugging in the measured screen current and voltage. As Figure 7.8 illustrates, in this configuration, it was possible to achieve around 4.6 mN of thrust at about 220 W of total power. In addition, the plot indicates that the relationship between the thrust and total power is almost linear. As a result, by extrapolating the trend, it can be estimated that the total power needed to produce 30 mN would be around 1.4 kW. However, at the screen grid voltage of 1.5 kV, the momentum transfer efficiency to the target is only about 0.35, as has been shown in Figure 5.25(b). Therefore, the IT side would, in fact, need to produce about 85 mN of thrust to transfer 30 mN to the debris as per LEOSWEEP mission requirements. Again, using the linear thrust to total power relationship, it can be seen that 4 kW of total power would be needed to produce 85 mN of thrust. This is very inefficient, and therefore, in reality, a much higher screen grid voltage would be used. As mentioned before, results only for the 1.5 kV case are presented in this section because such a voltage was the maximum at which the IC1 ion optics system could work.
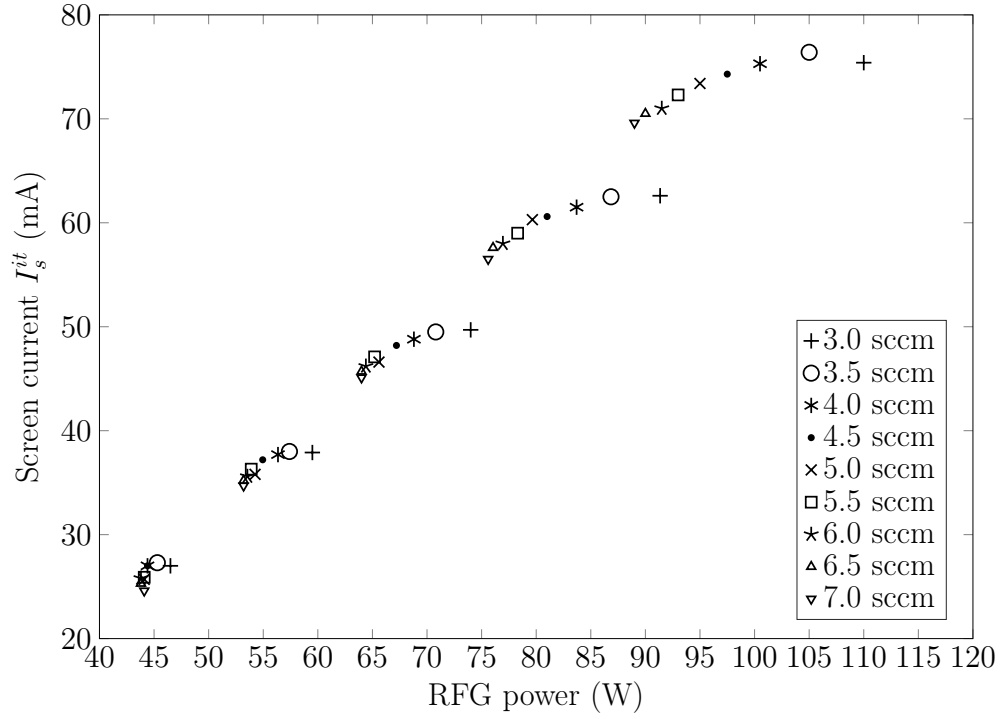
Figure 7.7: Configuration AIT: total efficiency at various mass flow rates vs RFG power ($U_s = 1.5$ kV, $U_{a1} = -250$ V).

Figure 7.8: Configuration AIT: total power at various mass flow rates vs thrust ($U_s = 1.5$ kV, $U_{a1} = -250$ V).

7.3 Configuration AIC

7.3.1 Performance mapping

Similarly, in this section, performance mapping for Configuration AIC is performed. Remember that in this configuration, the IT ion optics side is blocked. Therefore, the ion beam is extracted only from the IC side. Figure 7.9 shows the DST thruster in Configuration AIC with extraction turned on. As can be seen from Figure 7.9(a), on the IC side the beam is extracted throughout all of the grid area, which was not the case for the IT side. Just by qualitatively looking at the beam from the side in Figure 7.9(b), it can be seen that the beam divergence is higher compared to that from the IT side, which has been shown in the previous section.

(a) Front.

(b) Side.

Figure 7.9: Extracted ion beam from the IC ion optics side in Configuration AIC from two different view angles.

As in Configuration AIT, the performance mapping is performed by plotting the screen grid, accel grid, and the RFG currents as functions of the RFG power at different mass flow rates. Figure 7.10 depicts the screen grid current I_s^{ic} variation with the RFG power. Note that, as mentioned previously, the screen current plotted in Figure 7.10 represents the electron current collected by the screen grid on the IT side since the IC1 ion optics system does not have a screen grid. Additionally, note that in this configuration, the

accel voltage U_{a2} was set to -200 V. This accel voltage value was found to produce the lowest magnitude of accel current, increasing the thruster's efficiency.
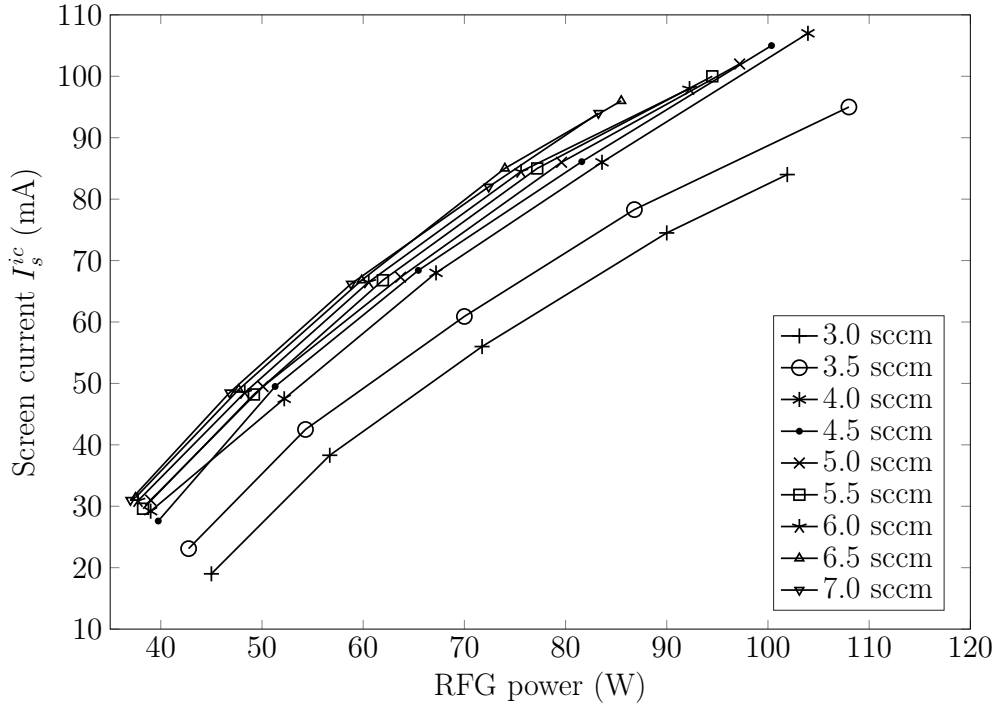

Figure 7.10: Configuration AIC: IC side screen grid current at various mass flow rates vs RFG power ($U_s = 1.5$ kV, $U_{a2} = -200$ V).

Similarly to what was observed while analysing Configuration AIT, it can be seen from Figure 7.10 that as the RFG power goes up, the screen current increases as well. The maximum screen current achieved in this case is nearly 107 mA at 4 sccm and 105 W of RFG power. This is about 30 mA (or 40%) more compared to the screen current obtained in Configuration AIT at similar operational conditions. Also, in Configuration AIC, the levelling off of the screen current as the RFG power rises is more pronounced. Furthermore, at a constant RFG power, a change in the mass flow rate causes a bigger difference in the screen current compared to Configuration AIT.

As with the screen current, the accel current I_a^{ic} also increases with the RFG power, as depicted in Figure 7.11. The reason for this has to do with the charge exchange phenomenon occurring in the space between the grids, as mentioned before. For instance, at about 85 W and 7.0 sccm, the accel current reaches its maximum value of roughly 2 mA, which is about 2% of the screen current. However, since there is no physical accel grid as in Configuration AIT, it cannot be concluded that the ion focusing is in the optimal perveance range. This is because ions could be hitting the ceramic (non-conductive) part of the IC1 grid and no current would be observed. Finally, the RFG current variation with the RFG power is shown in Figure 7.12. Again, similarly

to Configuration AIT, the RFG current goes up as the RFG power rises, and, for a constant RFG power, decreases as the flow rate increases.

Figure 7.11: Configuration AIC: IC side accel grid current at various mass flow rates vs RFG power ($U_s = 1.5$ kV, $U_{a2} = -200$ V).
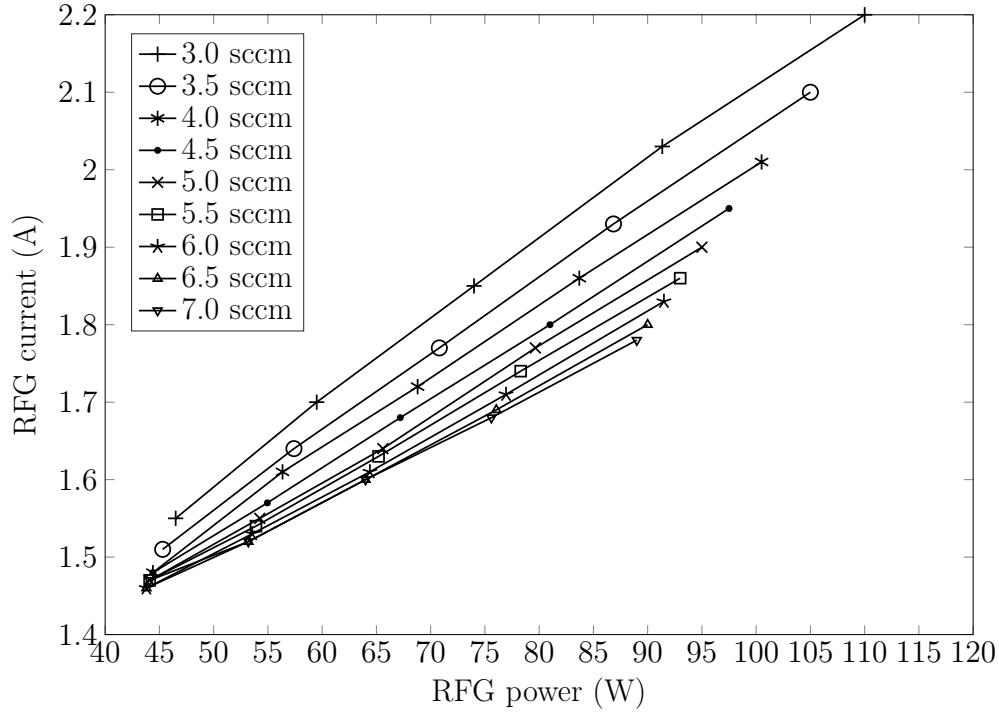

Figure 7.12: Configuration AIC: RFG current at various mass flow rates vs RFG power ($U_s = 1.5$ kV, $U_{a2} = -200$ V).

7.3.2   Performance analysis

Figure 7.13 demonstrates how the discharge loss varies as a function of the mass utilisation efficiency. The trends observed in Figure 7.13 are similar to the ones seen in Configuration AIT. In Configuration AIC, however, since the screen current is higher, the maximum mass utilisation efficiencies reached are higher as well. For instance, at 3 sccm, the maximum mass utilisation efficiency is about 0.4 and the discharge loss is approximately 1,200 W/A, while the mass utilisation efficiency is 0.35 and the discharge loss is 1,500 W/A at the same mass flow rate in Configuration AIT. Due to the higher mass utilisation efficiencies, a specific impulse of nearly 1,800 s is attained at 3 sccm and 100 W of power, as displayed in Figure 7.14. Also, the maximum total efficiency has risen to about 20% as well, as displayed in Figure 7.15.
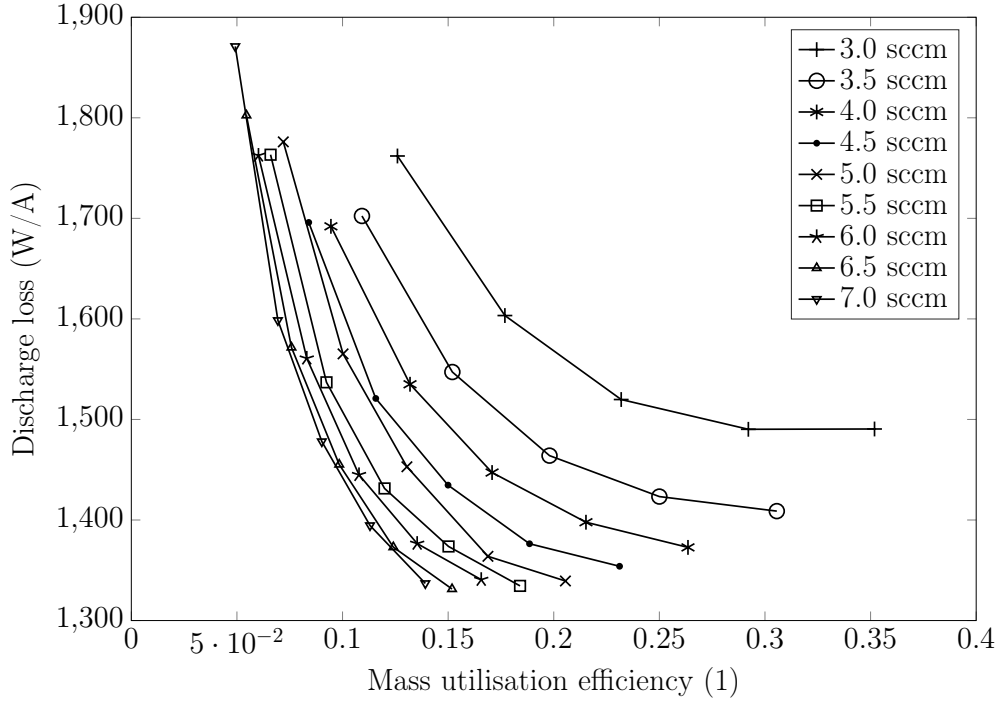

Figure 7.13: Configuration AIC: discharge loss at various mass flow rates vs mass utilisation efficiency ($U_s = 1.5$ kV, $U_{a1} = -200$ V).

The thrust achieved in Configuration AIC is shown in Figure 7.16. Figure 7.16 illustrates that, as was observed while discussing Configuration AIT, the total power increases roughly linearly with the thrust. In addition, as before, the thrust achieved was calculated by using the screen grid current and voltage as measured by the SCREEN power supply. Figure 7.16 shows that the maximum thrust achieved is about 6.5 mN at approximately 260 W of total power. Remember that in Configuration AIT, at the same mass flow rate, 210 W of total power was needed to achieve 4.5 mN of thrust. Since in both configurations the RFG power is about the same, it can be concluded that Configuration AIC can produce about 40% more thrust at nearly the same operational conditions compared to Configuration AIT. In order to achieve higher thrust values,

more RFG power and higher screen grid voltages would be needed. As mentioned before, running the thruster with such a low screen voltage would be impractical since due to the plasma being common to both extraction systems, it would mean that the same screen grid voltage is applied on the IT side as well. Additionally, the momentum transfer efficiency at 1.5 kV is only about 0.35. Therefore, the IT side would be required to produce about 85 mN of thrust, but the IC side would need to produce 30% even more thrust (110 mN), resulting in the total power of about 4.2 kW.
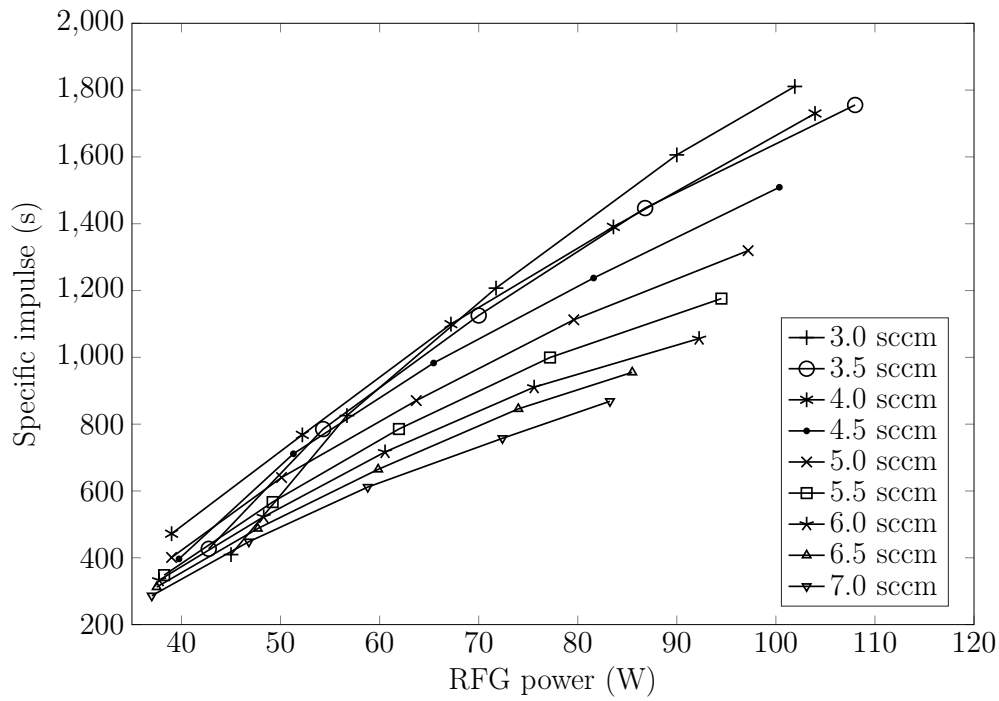
Figure 7.14: Configuration AIC: specific impulse at various mass flow rates vs RFG power ($U_s = 1.5$ kV, $U_{a1} = -200$ V).
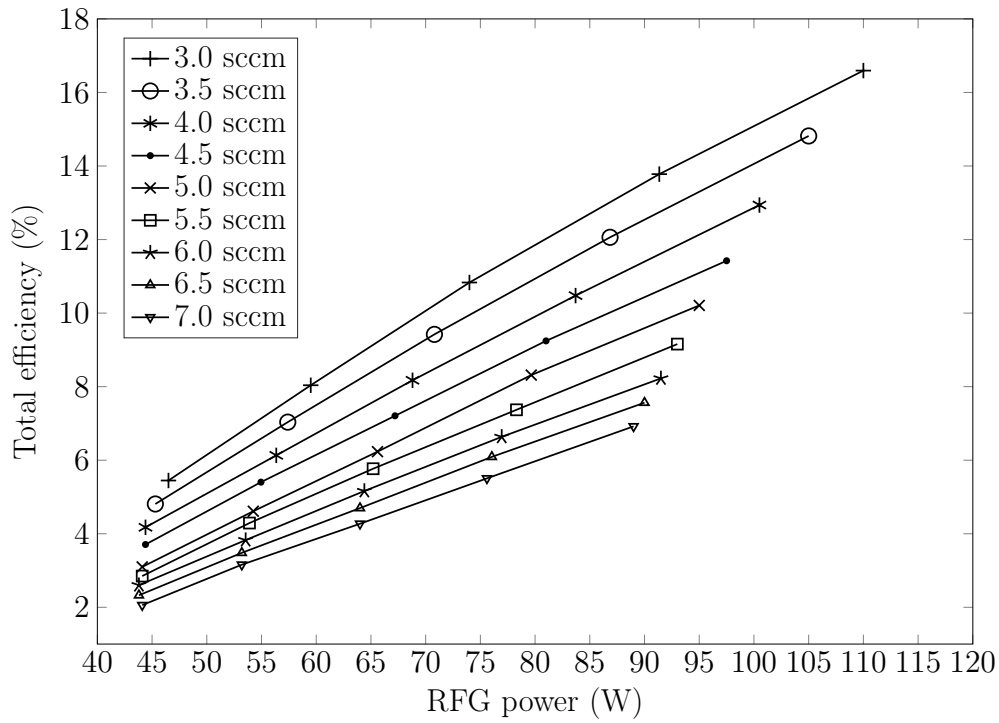
Figure 7.15: Configuration AIC: total efficiency at various mass flow rates vs RFG power ($U_s = 1.5$ kV, $U_{a1} = -200$ V).
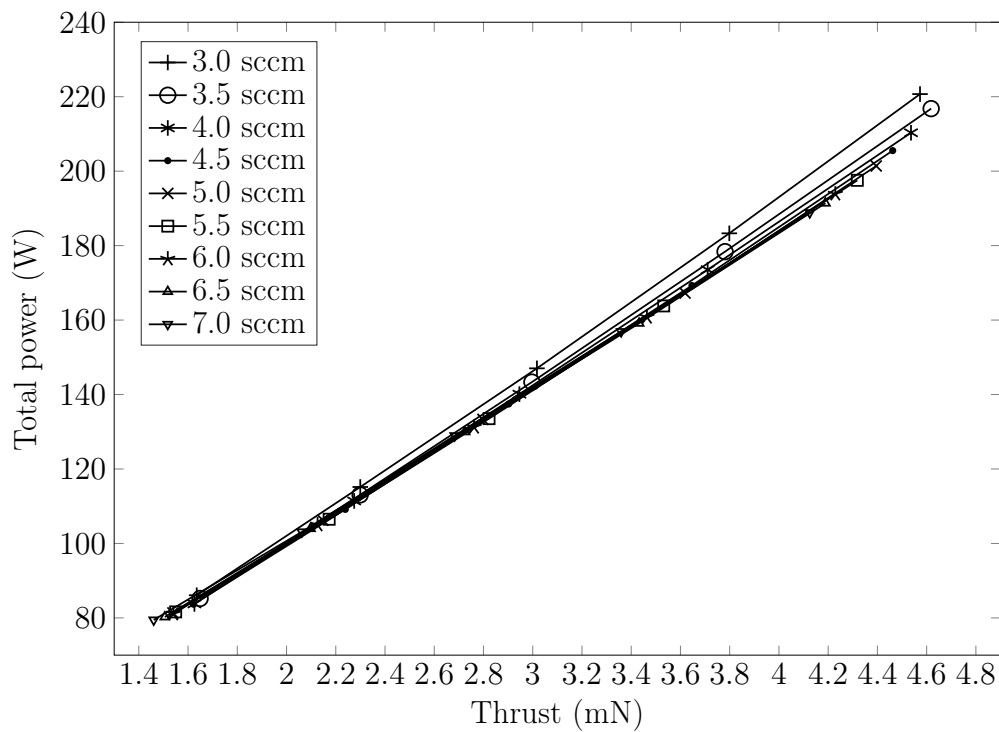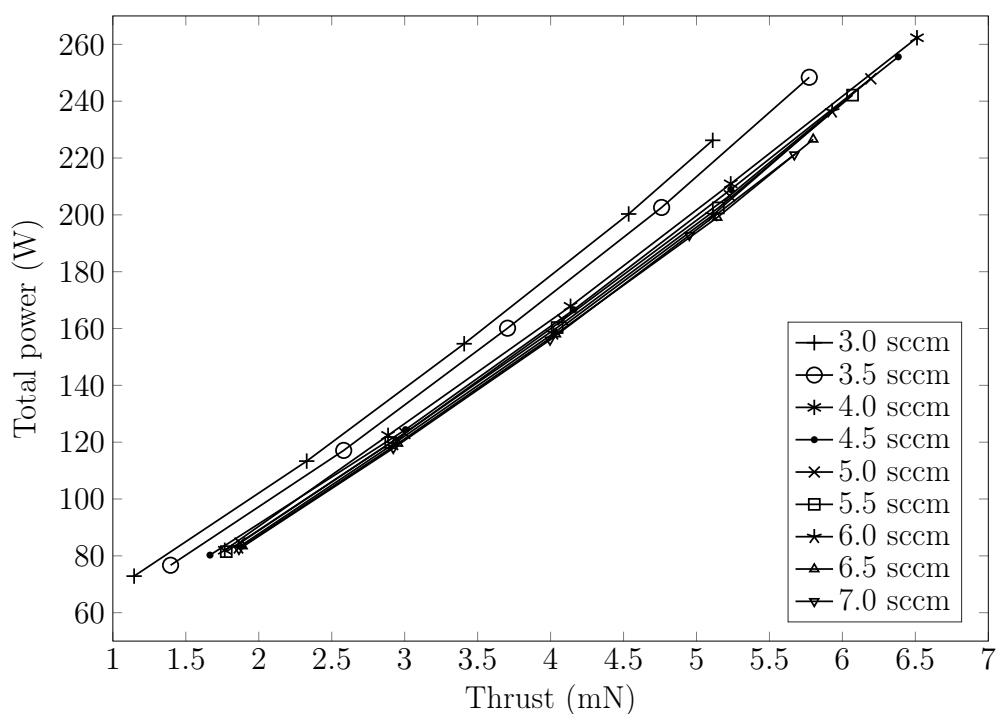

Figure 7.16: Configuration AIC: total power at various mass flow rates vs thrust ($U_s = 1.5$ kV, $U_{a1} = -200$ V).
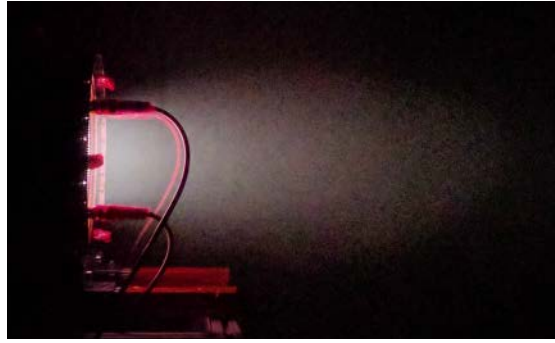
7.4 Configuration ADST

7.4.1 Performance mapping

This section presents the performance mapping results for Configuration ADST. In this configuration, both the IT and IC ion optics systems are active and therefore there are two ion beams being extracted from each side, as shown in Figure 7.17. First, notice that since the view port was facing towards the IC side, the beam from the IC side appears much brighter than that from the IT side. Also, the IC1 ion optics system is semi-transparent to light from the plasma.
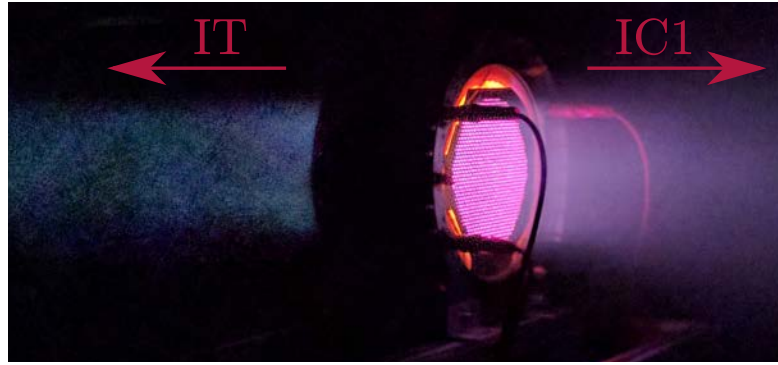
Figure 7.17: Extracted ion beams from the IT and IC1 ion optics systems in Configuration ADST.

In Configuration ADST, the thruster was tested with mass flow rates ranging from 6 to 14 sccm in 1 sccm increments. Note that these flow rates are exactly two times larger than the flow rates used while testing the thruster in Configuration AIT and Configuration AIC. Figure 7.18 displays the total screen grid current (expressed as $I_s^{it} + I_s^{ic}$) which is collected by the IT side screen grid. As can be seen in Figure 7.18, the screen grid current in Configuration ADST is roughly equal to a sum of the screen currents obtained in Configurations AIT and AIC where only a single ion optics side was active. This is because in Configuration ADST both ion optics systems are active and therefore there are two ion beams. As can be inferred from Figure 7.18, the maximum total screen grid current is about 200 mA at around 102 W and 11 sccm. This means that, for the same RFG power, the total extracted screen current can be roughly obtained by summing the I_s^{it} and I_s^{ic} currents, which was the prediction made in Chapter 5. Note, however, that the mass flow rate has to be doubled in the double-sided mode.

Since in Configuration ADST the accel grids from the IT and IC sides are both collecting currents, the results for each side are plotted individually. Figure 7.19 and Figure 7.20 display how the accel currents I_a^{it} and I_a^{ic} vary with the RFG power, respectively. As can be observed from the figures, the IT and IC accel currents are similar in magnitude, especially at higher RFG powers. For example, at 14 sccm, the IT accel current is 2.3

mA, while the IC accel current is 2.4 mA. Nevertheless, since the IC side extracts a larger beam current, a percentage of the extracted current hitting the accel grid is smaller in the case of the IC side in comparison to the IT side. However, as mentioned before, due to the IC1 grid being made out of a non-conductive material, it is not possible to know the exact current hitting the grid. Additionally, the IC accel current is about 20% lower than the IT accel current at low RFG powers. For instance, at 14 sccm and 45 W of RFG power, the IT accel current is nearly 0.8 mA, while the IC accel current at the same conditions is about 0.6 mA.
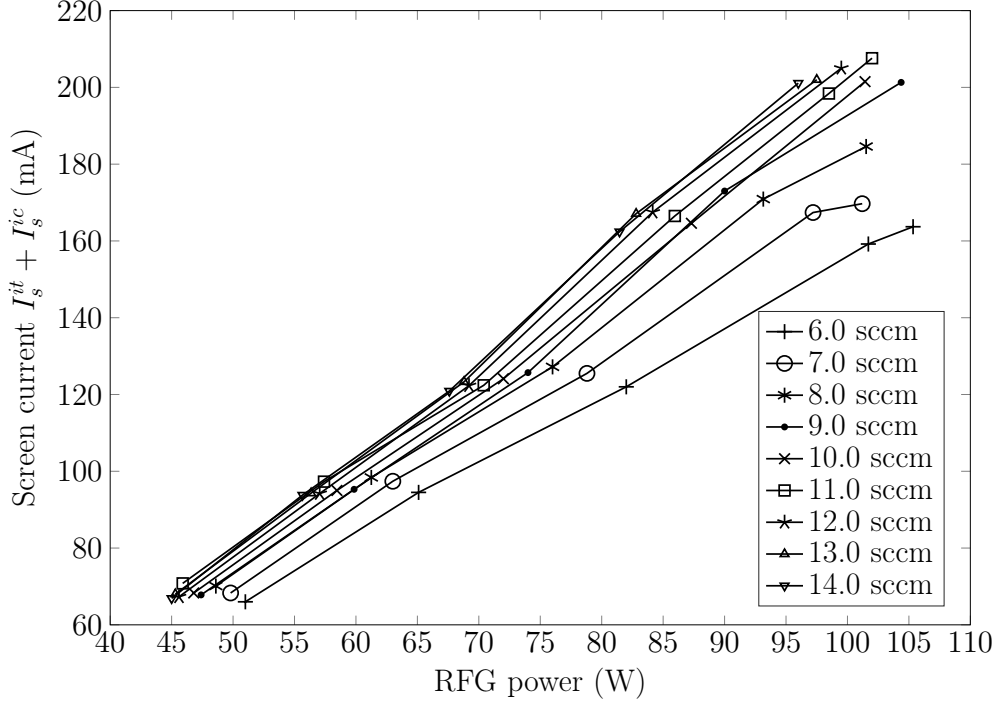

Figure 7.18: Configuration ADST: total screen grid current at various mass flow rates vs RFG power ($U_s = 1.5$ kV, $U_{a1} = -250$ V, $U_{a2} = -200$ V).

Figure 7.21 depicts the RFG current variation with the RFG power. As Figure 7.21 indicates, even though the mass flow rates in Configuration ADST are two times higher, the RFG current is approximately the same as was observed in the single-sided cases AIT and AIC. This means that the plasma inside the discharge chamber is of about the same pressure and density. Therefore, a conclusion can be drawn that adding an additional extraction system does not substantially change the plasma parameters if the mass flow rate (or the neutral gas pressure) into the discharge chamber is kept the same.
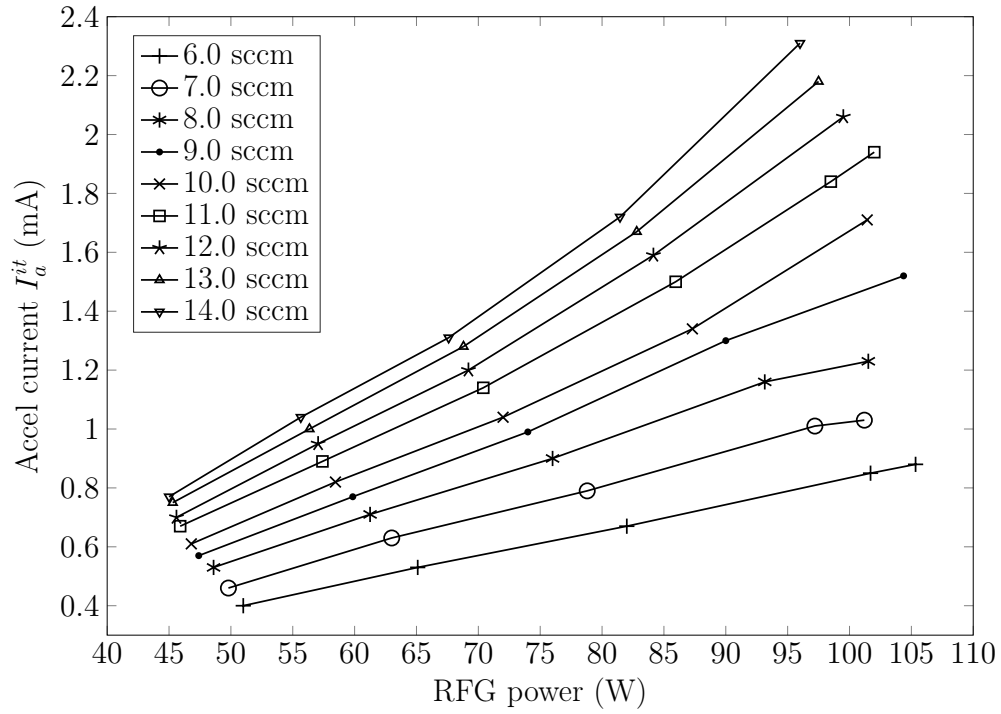
Figure 7.19: Configuration ADST: IT side accel grid current at various mass flow rates vs RFG power ($U_s = 1.5$ kV, $U_{a1} = -250$ V, $U_{a2} = -200$ V).
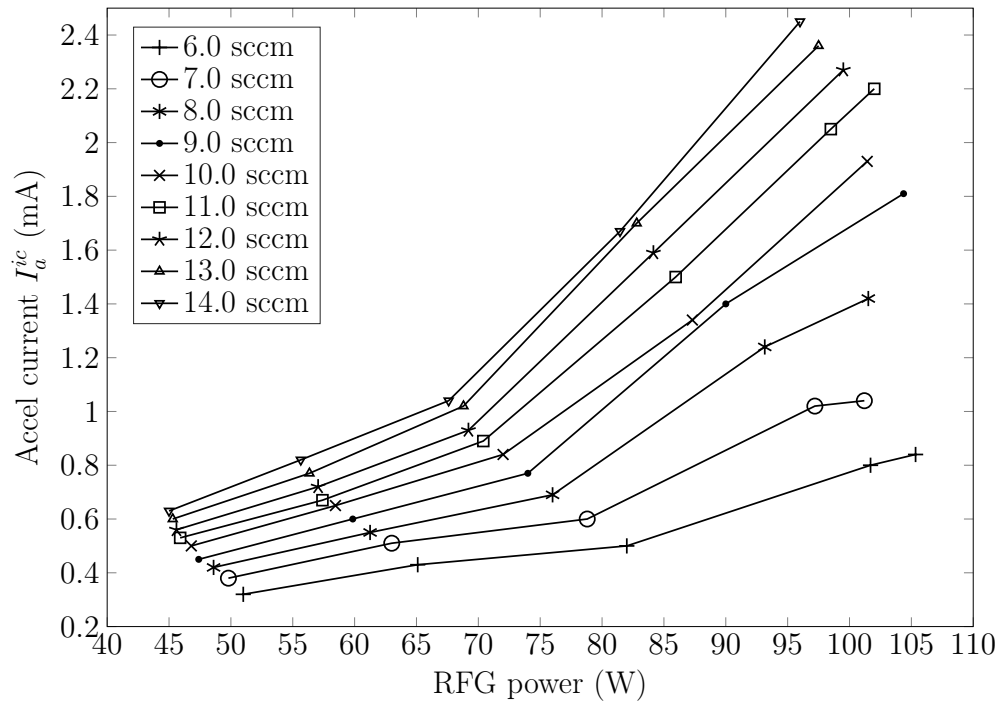
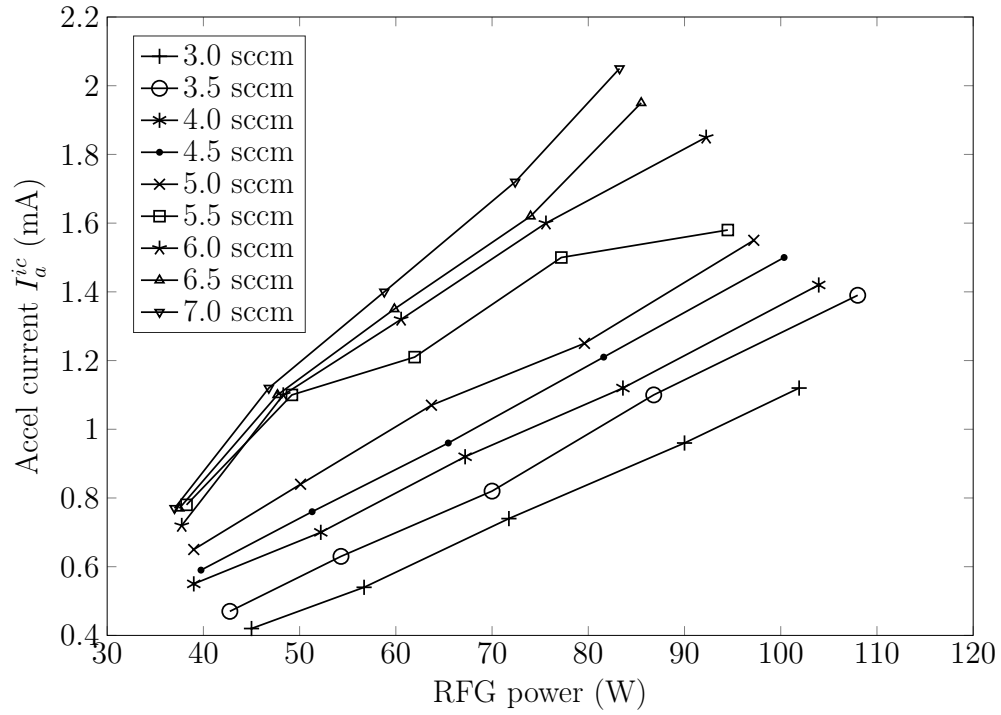

Figure 7.20: Configuration ADST: IC side accel grid current at various mass flow rates vs RFG power ($U_s = 1.5$ kV, $U_{a1} = -250$ V, $U_{a2} = -200$ V).
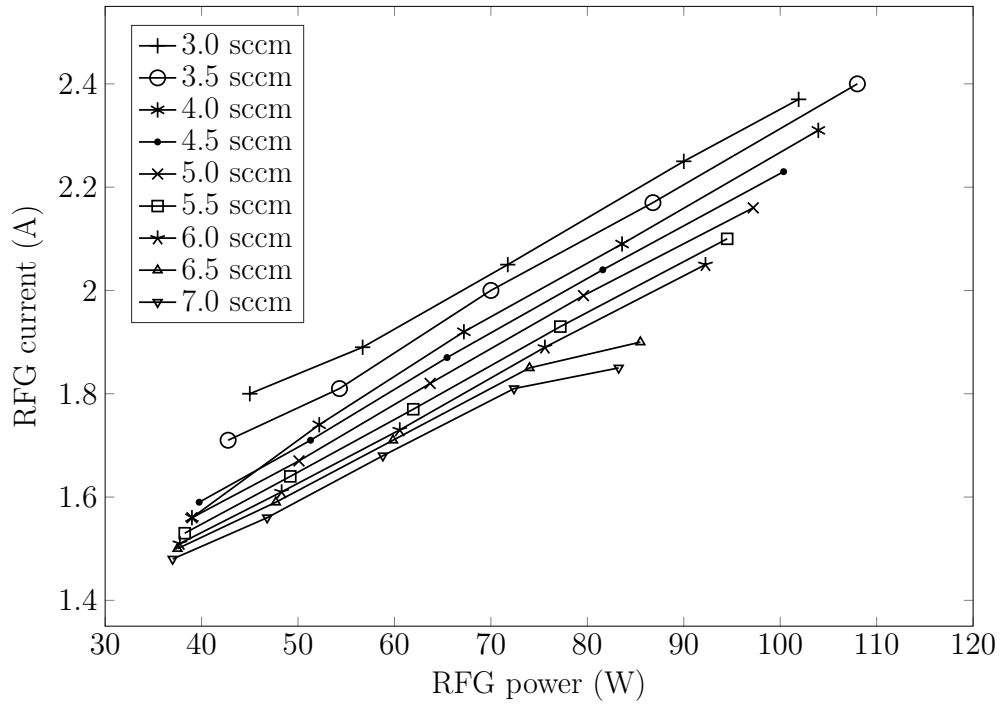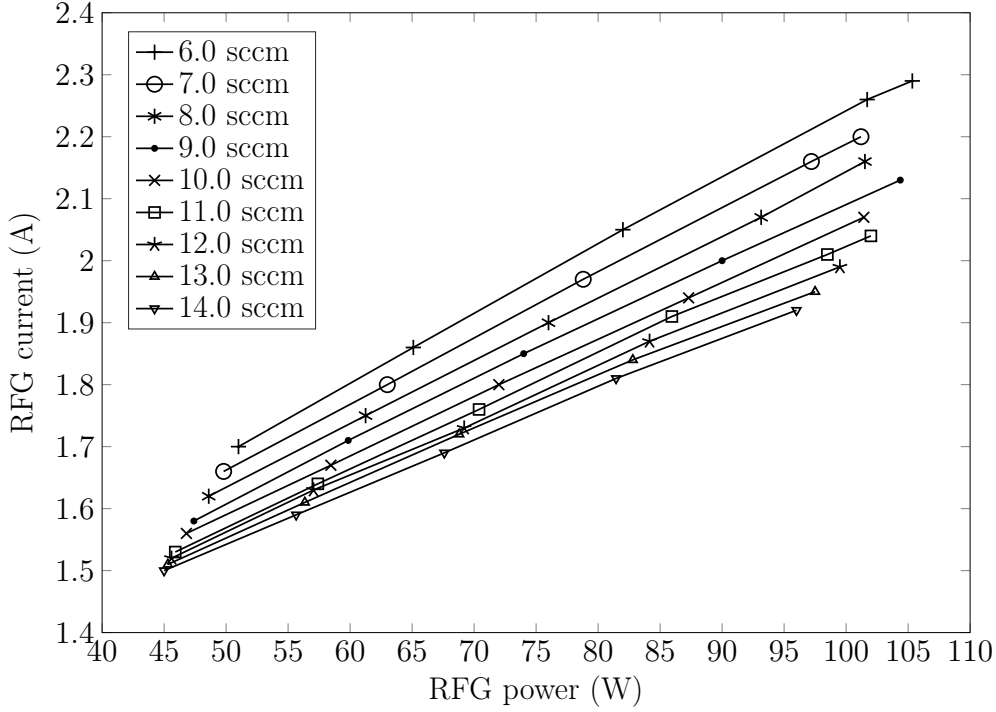
Figure 7.21: Configuration ADST: RFG current at various mass flow rates vs RFG power ($U_s = 1.5$ kV, $U_{a1} = -250$ V, $U_{a2} = -200$ V).

7.4.2   Performance analysis

In the performance analysis section, the performance parameters are plotted for the thruster as a whole, that is, when both ion optics sides are active. Note that when analysing the thruster's performance in the double-sided mode, it is assumed that the thruster behaves as two individual thrusters. That is, the total thrust is defined as $T = T^{it} + T^{ic}$, while the total beam current is defined as $I_b = I_b^{it} + I_b^{ic}$. These definitions of thrust and beam current are then used to calculate the discharge loss, specific impulse and other performance parameters. This was done to have the double-sided thruster's performance easily comparable to the performance of single-sided thrusters. As can be seen in Figure 7.22, the discharge loss is about 650 W/A at 6 sccm and 0.4 mass utilisation efficiency. Such a discharge loss is almost two times lower compared to Configurations AIT and AIC. This comes from the fact that in Configuration ADST, two ion beams are being extracted for roughly the same RFG power. The trend behaviour, however, is about the same as for the single-sided cases. Also, the highest achievable mass utilisation efficiency in Configuration ADST is approximately the same as for the single-sided cases and equal to 0.4. Similarly, the maximum specific impulse is equal to approximately 1,800 s, as seen in Figure 7.23. This is because even though two ion beams are being extracted in Configuration ADST, the mass flow rate is about two times higher as well. Therefore, the specific impulse does not improve in Configuration ADST.
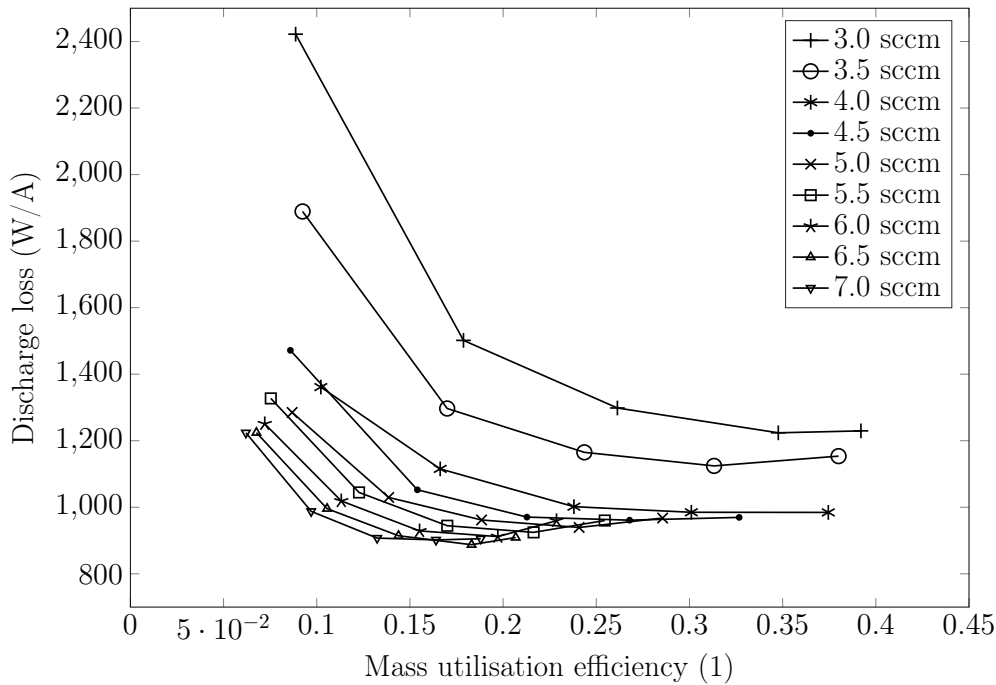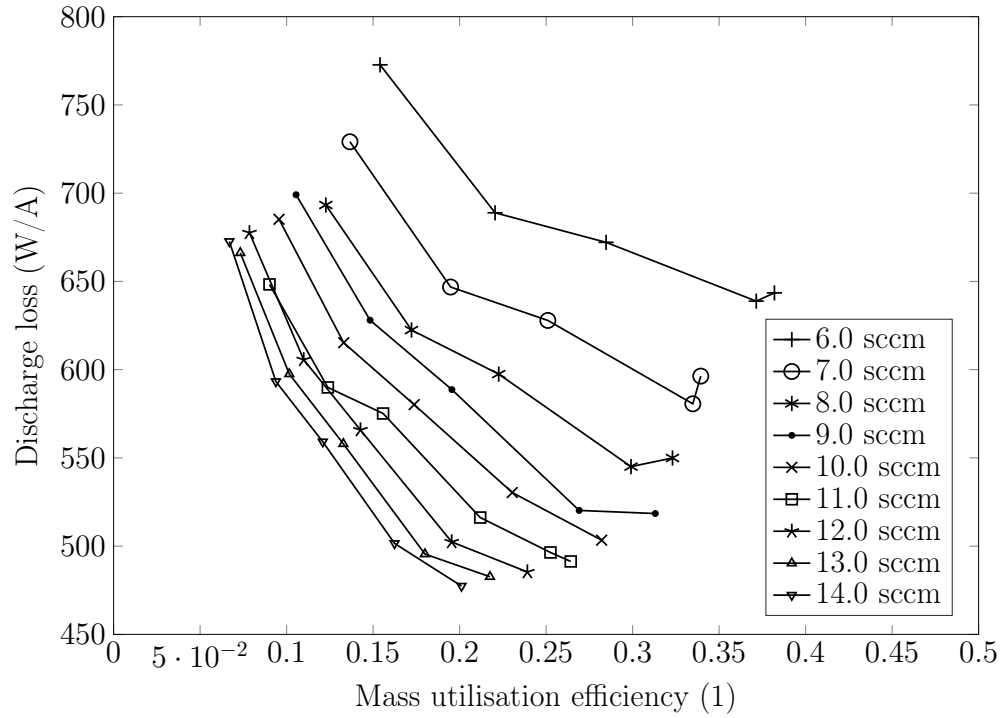
Figure 7.22: Configuration ADST: discharge loss at various mass flow rates vs mass utilisation efficiency ($U_s = 1.5$ kV, $U_{a1} = -250$ V, $U_{a2} = -200$ V).
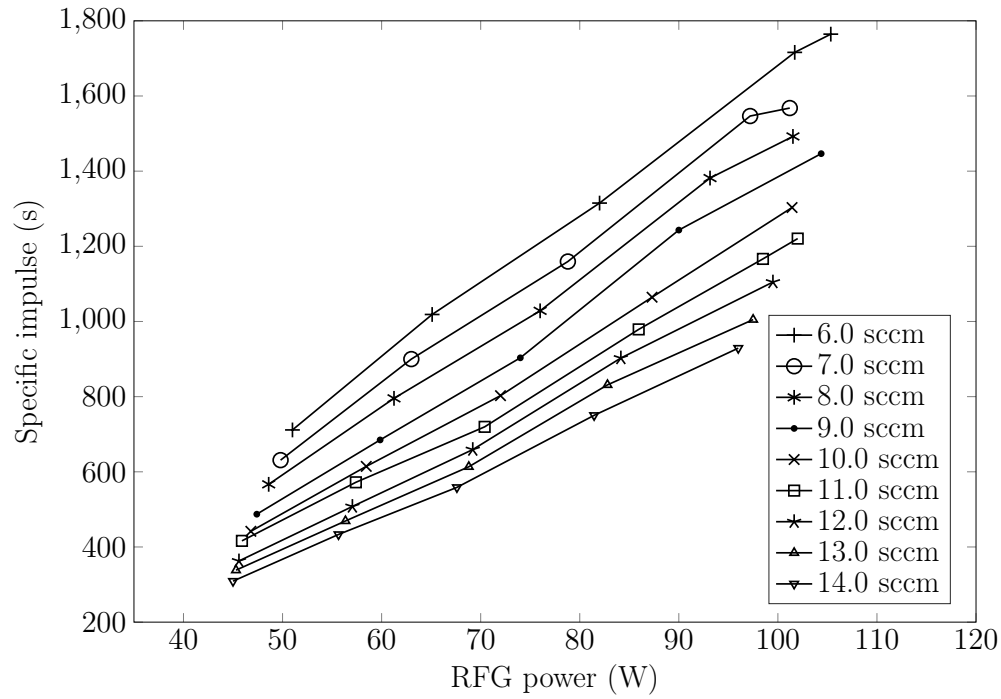
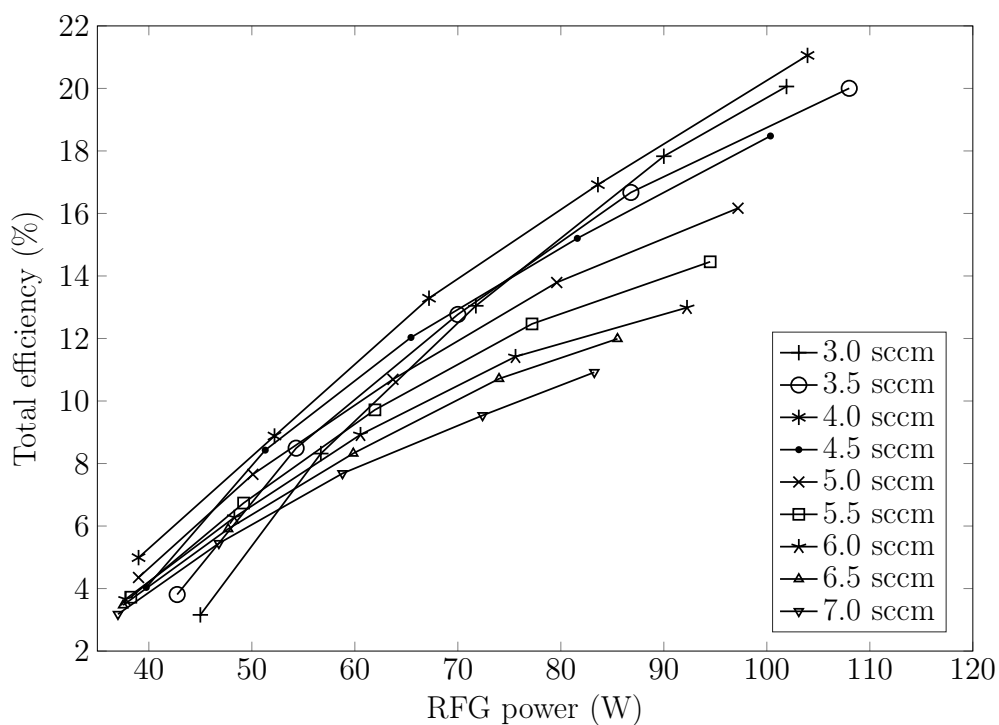Figure 7.23: Configuration ADST: specific impulse at various mass flow rates vs RFG power ($U_s = 1.5$ kV, $U_{a1} = -250$ V, $U_{a2} = -200$ V).
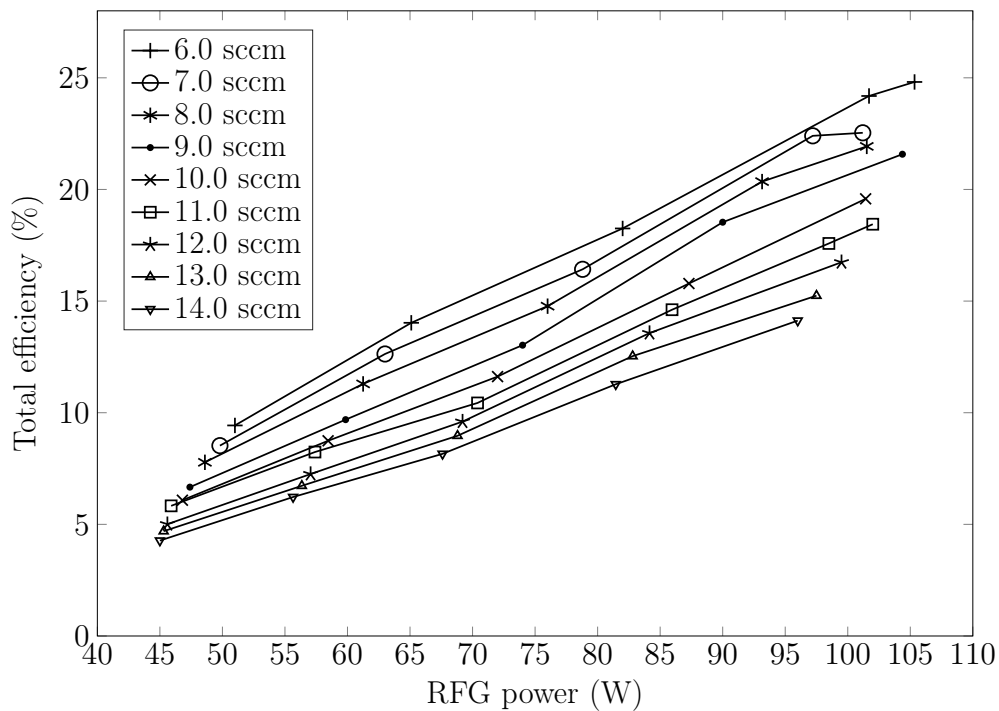
Figure 7.24: Configuration ADST: total efficiency at various mass flow rates vs RFG power ($U_s = 1.5$ kV, $U_{a1} = -250$ V, $U_{a2} = -200$ V).
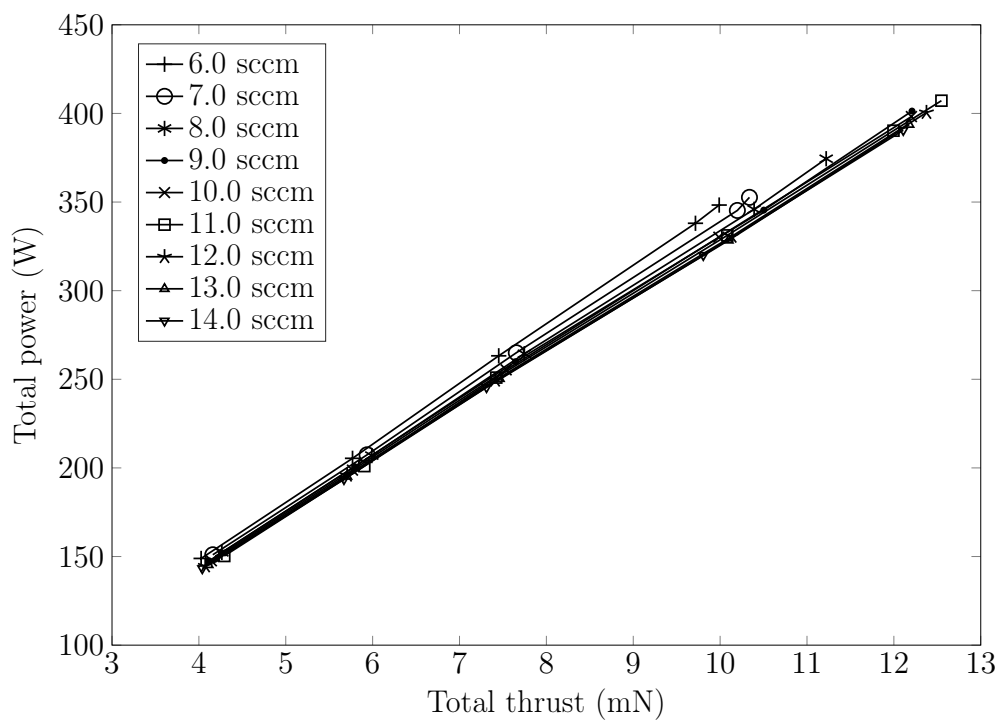
Figure 7.25: Configuration ADST: total power at various mass flow rates vs thrust ($U_s = 1.5$ kV, $U_{a1} = -250$ V, $U_{a2} = -200$ V).

From Figure 7.24, it can be seen that the total efficiency of the thruster is still approximately the same as for the single-sided cases. This is because the total efficiency is determined mostly by the design of the thruster, that is, the coil shape and discharge chamber geometry. Since these parameters were kept the same, the total efficiency remained about the same as well even though two ion beams were extracted. Finally, Figure 7.25 displays the total power variation with the thrust. The thrust that is plotted in Figure 7.25 is obtained by using the total screen current from the IT and IC sides, as has been shown in Figure 7.18. Remember that the IC ion optics side does not have a screen grid. Therefore, it is not possible to estimate the thrust produced by each side individually. However, it can be seen that in Configuration ADST, the thrust is about double that compared to the previous cases. Notice that the total power also has increased. This is because even though the RFG power remains the same in the double-sided mode, the beam power increases nearly twofold due to the production of two ion beams.

7.5 Configuration A: performance comparison

7.5.1 AIT vs AIC

In this section, the performance parameters as obtained in Configurations AIT and AIC are compared to each other. The previous sections have already discussed some of the differences (or similarities) between the two configurations, but in this section, these are analysed in more detail. Figure 7.26 and Figure 7.27 depict the performance parameters for Configurations AIT and AIC at 4 and 7 sccm mass flow rates, respectively. However, the discussion will be focused solely on analysing Figure 7.26 since the results from Figure 7.27 are nearly the same in terms of the trends. The only difference between the 4 and 7 sccm cases, are the performance parameter magnitudes. Figure 7.27 was included to make the analysis more comprehensive and to show that the trend behaviour is not exclusive to the 4 sccm case analysed in this section.

As can be seen in Figure 7.26(a), the IC screen current is much higher compared to the IT screen current at the same mass flow rate. This is because the IC1 ion optics system has 1171 apertures, while the IT ion optics system has 948 apertures. The difference in the screen currents between the sides changes with the RFG power: the difference varies from around 20 mA at 60 W to about 30 mA at 100 W of RFG power. The IC side also has a lower accel current, as seen in Figure 7.26(b). Since the IC side produces more screen current, it also achieves a higher mass utilisation efficiency at a given power. For instance, at 100 W the mass utilisation efficiency for the IT side is about 0.25, while that for the IC side is about 0.35, as shown in Figure 7.26(c).
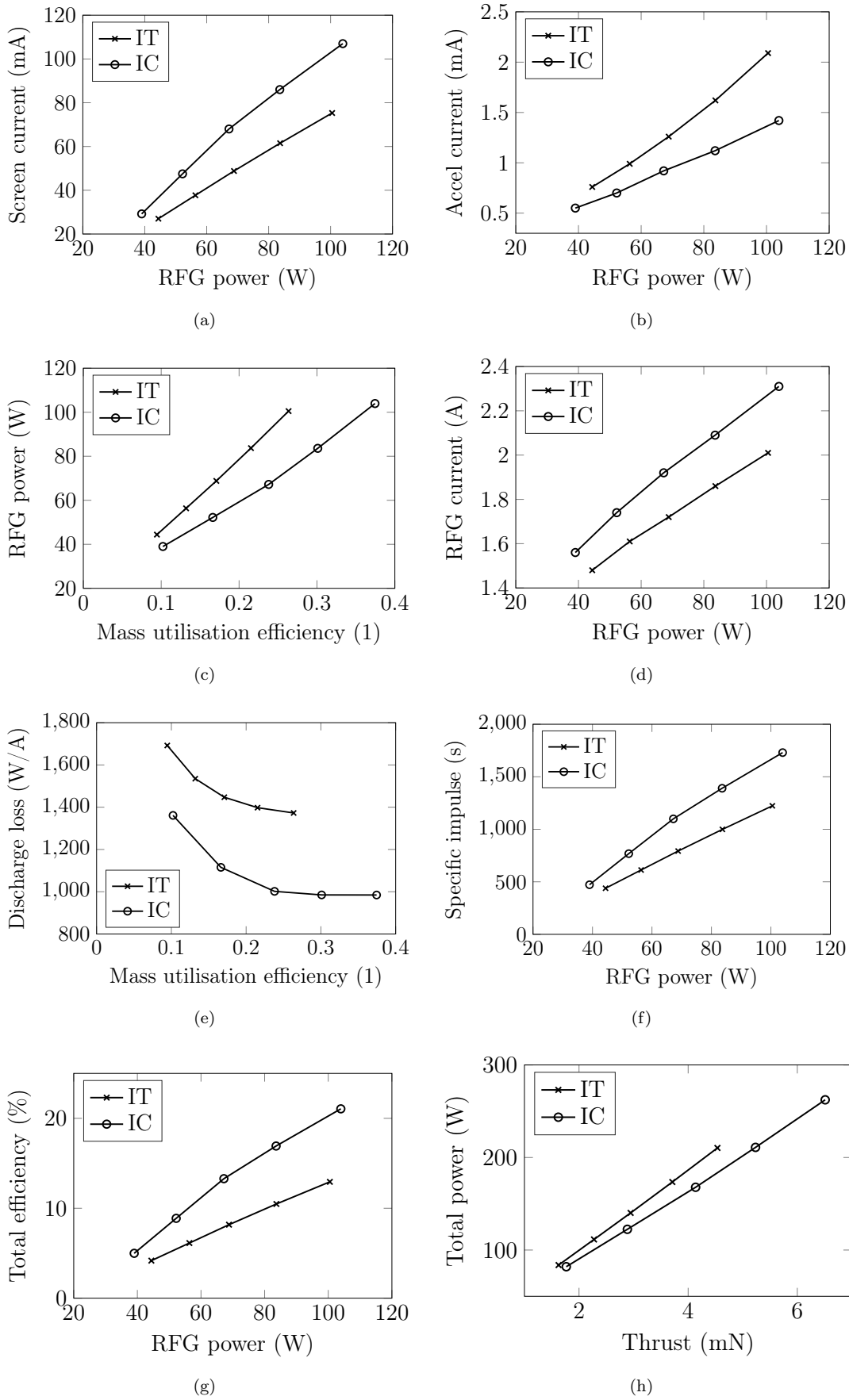
Figure 7.26: Performance parameters for Configurations AIT and AIC at 4 sccm ($U_s = 1.5$ kV, $U_{a1} = -250$ V, $U_{a2} = -200$ V).
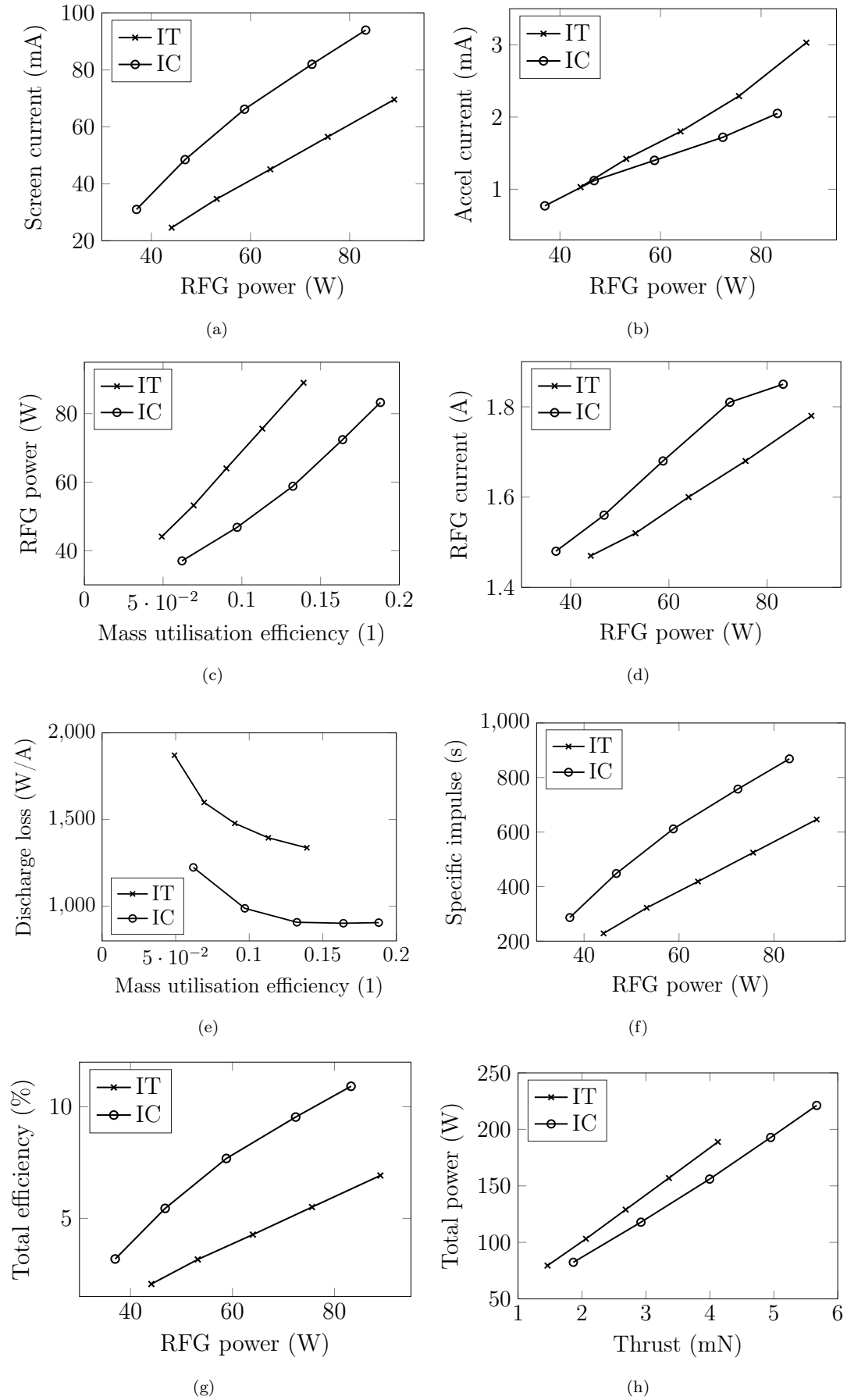
Figure 7.27: Performance parameters for Configurations AIT and AIC at 7 sccm ($U_s = 1.5$ kV, $U_{a1} = -250$ V, $U_{a2} = -200$ V).

The plasma parameters, however, for the IT and IC sides are different. This can be discerned by looking at Figure 7.26(d). Figure 7.26(d) shows that the RFG currents are different for the two cases. This means that the plasma parameters are different as well. The plasma parameters are dissimilar because the neutral gas pressure inside the discharge chamber is not the same due to different open area fractions of the grids. Since the IC side has more apertures, its open area is greater. Therefore, a prediction can be made that, at the same mass flow rate, the neutral gas pressure inside the discharge chamber must be lower in Configuration AIC than in Configuration AIT. This, in turn, means that the plasma density in Configuration AIC is lower and, as a consequence, the thruster's resistance is smaller. As a result, at the same RFG power, the RFG current in Configuration AIC must be higher. As can be discerned from Figure 7.26(d), this is indeed the case.

Furthermore, as seen in Figure 7.27(e), at the mass utilisation efficiencies starting from about 0.2, Configuration AIC has a discharge loss that is nearly 400 W/A lower. Additionally, the IC side has a specific impulse by about 500 s higher, as displayed in Figure 7.27(f), and a total efficiency that is about 5% more compared to Configuration AIT, as depicted in Figure 7.27(g). Finally, the thrust produced by Configuration AIC, at the same total power as in Configuration AIC, is about 0.5 mN higher. Therefore, it can be concluded that increasing the number of apertures in a grid system does in fact increase the ion optics efficiency, specific impulse and thrust. Observe that these are the predictions that have been made in Chapter 5.

7.5.2　AIT vs AIC vs ADST

The issue with having only one screen grid at the IC side, as in Configuration ADST, is that it is not possible to determine how much thrust is produced from the IT and IC sides independently without doing the beam plume measurements. Additionally, since the IT and IC1 ion optics systems are different, it cannot be said that the thruster's performance at 10 sccm in Configuration ADST is equivalent to a sum of the performance parameters at 5 sccm in Configuration AIT and 5 sccm in Configuration AIC. However, the results based on the equivalent mass flow rates from Configurations AIT and AIC could be used to estimate the thrust produced from the IT and IC sides independently in Configuration ADST. To do so, a combination of mass flow rates has to be found that produces a similar neutral gas pressure inside the discharge chamber as in Configuration ADST.
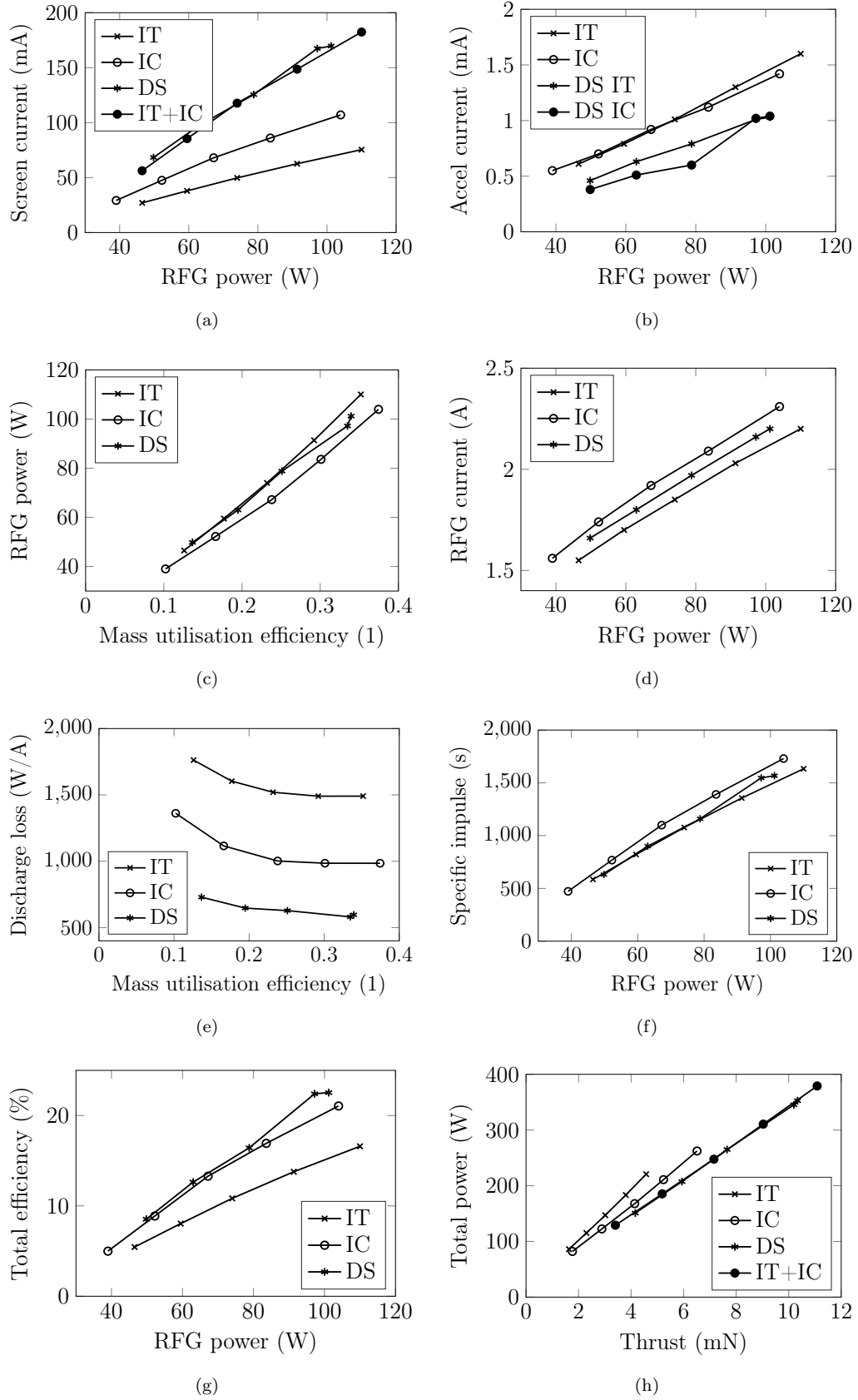
Figure 7.28: Performance parameters for Configurations AIT at 3 sccm, AIC at 4 sccm and ADST at 7 sccm ($U_s = 1.5$ kV, $U_{a1} = -250$ V, $U_{a2} = -200$ V).
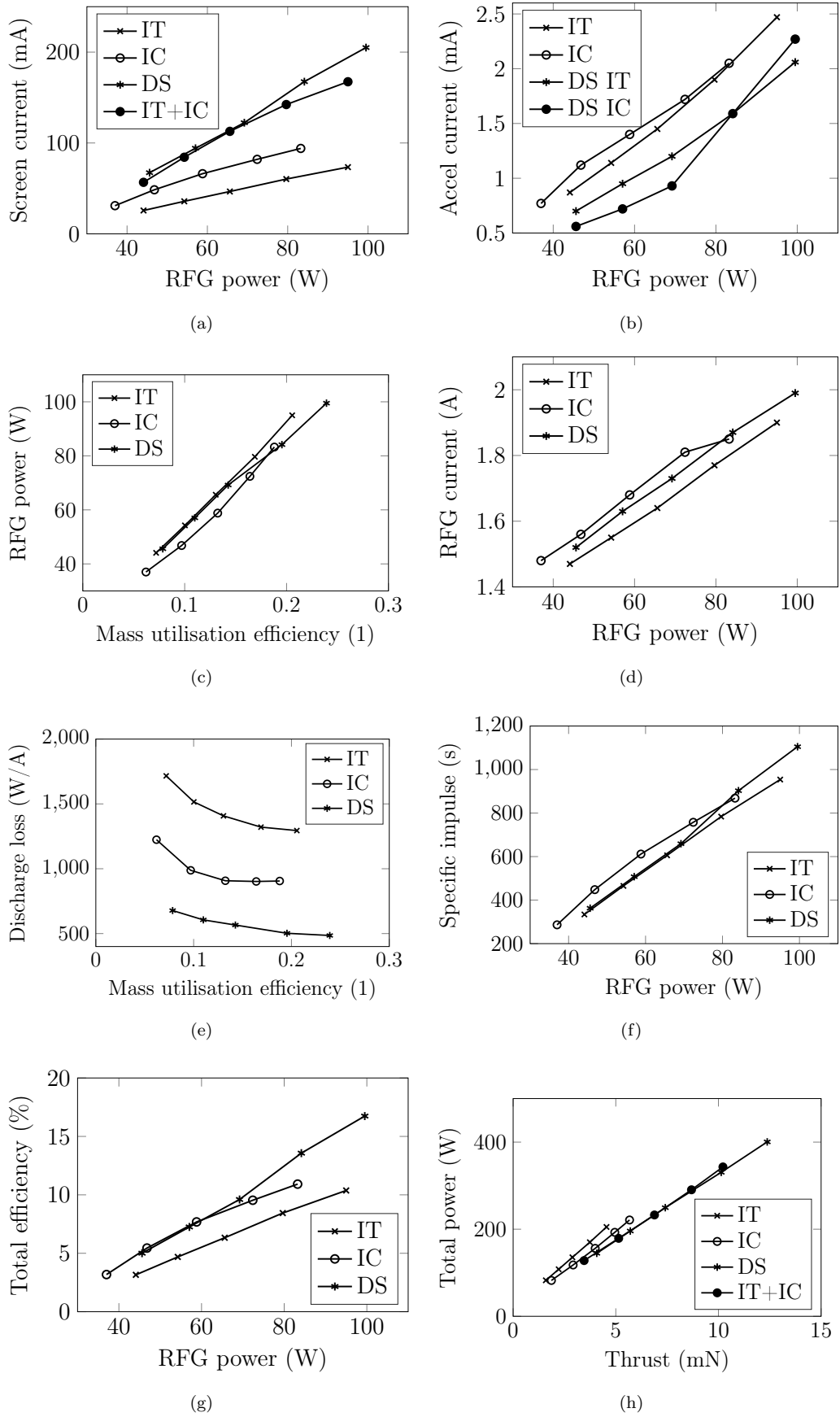
Figure 7.29: Performance parameters for Configurations AIT at 5 sccm, AIC at 7 sccm and ADST at 12 sccm ($U_s = 1.5$ kV, $U_{a1} = -250$ V, $U_{a2} = -200$ V).

For instance, based on the Clausing factors, it was calculated using the model developed in this thesis that regarding the plasma parameters, the thruster running at 7 sccm in Configuration ADST should be equal to the thruster operating at 4 sccm in Configuration AIC and 3 sccm in Configuration AIT. To check if this assumption is valid, Figure 7.28 compares the performance parameters as obtained by testing the AIT, AIC and ADST configurations at the above-mentioned mass flow rates. If the model results are correct, then the screen current measured in Configuration ADST (DS) should be about equal to the sum of currents measured in Configurations AIT and AIC (IT+IC). As can be seen from Figure 7.28(a), this indeed is the case. However, the IT and IC accel currents that were measured in Configuration ADST do not match the ones obtained in Configurations AIT and AIC, as shown in Figure 7.28(b). This could be due to slight differences in the number of the neutral gas atoms between the ion optics systems or in the sheath shapes.

To reaffirm the previously stated theory, the RFG power variation with the mass utilisation efficiency is plotted in Figure 7.28(c). Since the prediction has been made that the plasma parameters in both cases are about the same, all the cases should have nearly the same RFG power requirements for the same mass utilisation efficiency values. This is precisely what can be seen in Figure 7.28(c). Additionally, the same should be expected by looking at the plot of the RFG current vs the RFG power in Figure 7.29(d). This is because due to the plasma parameters being similar, the RFG current should also be similar since the thruster's resistance in all the cases must be approximately the same.

The same explanation can also be used in predicting the specific impulse trends, as displayed in Figure 7.28(f). However, it can be observed from Figure 7.29(e) that the discharge loss obtained in Configuration ADST is about 400 W/A and 1,000 W/A smaller than those obtained in Configurations AIC and AIT, respectively. This is because even though the plasma is the same in all cases, Configuration ADST produces two ion beams and therefore the power to produce 1 mA is much lower. Figure 7.28(g) displays that the total efficiency in Configuration ADST is about the same as in Configuration AIC at low RFG powers. Nevertheless, the total efficiency becomes about a few percent higher as the RFG power goes past about 80 W. Finally, the thrust produced in Configuration ADST should be equal to a sum of thrusts produced in Configurations AIT and AIC. As depicted in Figure 7.28(h), this is in fact the case. As a result, it proves that the model results are correct and the plasma parameters are indeed the same at these flow rates. Therefore, it is possible to estimate the thrust produced by the IT and IC1 ion optics systems individually while the thruster is working at 7 sccm in Configuration DST.

For instance, Figure 7.28(h) depicts that at the total power of 350 W, the IT thrust is about 4.1 mN while the IC thrust is about 6.3 mN, which is 54% more. Therefore, it can be concluded that Configuration ADST satisfies the LEOSWEEP mission requirements. That is, different thrust magnitudes can be produced from the IT and IC sides as required for the impulse transfer and impulse compensation, respectively. As mentioned before,

this difference in the thrust magnitudes was controlled by having the ion optics systems with different numbers of apertures, as the theory from Chapter 5 predicted. For a more comprehensive analysis, in addition to the mass flow rate of 7 sccm, Figure 7.29 presents a different case where a mass flow rate of 12 sccm is investigated. In this case, the model predicts that the plasma parameters found in Configuration ADST at 12 sccm are equal to the plasma parameters present in Configurations AIT at 5 sccm and Configuration AIC at 7 sccm. Even though this case is different from the previous one, the conclusions are the same and will not be reiterated.

7.6   Configuration BDST

7.6.1   Performance mapping

The previous sections were aimed at analysing Configuration A. Remember that in Configuration ADST, the thruster had only one screen grid as a part of the IT ion optics system. In this section, however, Configuration BDST is investigated. In this configuration, there are screen grids located at each ion optics side. Also, the IC side has the IC2 ion optics system which consists of screen and accel grids made out of titanium. Additionally, note that in Configuration B, the thruster was only operated in the double-sided mode. That is, both sides of the thruster were active. Figure 7.30 depicts the thruster firing in Configuration BDST. As can be seen, the beam from the IT side is not as wide and has a lower divergence compared to the beam from the IC side. Also, the IC2 ion optics system is not as bright as the IC1 ion optics system shown before since the titanium grids block all the light from the plasma.
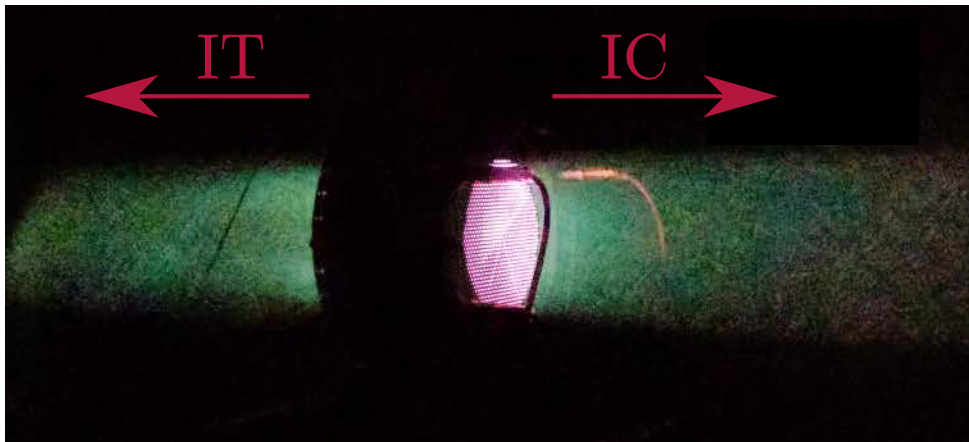
Figure 7.30: Extracted ion beams from the IT and IC2 ion optics systems in Configuration BDST.

As before, the performance mapping of the thruster was performed using the mass flow rates varying from 6 sccm to 14 sccm in 1 sccm increments. The screen grid

voltage, however, was different compared to Configuration A. In Configuration BDST, the thruster was tested up to 2.5 kV. This is because the IC2 ion optics system could be operated between $1 - 2.5$ kV without producing sparks. Additionally, there were two screen currents being recorded: I_s^{it} on the IT side and I_s^{ic} on the IC side. Figure 7.31 displays how both screen currents vary with the RFG power. First, notice that since the IC2 ion optics system has more apertures, the screen current is higher as well. For instance, at the RFG power of 100 W and 14 sccm, the electron current hitting the IT side screen grid is about 50 mA while that hitting the IC side screen grid is nearly 90 mA. The trends, however, are almost identical to the ones observed in Configuration A.

Figure 7.32 shows the I_a^{it} and I_a^{ic} accel current variations for each ion optics side. As Figure 7.32 indicates, the IT side accel current is larger than that from the IC side throughout most of the operational points. For example, at the RFG power of 100 W and 14 sccm, the IT accel current is about 2.2 mA while the IC accel current is about 1 mA. This means that at these conditions the IC accel current is only about 1% of the extracted beam current. Finally, it can be seen in Figure 7.33 that the RFG current decreases with the mass flow rate, as was discussed before. Additionally, it can be observed that the RFG current is in the same range as for Configuration A. This means that, at the same RFG powers and mass flow rates, the plasma parameters remained nearly unchanged even though a new ion optics system was introduced.
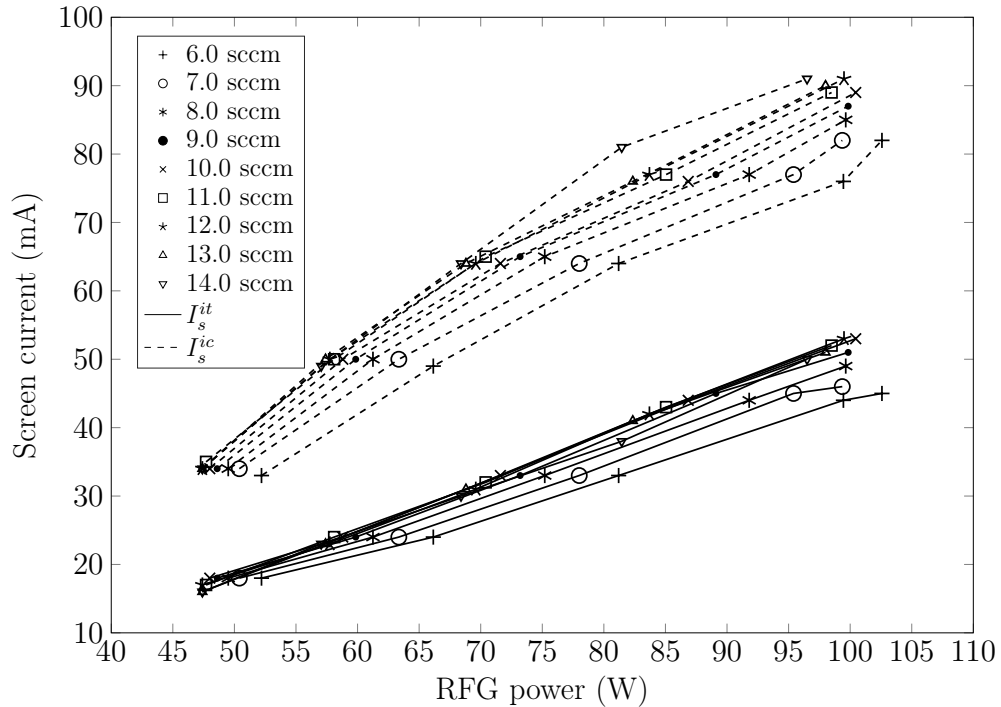
Figure 7.31: Configuration BDST: screen currents for the IT and IC sides at various mass flow rates vs RFG power ($U_s = 2.5$ kV, $U_{a1} = -250$ V, $U_{a2} = -150$ V).
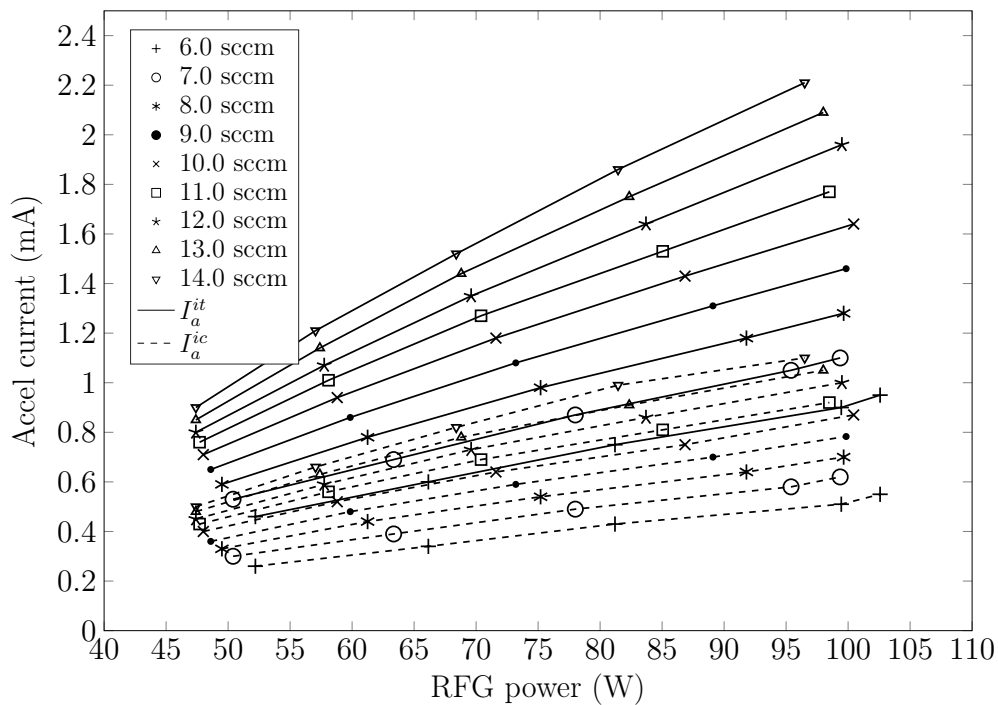
Figure 7.32: Configuration BDST: accel currents for the IT and IC sides at various mass flow rates vs RFG power ($U_s = 2.5$ kV, $U_{a1} = -250$ V, $U_{a2} = -150$ V).
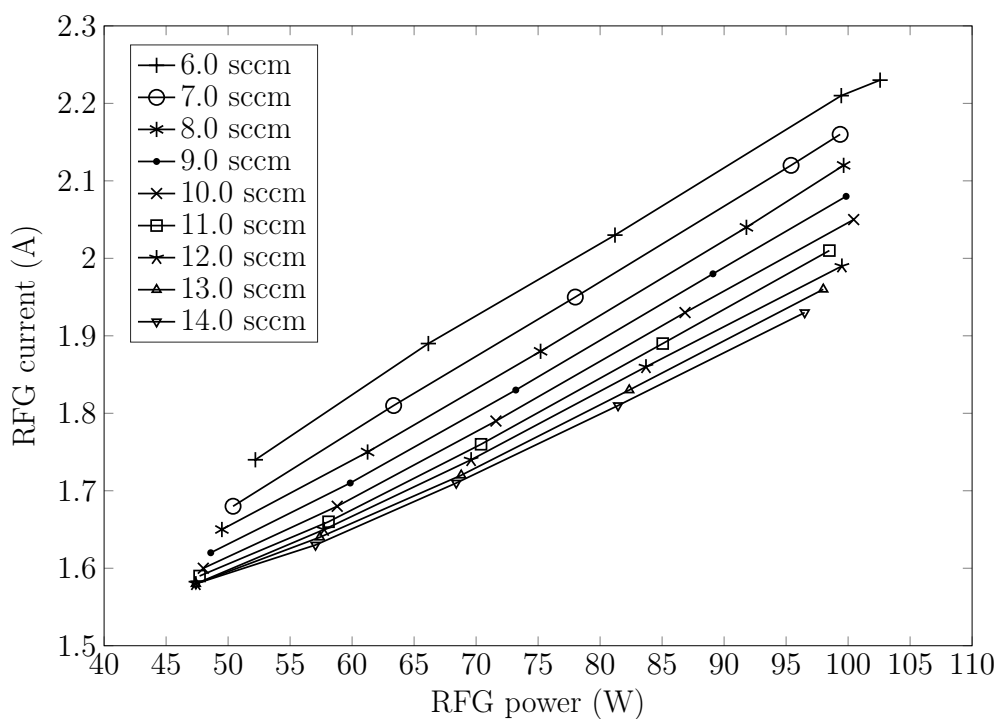
Figure 7.33: Configuration BDST: RFG current at various mass flow rates vs RFG power ($U_s = 2.5$ kV, $U_{a1} = -250$ V, $U_{a2} = -150$ V).

7.6.2 Performance analysis

The discussion regarding the performance analysis is started by depicting in Figure 7.34 how the discharge loss varies with the mass utilisation efficiency. It can be seen, that the highest mass utilisation efficiency achieved in Configuration BDST is equal to about 0.3 at 6 sccm. At this point, the discharge loss is about 800 W/A, which is about 150 W/A higher compared to Configuration ADST. This is because in Configuration ADST, a screen current that is about 50 mA greater compared to Configuration BDST was achieved. Figure 7.35 depicts that in Configuration BDST the maximum specific impulse obtained is about 1,800 s at 6 sccm. Note that such a specific impulse value is similar to that obtained in Configuration ADST. This is because even though the screen current obtained in Configuration BDST is lower than in Configuration ADST, in Configuration BDST, the screen voltage U_s is higher by 1 kV, which results in the specific impulse I_{sp} being higher as well since $I_{sp} \propto \sqrt{U_s}$. Furthermore, Figure 7.36 shows that the maximum total efficiency is about 20% at 100 W of RFG power and 6 sccm flow rate.
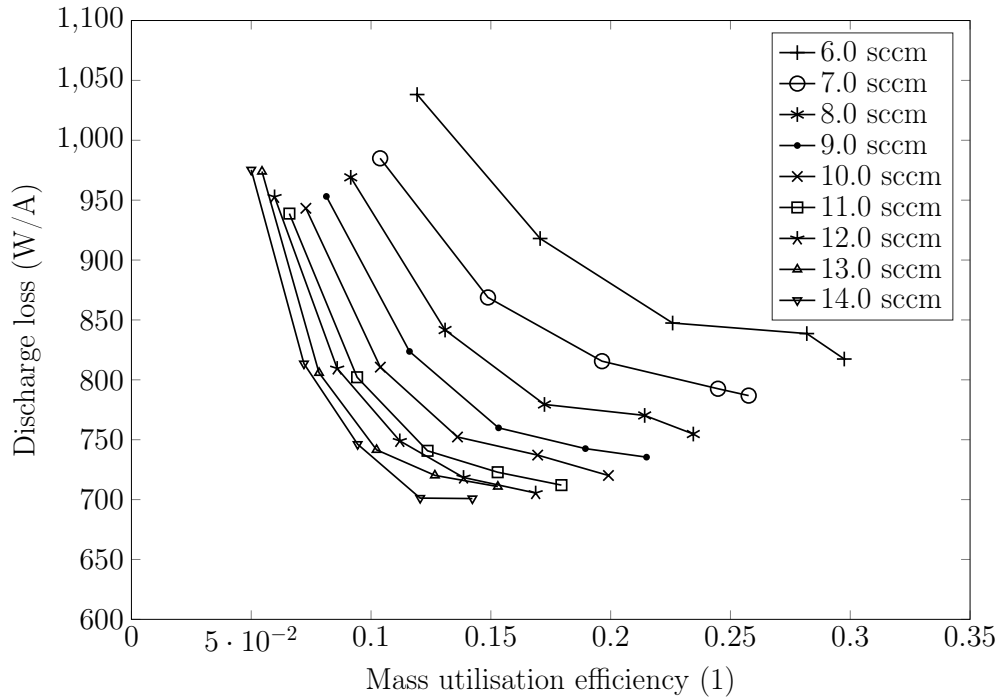
Figure 7.34: Configuration BDST: discharge loss at various mass flow rates vs mass utilisation efficiency ($U_s = 2.5$ kV, $U_{a1} = -250$ V, $U_{a2} = -150$ V).
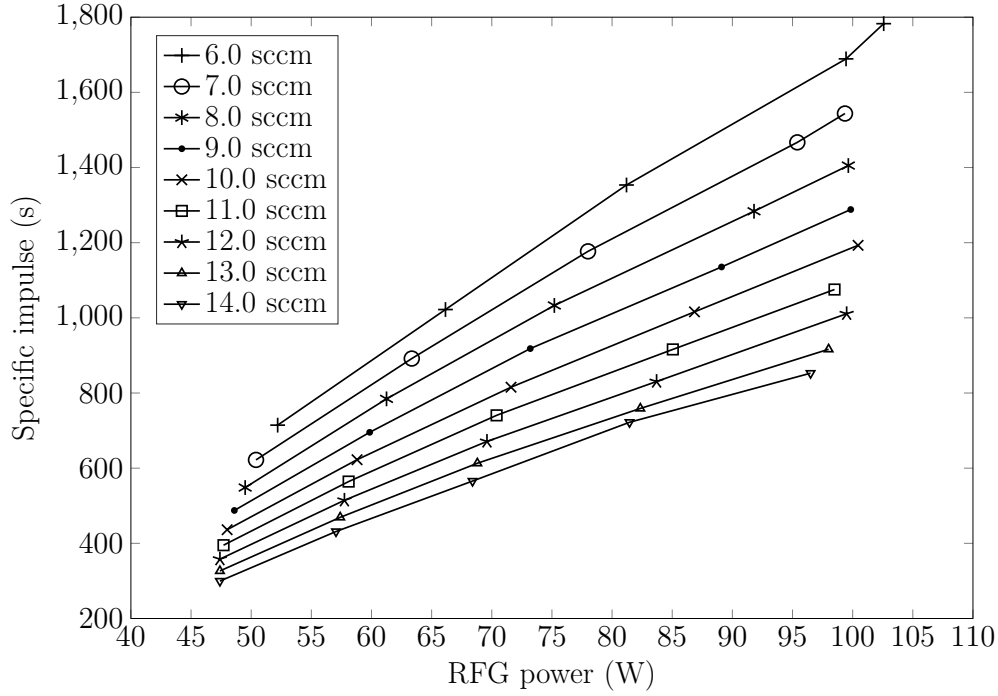
Figure 7.35: Configuration BDST: specific impulse at various mass flow rates vs RFG power ($U_s = 2.5$ kV, $U_{a1} = -250$ V, $U_{a2} = -150$ V).

Finally, as Figure 7.37 depicts, in Configuration BDST, it is possible to predict the thrust magnitudes generated from each ion optics system because the exact IT and IC screen current values were recorded during the experiments. Figure 7.37 shows that the IC side constantly produces more thrust compared to the IT side. Additionally, it can be seen that, depending on the operational conditions, the difference in the thrust values between the IT and IC sides varies from about 1 mN to 3 mN. For instance, at 440 W of total power and 9 sccm, the thrust achieved by the IC side is about 7 mN, while that from the IT side is approximately 4 mN. Therefore, the IC side produces 75% more thrust at these operational conditions. It can be concluded that since the IC2 ion optics system has a higher number of apertures it produces more thrust compared to the IT ion optics system, which is what has been observed in Configuration ADST.
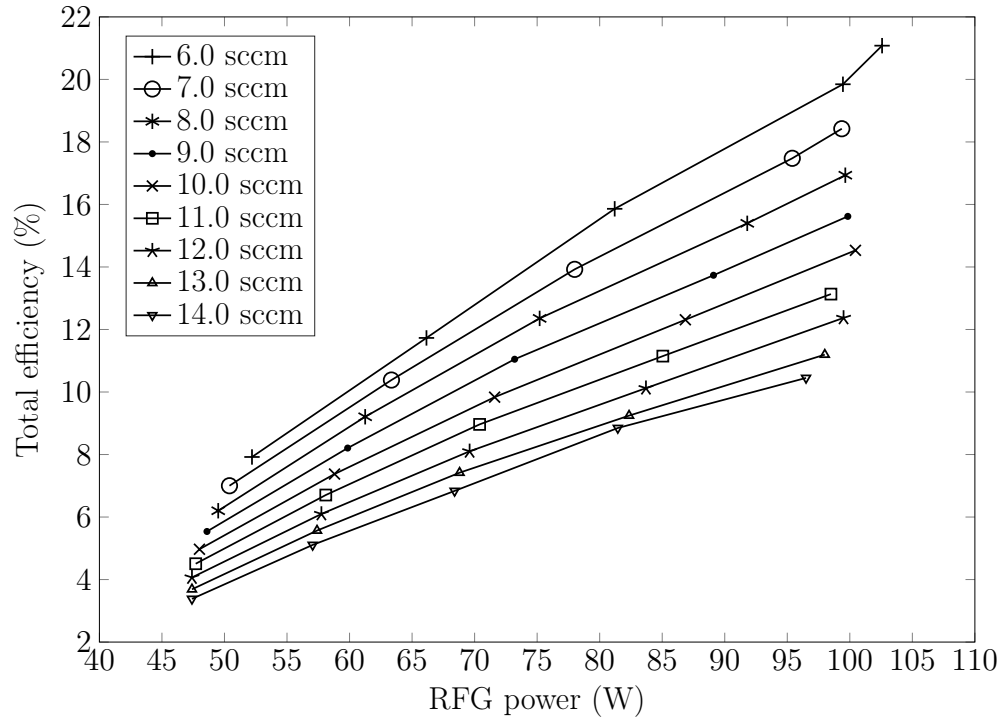
Figure 7.36: Configuration BDST: total efficiency at various mass flow rates vs RFG power ($U_s = 2.5$ kV, $U_{a1} = -250$ V, $U_{a2} = -150$ V).
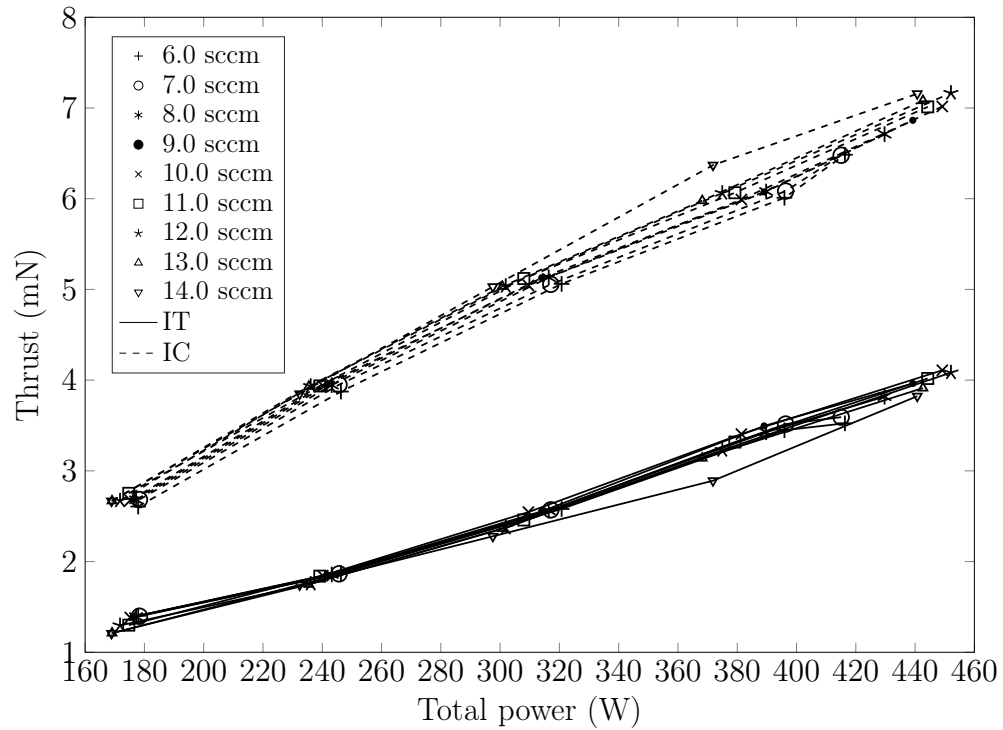
Figure 7.37: Configuration BDST: thrust at various mass flow rates vs total power ($U_s = 2.5$ kV, $U_{a1} = -250$ V, $U_{a2} = -150$ V).

7.7   Configuration BDST: thrust control

7.7.1   Varying total power and mass flow rate

As discussed before, the IC side produces more thrust than the IT side. However, this difference in thrusts depends on the operating conditions. For instance, as the RFG power is altered, the plasma density changes and, as a result, the sheath shape changes. Therefore, since the ion optics systems are not the same, the focusing efficiency varies and this influences the difference in thrusts. Nevertheless, this behaviour of the thruster is actually beneficial. This is because it could happen that during the LEOSWEEP mission different ratios of the IC to IT thrust need to be produced. Therefore, Figure 7.38 displays how the thrust magnitudes from the IT and IC sides change with the mass flow rate and the total power. Notice that there are four trends plotted in total. The first two trends show the IC and IT side thrusts. The third trend shows the difference between the IC and IT thrusts given as IC-IT. This difference is important because it indicates how much thrust is produced to accelerate the thruster in one or the other direction. This is the key to the differential thrust control, as discussed by Collingwood (2011). Finally, the IC/IT-1 expression is also plotted to show (in percentage) how much the IC thrust magnitude is larger (or smaller) than the IT thrust magnitude.

Figure 7.38(d) depicts that at 180 W of total power, the IC/IT-1 value is about 90%. However, as the total power increases, IC/IT-1 goes down to around 70% at about 450 W of total power. In the same figure, it can also be observed that the thrust difference IC-IT increases from about 1.3 mN at 180 W to about 3 mN at 450 W. The IC-IT value of 3 mN means that the satellite the thruster is attached to will effectively be subjected to 3 mN of force in the IC direction. This value again can be changed, by varying the total power and mass flow rate. For instance, Figure 7.38(h) shows that the IC thrust is about 120% higher than the IT thrust as the total power varies from 170 W to 380 W. By having the thruster's performance analysed as in Figure 7.38, the best total power and mass flow rate depending on the mission requirements at a particular time can be chosen. If, for example, the IC to IT thrust ratio needs to be changed, the operator could change the total power or the mass flow rate until the required ratio is achieved. This allows for a lot of flexibility when designing an IBS type mission using the DST thruster.

(a) 7 sccm.

(b) 8 sccm.

(c) 9 sccm.

(d) 10 sccm.

(e) 11 sccm.

(f) 12 sccm.

(g) 13 sccm.

(h) 14 sccm.
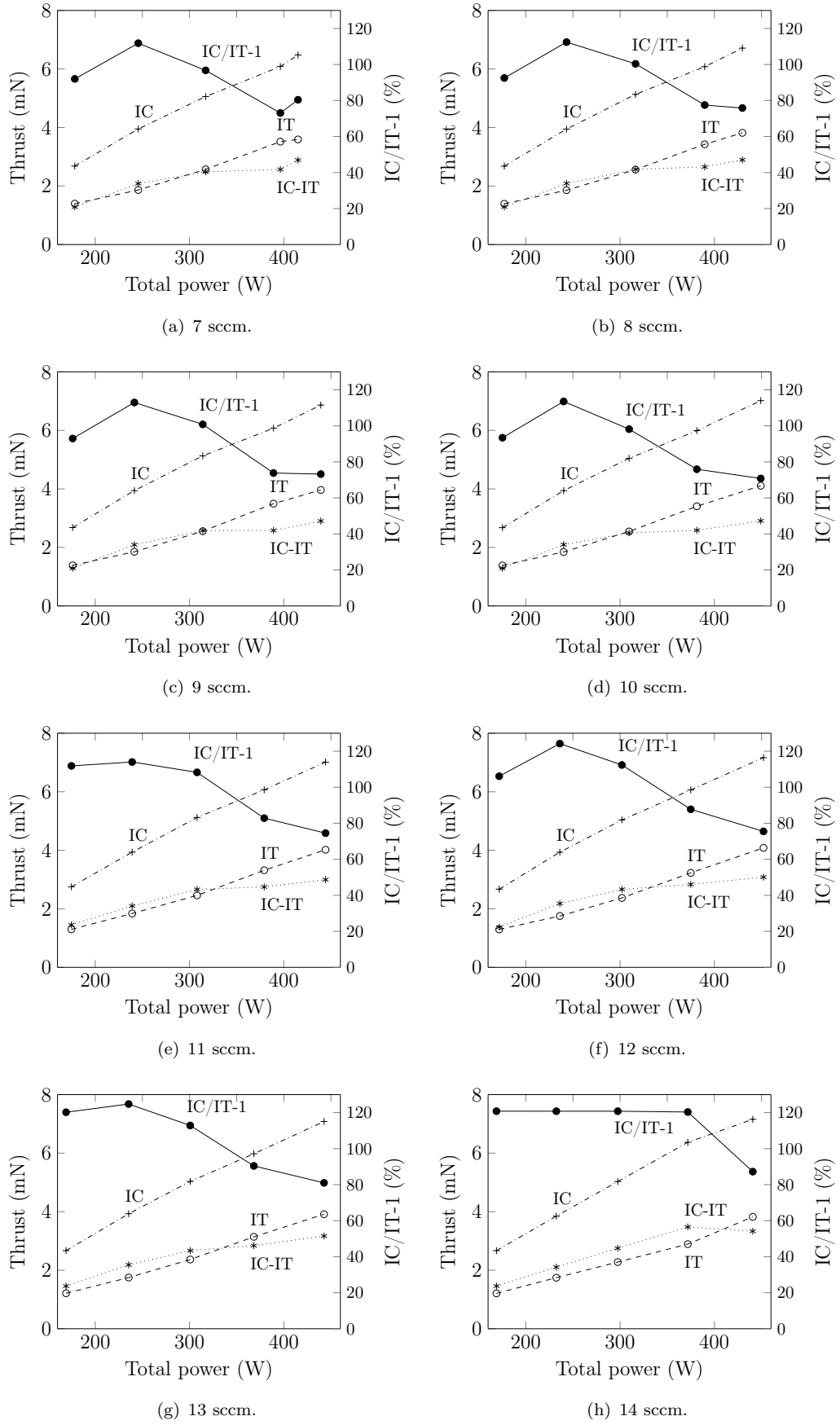
Figure 7.38: Configuration BDST: thrust variation for the IT and IC sides with total power and mass flow rate ($U_s = 2.5$ kV, $U_{a1} = -250$ V, $U_{a2} = -150$ V).

7.7.2   Varying screen grid voltage

Another way to control the IC-IT and IC/IT-1 parameters is by changing the screen grid voltage in addition to changing the total power, as shown in Figure 7.39. This method results in much larger changes in the thrust values produced by the IT and IC sides. For instance, as can be seen in Figure 7.39(a), the IC/IT-1 value changes from about 80% at 106 W to 0% at 160 W. This means that at the power of 106 W both sides produce the same amount of thrust since IC-IT is equal to 0. Therefore, the satellite would not feel any acceleration. Such a wide range of IC/IT ratios is possible since at 1 kV, the ion beam produced by the IC ion optics system is not focused. That is to say: the effective grid transparency is very low. Therefore, Figure 7.39(a) depicts that the IC thrust magnitude starts to decrease and is being overtaken by the IT thrust when the total power goes above 160 W.

(a) 1 kV.   (b) 1.5 kV.

(c) 2 kV.   (d) 2.5 kV.
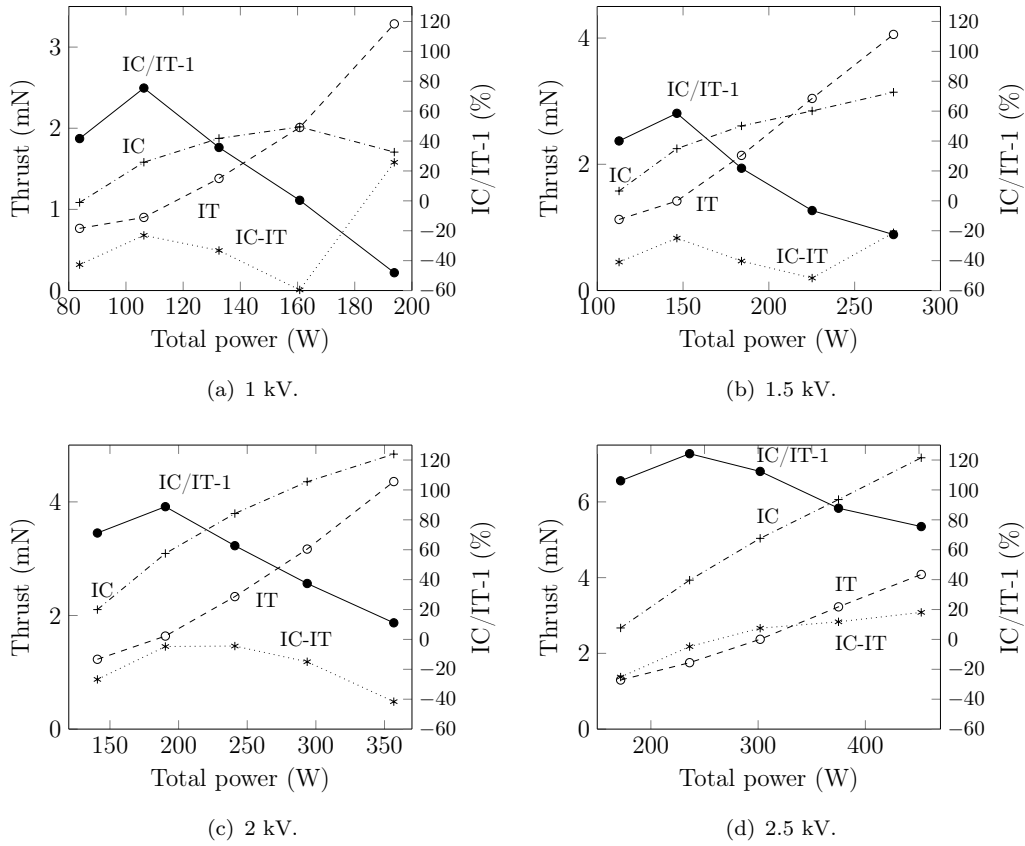
Figure 7.39: Configuration BDST: thrust variation for the IT and IC sides with the screen grid voltage at 12 sccm ($U_{a1} = -250$ V, $U_{a2} = -150$ V).

Even though such a method of operating the thruster is very inefficient due to the poor focusing of one of the ion optics side beams, a very wide range of the IC/IT ratios is achievable. A similar behaviour to that observed at the 1 kV case, is also displayed in Figure 7.39(b) at 1.5 kV. In this figure, even though the IC thrust is always increasing,

the IT thrust overtakes the IC thrust at about 220 W, resulting in the IC/IT-1 parameter being negative. However, when the screen grid voltage goes above 2 kV, the beam focusing becomes much more efficient. Therefore, the IC thrust is always higher than the IT thrust, and IC/IT-1 is always positive, as can be seen in Figure 7.39(c) and Figure 7.39(d).

To better understand how the screen voltage affects the plasma parameters, the beam focusing and thus the thrust, the performance parameter variation with the screen grid voltage at 12 sccm flow rate is depicted in Figure 7.40. As shown in Figure 7.40(a), for high RFG powers, the IT screen current decreases as the screen voltage goes up. For instance, at approximately 100 W of RFG power, the screen current is 68 mA at 1 kV, while at 2.5 kV the screen current is 53 mA. In contrast, Figure 7.40(b) depicts that the IC screen current increases as the screen voltage goes up. For instance, at about 100 W of RFG power, the screen current is 35 mA at 1kV, while at 2.5 kV the screen current is 91 mA. Such a discrepancy in the trends between the IT and IC currents is caused by the difference in the plasma parameters and the sheath shape as the screen grid voltage changes. Regarding the accel current, the IT accel current decreases substantially at high RFG powers and remains nearly unchanged at low RFG powers as the screen grid voltage increases, as shown in Figure 7.40(c). For instance, at about 50 W, the accel currents for all the screen grid voltage cases are approximately 0.8 mA. However, the difference in the accel currents at 100 W between 1 kV and 2.5 kV cases is about 1 mA. For the IC side, this is not the case, it seems that the accel current is not much affected by the change in the screen voltage, as seen in Figure 7.40(d).

Figure 7.40(e) depicts that as the screen voltage is increased, the discharge loss goes down significantly. For instance, at the mass utilisation efficiency of 0.14, the discharge loss goes from about 900 W/A to about 700 W/A as the screen voltage increases from 1.0 to 2.5 kV, respectively. This is because the extracted beam currents go up with the screen voltage, as was shown before. Figure 7.40(f) indicates that the total efficiency also improves with the screen voltage. The total efficiency goes from about 5% to about 12% at 100 W of RFG power. Similarly, the specific impulse also increases from about 450 s to 1,000 s at 100 W of RFG power, as displayed in Figure 7.40(h). Finally, Figure 7.40(g) illustrates that the RFG current increases only by about 5% at the maximum as the screen voltage increases. This shows that the plasma parameters do not change much when the screen voltage changes. However, the change in the plasma parameters comes mainly from the reduced neutral gas pressure inside the discharge chamber as the screen current increases. This in turn causes a change in the ion density and the plasma sheath shape. As a result, the screen currents vary widely, as depicted in Figure 7.40(a) and Figure 7.40(b).
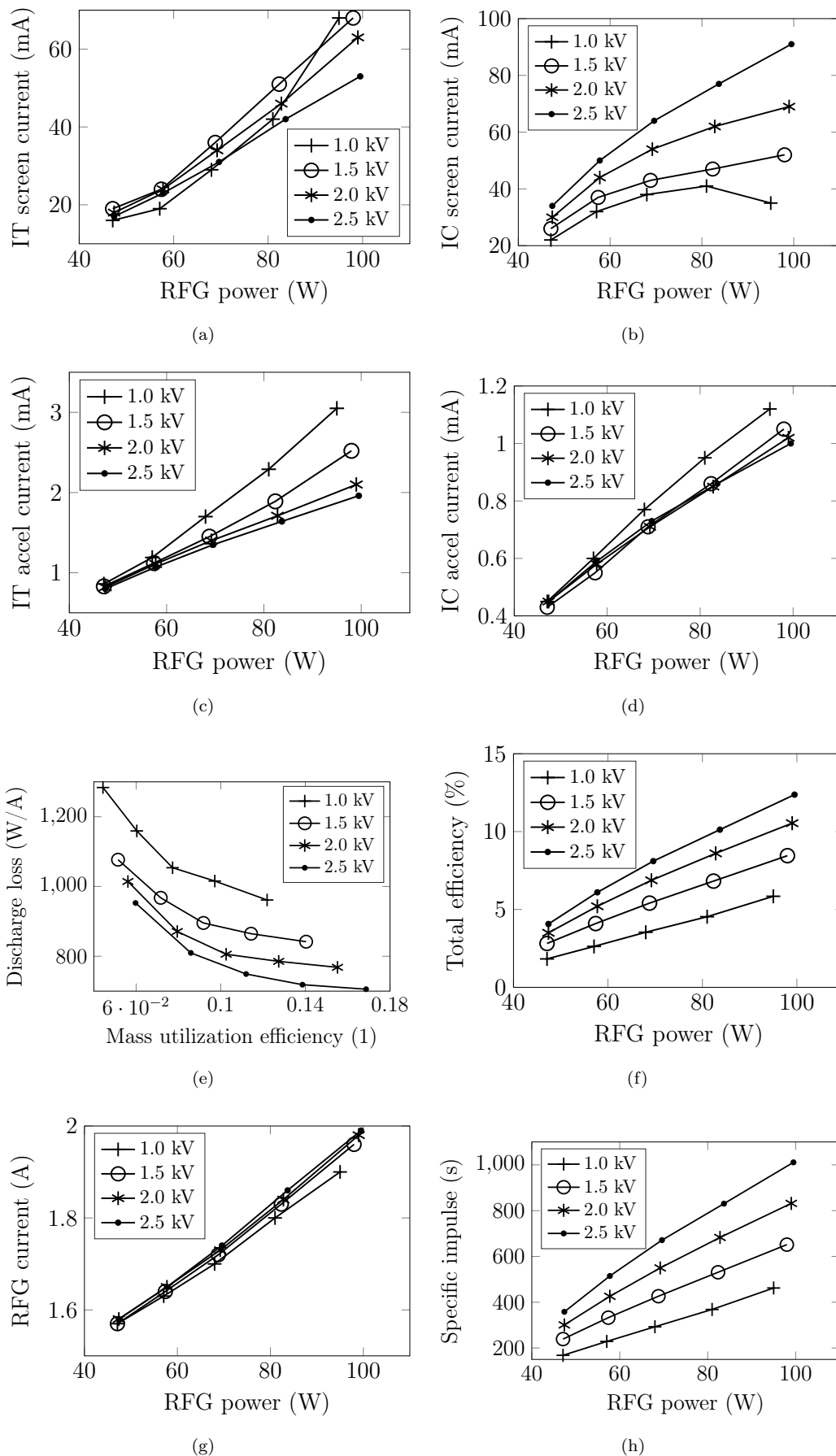
Figure 7.40: Configuration BDST: performance parameters vs RFG power at different screen grid voltages at 12 sccm ($U_{a1} = -250$ V, $U_{a2} = -150$ V).

7.7.3 Varying accel grid voltage

The final way to vary the IT and IC screen currents is to change the accel voltages. Figure 7.41 displays changes in various performance parameters with respect to a nominal accel voltage of 250 V for the IT case and 150 V for the IC case. It can be seen in Figure 7.41(a) that the change in the IT and IC side screen currents at 250 V is 0 since the thruster works at the nominal IT accel voltage. However, when the IT accel voltage is reduced to 0 V, the IT screen current decreases by nearly 1 mA, while the IC screen current goes down by about 0.2 mA. What is more, as displayed in Figure 7.41(a), by increasing the IT accel voltage to 400 V, both the IT and IC screen currents increase by about 0.5 mA. Furthermore, while changing the IT accel voltage, the IC accel current does not change, as shown in Figure 7.41(b). Nevertheless, the IT accel current decreases by about 0.4 mA when the IT accel voltage goes to 0 and increases by about 0.1 mA when the voltage goes to 400 V. Figure 7.41(c) depicts that the IT thrust changes from being lower by 40 μN at the IT accel voltage of 0 V to being higher by 30 μN at 400 V. Whereas, the IC thrust changes from being lower by 13 μN at the IT accel voltage of 0 V to being higher by 35 μN at 400 V. The change in the IC/IT-1 percentage value from the nominal is about 4% at the IT accel voltage of 0 V to almost no change at 400 V.

Furthermore, Figure 7.41(d) indicates that as the IC accel voltage goes up to 400 V, the IC screen current increases by 1.5 mA, while the IT screen current remains about the same. Upon reducing the IC accel voltage, the IC screen current remains unchanged, while the IT screen current increases by 1.5 mA. The IT accel current almost does not change with the IC accel voltage, as depicted in Figure 7.41(e). Whereas, the IC accel current increases by about 0.15 mA at 400 V, and decreases by about 0.15 mA at 0 V. Figure 7.41(f) shows that as the IC accel voltage is reduced to 0 V, the IT thrust increases by about 100 μN, while the IC thrust remains nearly the same. However, upon increasing the IC accel voltage to 400 V, the IT thrust remains unchanged, while the IC thrust increases by 100 μN. Finally, a variation in the change of the IC/IT-1 value from -12% to 6% occurs as the IC accel voltage is varied from 0 to 400 V, respectively. As has been shown, the IT and IC thrust values can be modified by changing the accel voltages. However, the maximum change is only about 100 μN. Therefore, the previously discussed changes in the screen grid voltage, RFG power and mass flow rate should be used for significant variation in the thrust values. However, changing the accel voltage should be employed for very fine thrust adjustments.

(a)

(b)

(c)

(d)

(e)

(f)
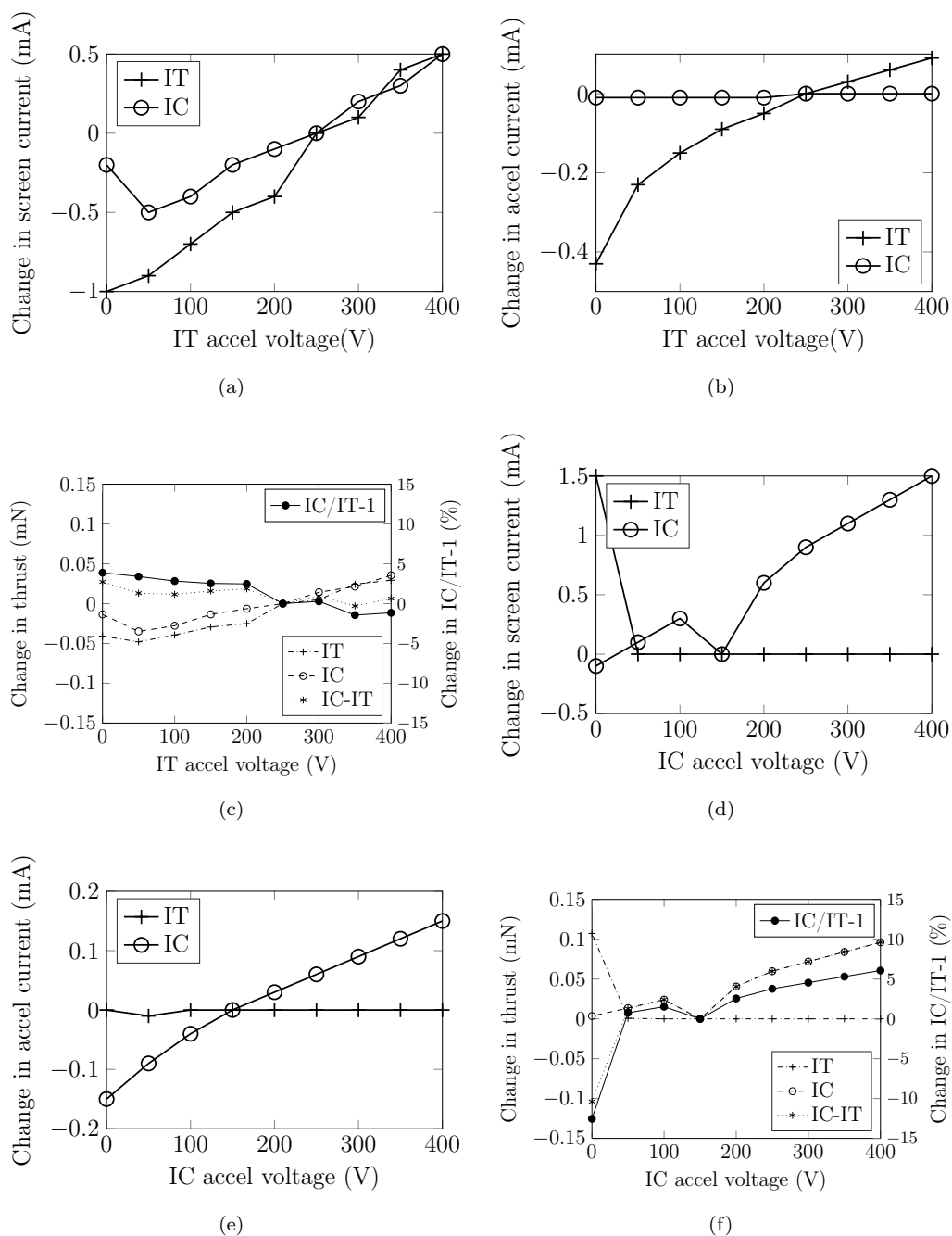
Figure 7.41: Configuration BDST: performance parameter variation for the IT and IC sides with the accel voltage at 10 sccm ($U_s = 2.0$ kV). IT accel nominal voltage 250 V, IC accel nominal voltage 150 V. Note that all accel voltages are biased negatively ($-$).

7.8   Summary

This chapter has presented the experimental results obtained while testing the Double-Sided Thruster (DST) at the University of Southampton vacuum facility. The experimental campaign has shown promising results regarding the applicability of the double-sided thruster concept for the IBS type missions. In particular, two ion beams from the same discharge chamber have been extracted. Also, it was possible to achieve 30% more thrust from the IC ion optics side compared to the IT side, which was one of the LEOSWEEP mission requirements. For instance, the following parameters have been recorded during the experimental campaign for various configurations:

- Configuration AIT: IT thrust = 4.5 mN, screen voltage = 1.5 kV, total power = 210 W, mass utilisation efficiency = 27%, specific impulse = 1,220 s, total efficiency = 13%;

- Configuration AIC: IC thrust = 6.5 mN, screen voltage = 1.5 kV, total power = 262 W, mass utilisation efficiency = 37%, specific impulse = 1,730 s, total efficiency = 21%;

- Configuration ADST: IT thrust = 4.1 mN, IC thrust = 6.3 mN, screen voltage = 1.5 kV, total power = 350 W, mass utilisation efficiency = 34%, specific impulse = 1,570 s, total efficiency = 22.5%;

- Configuration BDST: IT thrust = 3.6 mN, IC thrust = 6.5 mN, screen voltage = 2.5 kV, total power = 416 W, mass utilisation efficiency = 26%, specific impulse = 1,545 s, total efficiency = 18.5%.

Furthermore, by analysing the results, it was observed that the IT to IC thrust ratio (IC/IT-1) strongly depends on the mass flow rate, RFG power and the screen grid voltage. For instance, it was shown that the IC/IT-1 parameter varies from 120% to -50%. Therefore, the DST thruster could be suitable for a wide range of IBS mission scenarios. What is more, by varying the accel voltage it was possible to achieve changes in the IT and IC thrust magnitudes equal to about ± 100 μN. As a result, the accel voltage could be changed when fine thrust adjustments are needed. Nevertheless, the DST thruster presents a more limited range of the IC/IT thrust ratios compared to two single-sided thrusters. For instance, for some IBS type missions, it might be more desirable to have independent control of the IT and IC thrust magnitudes. Furthermore, during an IBS type mission, it could happen that some IC/IT thrust ratios cannot be reached using the DST thruster. Therefore, an IBS mission has to be designed keeping the available IC/IT thrust ratios as constraints. These constraints might increase the complexity/cost of the mission thus offsetting the benefits of the DST thruster. More research is still needed to determine the throtability limits of a double-sided thruster before its full potential for the IBS type missions can be ascertained.

8

Conclusion

This chapter draws main conclusions based on the work presented in this thesis. In particular, a summary of the thesis is provided together with a discussion on the key findings, the significance of the work, the future work and outlook.

8.1   Summary of the thesis

8.1.1   RF gridded ion thruster model

To meet the requirements of such missions as Darwin, LISA and NGGM, ion thrusters have to be scaled down to only a few centimetres in size. As a result, they often suffer from poor performance and thermal issues. Therefore, various modelling tools are needed to help design and optimise such thrusters. This is especially the case for RF gridded ion thrusters because their operation encompasses many different physics phenomena, requiring a holistic modelling approach. However, RF thruster models that have been developed so far concentrate either on predicting the thruster's performance (Volkmar and Ricklefs, 2015), thermal behaviour (Gartner et al., 2013) or plasma parameters (Froese, 2007). Therefore, there is a need for an RF thruster model that could, instead of concentrating on a particular aspect of the RF thruster operation, focus on predicting all the main performance, thermal and plasma parameters.

A multi-physics radio frequency gridded ion thruster model composed of multiple sub-models has been presented in the thesis to address the above-mentioned problems. The model is more representative of the real-life conditions compared to the other models developed, for instance, by Volkmar and Ricklefs (2015), Chabert and Braithwaite (2011) and Gartner et al. (2013). This is because the model developed in the thesis uses a full 3D geometry of a thruster when solving electromagnetic fields and temperature distributions. In addition, the model takes into account all the major factors influencing the thruster's performance: beam extraction, neutral gas flow, plasma production, electromagnetic field distribution, circuit losses and temperature distribution. The model combines all these phenomena to give a comprehensive/holistic description of an RF ion thruster's behaviour and performance with a minimum number of simplifications and assumptions. However, the complexity of the model was kept to a minimum to allow for easily interpretable results and short solution times. For instance, it takes up to 1.5 hours to solve the model for a given operational point using a 16 GB, 2.8 GHz computer. As a result, the plasma is represented using a 0D model instead of fluid or kinetic models, which are much more complex. Finally, the model uses only commercially available (COMSOL, Matlab) or open-source (IBSIMU) software to allow anyone to design a similar model by following the guidelines described in the thesis.

The goal of the thesis was to make the RF ion thruster design more straightforward, hoping RF thrusters would be more often chosen as candidates for various space missions. Furthermore, to save time and cost associated with experimental testing, the model has been designed in such a way to simulate the actual RF ion thruster behaviour upon testing. To make the model results more representative of actual experimental conditions, the RFG input voltage and the propellant mass flow rate are used as the inputs to the model. To check if the model is accurate and can be used to predict a real-life thruster's performance, the model was compared to the RIT 3.5 experimental data. An error of up to 13% was observed between the experimental and modelled RFG voltage and current values. The error in predicting the experimental trends was shown to be below 6%. Finally, it has been demonstrated that the model can predict the RIT 3.5 temperature distribution within an error of approximately 10%.

What is more, the model can be used to gauge different thruster geometries and performances, acting as a tool for designing and optimising RF ion thrusters for specific mission requirements. By analysing the model results, it is also possible to better understand the physical processes occurring in the RF ion thrusters. This allows an engineer to make informed design decisions right from the start and avoid a lengthy iterative design process, saving time and money in the development stage. For instance, the model enables to determine a minimum RFG input power and mass flow rate that is needed to produce a particular beam current (or thrust) for a given mission profile. An especially useful feature of the model is that it allows analysing the thruster's behaviour through the electrical parameters. Therefore, the total resistance and inductance of the thruster

can be ascertained. This permits choosing the matching capacitors and optimum operational frequency and tracking the power losses to different components. Also, using the electrical parameters helps identify the main factors influencing the design of an RF ion thruster and the RFG itself.

The model has shown that the electric field skin depth δ_E for the RIT 3.5 thruster is equal to about 60% of the discharge chamber radius, which is almost the same as for the electric field decay in a vacuum. Whereas, the magnetic field skin depth δ_B is much larger than the thruster's radius. Since both skin depths are very large, a significant increase in the ion density is still possible for the RIT 3.5 thruster, without having a condition when no more power can be transferred to the plasma due to a very thin skin layer (Chabert and Braithwaite, 2011). What is more, the model estimated that the beam current density at which the RIT 3.5 thruster operates is only about half of the Child-Langmuir limit, which means that the ion density could be increased nearly twofold. This would increase the thrust produced by the RIT 3.5 thruster. However, a rise in the ion density would also require an increase in the RFG power and mass flow rate. This might cause thermal issues or require too much power. As a consequence, each change in the operational parameters affects the other ones and therefore has to be weighed against the mission requirements. This can now be achieved using the RF gridded ion thruster model developed in this thesis.

For the first time, a model has been created that predicts the thruster's performance and temperature distribution in a self-consistent/coupled fashion. This is because the model includes the thruster's temperature effect on the plasma parameters/performance and vice versa. Such a coupling is representative of the real-life conditions observed while testing RF thrusters. The developed model is in contrast to the other RF thruster models designed, for example, by Volkmar and Ricklefs (2014, 2015), Chabert et al. (2012) or Gartner et al. (2013) which only looked at a specific aspect of the RF thruster operation, concentrating on either predicting the thruster's performance or the temperature distribution but not both in a coupled fashion. From the model results, it was observed that if the coupling between the thruster's temperatures and performance is not consistent, an error of up to about 10% in the RFG input power can be incurred at high mass utilisation efficiencies. The error, however, depends on the thruster's temperatures that are set as a constant in performing the simulations. The 10% discrepancy occurred when the discharge chamber wall temperature was set to 400 K, which is a typical temperature value used when analysing the RF ion thruster performance.

In particular, the model was also used to analyse the temperature effect on the thruster's performance. It was noticed that as thruster's temperatures increase, the coil current and reflected thruster's resistance also increase. This results in the RFG input power going up. For instance, it was observed that if the thruster's discharge chamber wall temperature rises from 310 to 480 K, the RFG input power goes up by about 20%. This shows that it is important to keep the thruster as cool as possible. This could

be achieved by changing the thruster's design. Additionally, when planning a space mission, the environmental thermal fluxes to the thruster have to be minimised. This is particularly the case for missions that work with low power thrusters. The model can also be used to judge the thermal thruster's design because it provides a 3D surface temperature distribution plot. By investigating the RIT 3.5 temperature distribution plot, it was observed that the coil temperature gets above 200 ℃, which makes it the hottest component in the thruster. Considering that copper, which is commonly used to manufacture the RF coils, has quite a high thermal expansion coefficient, a significant change in the coil's shape could occur. Therefore, this could considerably reduce the thruster's performance. What is more, the model predicted that in the RIT 3.5 thruster, the matching capacitors reach about 150 ℃. The designer must check that the capacitors' temperatures do not go above around 200 ℃ throughout the operational envelope of the thruster. This can now be performed using the model presented in this thesis.

8.1.2   Double-sided ion thruster concept

The LEOSWEEP mission proposes to de-orbit a 1.5-ton launcher upper stage from a nearly polar low Earth orbit (LEO) in 170 days using the Ion Beam Shepherd (IBS) method proposed by Bombardelli et al. (2011). The IBS method is a contactless space debris removal concept where the momentum to the debris is imparted by a high-energy collimated neutralised plasma beam produced by the Impulse Transfer Thruster (ITT). To compensate for the thrust produced by the ITT, a second thruster, called an Impulse Compensation Thruster (ICT), is also required. The LEOSWEEP project team plans to use a radio frequency (RF) ion thruster as the ITT due to its capability to produce a low divergence beam, which was shown to significantly increase the momentum transfer efficiency. Nevertheless, the most optimum thruster option to act as the ICT has not been chosen yet. In this thesis, a novel Double-Sided Thruster (DST) concept for the IBS type missions has been proposed. The concept thruster produces two ion beams from the same discharge chamber: the beam from one side of the thruster is used for the IT, while the beam from the other side is employed for the IC. Therefore, instead of the two-thruster design, a single double-sided thruster simultaneously producing two ion beams can be used. The main advantage of such a design is a much simpler sub-system architecture, lower cost, and lower total mass, with the total power and propellant requirements similar (or better) to those of the two-thruster system.

A double-sided ion thruster has been designed, using the RF ion thruster model developed in this thesis, to meet the LEOSWEEP mission requirements. The primary requirement imposed by the LEOSWEEP mission is that 30 mN of thrust must be transferred to the debris target. The behaviour of the DST has been simulated to optimise the discharge chamber and coil geometries, screen grid voltage and predict the thruster's performance. First, the simulations have shown that the screen grid voltage

of 3 kV results in the lowest total power, which has been estimated to be around 2.8 kW. Second, to fulfil the LEOSWEEP mission requirements, the model has predicted that the IT side of the DST thruster would have to produce 33 mN, while the IC side would have to provide 43 mN of thrust. This means that the IC thrust must be around 30% larger compared to the IT thrust. Finally, the simulations predicted that the DST thruster would need about 270 W of RFG power to obtain the thrust magnitudes mentioned above. This means that the DST requires roughly half the RFG power compared to two single-ended RF ion thrusters.

Next, the DST thruster was compared to a system of two single-sided thrusters. The analysis has shown that the double-sided ion thruster should use 100 W less power and 9 kg less propellant than a combination of two single-sided ITT thrusters for the IT and IC purposes. However, compared to a system that uses the ITT thruster for the IT and the RIT 15 thruster for the IC, the DST thruster needs around 300 W more power and 8 kg less propellant. A combination of the ITT thruster for the IT and a Hall SPT-70 thruster for the IC has been shown to offer the lowest total power of the system equal to 2,050 W, which is 800 W less than that predicted if the DST thruster is used. However, when the SPT-70 thruster is employed, the total propellant consumption is the highest at 47 kg, which is 26 kg more than what the DST thruster requires. The study excluded the total system mass analysis, where the double-sided thruster should have the lowest total mass due to its inherent simplicity compared to the other two-thruster systems.

To prove the double-sided thruster concept, an extensive experimental campaign was performed at the University of Southampton vacuum facility. The DST thruster was designed in such a way that it could be run in two configurations: Configuration A and Configuration B. In Configuration A, the IT ion optics system was composed of three carbon-carbon grids. Whereas, the IC ion optics system (denoted as IC1) had a single SILUX (ceramic) grid with an aluminium layer. In Configuration B, the same IT ion optics system was used as in Configuration A, but the IC ion optics system (denoted as IC2) was composed of two titanium grids. In addition, in Configuration A, each side of the ion optics could be blocked. This meant that the thruster could be tested while only either the IT or IC sides were active. Furthermore, to extract 30% more thrust from the IC ion optics system compared to the IT ion optics system, the IC ion optics system was designed with 24% more apertures than the IT ion optics system. During the experimental campaign, the thruster's performance was mapped by varying the mass flow rate, screen/accel grid voltages and the RFG power. However, while testing, only an RFG that goes to a maximum power of about 100 W was available. This meant that the conditions as simulated by the model could not be reached. However, 100 W of RFG power proved to be enough to validate the concept.

Configuration (thruster) / Performance	AIT	AIC	ADST	BDST	RIT 3.5	RIT 10
Active grid diameter (cm)	13	13	13	13	3.5	10
Thrust IT side (mN)	4.5	-	4.1	3.6	1	15
Thrust IC side (mN)	-	6.5	6.3	6.5	-	-
Screen voltage (V)	1500	1500	1500	2500	1000	1500
IT screen current (mA)	75.5	-	67.5	46.2	19.5	234
IC screen current (mA)	-	107	102.4	82.5	-	-
RFG power (W)	100	104	100	100	21	108
Beam power (W)	110	158	252	316	19.5	351
Total power (W)	210	262	352	416	40.5	459
Specific power (W/mN)	46.4	40.3	33.9	41.2	40.5	30.6
Specific impulse (s)	1220	1730	1570	1545	2800	3400
Mass utilisation efficiency (%)	27	37	34	26	68	69
Electrical efficiency (%)	52	60	72	76	48	76
Discharge loss (W/A)	1372	984	596	787	1077	461
Total efficiency (%)	13	21	22.5	18.5	33	52
Operational frequency (MHz)	1.23	1.23	1.23	1.23	3.1	1

Table 8.1: Summary of the DST thruster's performance parameters in various configurations, including the RIT 3.5 and RIT 10 thrusters' performance data.

The experimental test campaign has been successful. It has been proven that the DST thruster has potential to be used as an alternative for the IBS type missions. In addition, it was shown that it is possible to control the thrust produced by the IT and IC sides by varying the number of apertures in the ion optics systems. Also, by changing the operational parameters, a wide range of the IC to IT thrust ratios was obtained. For instance, a variation in the IC to IT thrust ratios from about -50% to 120% was observed. Furthermore, it was shown that by varying the accel voltage, the IT and IC thrust magnitudes could be changed by about ± 100 μN. This variation of the thrust is crucial for the IBS missions. The DST thruster's performance parameters as obtained during the experimental campaign for various configurations are summarised in Table 8.1. For comparison, the performance values of the RIT 3.5 and RIT 10 thrusters (Goebel and Katz, 2008; Koschade et al., 1972) are included as well.

As can be seen from Table 8.1, in Configuration ADST, the thrust produced from the IT side is 4.1 mN, while the thrust generated from the IC side is 6.3 mN, which is about 50% larger compared to the IT side. Note, however, that these thrust values are very close to those obtained while testing the thruster in the single-sided Configurations AIT and AIC. Also, note that the maximum screen voltage that could be reached in Configuration A was 1.5 kV. This was limited by the IC1 ion optics system producing sparks above 1.5 kV. As Table 8.1 depicts, in Configuration ADST, the RFG power is 100 W, which is about the same as that in Configurations AIT and AIC. Furthermore, the IT and IC screen currents in Configuration ADST are nearly identical to those in Configurations AIT and AIC. Therefore, it can be assumed that introducing an additional ion optics system does not cause a significant increase in the RFG power. However, the mass flow rate has to be increased to account for a greater open area fraction due to two ion optics systems. This is why even though two ion beams are extracted in Configuration ADST, the specific impulse and the mass utilisation efficiency equal to 1,570 s and 34%, respectively, are nearly identical to those found in Configurations AIT and AIC. Furthermore, in Configuration ADST, the total efficiency is 22.5%, which is 1.5% higher compared to Configuration AIC and 9.5% higher compared to Configuration AIT. Such low mass utilisation and total efficiency values were obtained due to the 100 W power limit imposed by the RFG. To achieve higher values, the RFG power would need to be increased to around 200 W.

What is more, Configuration ADST has a discharge loss of about 596 W/A, which is about two times lower than that observed in Configurations AIT and AIC. This happens because two ion beams are extracted in Configuration ADST. However, such a discharge loss is still higher compared to the RIT 10 thruster. In Configurations AIT and AIC, the discharge losses are comparable to those found in the RIT 3.5 thruster and are more than two times larger as observed in the RIT 10 thruster. This is because the DST thruster's discharge chamber diameter and ion optics systems' dimensions have not been optimised. Table 8.1 shows that in Configuration BDST, it was possible to reach a screen voltage

of 2.5 kV. Additionally, in Configuration BDST, the IT thrust is 3.6 mN, while the IC thrust is 6.5 mN, which is about 80% larger compared to the IT thrust. Note that the RFG power and specific impulse values between Configurations ADST and BDST are similar even though in Configuration BDST the IT and IC screen currents are 30% and 20% smaller than those in Configuration ADST, respectively. This is due to the screen voltage being 1 kV larger in Configuration BDST compared to Configuration ADST. However, the difference in the mass utilisation efficiency values between Configurations ADST and BDST is about 8% due to the lower screen currents, as mentioned above. Similarly, Configuration BDST has a higher discharge loss compared to Configuration ADST.

8.2   Significance of the work

The following list summarises the main achievements of the thesis:

- a multi-physics RF gridded ion thruster model composed of multiple sub-models has been developed; for the first time there is a model that can be used to simulate the thruster's temperatures, plasma parameters, neutral gas distribution, ion beam extraction, performance parameters and RF circuit behaviour in a self-consistent fashion;

- the model has been validated against the RIT 3.5 experimental data; the validation results have shown that the model can predict the RIT 3.5 performance and thermal data within about 15% error; the high accuracy of the model makes it suitable to be used as an RF gridded ion thruster design tool;

- the designed model is available for everyone to use since it has been built using commercially available software such as COMSOL, MatLab and IBSIMU;

- a novel Double-Sided Thruster (DST) concept has been presented for the IBS type missions; the DST thruster has been designed using the model developed in the thesis; the model results have shown that the DST thruster is comparable to a two-thruster system in terms of power and propellant requirements; however, the main advantage of the DST thruster is the simpler sub-system architecture;

- a DST thruster has been designed and built with only one discharge chamber, one coil and two ion optics systems; therefore, such a thruster is the first of its kind;

- an extensive experimental campaign has been performed to test the concept; the thruster has been tested with single-grid, two-grid and three-grid ion optics systems; it is one of the first times an ion optics system with a single-grid has been used; additionally, the thruster has also been tested in single-sided configurations;

- the experimental campaign has been successful; it has been shown that the DST thruster is a plausible alternative for IBS type missions; in particular, the experimental campaign has shown that it is possible to achieve more thrust from one side of the thruster by varying the number of apertures in each ion optics systems;

- the DST experimental campaign has shown that the RFG power stays approximately the same when an additional ion optics system is added, provided that the mass flow rate is increased; in addition, the thrust values produced from each end of the thruster can be controlled by varying the mass flow rate, RFG power and screen/accel voltages;

- a variation in the IT/IC-1 thrust ratios from about -50% to 120% has been obtained; this proves that the thruster can be used for a broad range of IBS mission scenarios;

- it has been observed that by varying the accel voltage, the IT and IC thrust magnitudes change by about $\pm 100 \ \mu$N; therefore, changing the accel voltage can be used for fine thrust control of the satellite.

8.3   Future work and outlook

The RF gridded ion thruster model developed in this thesis can potentially be used to gauge different thruster geometries and performances. Therefore, the model can act as a tool for designing and optimising RF ion thrusters to make them more attractive for specific space missions. However, there are a few possible modification/additions that, if introduced, would make the model even more comprehensive and useful as described in the list below:

- possibility of including environmental heat fluxes based on a particular mission profile/orbit;

- possibility of accounting for mechanical deformations of the coil and grids due to thermal stresses, and to check how these affect the thruster's performance;

- introduction of a more detailed stochastic (non-local) heating model;

- proposal of a more comprehensive plasma confinement model due to magnetic field effects.

The analysis presented in this thesis was aimed at proving the double-sided concept viability for IBS type missions. The simulation results and experimental data proved that the double-sided thruster has potential to be used for IBS missions. Nevertheless, there is still much work that needs to be done to move the DST from a concept model to

an engineer or flight model. In addition, due to the limitations regarding the available equipment and the vacuum facility, as well as time constraints, there were many tests that could not be performed. The list below summarises the steps that could be taken to further develop the DST thruster:

- perform detailed beam plume diagnostics to measure the extracted current magnitudes from both sides of the thruster;

- conduct thrust measurements to verify the thrust magnitudes produced from both sides of the thruster;

- perform experimental tests that measure the thrust magnitude transferred onto a target;

- investigate the thruster's performance using an RFG that can reach up to 300 W of power;

- optimise the discharge chamber diameter and ion optics geometries to reduce the discharge loss and increase the total efficiency of the thruster.

The electric propulsion technology has reached a stage of commercialisation. The challenge now is to integrate the electric thrusters with the power and propellant management subsystems available on the spacecraft. This is especially true for various types of SmallSats. The electric thrusters can be scaled down to a few centimetres in size and still work efficiently, as was shown by the RIT 3.5 thruster. However, the solar panels, power processing units and propellant management systems are not easily scalable to the size and mass constraints imposed by SmallSats. In addition, electric propulsion thrusters will always be confined to the inner solar system if they keep relying on solar panels for energy production. Therefore, if electric thrusters are to be used to reach the outer solar planets such as Uranus or Neptune, or to go even beyond the solar system, new types of energy sources will be needed. For instance, the energy could come from radioisotope thermoelectric generators (RTG's) or other nuclear energy sources, or fusion energy. Finally, the main task now for electric propulsion engineers is to design and optimise the thrusters for various new types of missions. The previous examples include such mission as Dawn (Garner et al., 2013), GOCE (Wallace et al., 2011) and BepiColombo (Lewis et al., 2015). Hopefully, the LEOSWEEP mission will join this list in the future. The author hopes that people developing the LEOSWEEP mission will use the modelling tools and the DST thruster's design/data presented in this thesis.

A

RIT 3.5 experimental campaign results

Table A.1 summarises the results from the RIT 3.5 experimental campaign that was held in Giessen, Germany at the TransMIT vacuum facilities. In particular, the RIT 3.5 thruster was tested in the R2D2 vacuum facility. The results displayed in Table A.1 were used to validate the RF gridded ion thruster model developed in this thesis. Note that all tests were performed using xenon as the propellant. Additionally, the pressure in the main vacuum chamber was about 10^{-5} mbar throughout the operation of the thruster. Table A.1 gives values for the following parameters: $\dot{m}_{in}$ - propellant mass flow rate, U_s - screen grid voltage, I_s - screen grid current, I_a - accel grid current, U_{in} - RFG input voltage, I_{in} - RFG input current, η_m - mass utilisation efficiency, P_{in} - RFG power, P_b - total beam power, $P_t = P_{in} + P_b$ - total input power to the thruster (excluding the neutraliser's power), T - thrust calculated based on the screen grid voltage and current, T_1 to T_8 - temperatures of the temperature sensors TS1 to TS8. All performance values were recorded multiple times to ensure that equilibrium conditions had been reached. The temperature values were recorded after about 60 min of operation at a particular point.

$\dot{m}_{in}$ (sccm)	U_s (V)	I_s (mA)	U_a (V)	I_a (mA)	U_{in} (V)	I_{in} (A)	η_m (1)	P_{in} (W)	P_b (W)	P_t (W)	T (μN)	T_1 (°C)	T_2 (°C)	T_3 (°C)	T_4 (°C)	T_5 (°C)	T_6 (°C)	T_7 (°C)	T_8 (°C)
0.20	262	1.95	150	0.067	5.97	1.34	0.13	7.99	0.51	8.50	51	50.5	51.6	45.2	41.1	51.6	67.8	33.6	33.5
0.20	500	2.11	150	0.058	6.01	1.35	0.15	8.09	1.06	9.15	75	51.5	52.7	46.5	42.3	53.1	69.9	34.2	34.0
0.20	637	2.51	150	0.092	6.15	1.36	0.17	8.34	1.58	9.92	100	52.8	54.1	47.5	43.1	54.3	71.4	34.7	34.6
0.20	750	3.49	150	0.134	6.49	1.38	0.24	8.94	2.57	11.51	150	55.3	56.6	49.2	44.4	56.5	74.3	35.5	35.4
0.20	488	5.56	150	0.078	7.52	1.49	0.39	11.17	2.72	13.89	200	59.6	61.4	52.2	47.1	61.4	81.4	37.2	37.0
0.20	1000	5.08	150	0.236	7.17	1.46	0.34	10.48	4.93	15.41	251	59.9	61.5	52.4	47.2	60.8	80.4	37.3	37.3
0.26	1100	9.49	150	0.200	8.35	1.48	0.48	12.40	9.76	22.16	500	62.1	64.1	52.6	47.2	63.1	82.6	37.4	37.7
0.30	1200	13.46	150	0.220	9.95	1.67	0.60	16.65	15.52	32.17	750	76.4	79.4	64.1	58.0	79.0	104.3	43.2	43.3
0.37	1100	9.68	150	0.464	7.73	1.17	0.35	9.05	10.28	19.33	500	63.4	65.1	55.6	48.9	62.1	78.8	38.6	38.9
0.37	1100	10.62	150	0.481	8.02	1.25	0.42	10.01	12.21	22.21	580	66.3	69.2	58.3	52.2	65.8	84.1	39.3	39.6
0.37	1200	13.62	150	0.386	9.14	1.36	0.50	12.39	16.08	28.48	750	74.8	77.3	64.7	57.2	74.3	95.6	43.1	43.2
0.37	1200	14.19	150	0.392	9.85	1.40	0.55	13.8	17.51	31.30	800	77.6	81.6	67.5	60.5	77.1	100.1	43.8	44.1
0.37	1000	19.52	150	0.219	13.13	2.07	0.73	27.13	19.52	46.65	1000	99.1	104.9	80.0	75.5	106.7	144.2	51.3	50.9
0.40	1000	19.54	150	0.251	11.93	1.75	0.68	20.93	19.51	40.44	1000	88.0	92.4	72.6	65.8	91.8	122.2	47.2	47.2
0.51	1350	26.97	150	0.325	13.96	1.93	0.74	27.01	36.34	63.35	1600	104.4	110.5	85.8	79.6	109.7	144.3	55.0	54.8
0.61	1158	25.77	150	0.631	12.62	1.29	0.58	16.29	29.42	45.72	1400	86.0	89.9	72.4	64.0	85.8	107.6	47.0	47.3
0.61	1350	27.23	150	0.579	12.66	1.38	0.62	17.46	36.35	53.81	1600	89.7	93.9	75.4	67.0	89.7	113.2	48.7	48.9
0.61	1350	29.04	150	0.585	13.07	1.63	0.68	21.31	40.01	61.32	1750	97.2	101.3	81.2	74.1	100.2	129.8	50.3	50.6
0.61	1321	30.79	150	0.490	13.96	1.73	0.70	24.07	40.44	64.51	1800	104.8	110.8	87.6	80.3	107.8	138.9	55.6	55.3
0.61	1500	32.07	150	0.454	14.42	1.83	0.73	26.38	47.91	74.29	2000	109.2	115.7	90.9	84.0	113.0	146.5	57.3	57.0
0.74	1625	38.62	200	0.631	15.41	1.78	0.72	27.41	62.36	89.77	2500	113.4	120.6	93.5	86.8	116.8	150.1	58.3	58.3

Table A.1: RIT 3.5 performance and thermal data obtained in the R2D2 vacuum facility.

B

Cross-section data

Elastic scattering, ionization and excitation cross-sections for xenon are provided in Table B.1 and Table B.2. The cross-section data was obtained from the SIGLO database (2015) that was compiled using the results from the work by Meunier et al. (1995). These cross-sections were used in constructing the Boltzmann COMSOL module. The following notation is used in the tables: e - electron, Xe - neutral xenon atom, Xe+ - singly charged xenon ion, Xes - excited xenon atom. Note that the first column of each table shows the electron energy in eV, while the second column shows the cross-section size in m^2.

Elastic		Ionisation (12.12 eV)	
e+Xe ⇒ e+Xe		e+Xe ⇒ 2e+Xe+	
0.0000e+0	1.3050e-18	1.2120e+1	0.0000e+0
1.0000e-2	8.4250e-19	1.2500e+1	1.1000e-21
2.0000e-2	6.7140e-19	1.3000e+1	2.5600e-21
3.0000e-2	5.5710e-19	1.3500e+1	4.1200e-21
4.0000e-2	4.7240e-19	1.4000e+1	5.7100e-21
6.0000e-2	3.5330e-19	1.4500e+1	7.4200e-21
8.0000e-2	2.7290e-19	1.5000e+1	9.0600e-21
1.0000e-1	2.1530e-19	1.5500e+1	1.0700e-20
1.2000e-1	1.7240e-19	1.6000e+1	1.2300e-20
1.6000e-1	1.1400e-19	1.6500e+1	1.3800e-20
2.0000e-1	7.7870e-20	1.7000e+1	1.5300e-20
2.6000e-1	4.6030e-20	1.7500e+1	1.6700e-20
3.0000e-1	3.3370e-20	1.8000e+1	1.8000e-20
3.6000e-1	2.1540e-20	1.9000e+1	2.0500e-20
4.0000e-1	1.6610e-20	2.0000e+1	2.2700e-20
4.4000e-1	1.3180e-20	2.1000e+1	2.4900e-20
5.0000e-1	9.9300e-21	2.2000e+1	2.7300e-20
5.6000e-1	8.1910e-21	2.3000e+1	2.9200e-20
6.0000e-1	7.6520e-21	2.4000e+1	3.0900e-20
6.2000e-1	7.5410e-21	2.6000e+1	3.3600e-20
6.4000e-1	7.5300e-21	2.8000e+1	3.6100e-20
6.6000e-1	7.6100e-21	3.0000e+1	3.8500e-20
6.8000e-1	7.7900e-21	3.2000e+1	4.0400e-20
7.0000e-1	8.0700e-21	3.4000e+1	4.1800e-20
7.6000e-1	9.4500e-21	3.6000e+1	4.2900e-20
8.0000e-1	1.0550e-20	3.8000e+1	4.3900e-20
1.0000e+0	1.7200e-20	4.0000e+1	4.4700e-20
1.2000e+0	2.5500e-20	4.5000e+1	4.6800e-20
1.4000e+0	3.5300e-20	5.0000e+1	4.8300e-20
1.8000e+0	5.9800e-20	5.5000e+1	4.9400e-20
2.2000e+0	8.9500e-20	6.0000e+1	5.0300e-20
2.6000e+0	1.2400e-19	6.5000e+1	5.0800e-20
3.0000e+0	1.6100e-19	7.0000e+1	5.1200e-20
4.0000e+0	2.4100e-19	8.0000e+1	5.1800e-20
5.0000e+0	2.8000e-19	9.0000e+1	5.2600e-20
6.0000e+0	2.8000e-19	1.0000e+2	5.3800e-20
8.0000e+0	2.6000e-19	1.1000e+2	5.4500e-20
1.0000e+1	2.0000e-19	1.2000e+2	5.4500e-20
1.2000e+1	1.3500e-19	1.3000e+2	5.4100e-20
1.5000e+1	9.5000e-20	1.4000e+2	5.2800e-20
2.0000e+1	7.0000e-20	1.5000e+2	5.1900e-20
2.5000e+1	5.9000e-20	1.6000e+2	5.0600e-20
3.0000e+1	5.1000e-20	1.8000e+2	4.8300e-20
4.0000e+1	4.2000e-20	2.0000e+2	4.5800e-20
5.0000e+1	3.6000e-20	3.0000e+2	3.8900e-20
6.0000e+1	3.2000e-20	4.0000e+2	3.3600e-20
8.0000e+1	2.7000e-20	6.0000e+2	2.6000e-20
1.0000e+2	2.4000e-20	8.0000e+2	2.1900e-20
1.2000e+2	2.1500e-20	1.0000e+3	1.8800e-20
1.5000e+2	1.9000e-20		
2.0000e+2	1.6500e-20		
2.5000e+2	1.4500e-20		
3.0000e+2	1.3000e-20		
5.0000e+2	9.4000e-21		
1.0000e+3	5.8000e-21		

Table B.1: Xenon (Xe) elastic scattering and ionisation cross-sections.

Excitation (8.31 eV)	
e+Xe ⇒ e+Xes	
8.3100e+0	0.0000e+0
8.4700e+0	2.5000e-22
8.8400e+0	6.3000e-22
9.0360e+0	1.0270e-21
9.3800e+0	8.7000e-22
9.5200e+0	1.8000e-21
9.7300e+0	1.0260e-21
1.0490e+1	1.1580e-21
1.0970e+1	1.1800e-21
1.1650e+1	1.1600e-21
1.2200e+1	1.1260e-21
1.4980e+1	8.5700e-22
1.7460e+1	6.3600e-22
2.0050e+1	4.6400e-22
2.3680e+1	3.1100e-22
2.7460e+1	2.1700e-22
3.3360e+1	1.1800e-22
3.5100e+1	1.0400e-22
5.0000e+1	0.0000e+0

Excitation (8.44 eV)	
e+Xe ⇒ e+Xes	
8.4400e+0	0.0000e+0
1.5090e+1	3.4200e-21
1.7180e+1	4.2100e-21
1.9040e+1	4.7700e-21
2.1850e+1	5.3300e-21
2.5060e+1	5.7100e-21
2.8570e+1	6.0000e-21
3.3740e+1	6.1200e-21
4.1300e+1	6.0560e-21
6.3880e+1	5.3900e-21
8.5460e+1	4.7380e-21
1.0000e+2	4.4200e-21
3.0500e+2	0.0000e+0

Excitation (9.69 eV)	
e+Xe ⇒ e+Xes	
9.6900e+0	0.0000e+0
1.0040e+1	1.0570e-21
1.0600e+1	2.1270e-21
1.1320e+1	3.1940e-21
1.2270e+1	4.3040e-21
1.3180e+1	4.8400e-21
1.4400e+1	5.3200e-21
1.5740e+1	5.5600e-21
1.6740e+1	5.6600e-21
1.8360e+1	5.6900e-21
2.0810e+1	5.6300e-21
2.5770e+1	5.3600e-21
3.3270e+1	4.8900e-21
3.9650e+1	4.5500e-21
5.0000e+1	3.8000e-21
1.0000e+2	2.2600e-21
2.0000e+2	1.3000e-21
5.0000e+2	6.1000e-22
1.0000e+3	3.3400e-22

Excitation (10 eV)	
e+Xe ⇒ e+Xes	
1.0000e+1	0.0000e+0
1.1440e+1	4.6000e-21
1.2350e+1	6.4000e-21
1.3040e+1	7.4700e-21
1.4170e+1	8.6700e-21
1.5120e+1	9.2900e-21
1.6250e+1	9.8900e-21
1.7440e+1	1.0230e-20
1.9210e+1	1.0570e-20
2.1380e+1	1.0750e-20
2.4940e+1	1.0800e-20
3.3010e+1	1.0380e-20
4.0000e+1	9.8000e-21
1.0000e+2	4.9000e-21
2.0000e+2	2.8000e-21
5.0000e+2	1.3200e-21
1.0000e+3	7.3000e-22

Excitation (11 eV)	
e+Xe ⇒ e+Xes	
1.1000e+1	0.0000e+0
1.1260e+1	4.1400e-22
1.2560e+1	9.0000e-22
1.3940e+1	1.2800e-21
1.5210e+1	1.4200e-21
1.6540e+1	1.4200e-21
1.8850e+1	1.3700e-21
2.3000e+1	1.1600e-21
2.7680e+1	8.9000e-22
3.2930e+1	6.9000e-22
3.8810e+1	5.2000e-22
4.6560e+1	3.7000e-22
6.2430e+1	1.9000e-22
8.0100e+1	8.5000e-23
1.0000e+2	9.0000e-24
2.0000e+2	0.0000e+0

Excitation (11.7 eV)	
e+Xe ⇒ e+Xes	
1.1700e+1	0.0000e+0
1.3590e+1	7.4400e-22
1.5790e+1	1.8400e-21
1.8750e+1	3.5200e-21
2.3150e+1	5.6000e-21
2.8510e+1	7.0700e-21
3.0870e+1	7.4800e-21
3.4060e+1	7.8700e-21
3.7940e+1	8.2000e-21
4.2210e+1	8.3900e-21
4.8110e+1	8.4800e-21
5.2740e+1	8.4800e-21
5.9800e+1	8.3800e-21
7.2840e+1	8.0300e-21
1.0000e+2	7.1900e-21
2.0000e+2	4.3400e-21
5.0000e+2	1.9000e-21
1.0000e+3	1.1000e-21

Table B.2: Xenon (Xe) excitation cross-sections.

C

DST experimental campaign results

− "min" - input mass flow rate to the thruster;
− "URFG" - RFG input voltage;
− "IRFG" - RFG current;
− "PRFG" - RFG power;
− "US" - IT & IC screen grid voltages;
− "IS" IT & IC total screen grid current;
− "USIT" - IT screen grid voltage;
− "ISIT" - IT screen grid current;
− "UAIT" - IT accel grid voltage;
− "IAIT" - IT accel grid current;
− "ISIC" - IC screen grid current;

− "UAIC" - IC accel grid voltage;
− "IAIC" - IC accel grid current.

Additionally, the Excel file is composed of many sheets. Each sheet represents a different operational condition. This could be a different screen grid voltage, the type of configuration used or whether any sides of the thruster are blocked. Note that the thruster was tested in Configuration AIT, Configuration AIC, Configuration ADST and Configuration BDST. In the Excel file, the following operational conditions are presented:

− "AIT 1.0kV" - Configuration AIT, only IT side active, screen grid voltage 1.0 kV;
− "AIT 1.5kV" - Configuration AIT, only IT side active, screen grid voltage 1.5 kV;
− "AIT 2.0kV" - Configuration AIT, only IT side active, screen grid voltage 2.0 kV;
− "AIT 2.5kV" - Configuration AIT, only IT side active, screen grid voltage 2.5 kV;
− "AIT 3.0kV" - Configuration AIT, only IT side active, screen grid voltage 3.0 kV;
− "AIC 1.5kV" - Configuration AIC, only IC side active, screen grid voltage 1.5 kV;
− "ADST 1.0kV" - Configuration ADST, IT and IC active, screen grid voltage 1.0 kV;
− "ADST 1.5kV" - Configuration ADST, IT and IC active, screen grid voltage 1.5 kV;
− "BDST 1.0kV" - Configuration BDST, IT and IC active, screen grid voltage 1.0 kV;
− "BDST 1.5kV" - Configuration BDST, IT and IC active, screen grid voltage 1.5 kV;
− "BDST 2.0kV" - Configuration BDST, IT and IC active, screen grid voltage 2.0 kV;
− "BDST 2.5kV" - Configuration BDST, IT and IC active, screen grid voltage 2.5 kV.

References

Airbus (2003). Ion propulsion systems. http://www.space-propulsion.com/spacecraft-propulsion/ion-propulsion/ [Accessed: 2017-01-10].

Aliev, Y. M., Kaganovich, I. D., and Schlüter, H. (1997). Quasilinear theory of collisionless electron heating in radio frequency gas discharges. *Physics of Plasmas*, 4(7):2413–2421.

Bassner, H., Killinger, R., Leiter, H., and Müller, J. (2001). Development steps of the RF-ion thrusters RIT. In *27th International Electric Propulsion Conference*, Pasadena, CA.

Bauder, U., Herdrich, G., and Fasoulas, S. (2013). Modeling of a DC-RF plasmathruster with the Navier-Stokes code SINA. In *33rd International Electric Propulsion Conference*, Washington, D.C.

Bejan, A. and Kraus, A. D. (2003). *Heat Transfer Handbook*. John Wiley & Sons, Hoboken, New Jersey, 1st edition.

Bober, A. S., Kim, V. P., Popov, G. A., and et al. (1991). State of the works of electrical thrusters in the USSR. In *22nd International Electric Propulsion Conference*, Viareggio, Italy.

Bombardelli, C. and Pelaez, J. (2011a). Ion Beam Shepherd for asteroid deflection. *Journal of Guidance, Control, and Dynamics*, 34(4):1270–1272.

Bombardelli, C. and Pelaez, J. (2011b). Ion Beam Shepherd for contactless space debris removal. *Journal of Guidance, Control and Dynamics*, 34(3):916–920.

Bombardelli, C., Urrutxua, H., Palaez, J., and et al. (2011). Space debris removal with an Ion Beam Shephard satellite: dynamics and control. In *62nd International Astronautical Congress*, Cape Town, South Africa.

Boylestad, R. L. (1997). *Introductory Circuit Analysis*. Prentice-Hall, New Jersey, 8th edition.

Brophy, J. and Rodgers, D. (2000). Ion propulsion for a Mars sample return mission. In *36th AIAA/ASME/SAE/ASEE Joint Propulsion Conference and Exhibit*, Las Vegas, NV.

227

Brophy, J. R. (1984). *Ion Thruster Performance Model.* PhD dissertation, Colorado State University, Fort Collins, CO.

Brophy, J. R. (2002). NASA's Deep Space 1 ion engine. *Review Scientific Instruments*, 73(2):1071–1078.

Brophy, J. R. and Muirhead, B. (2013). Near-Earth Asteroid Retrieval Mission (ARM) study. In *33rd International Electric Propulsion Conference*, Washington, DC.

Chabert, P. and Braithwaite, N. (2011). *Physics of Radio-Frequency Plasmas.* Cambridge University Press, Cambridge.

Chabert, P., Lichtenberg, A. J., Lieberman, M. A., and Marakhtanov, A. M. (2003). Dynamics of steady and unsteady operation of inductive discharges with attaching gases. *Journal of Applied Physics*, 94(2):831–843.

Chabert, P., Monreal, J. A., Bredin, J., and et al. (2012). Global model of a gridded-ion thruster powered by a radiofrequency inductive coil. *Physics of Plasmas*, 19(7):073512.

Chen, F. F. (2006). *Introduction to Plasma Physics and Controlled Fusion.* Springer, New York, NY, 2nd edition.

Choueiri, E. Y. (2004). A critical history of electric propulsion: the first 50 years (1906-1956). *Journal of Propulsion and Power*, 20(2):193–203.

Cichocki, F., Merino, M., Ahedo, E., and et al. (2015). Electric propulsion subsystem optimization for "Ion Beam Shepherd" missions. In *30th ISTS, 34th IEPC and 6th NSAT Joint Conference*, Hyogo-Kobe, Japan.

Cichocki, F., Merino, M., Ahedo, E., and et al. (2017). Electric propulsion subsystem optimization for "Ion Beam Shepherd" missions. *Journal of Propulsion and Power*, 32(2):370–378.

Clausing, P. (1971). The flow of highly rarefied gases through tubes of arbitrary length. *Journal of Vacuum Science and Technology*, 8(5):636–646.

Closs, M. F. (2001). *Numerical Modelling and Optimization of Radio-Frequency Ion Thrusters.* PhD dissertation, Physics Dept., University der Bundeswehr, Munich.

Collingwood, C. (2011). *Investigation of a Miniature Differential Ion Thruster.* PhD dissertation, University of Southampton, Southampton.

COMSOL Group (2016). Comsol. Multi-Physics Software Package, Ver. 5.1, Stockholm, 2015.

Farnell, C. C. (2007). *Performance and Lifetime Simulation of Ion Thruster Optics.* PhD dissertation, Colorado State University, CO.

Feili, D., Lotz, B., Bonnet, S., and et al. (2009). μNRIT-2.5 - a new optimized microthruster of Giessen University. In *31st International Electric Propulsion Conference*, Ann Arbor, MI.

Feili, D., Smirnova, M., Dobkevicius, M., and et al. (2015a). Design, construction and testing of a radio frequency mini ion engine according to the propulsion requirements of the Next Generation Gravity Missions 'NGGM'. In *30th ISTS, 34th IEPC 6th NSAT Joint Conference*, Kobe-Hyogo.

Feili, D., Smirnova, M., Dobkevicius, M., and et al. (2015b). Impulse transfer thruster for an Ion Beam Shepherd mission. In *30th ISTS, 3th IEPC and 6th NSAT Joint Conference*, Kobe, Japan.

Fortescue, P. W., Swinerd, G., and Stark, J. (2011). *Spacecraft Systems Engineering*. John Wiley & Sons, Chichester, 4th edition.

Freisinger, J., Groh, K., Krempel-Hesse, J., and et al. (1988). Non-propulsive application of the RF-ion thruster for material processing with reactive gases. In *20th Electric Propulsion Conference*, Garmisch-Partenkirchen, Germany.

Froese, A. (2007). *Particle-in-Cell Simulations of Nonlocal and Nonlinear Effects in Inductively Coupled Plasmas*. PhD dissertation, University of Saskatchewan, Saskatoon.

Garner, E. C., Rayman, M., and Brophy, J. R. (2013). In-flight operation of the Dawn ion propulsion system through year one of cruise to Ceres. In *49th AIAA/ASME/SAE/ASEE Joint Propulsion Conference*, San Jose, CA.

Gartner, W., Lotz, B., and Meyer, B. K. (2013). 3D thermal simulation of a μN-RIT. In *33rd International Electric Propulsion Conference*, Washington, D.C.

Goddard, R. H. (1906-1907). *The Green Notebooks*, 1:1–180.

Godyak, V. (2013). Ferromagnetic enhanced inductive plasma sources. *Journal of Physics D: Applied Physics*, 46(28):283001.

Godyak, V. A., Piejak, R. B., and Alexandrovich, B. M. (1998). Experimental evidence of collisionless power absorption in inductively coupled plasma. *Physical Review Letters*, 80(15):3264–3267.

Goebel, D. and Katz, I. (2008). *Fundamentals of Electric Propulsion*. John Wiley & Sons, Hoboken, NJ.

Goebel, D. M. (2008). Analytical discharge model for RF ion thrusters. *IEEE Transactions on Plasma Science*, 36(5):2111–2121.

Goldston, R. J. and Rutherford, P. H. (1995). *Introduction to Plasma Physics*. IOP Publishing, Bristol, 1st edition.

Griffiths, D. J. (1999). *Introduction to Electrodynamics*. Prentice Hall, Upper Saddle River, NJ, 3rd edition.

Groh, K. H. and Loebt, H. W. (1991). State-of-the-art of radio-frequency ion thrusters. *Journal of Propulsion and Power*, 7(4):573–579.

Grover, F. W. (1946). *Inductance calculations: working formulas and tables*. D. Van Nostrand, New York.

Gudmundsson, J. T. and Lieberman, M. A. (1997). Magnetic induction and plasma impedance in a cylindrical inductive discharge. *Plasma Sources Science and Technology*, 6(4):540–550.

Hagelaar, G. and Pitchford, L. (2005). Solving the Boltzmann equation to obtain electron transport coefficients and rate coefficients for fluid models. *Plasma Sources Science and Technology*, 14(4):722–733.

Haynes, W. M. (2016). *CRC Handbook of Chemistry and Physics*. CRC Press, Boca Raton, FL, 97th edition.

Hittorf, W. (1884). About the ionization of gases or Ueber die electricitätsleitung der gase. *Annalen der Physik*, 257(1):90–139.

Holman, J. P. (2010). *Heat Transfer*. McGraw-Hill, London, UK, 10th edition.

Huba, J. D. (2016). *NRL Plasma Formulary*. Naval Research Laboratory, Washington, D.C.

Jahn, R. G. (1968). *Physics of Electric Propulsion*. McGraw-Hill, New York, NY.

Kaganovich, I. D. and Polomarov, O. (2003). Self consistent system of equations for a kinetic description of the low-pressure discharges accounting for the nonlocal and collisioneless electron dynamics. *Physical Review Letters*, 68(2):1–12.

Kalvas, T., Tarvainen, O., Ropponen, T., and et al. (2010). IBSIMU: a three-dimensional simulation software for charged particle optics. *Review of Scientific Instruments*, 81(2):02B703.

Kasai, T., Tsojita, D., Nakano, E., and et al. (2015). On orbit demonstration plan and development status of electrodynamic tether technology on HII transfer vehicle. In *Sgobba T., Rongier I. (eds) Space Safety is No Accident*, Springer, Cham.

Killinger, R., Leiter, H., and Kukies, R. (2007). RITA ion propulsion systems for commercial and scientific applications. In *43rd AIAA/ASME/SAE/ASEE Joint Propulsion Conference & Exhibit*, Cincinnati, OH.

Kilter, M. and Karlsson, A. (2004). Micropropulsion technologies for the European high-precision formation flying interferometer DARWIN. In *4th International Spacecraft Propulsion Conference*, Sardinia, Italy.

Kim, V., Popov, G., Arkhipov, B., and et al. (2001). Electric propulsion activity in Russia. In *27th International Electric Propulsion Conference*, Pasadena, CA.

Kitamura, S., Hayakawa, Y., and Kawamoto, S. (2011). A reorbiter for GEO large space debris using ion beam. In *32nd International Electric Propulsion Conference*, Wiesbaden, Germany.

Koppel, C. R. and Estublier, D. (2005). The SMART-1 Hall effect thruster around the Moon: in flight experience. In *29th International Electric Propulsion Conference*, Princeton, NJ.

Koschade, S. E., Pinks, W., Trojan, F., and Loeb, H. W. (1972). Development of a flight prototype of the RF ion thruster RIT 10. In *9th Electric Propulsion Conference*, Bethesda, MD.

Kuninaka, H. (2005). Ambitious challenges of Japanese electric propulsion. In *29th International Electric Propulsion Conference*, Princeton, NJ.

Lee, R. Q. and Nakanishi, S. (1981). *Recent Work on an RF Ion Thruster*. NASA Technical Note, Washington, D.C, 1st edition.

Leiter, H., Ellerbrock, H., Berger, M., and et al. (2011). Development of a miniaturized RF ion engine system for commercial and scientific applications. In *47th AIAA/ASME/SAE/ASEE Joint Propulsion Conference & Exhibit*, San Diego, CA.

Leiter, H., Killinger, R., Bassner, H., and et al. (2003). Development and performance of the advanced radio frequency ion thruster RIT-XT. In *28th International Electric Propulsion Conference*, Toulouse, France.

Leiter, H., Killinger, R., Bassner, H., and Müller, J. (2009). Development and performance of the advanced radio frequency ion thruster RIT-XT. In *38th Joint Propulsion Conference*, Indianapolis, IN.

Leiter, H. J., Killinger, R., Bassner, H., and et al. (2001). Development of the radio frequency ion thruster RIT-XT: a status report. In *27th International Electric Propulsion Conference*, Pasadena, CA.

Leiter, H. J., Loeb, H. W., and Schartner, K. H. (2000). The RIT 14 ion engines - a survey of the present state of radio frequency ion thruster technology and its future potentiality. In *3rd International Conference on Spacecraft Propulsion*, Cannes, France.

Lewis, R. A., Luna, J. P., and Coombs, N. (2015). Qualification of the T6 thruster for BepiColombo. In *30th ISTS, 34th IEPC and 6th NSAT Joint Conference*, Hyogo-Kobe, Japan.

Liard, L., Raimbault, J. L., Rax, J. M., and Chabert, P. (2007). Plasma transport under neutral gas depletion conditions. *Journal of Physics D: Applied Physics*, 40(17):5192–5195.

Lieberman, M. and Lichtenberg, A. (2005). *Principles of Plasma Discharges and Materials Processing*. John Wiley & Sons, Hoboken, NJ, 2nd edition.

Lister, G. G., Li, Y.-M., and Godyak, V. A. (1996). Electrical conductivity in high-frequency plasmas. *Journal of Applied Physics*, 79(12):8993–8997.

Loeb, H. W., Freisinger, J., Groh, K. H., and Scharmann, A. (1988). State-of-the-art of the RIT ion thrusters and their spin-offs. In *39th Congress of the International Astronautical Federation*, Bangalore, India.

Loeb, W. H., Schartner, K. H., Weis, S., Feili, D., and Meyer, B. K. (2004). Development of RIT-microthrusters. In *55th International Astronautical Congress*, Vancouver, Canada.

Lotz, B. (2013). *Plasma Physical and Material Physical Aspects of the Application of Atmospheric Gases as a Propellant for Ion-Thruster of the RIT-Type*. PhD dissertation, Physics Dept., Justus-Liebig-University, Giessen.

Marcucci, M. G. and Polk, J. E. (2000). NSTAR xenon ion thruster on Deep Space 1: ground and flight tests. *Review of Scientific Instruments*, 71(3):1389–1400.

Merino, M., Ahedo, E., Bombardelli, C., and et al. (2011). Space debris removal with an Ion Beam Shepherd satellite: target-plasma interaction. In *47th AIAA/ASME/SAE/ASEE Joint Propulsion Conference & Exhibit*, San Diego, CA.

Meunier, J., Belenguer, P., and Boeuf, J. (1995). Numerical model of an AC plasma display panel cell in neon-xenon mixtures. *Journal of Applied Physics*, 78(2):731–745.

Meusemann, H. and Winter, M. (2005). Electric propulsion in Germany: current program and prospectives. In *29th International Electric Propulsion Conference*, Princeton, NJ.

Mistoco, V. F. M. (2011). *Modeling of Small Scale Radio-Frequency Inductive Discharges For Electric Propulsion Applications*. PhD dissertation, The Pennsylvania State University, Pennsylvania.

Monterde, M. P., Haines, M. G., Dangor, A. E., and et al. (1997). Kaufman-type xenon ion thruster coupling plasma: Langmuir probe measurements. *Journal of Physics D: Applied Physics*, 30(5):842–855.

Musk, E. (2016). Making humans a multiplanetary species. In *67th International Astronautical Congress*, Guadalajara, Mexico.

Nagaoka, H. (1909). The inductance coefficients of solenoids. *College of Science, Imperial University*, 27(6):1–33.

Neumann, H., Tartz, M., Scholze, F., and et al. (2007). Broad beam ion sources for electrostatic space propulsion and surface modification processes: from roots to present applications. *Contributions to Plasma Physics*, 47(7):487–497.

NG2 team (2011). Assessment of a Next Generation Gravity Mission to monitor the variations of Earth's gravity field. Technical Report NG2-ASG-FR, ESA/ESTEC.

Noord, J. V. (2007). NEXT ion thruster thermal model. In *43rd Joint Propulsion Conference and Exhibit*, Cincinnati, OH.

Patterson, M. J. and Benson, S. W. (2007). NEXT ion propulsion system development status and performance. In *43rd AIAA/ASME/SAE/ASEE Joint Propulsion Conference & Exhibit*, Cincinnati, OH.

Piejak, R. B., Godyak, V., and Alexandrovich, B. M. (1992). A simple analysis of an inductive RF discharge. *Plasma Sources Science and Technology*, 1(3):179–186.

Poynting, J. H. (1884). On the transfer of energy in the electromagnetic field. *Philosophical Transactions of the Royal Society of London*, 175:343–361.

Rayman, M. D., Fraschetti, T. C., Raymond, C. A., and et al. (2006). Dawn: a mission in development for exploration of main belt asteroids Vesta and Ceres. *Acta Astronautica*, 58(11):605–616.

Reiser, M. (2008). *Theory and Design of Charged Particle Beams*. Wiley, New York, 1st edition.

Ruiz, M., Urdampilleta, I., Bombardelli, C., and et al. (2014). The FP7 LEOSWEEP project: Improving Low Earth Orbit Security with Enhanced Electric Propulsion. In *Space Propulsion 2014 Conference*, Cologne, France.

Schäfer, M. (1971). *Plasma Diagnostic in RIT 10 Ion Thruster or Plasmadiagnostik und Energiebilanzunterscuhung an dem HF-Ionentriebwerk RIT 10*. PhD dissertation, Physics Dept., University of Giessen, Giessen.

Schulze, J., Heil, B. G., Luggenhölscher, D., and et al. (2008). Stochastic heating in asymmetric capacitively coupled RF discharges. *Journal of Physics D: Applied Physics*, 41(19):195212.

Shkarofsky, I., Johnston, T., and Bachynski, M. (1996). *The Particle Kinetics of the Plasmas*. Addison-Wesley, Reading, MA.

Sico (2017). Sico technology is producing two types of quartzglass. http://www.sico.at/en/quartz.html [Accessed: 2017-01-15].

SIGLO database (2015). http://www.lxcat.laplace.univ-tlse.fr [Accessed: 2015-05-20].

Smirnova, M., Mingo, A. P., Kazakov, E., and et al. (2016a). RIT-3.5: a radio frequency mini ion engine according to the propulsion requirements of the Next Generation Gravity Missions 'NGGM'. In *2016 Space Propulsion Conference*, Rome, Italy.

Smirnova, M., Perez, A. M., Kazakov, E., and et al. (2016b). Ion Beam Shepherd mission LEOSWEEP: mission design to ion beam thruster testing. In *Space Propulsion 2016*, Rome, Italy.

Snyder, J. S., Goebel, D. M., Hofer, R. R., and et al. (2012). Performance evaluation of the T6 ion engine. *Journal of Propulsion and Power*, 28(2):371–379.

Speth, E., Ciric, M., Feist, J. H., and et al. (1999). RF ion sources for fusion applications: design, development and performance. *Fusion Engineering and Design*, 46(2–4):383–388.

Sutton, G. P. and Biblarz, O. (2010). *Rocket Propulsion Elements*. John Wiley & Sons, Hoboken, N.J, 8th edition.

Takao, Y., Eriguchi, K., and Ono, K. (2011). Two-dimensional particle-in-cell simulation of a micro RF ion thruster. In *32nd International Electric Propulsion Conference*, Wiesbaden, Germany.

Takao, Y., Koizumi, H., Komurasaki, K., and et al. (2014). Three-dimensional particle-in-cell simulation of a miniature plasma source for a microwave discharge ion thruster. *Plasma Sources Science and Technology*, 23(6):064004.

Tapley, B. D., Bettadpur, S., Watkins, M., and et al. (2004). The Gravity Recovery and Climate Experiment: mission overview and early results. *Geophysical Research Letters*, 31(9):L09607.

The MathWorks Inc. (2014). Matlab. Computation Software Package, Ver. 2014a, Natick, MA, 2015.

Thompson, J. J. (1890). On the discharge of electricity through exhausted tubes without electrodes. *Philosophical Magazine*, 32(197):321–326 & 445–464.

Toh, K. C. and Ng, K. K. (1997). Thermal contact conductance of typical interfaces in electronic packages under low contact pressures. In *Proceedings of the 1997 1st Electronic Packaging Technology Conference (Cat. No.97TH8307)*, pages 130–135.

Tsay, M. T. T. (2006). *Numerical Modelling of a Radio-Frequency Micro Ion Thruster*. MSc dissertation, MIT, Boston.

Turkoz, E. and Celik, M. (2014). 2-D electromagnetic and fluid models for inductively coupled plasma for RF ion thruster performance evaluation. *IEEE Transactions on Plasma Science*, 42(1):235 – 240.

Turner, M. M. (1993). Collisionless electron heating in an inductively coupled discharge. *Physical Review Letters*, 71(12):1844–1847.

Vahedi, V., Lieberman, M. A., DiPeso, G. T. D., and Rognlien, D. H. (1995). Analytical model of power deposition in inductively coupled plasma sources. *Journal of Applied Physics*, 78(3):1446–1458.

Volkmar, C. and Ricklefs, U. (2014). Modelling of electrical parameters of an inductively-coupled plasma generator in 3-Dimensional cartesian space. In *2014 Space Propulsion Conference*, Cologne, Germany.

Volkmar, C. and Ricklefs, U. (2015). Implementation and verification of a hybrid performance and impedance model of gridded radio-frequency ion thrusters. *European Physical Journal D*, 69(10):227.

Wallace, N., Jameson, P., Saunders, C., and et al. (2011). The GOCE ion propulsion assembly - lessons learnt from the first 22 months of flight operations. In *32nd International Electric Propulsion Conference*, Wiesbaden, Germany.

Weibel, S. E. (1967). Anomalous skin effect in a plasma. *Physics of Fluids*, 10(4):741–748.

William, H. J. (2001). *Engineering Electromagnetics*. McGraw-Hill International Book Company, Ann Arbor, MI, 6th edition.

Williams, S. N. and Carroll, V. C. (2000). Mars missions using solar electric propulsion. *Journal of Spacecraft and Rockets*, 37(1):71–77.

Winter, M. W., Eichhorn, C., Kurtz, M. A., and et al. (2007). Status on plasma diagnostic measurements on a RIT-10 ion thruster. In *30th International Electric Propulsion Conference*, Florence, Italy.

Wirz, R. and Goebel, D. (2008). Effects of magnetic field topography on ion thruster discharge performance. *Plasma Sources Science and Technology*, 17(3):035010.

Yogesh, J. and Kenneth, E. T. (1986). *Computational Heat Transfer*. Hemisphere Publishing Corporation, Springer-Verlag, Berlin, 1st edition.